UNIVERSITY OF OKLAHOMA

GRADUATE COLLEGE

A SUGGESTED DESIGN APPROACH FOR BUILT-UP COLD-FORMED COLUMNS BASED ON RESEARCH USING NONLINEAR FINITE ELEMENT METHOD

A DISSERTATION

SUBMITTED TO THE GRADUATE FACULTY

in partial fulfillment of the requirements for the

Degree of

DOCTOR OF PHILOSOPHY

By

KRISDA PIYAWAT
Norman, Oklahoma
2011

Downloaded from SHAREOK. Persistent Handle URL: https://hdl.handle.net/11244/318747

A SUGGESTED DESIGN APPROACH FOR BUILT-UP COLD-FORMED COLUMNS BASED ON RESEARCH USING NONLINEAR FINITE ELEMENT METHOD

A DISSERTATION APPROVED FOR THE
SCHOOL OF CIVIL ENGINEERING AND ENVIRONMENTAL SCIENCE

BY

Dr. Chris C.E. Ramseyer, Chair

Dr. K. K. Muraleetharan

Dr. Thomas Kang

Dr. John E. Fagan

Dr. Lisa M. Holliday

© Copyright by KRISDA PIYAWAT 2011
All Right Reserved.

To my family and Poopae

Acknowledgements

I wish to thank my advisor, Dr. Chris Ramseyer. This work would never be done without him. He helped me greatly, especially when I was really in a deep trouble. He gave me all the freedom in the world to work independently. I am also grateful to my committee members, Dr. Thomas Kang, Dr. Kyran Mish, Dr. John Fegan, Dr. K.K. Muraleetharan, and Dr. Lisa Holliday. You guys are great!.

Contents

1 INTRODUCTION **1**

2 LITERATURE REVIEW **6**
2.1 Buckling in Cold-Formed Sections 6
2.2 Buckling Provisions of the 2007 AISI Specifications 9
2.3 Experimental Study of Built-Up, Cold-Formed Sections 15
2.3.1 General 15
2.3.2 Specimen Geometry and Welding Detail 15
2.3.3 Summary of Experimental Results 18
2.4 Numerical Buckling Analyses of Build-Up, Cold-Formed Members . . . 22
2.4.1 Inherent Nonlinearities 23
2.4.2 Geometric Imperfection 27
2.4.3 Cold-Work Effect and Residual Stresses 31
2.5 Solution Strategy 33

3 PHASE I: ANSYS VALIDATION AND ABAQUS VERIFICATION[1] **47**
3.1 Overview of *Phase I* 47
3.2 Numerical Simulation of Buckling in Built-up, Cold-Formed Sections . . 48
3.2.1 Preprocessing Phase 48
3.2.2 Solution Phase 55
3.2.3 Postprocessing Phase 59
3.3 Conclusion 73
3.4 Discussion 73

4 PHASE II: FORMULATION OF THE PROPOSED DISTORTIONAL EQUATION[2] **75**
4.1 Overview of *Phase II* 75
4.2 Computational Modeling of Buckling in Built-up, Cold-formed Sections . 75
4.3 Parametric Study to Numerically Expand the Buckling-Capacity Archive 79
4.4 Formulation of the Distortional Equation 83
4.5 Evaluation of the Proposed Distortional Equation 90
4.6 Conclusion 92

5 CONCLUSIONS **96**

A LABVIEWS IMPLEMENTATION OF ARC-LENGTH METHOD **102**

B LOAD VS. DISPLACEMENT HISTORY **106**

C QUALITATIVE COMPARISON OF BUCKLED SHAPES **247**

List of Tables

1 Types of geometric nonlinear analyses by Bakker and Pekoz (2001). Stress stiffening is a coupling phenomena between membrane stresses and lateral displacements induced by bending (Cook, 1995; Cook et al., 2001). A member under a compressive membrane stress will buckle as soon as the membrane stress is large enough to reduce the bending stiffness to zero. 26

2 Material characteristics obtained from coupon tests performed on specimens of 0.5-in width and 2-in. length, cut from actual members (Whittle, 2007). The averaged values of three identical tests for each thickness are listed in an engineering format. ANSYS requires material stress-strain relation in this format, while the logarithmic format is required in ABAQUS. The relation between the two formats is: $\varepsilon_{\text{true}} = \ln(1+\varepsilon)$ and $\sigma_{\text{true}} = \sigma(1+\varepsilon)$. 50

3 The built-up characteristics of the 18 configurations. The fastening spacing a is taken as one third of an unbraced length for the *DW2* pattern to comply with the upper limit of the modified slenderness ratio, as the factor of $\left(\frac{a}{ri}\right)$ does not exceed $0.5\left(\frac{kL}{r}\right)_o$. 80

List of Figures

1 The layout of the proposed work to develop a distortional design equation. 5
2 The limit states in compressive cold-formed sections (Yu and LaBoube, 2010). 8
3 The nominal buckling strength of a built-up, *I*-section (also valid for an *R*-section) determined according to the 2007 AISI standard, Section C4.1.1, C4.1.2, and C4.2(b). 14
4 The pure-compression, experimental setups (Brueggen and Ramseyer, 2003; Whittle, 2007). 16
5 Section details of the single and built-up members. 17
6 Weld orientations. 18
7 Comparison of the experimental to the design capacities of the 2001 AISI specification. All the 55.5" members were conducted by Brueggen and Ramseyer (2003) whereas the members of *R1* and *R2* with 71" length were carried by Whittle and Ramseyer (2009). The rest were done by Biggs (2008). Three experimental repetitions per one given configuration were done in Brueggen and Ramseyer (2003), Whittle (2007), and Whittle and Ramseyer (2009). 20
8 Comparison of the experimental to the design capacities of the 2007 AISI specification. All the 55.5" members were conducted by Brueggen and Ramseyer (2003) whereas the members of *R1* and *R2* with 71" length were carried by Whittle and Ramseyer (2009). The rest were done by Biggs (2008). Three experimental repetitions per one given configuration were done in Brueggen and Ramseyer (2003), Whittle (2007), and Whittle and Ramseyer (2009). 21
9 Overview of possible errors in finite-element modeling of thin-walled members (Bakker and Pekoz, 2001). 23
10 ANSYS implicit-static model of the built-up, *R*-section. 24
11 ABAQUS explicit-dynamic model of the built-up, *I*-section. 24
12 Qualitative load-deformation responses of a cylindrical shell showing an importance of geometric perturbation (Cook et al., 2001). 29
13 An implementation of geometric imperfection through seeding a known deformed configuration of an Eigen mode onto a perfect configuration. The imperfection factor δ is taken as $\frac{L}{2000}$ (for a global imperfection) or according to the first expression of Eq. (27) (for a local imperfection). . . 30
14 The first Eigen of the *DW-R1* member. A flexural-torsional buckled shape is illustrated on an exaggerated scale for clarity. 31

15 Two nonlinear single-degree-of-freedom systems to review the implicit and explicit numerical schemes available for nonlinear buckling analyses. On the left, a nonlinear-geometric system of an elastic bar attached to a roller and a linear spring on the right end and pinned on the left end (Crisfield, 1998) is implicitly solved under the Newton-Raphson and Arc-Length methods as shown in Figs. 16 and 17. On the right, a nonlinear-hysteretic dynamic system of a unit mass with a Ramberg-Osgood restoring force (Jennings, 1964) is exited under an amplitude-modulated cyclic loading (Piyawat et al., 2008). At a given time step, the solution of the restoring force is iterated under the Newton-Raphson scheme, while the solution of displacement is advanced along the time span using an explicit Central-Difference integration. The implementation flowchart is given in Fig. 18. 35

16 A hardening load-displacement response history of a nonlinear SDOF of an elastic bar resting on a linear spring and subjected to an upward external force f_{ext} of 85 N (Crisfield, 1998). The system has geometric nonlinearity, since the stiffness depends on the deformed configuration, i.e., $K_t = K_t(u)$. The solutions of u are obtained iteratively using the forced-controlled Newton-Raphson method. The solutions converge along referenced forces of a constant increment of 5 N. Convergence is assumed upon an out-of-balance force of $|f_{\text{int}} - f_{\text{ext}}|$ less than 10^{-6} N. The convergence history including the incremental displacements Δu and required iteration number i as well as the iteration history of the fifth substep are also provided. 38

17 A snap-through response history of the first SDOF system shown in Fig. 15. Basically, the system is identical with the one in Fig. 16 except no linear spring supporting at the bar tip, i.e., $k_s = 0$. The spherical Arc-Length scheme is used to trace the solutions of the displacement u and the load proportional factor λ converging along referenced spherical arcs instead of linear referenced loads as in Fig. 16. Various convergence histories including the incremental displacement $\Delta\delta$, the incremental load factor $\Delta\lambda$, the arc radius ΔL, and the iteration history at 17^{th} substep are also included. 41

18 An implementation flowchart of a nonlinear-hysteretic SDOF system under an amplitude-modulated excitation. The restoring force r of the Ramberg-Osgood feature (Jennings, 1964) is iterated under the Newton-Raphson scheme. The displacement u is explicitly integrated along the time span using the Central-Difference integrator. 46

19 The modeling procedure to perform a nonlinear (large-displacement) buckling analysis. 49

20 The key details of the ANSYS implicit-static and the ABAQUS explicit-dynamic modelings. The differences between the two modeling schemes are highlighted in red. 52

21 ANSYS SOLID45/SHELL181 implicit-static model of the built-up, *R*-section. 54

22 The ABAQUS explicit-dynamic model of the built-up, *I*-section. 56
23 Load vs. deformation history of the 71”-long, *R3*-sections. 60
24 Compressive load-carrying validation and verification of the single sections under ANSYS implicit-static and ABAQUS explicit-dynamic. . . . 61
25 Compressive load-carrying validation of the built-up, *I*- and *R*-sections under the ANSYS implicit-static modeling. The ANSYS model is found inapplicable for asymmetrical, single-sided members prone to flexural or flexural-torsional buckling. 62
26 Flexural-torsional buckling of the 71”-long *C1* and *DW-R1* members. . . . 63
27 Local buckling of the lips in the 55.5”-long chord. 64
28 Distortional deformed shapes of 42”- and 71”-long *R3*-sections. 65
29 Distortional deformed shapes of 42”- and 71”-long *I3*-sections. 66
30 Plastic deformation around the weld of the 55.5”-long, *SW1-064R1* members. 67
31 Buckled shape of the 71”-long, *SW5-064R1* member. 67
32 Verification of the ANSYS implicit-static results under the ABAQUS explicit-dynamic simulation. 69
33 Reaction and energy time histories of 42.0”- and 55.5”-long, built-up sections. 70
34 Reaction and energy time history of the 71”-long, single-sided welding sections. 71
35 Reaction and energy time history of 71”-long, double-sided welding sections. 72
36 ANSYS SOLID45 FEM model of the built-up, *I*-section. 77
37 ANSYS SOLID45 FEM model of the built-up, *R*-section. 78
38 Parametric study of Members *DW2-I1* and *-R1* over varying unbraced lengths. A comparison to their corresponding experimental counterparts is made. 84
39 Parametric study of Members *DW2-I2* and *-R2* over varying unbraced lengths. A comparison to their corresponding experimental counterparts is made. 85
40 Parametric study of Members *DW2-I3* and *-R3* over varying unbraced lengths. A comparison to their corresponding experimental counterparts is made. 86
41 Parametric study of Members *DW2-I1* and *-R1* over varying unbraced lengths. A comparison to the nominal compressive strengths of the 2007 AISI specification and the proposed distortional equation (Eq. (61)) is made. 87
42 Parametric study of Members *DW2-I2* and *-R2* over varying unbraced lengths. A comparison to the nominal compressive strengths of the 2007 AISI specification and the proposed distortional equation (Eq. (61)) is made. 88
43 Parametric study of Members *DW2-I3* and *-R3* over varying unbraced lengths. A comparison to the nominal compressive strengths of the 2007 AISI specification and the proposed distortional equation (Eq. (61)) is made. 89
44 A three-dimensional surface fitting of 114 distortional-buckling data retrieved from Figs. 41-43. 91

45 Experimental compressive strength of *I1*- and *R1*-sections versus the corresponding proposed nominal strengths. 93
46 Experimental compressive strength of *I2*- and *R2*-sections versus the corresponding proposed nominal strengths. 94
47 Experimental compressive strength of *I3*- and *R3*-sections versus the corresponding proposed nominal strengths. 95
48 LabView implementation of spherical Arc-Length method to approximate a snap-through behavior of a nonlinear-geometric SDOF elastic bar as shown in Fig. 17. This VI is a driver containing subVIs as shown in Figs. 49 and 50. 103
49 A subVI of Iter.vi to perform iteration. This subVI is called by the driver VI in Fig. 48. 104
50 SubVIs of the driver VI in Fig. 48. 105
51 Overview of load vs. deformation history of *Chord*-sections presented in Figs. 52-54. 107
52 Load vs. deformation history of chord members 108
53 Load vs. deformation history of chord members 109
54 Load vs. deformation history of chord members 110
55 Overview of load vs. deformation history of *C*-sections presented in Figs. 56-70. 111
56 Load vs. deformation history of 55.5”-long, 0.064”-thick *C1* 112
57 Load vs. deformation history of 55.5”-long, 0.08”-thick *C1* 113
58 Load vs. deformation history of 55.5”-long, 0.1”-thick *C1* 114
59 Load vs. deformation history of 71”-long, 0.064”-thick *C1* 115
60 Load vs. deformation history of 71”-long, 0.08”-thick *C1* 116
61 Load vs. deformation history of 71”-long, 0.1”-thick *C1* 117
62 Load vs. deformation history of 71”-long, 0.064”-thick *C2* 118
63 Load vs. deformation history of 71”-long, 0.08”-thick *C2* 119
64 Load vs. deformation history of 71”-long, 0.1”-thick *C2* 120
65 Load vs. deformation history of 42”-long, 0.064”-thick *C3* 121
66 Load vs. deformation history of 42”-long, 0.08”-thick *C3* 122
67 Load vs. deformation history of 42”-long, 0.1”-thick *C3* 123
68 Load vs. deformation history of 71”-long, 0.064”-thick *C3* 124
69 Load vs. deformation history of 71”-long, 0.08”-thick *C3* 125
70 Load vs. deformation history of 71”-long, 0.1”-thick *C3* 126
71 Overview of load vs. deformation history of 42”-long *R3*-sections presented in Figs. 72-80. 127
72 Load vs. deformation history of 42”-long, 0.064”-thick *DW-R3* 128
73 Load vs. deformation history of 42”-long, 0.08”-thick *DW-R3* 129
74 Load vs. deformation history of 42”-long, 0.1”-thick *DW-R3* 130
75 Load vs. deformation history of 42”-long, 0.064”-thick *SW1-R3* 131
76 Load vs. deformation history of 42”-long, 0.08”-thick *SW1-R3* 132
77 Load vs. deformation history of 42”-long, 0.1”-thick *SW1-R3* 133
78 Load vs. deformation history of 42”-long, 0.064”-thick *DW1-R3* 134
79 Load vs. deformation history of 42”-long, 0.08”-thick *DW1-R3* 135

80 Load vs. deformation history of 42”-long, 0.1”-thick *DW1-R3* 136
81 Overview of load vs. deformation history of 55.5”-long, single-sided *R1*-sections presented in Figs. 82-87. 137
82 Load vs. deformation history of 55.5”-long, 0.064”-thick *SW1-R1*. 138
83 Load vs. deformation history of 55.5”-long, 0.08”-thick *SW1-R1*. 139
84 Load vs. deformation history of 55.5”-long, 0.1”-thick *SW1-R1*. 140
85 Load vs. deformation history of 55.5”-long, 0.064”-thick *SW2-R1*. 141
86 Load vs. deformation history of 55.5”-long, 0.08”-thick *SW2-R1*. 142
87 Load vs. deformation history of 55.5”-long, 0.1”-thick *SW2-R1*. 143
88 Overview of load vs. deformation history of 71”-long, single-sided *R1*-sections presented in Figs. 89-97. 144
89 Load vs. deformation history of 71”-long, 0.064”-thick *SW1-R1*. 145
90 Load vs. deformation history of 71”-long, 0.08”-thick *SW1-R1*. 146
91 Load vs. deformation history of 71”-long, 0.1”-thick *SW1-R1*. 147
92 Load vs. deformation history of 71”-long, 0.064”-thick *SW2-R1*. 148
93 Load vs. deformation history of 71”-long, 0.08”-thick *SW2-R1*. 149
94 Load vs. deformation history of 71”-long, 0.1”-thick *SW2-R1*. 150
95 Load vs. deformation history of 71”-long, 0.064”-thick *SW5-R1*. 151
96 Load vs. deformation history of 71”-long, 0.08”-thick *SW5-R1*. 152
97 Load vs. deformation history of 71”-long, 0.1”-thick *SW5-R1*. 153
98 Overview of load vs. deformation history of 71”-long, single-sided *R2*-sections presented in Figs 99-107. 154
99 Load vs. deformation history of 71”-long, 0.064”-thick *SW1-R2*. 155
100 Load vs. deformation history of 71”-long, 0.08”-thick *SW1-R2*. 156
101 Load vs. deformation history of 71”-long, 0.1”-thick *SW1-R2*. 157
102 Load vs. deformation history of 71”-long, 0.064”-thick *SW2-R2*. 158
103 Load vs. deformation history of 71”-long, 0.08”-thick *SW2-R2*. 159
104 Load vs. deformation history of 71”-long, 0.1”-thick *SW2-R2*. 160
105 Load vs. deformation history of 71”-long, 0.064”-thick *SW5-R2*. 161
106 Load vs. deformation history of 71”-long, 0.08”-thick *SW5-R2*. 162
107 Load vs. deformation history of 71”-long, 0.1”-thick *SW5-R2*. 163
108 Overview of load vs. deformation history of 71”-long, single-sided *R3*-sections presented in Figs 109-117. 164
109 Load vs. deformation history of 71”-long, 0.064”-thick *SW1-R3*. 165
110 Load vs. deformation history of 71”-long, 0.08”-thick *SW1-R3*. 166
111 Load vs. deformation history of 71”-long, 0.1”-thick *SW1-R3*. 167
112 Load vs. deformation history of 71”-long, 0.064”-thick *SW2-R3*. 168
113 Load vs. deformation history of 71”-long, 0.08”-thick *SW2-R3*. 169
114 Load vs. deformation history of 71”-long, 0.1”-thick *SW2-R3*. 170
115 Load vs. deformation history of 71”-long, 0.064”-thick *SW5-R3*. 171
116 Load vs. deformation history of 71”-long, 0.08”-thick *SW5-R3*. 172
117 Load vs. deformation history of 71”-long, 0.1”-thick *SW5-R3*. 173
118 Overview of load vs. deformation history of 55.5”-long, double-sided *R1*-sections presented Figs. 119-127. 174
119 Load vs. deformation history of 55.5”-long, 0.064”-thick *DW-R1*. 175

120 Load vs. deformation history of 55.5”-long, 0.08”-thick *DW-R1*. 176
121 Load vs. deformation history of 55.5”-long, 0.1”-thick *DW-R1*. 177
122 Load vs. deformation history of 55.5”-long, 0.064”-thick *DW1-R1*. 178
123 Load vs. deformation history of 55.5”-long, 0.08”-thick *DW1-R1*. 179
124 Load vs. deformation history of 55.5”-long, 0.1”-thick *DW1-R1*. 180
125 Load vs. deformation history of 55.5”-long, 0.064”-thick *DW2-R1*. 181
126 Load vs. deformation history of 55.5”-long, 0.08”-thick *DW2-R1*. 182
127 Load vs. deformation history of 55.5”-long, 0.1”-thick *DW2-R1*. 183
128 Overview of load vs. deformation history of 71”-long, double-sided *R1*-sections presented in Figs. 129-140. 184
129 Load vs. deformation history of 71”-long, 0.064”-thick *DW-R1*. 185
130 Load vs. deformation history of 71”-long, 0.08”-thick *DW-R1*. 186
131 Load vs. deformation history of 71”-long, 0.1”-thick *DW-R1*. 187
132 Load vs. deformation history of 71”-long, 0.064”-thick *DW1-R1*. 188
133 Load vs. deformation history of 71”-long, 0.08”-thick *DW1-R1*. 189
134 Load vs. deformation history of 71”-long, 0.1”-thick *DW1-R1*. 190
135 Load vs. deformation history of 71”-long, 0.064”-thick *DW2-R1*. 191
136 Load vs. deformation history of 71”-long, 0.08”-thick *DW2-R1*. 192
137 Load vs. deformation history of 71”-long, 0.1”-thick *DW2-R1*. 193
138 Load vs. deformation history of 71”-long, 0.064”-thick *DW5-R1*. 194
139 Load vs. deformation history of 71”-long, 0.08”-thick *DW5-R1*. 195
140 Load vs. deformation history of 71”-long, 0.1”-thick *DW5-R1*. 196
141 Overview of load vs. deformation history of 71”-long, double-sided *R2*-sections presented in Figs. 142-153. 197
142 Load vs. deformation history of 71”-long, 0.064”-thick *DW-R2*. 198
143 Load vs. deformation history of 71”-long, 0.08”-thick *DW-R2*. 199
144 Load vs. deformation history of 71”-long, 0.1”-thick *DW-R2*. 200
145 Load vs. deformation history of 71”-long, 0.064”-thick *DW1-R2*. 201
146 Load vs. deformation history of 71”-long, 0.08”-thick *DW1-R2*. 202
147 Load vs. deformation history of 71”-long, 0.1”-thick *DW1-R2*. 203
148 Load vs. deformation history of 71”-long, 0.064”-thick *DW2-R2*. 204
149 Load vs. deformation history of 71”-long, 0.08”-thick *DW2-R2*. 205
150 Load vs. deformation history of 71”-long, 0.1”-thick *DW2-R2*. 206
151 Load vs. deformation history of 71”-long, 0.064”-thick *DW5-R2*. 207
152 Load vs. deformation history of 71”-long, 0.08”-thick *DW5-R2*. 208
153 Load vs. deformation history of 71”-long, 0.1”-thick *DW5-R2*. 209
154 Overview of load vs. deformation history of 42”-long *I3*-sections presented in Figs. 155-163. 210
155 Load vs. deformation history of 42”-long, 0.064”-thick *DW-I3* 211
156 Load vs. deformation history of 42”-long, 0.08”-thick *DW-I3* 212
157 Load vs. deformation history of 42”-long, 0.1”-thick *DW-I3* 213
158 Load vs. deformation history of 42”-long, 0.064”-thick *SW1-I3* 214
159 Load vs. deformation history of 42”-long, 0.08”-thick *SW1-I3* 215
160 Load vs. deformation history of 42”-long, 0.1”-thick *SW1-I3* 216
161 Load vs. deformation history of 42”-long, 0.064”-thick *DW1-I3* 217

162 Load vs. deformation history of 42”-long, 0.08”-thick *DW1-I3* 218
163 Load vs. deformation history of 42”-long, 0.1”-thick *DW1-I3* 219
164 Overview of load vs. deformation history of 55.5”-long, *DW-I1* presented in Figs 165-167. 220
165 Load vs. deformation history of 55.5”-long, 0.064”-thick *DW-I1*. 221
166 Load vs. deformation history of 55.5”-long, 0.08”-thick *DW-I1*. 222
167 Load vs. deformation history of 55.5”-long, 0.1”-thick *DW-I1*. 223
168 Overview of load vs. deformation history of 71”-long, single-sided *I3*-sections presented in Figs 169-177. 224
169 Load vs. deformation history of 71”-long, 0.064”-thick *SW1-I3*. 225
170 Load vs. deformation history of 71”-long, 0.08”-thick *SW1-I3*. 226
171 Load vs. deformation history of 71”-long, 0.1”-thick *SW1-I3*. 227
172 Load vs. deformation history of 71”-long, 0.064”-thick *SW2-I3*. 228
173 Load vs. deformation history of 71”-long, 0.08”-thick *SW2-I3*. 229
174 Load vs. deformation history of 71”-long, 0.1”-thick *SW2-I3*. 230
175 Load vs. deformation history of 71”-long, 0.064”-thick *SW5-I3*. 231
176 Load vs. deformation history of 71”-long, 0.08”-thick *SW5-I3*. 232
177 Load vs. deformation history of 71”-long, 0.1”-thick *SW5-I3*. 233
178 Overview of load vs. deformation history of 71”-long, double-sided *I3*-sections presented in Figs. 179-190. 234
179 Load vs. deformation history of 71”-long, 0.064”-thick *DW-I3*. 235
180 Load vs. deformation history of 71”-long, 0.08”-thick *DW-I3*. 236
181 Load vs. deformation history of 71”-long, 0.1”-thick *DW-I3*. 237
182 Load vs. deformation history of 71”-long, 0.064”-thick *DW1-I3*. 238
183 Load vs. deformation history of 71”-long, 0.08”-thick *DW1-I3*. 239
184 Load vs. deformation history of 71”-long, 0.1”-thick *DW1-I3*. 240
185 Load vs. deformation history of 71”-long, 0.064”-thick *DW2-I3*. 241
186 Load vs. deformation history of 71”-long, 0.08”-thick *DW2-I3*. 242
187 Load vs. deformation history of 71”-long, 0.1”-thick *DW2-I3*. 243
188 Load vs. deformation history of 71”-long, 0.064”-thick *DW5-I3*. 244
189 Load vs. deformation history of 71”-long, 0.08”-thick *DW5-I3*. 245
190 Load vs. deformation history of 71”-long, 0.1”-thick *DW5-I3*. 246
191 Post-buckling, deformed shapes with von Mises stress contours of the chord and the channel members. 248
192 Post-buckling, deformed shapes with von Mises stress contours of *R1*-sections. 249
193 Post-buckling, deformed shapes with von Mises stress contours of *R2*-sections. 250
194 Post-buckling, deformed shapes with von Mises stress contours of *R3*-sections. 251
195 Post-buckling, deformed shapes with von Mises stress contours of *I1*- and *I3*-sections. 252

ABSTRACT

A deficiency of the 2007 AISI specification, Sections C4 and D1.2 for built-up, cold-formed members under pure compression is experimentally identified. The AISI specification is found to be exceedingly conservative, especially for distortional-buckling members with a larger cross section and a longer length. By using sequential batch-feeding, nearly a thousand nonlinear-buckling finite element simulations of built-up, cold-formed sections are carried out to validate the model prior to experimental work, identify the extent of the deficiency, and rectify the deficiency. In all, a simpler less-conservative design equation for cold-formed built-up members prone to distortional buckling is proposed in this two-phase work.

In *Phase I*, highly-nonlinear, finite-element models and a state-of-the-art modeling strategy are used to validate and verify the geometrically unstable built-up compression members which exhibit a variety of buckling behaviors. The finite element program ANSYS is used to validate over 265 experimental tests, while the use of the finite element program ABAQUS is used to verify the ANSYS results. Two totally different numerical schemes of implicit-static and explicit-dynamic under various iterative and non-iterative solution techniques, which include Newton-Raphson, Arc-Length, Riks, and Central-Difference integration methods, are converged toward identical solutions. A structural solid (brick) element is thoroughly examined and compared with a structural shell element (most commonly used in the modeling discipline for thin-walled structures) which provides advantages in: (1) advancing through a critical buckling state, (2) tracing a softening response of the post-buckling regime, and (3) assuring the modeling of a true structural failure (not a numerically induced one).

In *Phase II*, a parametric study of an additional 360 cold-formed built-up compression members are modeled to investigate new structural built-up configurations. The AISI specification flexural provision is applied in conjunction with the slenderness modification and the code predictions are compared to the results of the analytical models. A pro-

posed design equation is developed based on a regression analysis of a three-dimensional surface fitting. The proposed equation corrects the deficiency of the distortional provision. An evaluation of the proposed design equation shows good agreement with the experimentally measured capacities.

1 INTRODUCTION

Over 70% of all low rise commercial construction in the United States use thin-walled, cold-formed sections due to their high strength-to-weight capacity. These sections are commonly used as compression members in structural systems such as trusses and as wall struts. On the other hand, being a slender member with a large width-to-thickness ratio has consequences with several pronounced buckling issues. The members tend to fail at a critical stress well below the yield strength due to loss of stability (Cook et al., 2001), resulting from imperfections in loading (eccentricity) and/or in geometry out-of-straightness and out-of-flatness (Yu and LaBoube, 2010).

Over the past two decades, limited studies have been conducted in the area of built-up, cold-formed structural sections and even less in the area of closed sections with stitch-weld attachments (Whittle and Ramseyer, 2009). As a consequence, the provision for the built-up sections in the AISI specification has been substantially adopted from the AISC hot-rolled steel counterparts, while disregarding a significant difference in the failure behavior (Whittle, 2007; Whittle and Ramseyer, 2009). Built-up, hot-rolled sections that meet the AISC specification nearly always fail due to flexural buckling, whereas distortional buckling may be a possible failure mode in cold-formed sections (Biggs, 2008).

Recently, a series of over 265 pure-compression, buckling tests on built-up, cold-formed sections were carried out at the Donald G. Fears Structural Engineering Laboratory at the University of Oklahoma, by Brueggen and Ramseyer (2003), Whittle (2007), Biggs (2008), and Whittle and Ramseyer (2009). The objectives were: (1) to determine the maximum capacities for a variety of built-up members and to investigate the accuracy of the previous 2001 AISI specification (Sections C4.1 and C4.5 (AISI, 2001)) and (2) to validate the effectiveness of the modified slenderness ratio $\left(\frac{kL}{r}\right)_m$ for built-up members. The details relating to (1) the built-up characteristics, (2) the test setup and (3) the experimental results are given in Section 2.3. The following two conclusions were drawn. The provision upon using the modified slenderness ratio was found to be exceed-

ingly conservative, especially, for longer and thicker built-up members (Brueggen and Ramseyer, 2003; Whittle, 2007; Whittle and Ramseyer, 2009), but, on the other hand it was also overly unconservative for larger built-up sections prone to distortional buckling (Biggs, 2008). In addition it was suggested that there existed a need to consider a governing distortional failure mode in addition to the global flexural buckling mode. This recommendation has been implemented in Section C4.2 of the current 2007 AISI specification. Nonetheless, a simple comparison between the specification and the experimental strengths indicates that the specification is exceedingly conservative for larger and longer members that are governed by distortional buckling. This deficiency (poor estimation of nominal strength yet requiring unnecessarily complicated calculations) inspires the present work. This investigation carefully evaluates the existing experimental data, validates a finite element model, expands our understanding using analytical methods, and (as the ultimate contribution to the community) proposes a simpler more accurate design provision for the distortional buckling mode of failure for built-up, cold-formed compression members

To achieve these goals, a numerical simulation using the finite element method (FEM) was selected as an excellent candidate for obtaining analytical solutions (in addition to the experimental simulation). With the advancement in element technology, more robust implicit and explicit solution schemes, and more affordable computational resources, realistic analyses of geometrically unstable configurations, that take into account all the nonlinear sources may be possible. Not only can the ultimate capacity be accurately predicted, the deformed shape can also be visualized with associated stress contours, indicating a critical region. The two finite element programs, ANSYS and ABAQUS were used to (*Phase I*): create a state-of-the-art modeling strategy based upon validating and verifying over 265 tests (Chapter 3) and (*Phase II*): carry out a parametric study of previously uninvestigated configurations to expand the buckling-capacity archive for the development of the proposed distortional equation (Chapter 4). The proposed distortional design

equation was formulated using a least-square regression analysis of a three-dimensional surface fitting.

Two totally different numerical schemes, implicit-static and explicit-dynamic, under various iterative and non-iterative solution techniques, including Newton-Raphson, Arc-Length, Riks, and Central-Difference integration methods, are investigated and found to converge toward identical solutions to handle a softening-descending, post-buckling loading branch that includes both brittle- and ductile-failure mechanisms that are inherently unstable. In short, the road map of the present work is illustrated in Fig. 1.

In the upper left corner of Fig. 1, you will find a summary of the motivation and objectives of this research. In the lower left corner, the buckling-capacity archive of three two-dimensional arrays (whose elements represent the ultimate capacities of various built-up configurations) represents the research matrix of this work. Each array corresponds to one unique section thickness of 0.064, 0.08, and 0.1 in. (adopted to correspond with the 265 experimental tests). The array row-wise represents the three section widths (1.625, 2.625 and 3.625 in.) of two built-up orientations (*I*- and *R*-shape) and along the columns, 20 unbraced member lengths from 15 to 140 in. The elements in red (corresponding to the column lengths of 42, 55.5, and 71 in.) are the 265 experimental tests that are used to validate the numerical models. The elements in blue are analyzed using the numerical models used as part of the parametric study. The following is a summary of accomplishments of this work:

- Nearly 1,000 highly nonlinear buckling analyses of built-up, cold-formed sections with various intermediate welding patterns are performed through an intensive programming capability of sequential batch-feeding (ANSYS®, 2009b);
- Validation of the ANSYS implicit-static model using over 265 experimental tests;
- Verification of the ANSYS results using ABAQUS explicit-dynamic modeling (a systematic procedure to dynamically tackle a contact-formulation difficulty en-

countered in the ABAQUS static simulations (Bacque and K.J., 2009a,b));

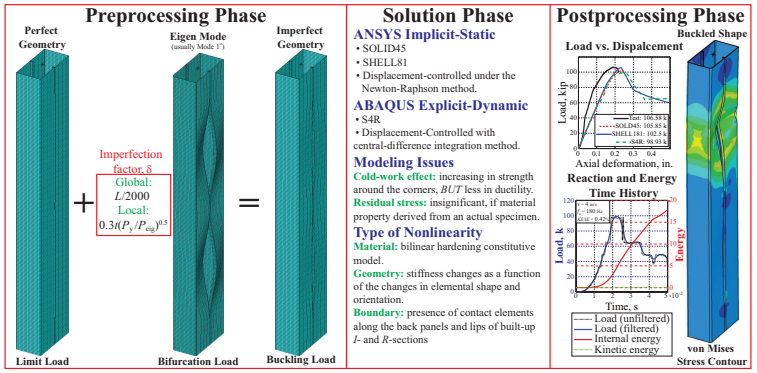
- Thorough comparison of the solution advantages to using structural brick element SOLID45 (more precise in geometric and equilibrium approximations (Bakker and Pekoz, 2001)) versus structural shell element SHELL181 (most commonly used in modelings of thin-walled structures) including the ability to:
  - advance through a critical buckling state;
  - trace a softening response of the post-buckling regime;
  - assure a true structural failure (not a numerical blowout);
- The creation of a more accurate and simpler distortional equation along with a suggested design approach for symmetrical built-up, cold-formed columns.

With the above accomplishments, the limited studies in the area of built-up, cold-formed sections have been surpassed. Cold-formed structures can be better designed with the suggested approach, which is the ultimate goal for any research on this topic, and is the main contribution of this work to the structural engineering community.

Motivation: An alleged experimentally-addressed deficiency of the 2007 AISI specification (Sections C4 and D1.2) for concentrically-loading built-up, cold-formed sections of being *exceedingly conservative*, especially, for larger and longer members prone to distortional buckling.

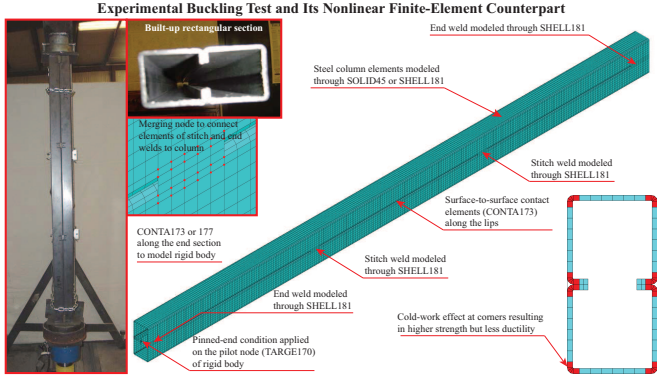
Objective: To numerically *justify* and *rectify* the addressed deficiency through a suggested design approach based on *a proposed distortional-buckling equation*.

***Phase I*:** Calibration of a state of the art modeling strategy (322 simulations). The two packages of ANSYS implicit-static and ABAQUS explicit-dynamic are seamlessly integrated to *validate* and *verify* over 265 experimental tests.

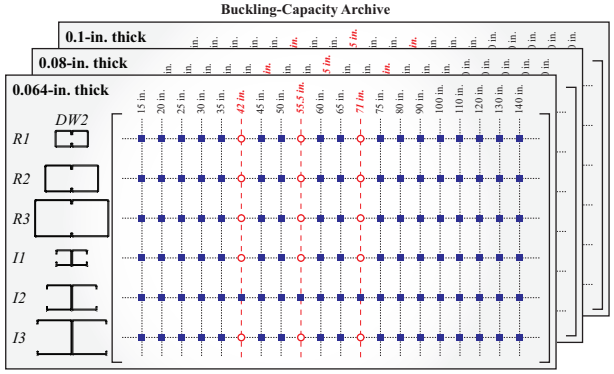


***Phase II*:** Numerical expansion of additional 360 uninvestigated configurations through a parametric study to *justify* and *rectify* the experimentally-highlighted deficiency upon the proposed distortional-buckling equation formulated through a regression analysis in the least square error sense of a 3D surface fitting.

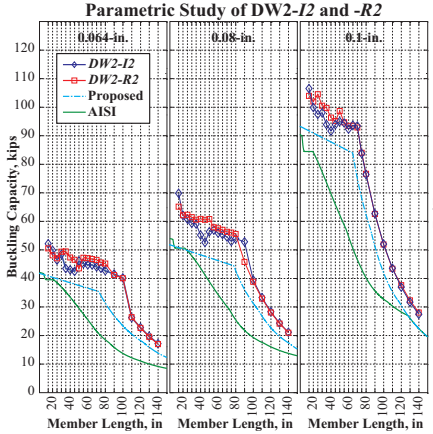
Experimental Buckling Test and Its Nonlinear Finite-Element Counterpart



Buckling-Capacity Archive



Parametric Study of DW2-*I2* and -*R2*



Least-Square Surface Fitting Correlating Buckling Capacity to the Out-of-Straightness (the Modified Slender Ratio) and the Out-of-Flatness (Thickness-to-Width)

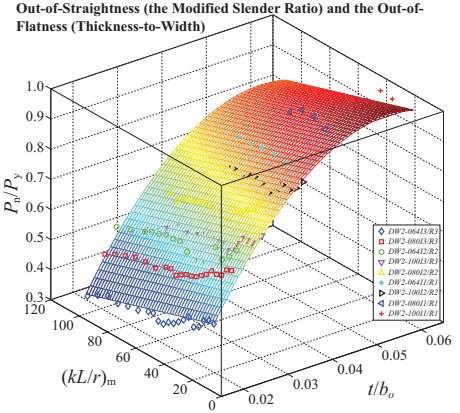


Figure 1: The layout of the proposed work to develop a distortional design equation.

2 LITERATURE REVIEW

Reviews of the relevant experimental and numerical studies related to buckling in built-up, cold-formed sections include:

- a series of experimental studies by a research team from the University of Oklahoma to confirm the appropriateness of the modified slenderness ratio in the AISI specification
- the numerical modeling aspects of buckling in built-up, cold-formed sections including the use of:
  - geometric perturbation to trigger an instability bypassing an exaggerated bifurcation load (a severe discontinuity in the response causing a numerical blowout)
  - a pinned-end condition when using rigid-body contact elements
  - types of inherent nonlinearities
  - embedded cold-work effects and residual stresses developed during the manufacturing process

2.1 Buckling in Cold-Formed Sections

While yielding (causing the failure of an entire member) is a primary concern for compact and extremely short columns, buckling (a geometric-induced instability causing a critical stress well less than the material yield strength) is prone to happen in cold-formed sections due to their relatively high width-to-thickness and slenderness ratios. Buckling can occur elastically or inelastically depending on whether the material proportional limit is exceeded. Figure 2 summarizes the limit states in compressive cold-formed sections (Yu and LaBoube, 2010). The two extreme failure modes of elastic buckling are broadly categorized as global and local, whereas the in-between distortional buckling is contributed

from the interaction of these two modes. Global buckling is induced by a geometric instability of the whole member (where the out-of-straight governs the behavior) while local buckling of an individual element is induced by the largest width-to-thickness ratio (commonly seen as a rippling in the webs, flanges, or lips along the member length). The three failure modes of global buckling are:

- flexural buckling, a bending (translation) about the weak principal axis, likely in slender closed sections with two axis of symmetry. Also known as Euler buckling.
- torsional buckling, a twisting about the shear center, likely to occur in open or cruciform sections due to lack of the torsional rigidity
- torsional-flexural buckling, a bending and twisting, simultaneously, likely to occur in open, slender sections with one axis of symmetry

The theoretical critical stresses σ_{cr} of flexural and local buckling are given as follows:

$$\sigma_{cr} = \begin{cases} \frac{(\pi^2 E)}{\left(\frac{kL}{r}\right)^2} & \text{; flexural (Euler) buckling} \\ \frac{k\pi^2 E}{12(1-\nu^2)} \left(\frac{t}{b}\right)^2 & \text{; local buckling} \end{cases} \tag{1}$$

The slenderness ratio of $\left(\frac{kL}{r}\right)$ (to account for the effect of being out-of-straight in flexural buckling) consists of k, L, and r referring, respectively, to: (1) an effective-length factor (taken as 1.0 for a flexural column under a pinned-end support and taken as 4.0 for a local-buckling, simply-supported plate under uniform compression), (2) an unbraced column length, (3) a radius of gyration (taken as $\sqrt{\frac{I}{A}}$, where I and A are a moment of inertia and a cross-sectional area). The ratio of $\left(\frac{t}{b}\right)$ (to account for the effect of being out-of-flatness in local buckling) consists of a section thickness and the largest section width. The material properties of the modulus of elasticity and Poisson's ratio are denoted as E and ν, and typically taken as 29.5e3 ksi and 0.3 for cold-formed steel.

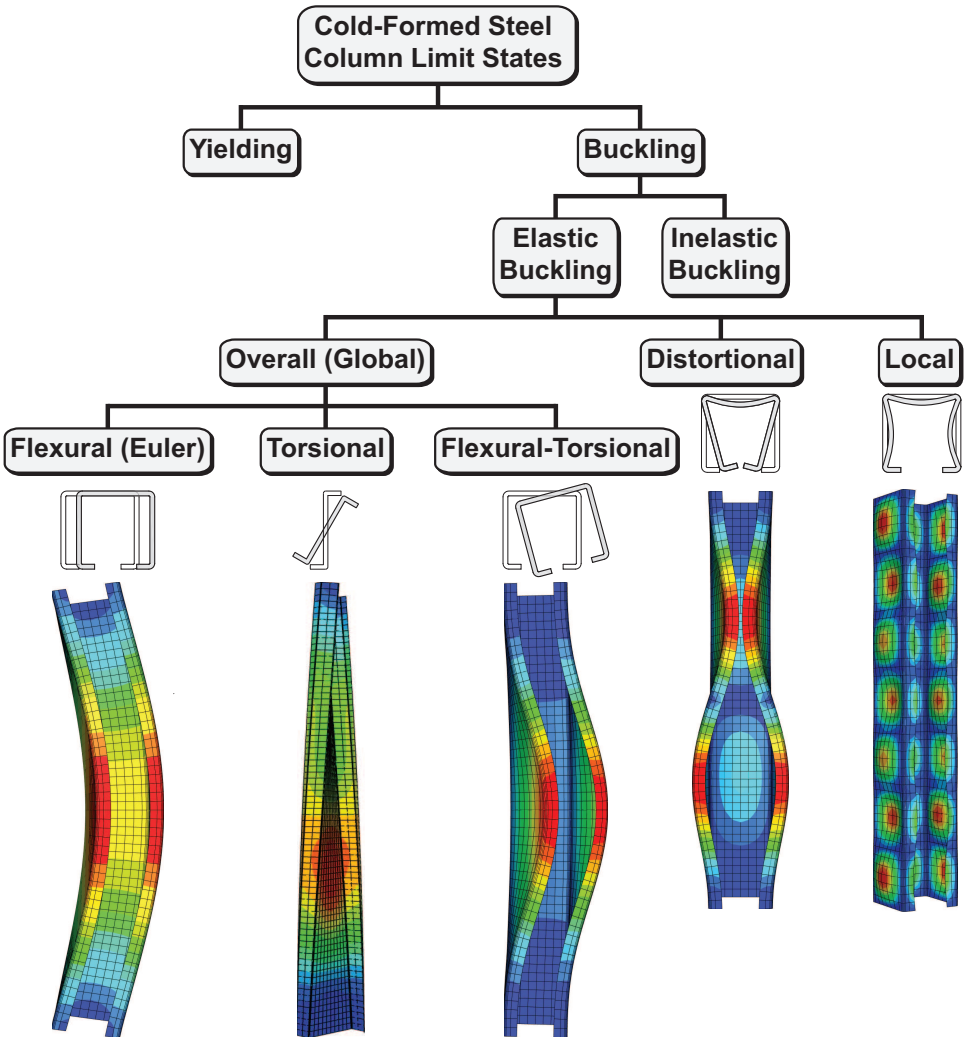


Figure 2: The limit states in compressive cold-formed sections (Yu and LaBoube, 2010).

2.2 Buckling Provisions of the 2007 AISI Specifications

The provisions for built-up, cold-formed sections subjected to pure compression are included in the 2007 AISI specification under Sections C4 and D1.2 (AISI, 2007). The failure modes of flexural, flexural-torsional and distortional bucklings, specifically given in Sections C4.1.1, C4.1.2, and C4.2(b), respectively, are applicable to the built-up configurations tested in the experimental research at the University of Oklahoma (Brueggen and Ramseyer, 2003; Whittle, 2007; Biggs, 2008; Whittle and Ramseyer, 2009). The nominal strength of the first two modes is given as follows:

$$P_n = \begin{cases} \left[\left(0.658^{\lambda_c^2}\right)\sigma_y\right] A_e & ; \lambda_c \leq 1.5 \\ \\ \left[\left(\frac{0.877}{\lambda_c^2}\right)\sigma_y\right] A_e & ; \lambda_c > 1.5 \end{cases} \tag{2}$$

Where

$$\lambda_c = \sqrt{\frac{\sigma_y}{\sigma_e}} \tag{3}$$

$$\sigma_e = \begin{cases} \frac{\pi^2 E}{\left(\frac{kL}{r}\right)_m^2} & ; \text{flexural} \\ \frac{1}{Ar_o^2}\left[GJ + \frac{\pi^2 E C_w}{(kL)^2}\right] & ; \text{flexural-torsional} \end{cases} \tag{4}$$

$$\left(\frac{kL}{r}\right)_m = \sqrt{\left(\frac{kL}{r}\right)_o^2 + \left(\frac{a}{r_i}\right)^2} \tag{5}$$

$$r_o = \sqrt{r_x^2 + r_y^2 + x_o^2} \tag{6}$$

In Eq. (2), the buckling strength P_n is defined as elastic, when the slenderness parameter of λ_c (Eq. (3)) exceeds 1.5; otherwise it is defined as inelastic. The governing buckling stress σ_e (in Eq. (4)) is taken as the least of the flexural (Euler) and the flexural-torsional buckling stresses. The material properties consisting of (1) modulus of elasticity, (2) shear modulus, (3) Poisson's ratio, and (4) yield stress are denoted as E, G, μ, and σ_y, respectively. The required sectional properties include: (1) A, the full unreduced cross-sectional

area, (2) A_e, the effective cross-sectional area of uniform compression determined according to the effective-width concept, (3) J, the Saint-Venant torsional constant, (4) C_w, the torsional warping constant, (5) r_x and r_y, the radii of gyration about the centroidal principal axes (defined as $\sqrt{\frac{I}{A}}$, where I is the second moment of inertia about the x- and y-axis), (6) r_o, the polar radius of gyration about the shear center, and (7) x_o, the distance from the shear center to the centroid along the principal x-axis (taken as negative).

In Eq. (5), the terms of $\left(\frac{kL}{r}\right)_m$ and $\left(\frac{kL}{r}\right)_o$ refer to the modified and unmodified (overall) slenderness ratios about the weak axis (as r is taken as the least between r_x and r_y). k is the effective length factor (taken as 1.0 for a pinned-end support). L is the unbraced length. a is the stitch weld spacing and r_i, the minimum radius of gyration of an individual section. According to the built-up provision (Section D1.2), a modification factor of $\left(\frac{a}{r_i}\right)$ is required when two elements in a built-up member globally buckle separately from one another to account for a relative deformation-induced shear force in the connectors. The factor is limited and is not to exceed $0.5\left(\frac{kL}{r}\right)_o$; otherwise, additional stitch welds are required. Examples of how to determine of A, A_e, J, C_w, r_x, r_y, and x_o can be found in Examples *I-1*, *I-8*, and *III-9* of the 2008 AISI manual (AISI, 2008).

Flexural buckling tends to occur in slender members, where the out-of-straightness significantly dominates its out-of-flatness. The mixed mode of flexural-torsional buckling tends to occur when there is an insufficient torsional rigidity in slender members with open sections. The out-of-straightness is usually accounted for using a slenderness ratio of $\left(\frac{kL}{r}\right)_o$ and the out-of-flatness using a thickness-to-width ratio of $\left(\frac{t}{b}\right)$. The theoretical threshold that allows a member to remain elastic and induces elastic flexural buckling is taken as half the yield strength (σ_y). The associated lower bound in slenderness ratio is defined as follows (Yu and LaBoube, 2010):

$$\left(\frac{kL}{r}\right)_{lim} = \sqrt{\left(\frac{2\pi^2 E}{\sigma_y}\right)} \tag{7}$$

As the member length becomes sufficiently shorter, making the slenderness ratio smaller than the slender limit in Eq. (7), the interaction between the effects of out-of-straightness and out-of-flatness is triggered. Failure tends to become more localized, similar to a thin plate subjected to an in-plane membrane stress, resulting in a transition to distortional buckling. Aside from being bent about the weak axis, the member also has a distortion in the web, flange, or lip along the length. This type of failure modes is very common for large built-up sections. The nominal distortional buckling strength ($P_{n,d}$) according to Section C4.2(b) is given as follows:

$$P_{n,d} = \begin{cases} P_y & ; \lambda_d \leq 0.561 \\ \left(1 - 0.25\left(\frac{P_{crd}}{P_y}\right)^{0.6}\right)\left(\frac{P_{crd}}{P_y}\right)^{0.6} P_y & ; \lambda_d > 0.561 \end{cases} \tag{8}$$

Where

$$\lambda_d = \sqrt{\frac{P_y}{P_{crd}}} \tag{9}$$

$$P_{crd} = A\sigma_d \tag{10}$$

$$\sigma_d = \frac{k_{\phi fe} + k_{\phi we}}{\tilde{k}_{\phi fg} + \tilde{k}_{\phi wg}} \tag{11}$$

In Eq. (8), the distortional load factor λ_d (Eq. (9)) limits $P_{n,d}$ as the squash load P_y (defined as a product of σ_y and A), as its value becomes equal to or less than 0.561. The parameters of σ_d and P_{crd} refer to the elastic distortional-buckling stress and its corresponding load. The former (Eq. (11)) is defined as the ratio of the provided elastic rotational stiffness ($k_{\phi fe}$ and $k_{\phi we}$) to the required geometric rotation stiffness ($\tilde{k}_{\phi fg}$ and $\tilde{k}_{\phi wg}$) of the flange and the web to the flange/web juncture. These rotational stiffnesses

(as given in Section C3.1.4) are defined as follows:

$$k_{\phi fe} = \left(\frac{\pi}{L}\right)^4 \left(EI_{xf}(x_o - h_x)^2 + EC_{wf} - E\frac{I_{xyf}^2}{I_{yf}}(x_o - h_x)^2\right) + \left(\frac{\pi}{L}\right)^2 GJ_f \quad (12)$$

$$k_{\phi we} = \frac{Et^3}{6h_o(1-\mu^2)} \quad (13)$$

$$\tilde{k}_{\phi fg} = \left(\frac{\pi}{L}\right)^2 \left[A_f \left((x_o - h_x)^2 \left(\frac{I_{xyf}}{I_{yf}}\right)^2 - 2y_o(x_o - h_x)\left(\frac{I_{xyf}}{I_{yf}}\right) + h_x^2 + y_o^2\right) + I_{xf} + I_{yf}\right] \quad (14)$$

$$\tilde{k}_{\phi wg} = \left(\frac{\pi}{\min(L, L_{cr})}\right)^2 \frac{th_o^3}{60} \quad (15)$$

$$L_{cr} = \left(\frac{6\pi^4 h_o(1-\mu^2)}{t^3}(I_{xf}(x_o - h_x)^2 + C_{wf} - \frac{I_{xyf}^2}{I_{yf}}(x_o - h_x)^2)\right)^{\frac{1}{4}} \quad (16)$$

Where: (1) b_o, h_o, and D, the outer dimensions of the flange, web, and lip, respectively, whereas b and d are their on-center counterparts, (2) t, the section thickness, (3) x_{of} and y_{of}, the distances along the x- and y-axis from the flange/web juncture to the centroid of the flange, (4) h_x, the x-axis distance from the centroid of the flange to the shear center of the flange, (5) C_{wf}, the warping torsional constant of the flange, (6) A_f, the cross-sectional area of the compressive flange and the lip, (7) I_{xf} and I_{yf}, the x- and y-axis moments of inertia of the flange, (8) I_{xyf}, a product of moment of inertia of the flange, and (9) J_f is the Saint-Venant torsion constant of the compression flange and the lip.

These aforementioned geometric parameters are determined as follows:

$$b = b_o - t \tag{17}$$

$$d = D - 0.5t \tag{18}$$

$$x_{of} = \frac{b^2}{2(b+d)} \tag{19}$$

$$y_{of} = \frac{-d^2}{2(b+d)} \tag{20}$$

$$h_x = \frac{-(b^2+2db)}{2(b+d)} \tag{21}$$

$$A_f = (b+d)t \tag{22}$$

$$I_{xf} = \left(\frac{(tb)^2+4bd^3+t^2bd+d^4}{12(b+d)}\right)t \tag{23}$$

$$I_{yf} = \left(\frac{b^4+4db^3}{12(b+d)}\right)t \tag{24}$$

$$I_{xyf} = \frac{t(bd)^2}{4(b+d)} \tag{25}$$

$$J_f = \frac{bt^3+dt^3}{3} \tag{26}$$

Equation (15) indicates that $P_{n,d}$ (Eq. (8)) becomes constant for a longer length L as the critical length L_{cr} (Eq. (16)) has been exceeded. The governing buckling strength for a given built-up section is taken as the least of the nominal strengths determined from Eqs. (2) and (8). An example of the AISI design curve for a built-up, *I*-section determined according to Eqs. (8)-(26) is presented in Fig. 3.

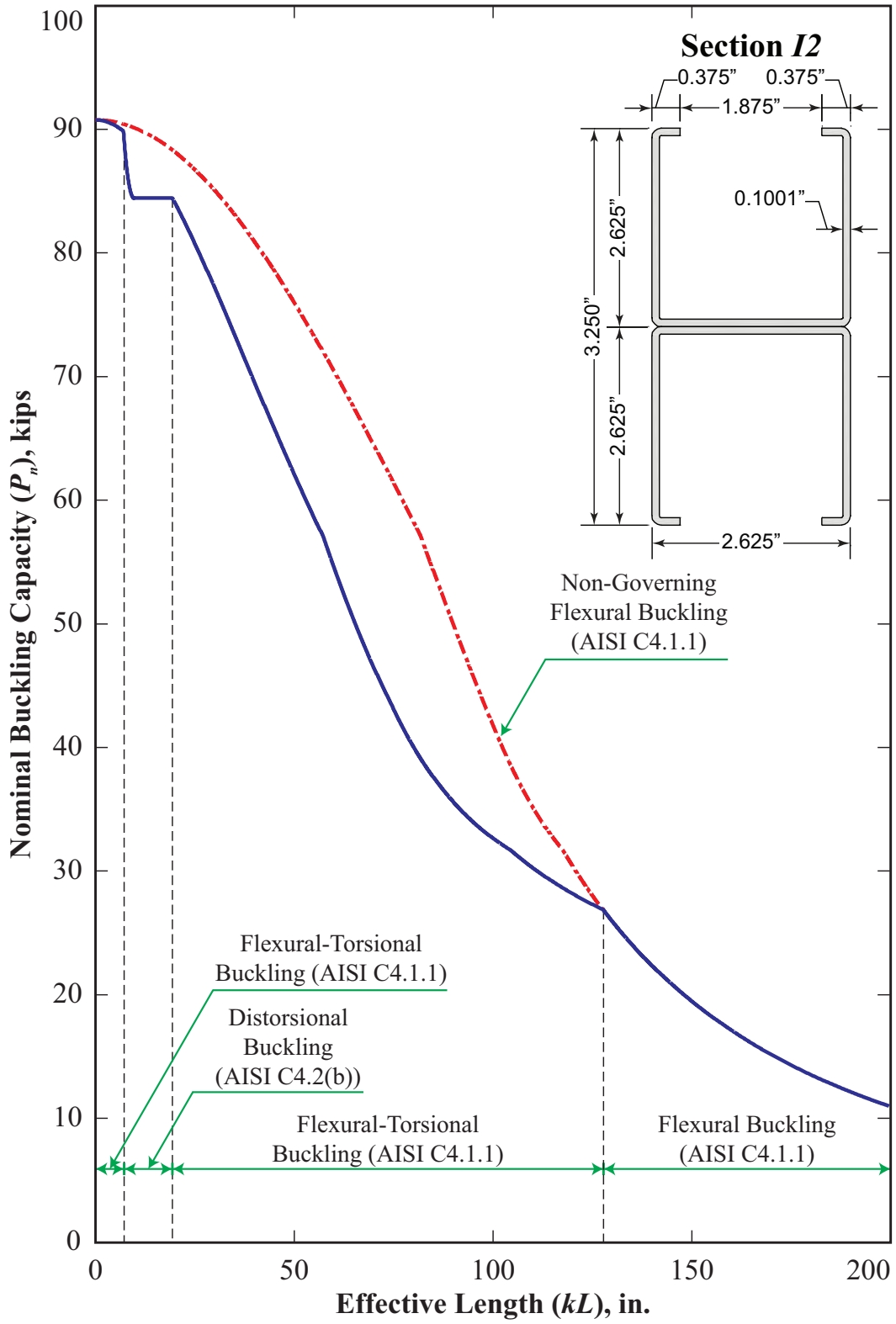


Figure 3: The nominal buckling strength of a built-up, *I*-section (also valid for an *R*-section) determined according to the 2007 AISI standard, Section C4.1.1, C4.1.2, and C4.2(b).

2.3 Experimental Study of Built-Up, Cold-Formed Sections

2.3.1 General

A series of experimental studies on the axial load capacity of cold-formed members was conducted by a research group in the Donald G. Fears Structural Engineering Laboratory at the University of Oklahoma (Brueggen and Ramseyer, 2003; Whittle, 2007; Biggs, 2008; Whittle and Ramseyer, 2009). This series of tests together comprise the largest experimental study of cold-formed built-up members. The objectives of the test were to: (1) determine maximum buckling capacities for a variety of built-up members, (2) investigate the accuracy of the 2001 AISI specification, and (3) determine the effectiveness of the modified slenderness ratio for built-up members. Various member properties and geometries commonly used in cold-formed trusses were examined to obtain a broad range of experimental data that could more thoroughly represent the buckling behavior of built-up, cold-formed sections. In all, over 265 pure-compression tests on single and built-up sections of square-lipped *C*-channels were carried out. The members were subjected to pure compression with pinned-end conditions that was achieved by using a swivel pivoting head. The test setups and the section detail are shown in Figs. 4 and 5, respectively. The compression force was applied using a hydraulic hand pump, and the corresponding axial deformation was measured using a Linear Variable Displacement Transducer (LVDT).

2.3.2 Specimen Geometry and Welding Detail

The three chosen widths for the specimens were 1.625, 2.625, and 3.625 in., denoted as ***1***, ***2***, and ***3***, respectively, in the last number of the specimen identification. Each group with the same width consists of specimens with three nominal thicknesses of 0.064, 0.08, and 0.1 in. and three member lengths of 42, 55.5, and 71 in. The two built-up orientations of openside-facing and -opposing (referred to as ***R*** and ***I***; see the right panel of Fig. 4) were fabricated using two channels stitch welded together on one or both sides along the



Figure 4: The pure-compression, experimental setups (Brueggen and Ramseyer, 2003; Whittle, 2007).

length (referred to as ***SW*** and ***DW***, see Fig. 6). In addition to the case of no intermediate stitch weld (i.e., end welds only), three intermediate stitch patterns were used as follows: one weld at mid-point, two welds at third-points, and five welds at sixth-points. They are denoted in the specimen identification using the total number of the intermediate welds as ***1-***, ***2-*** and ***5-***, respectively.

For instance, the specimen identification *DW2-064R1* refers to the following variables: ***D***ouble-side ***W***elded specimen with ***2*** intermediate stitch welds at the third-points, which is a 0.***064*** in. thick, ***R***-section with ***1***.625 in. width. And, the specimen identification *DW-100I2* refers to the following variables: ***D***ouble-side ***W***elded specimen with no intermediate stitch welds, which is a 0.***100*** in. thick, ***I***-section with ***2***.625 in. width.

The length of the end and intermediate welds were varied according to the width and the member length. The end welds were 4 in. for *I3*- and *R3*-sections with 42 in. and 71 in. lengths, 2 in. for *R1*- and *R2*-sections with 71 in. length, and 1 in. for *R1*-sections with 55.5 in. length. The intermediate welds were 1.5 in. for sections with 55.5 in. length and 1 in. for the rest. All welds were approximately 3/16th in. thick.

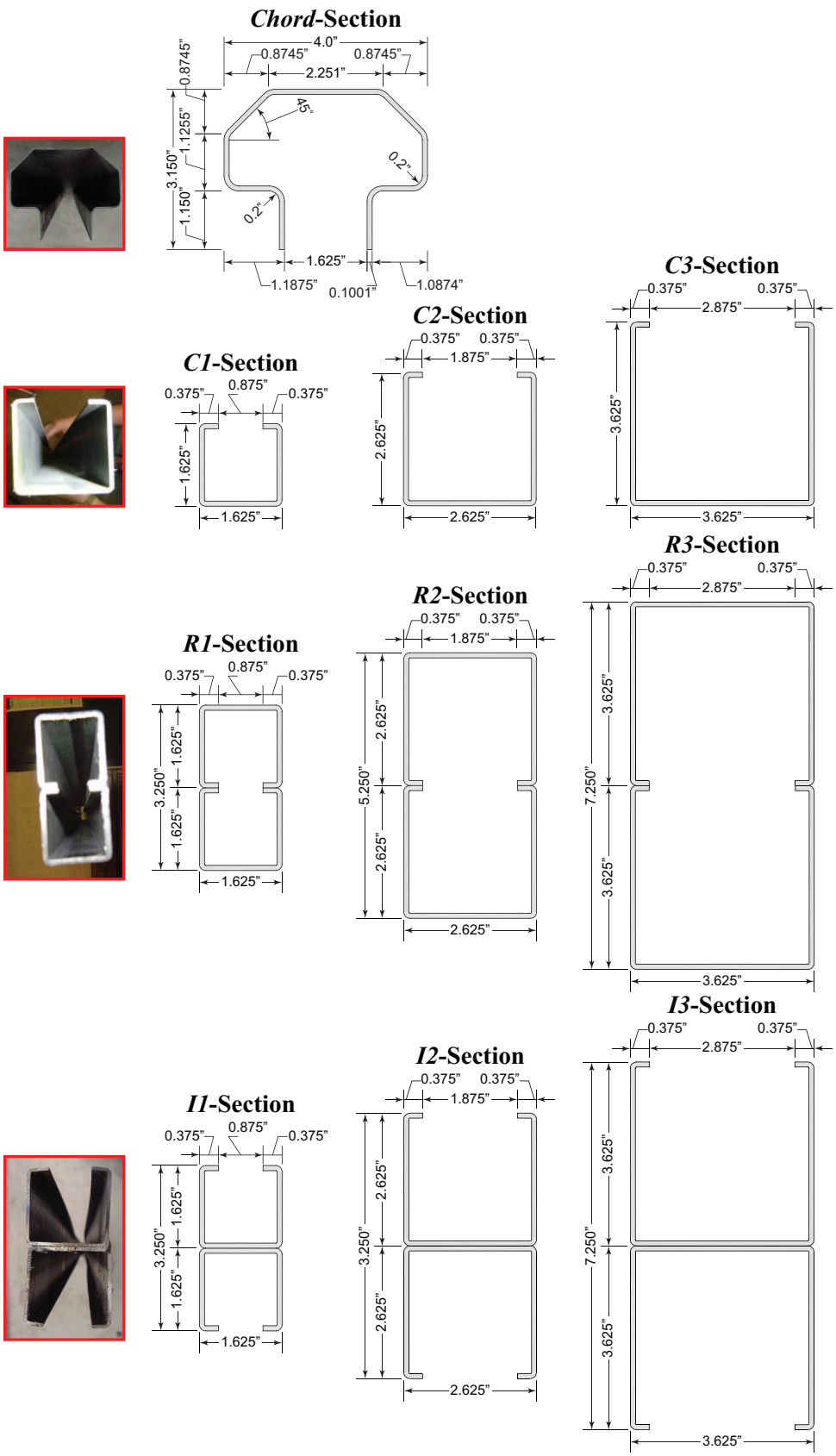


Figure 5: Section details of the single and built-up members.

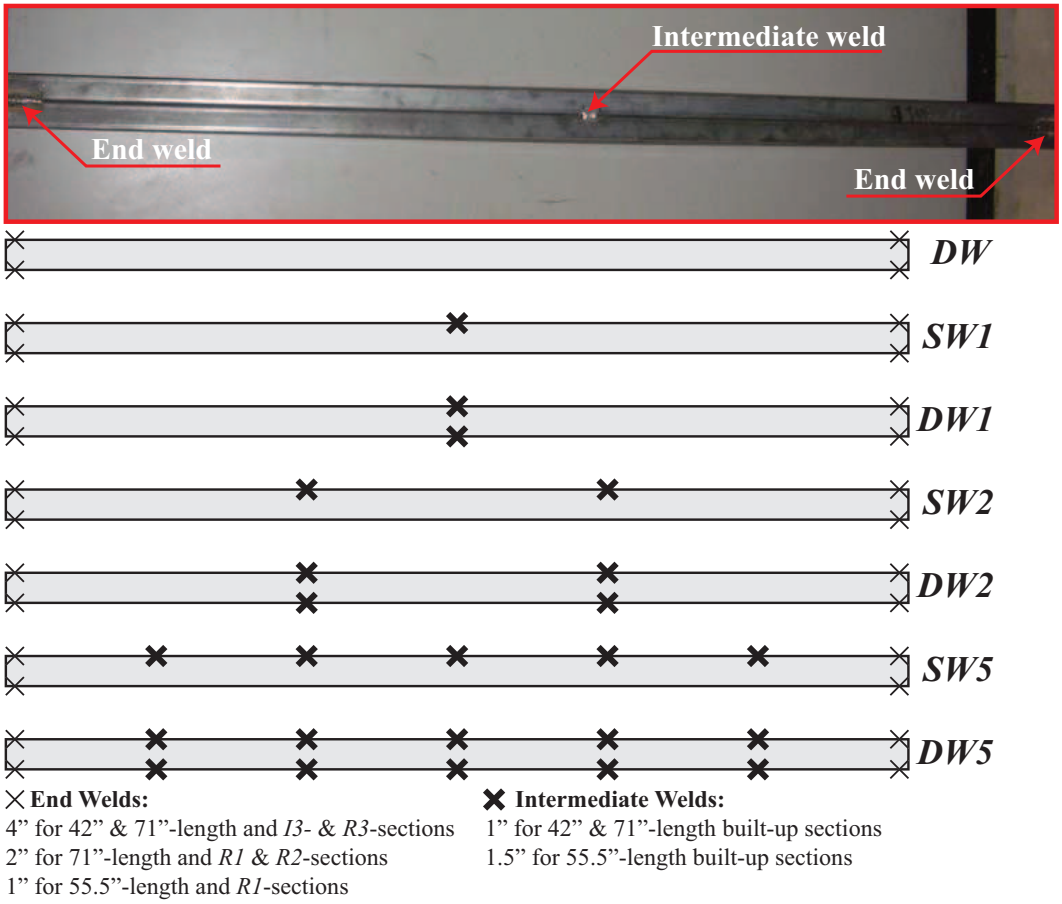


Figure 6: Weld orientations.

2.3.3 Summary of Experimental Results

Comparisons between the experimental to the nominal design strengths according to the former 2001 and the current 2007 AISI specifications (AISI, 2001, 2007), are shown in Figs. 7 and 8, respectively. In Fig. 7, it is noted that the modified slenderness ratio $\left(\frac{kL}{r}\right)_m$ was conservative, and for longer and thicker flexural members it tends to be exceedingly conservative. On the other hand, the specification became unconservative for members prone to distortional buckling. The unmodified slenderness ratio $\left(\frac{kL}{r}\right)_o$ with the spacing limit yielded a consistently conservative estimation. The member orientation had a strong impact on the failure load. In addition, the need to consider a distortional mode in addition to the governing flexural buckling mode, was recommended.

In the 2007 AISI specification, due to the work of Brueggen and Ramseyer (2003),

Whittle (2007), Biggs (2008), and Whittle and Ramseyer (2009), a distortional provision had been implemented under Section C4.2. Nonetheless, the calculations are complicated (see Section 2.2 for equations and Fig. 3 for the design curve), but are not very accurate. These equations result in an exceedingly conservative estimation for larger and longer distortional members (see Fig. 8).

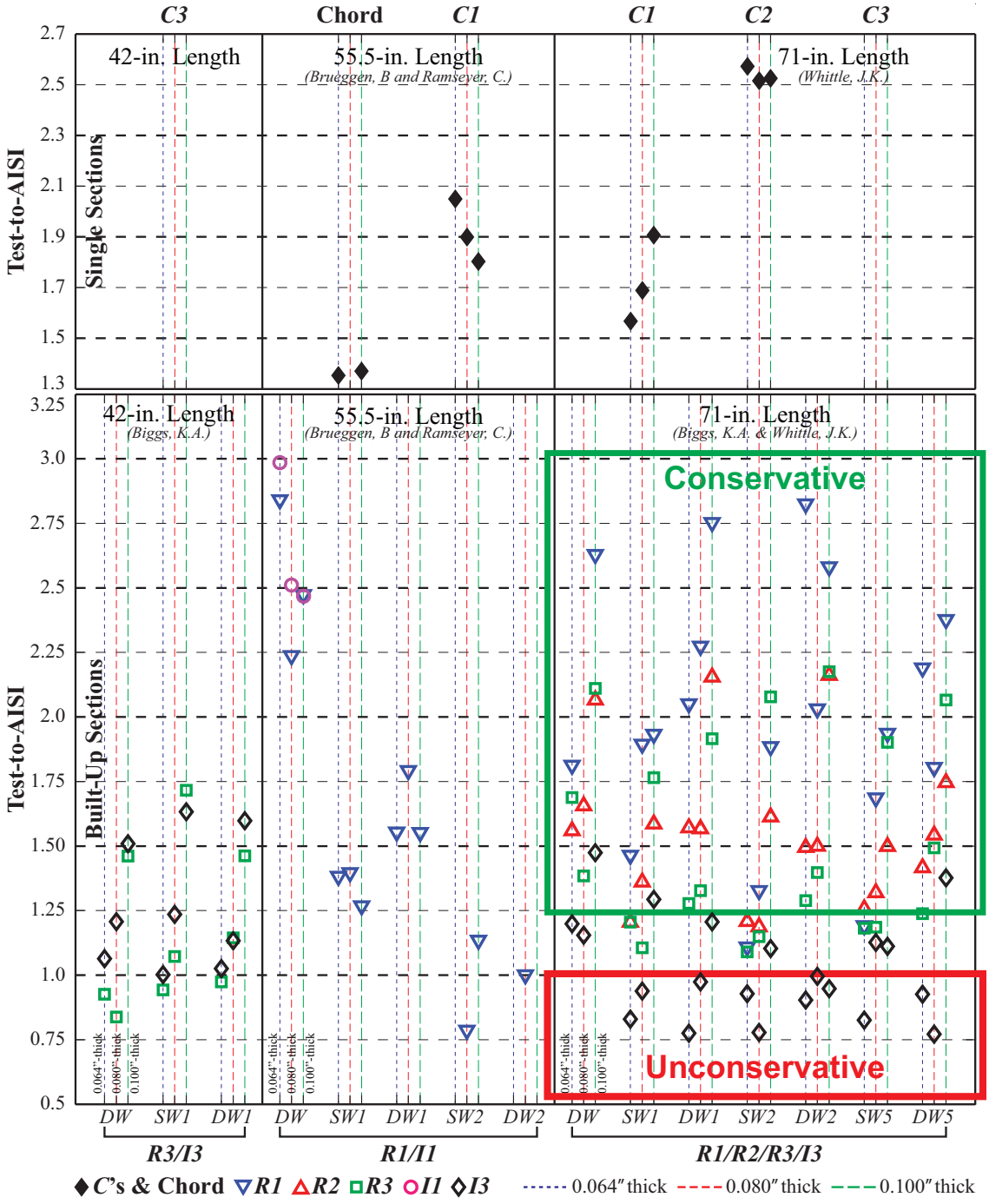


Figure 7: Comparison of the experimental to the design capacities of the 2001 AISI specification. All the 55.5" members were conducted by Brueggen and Ramseyer (2003) whereas the members of *R1* and *R2* with 71" length were carried by Whittle and Ramseyer (2009). The rest were done by Biggs (2008). Three experimental repetitions per one given configuration were done in Brueggen and Ramseyer (2003), Whittle (2007), and Whittle and Ramseyer (2009).

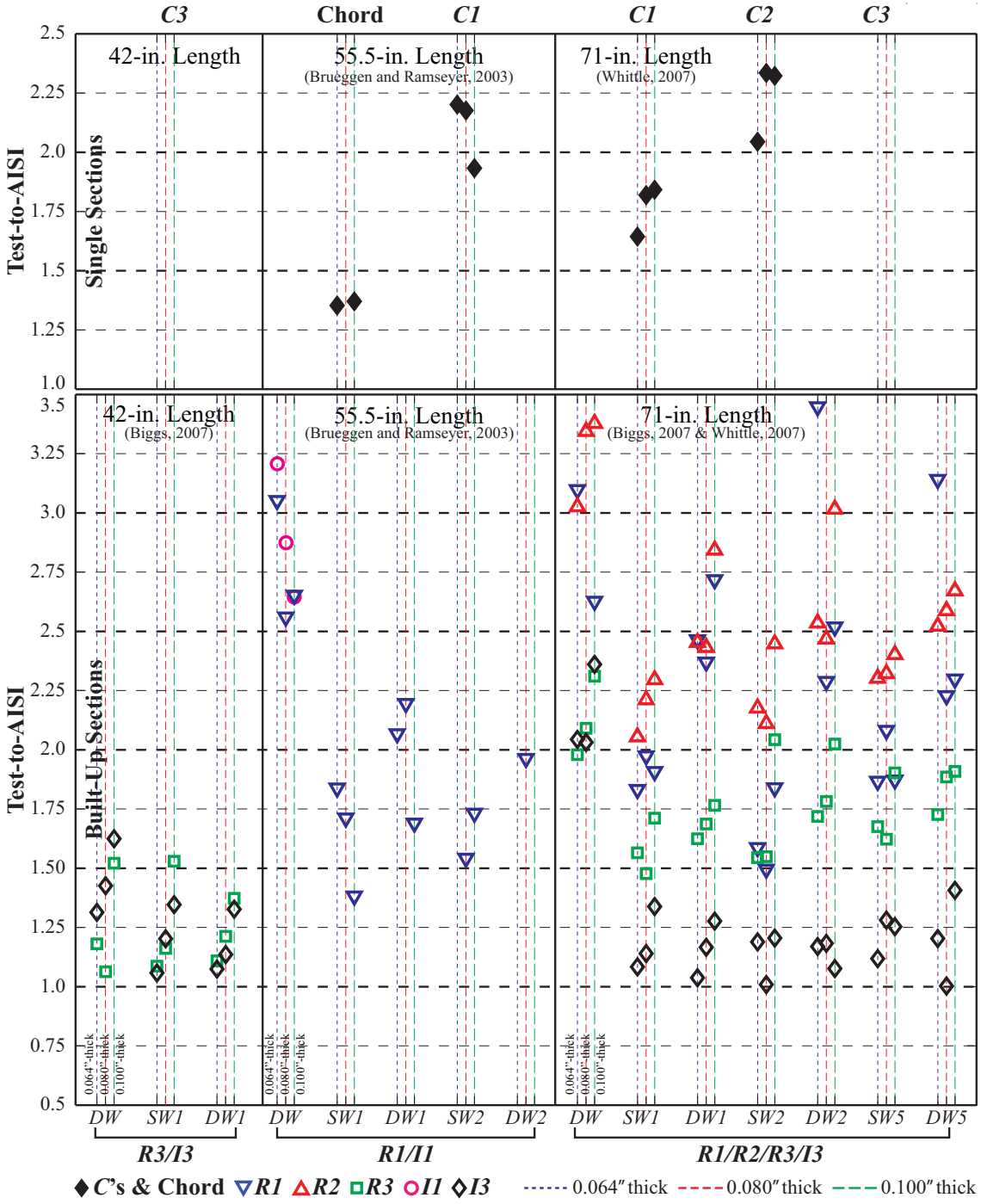


Figure 8: Comparison of the experimental to the design capacities of the 2007 AISI specification. All the 55.5" members were conducted by Brueggen and Ramseyer (2003) whereas the members of *R1* and *R2* with 71" length were carried by Whittle and Ramseyer (2009). The rest were done by Biggs (2008). Three experimental repetitions per one given configuration were done in Brueggen and Ramseyer (2003), Whittle (2007), and Whittle and Ramseyer (2009).

2.4 Numerical Buckling Analyses of Build-Up, Cold-Formed Members

Numerical analysis using the finite element method (FEM) has long been used in structural engineering, since as early as 1960s (Bathe, 1996). It is now well accepted as the most powerful and reliable analytical approximation technique in various scientific disciplines including continuum mechanics (Lagrangian or material coordinates) and fluid dynamics (Eulerian or spatial coordinates). A complicated domain is broken into a number of smaller simplified and solvable mathematical domains whose solutions in an approximate sense are then assembled to establish the complicated solution (Mish et al., 2000). Using FEM the solution to coupled-field problems such as soil-structure interactions and thermal-induced stresses in structures are made possible. The availability of modern robust computational resources makes the technique even more attractive. With well developed and reliable FEM packages such as ABAQUS and ANSYS, and a systematic procedure to tackle errors in the model as summarized in Fig. 9 (Bakker and Pekoz, 2001), FEM simulation was chosen as the proper tool for in-depth research. At present no substantial numerical work has been carried out on cold-formed built-up column members. Developing a reliable state-of-the-art modeling strategy based upon the readily available experimental results (in Section 2.3) has not been done prior to this work.

The ANSYS implicit-static and the ABAQUS explicit-dynamic FEM models of the built-up members presented in Figs. 4 and 5 are shown in Figs. 10 and 11. The important background issues that need to be dealt with in performing a nonlinear (large-displacement) buckling analysis include: (1) inherent nonlinearities, (2) imperfections to avoid a bifurcation (i.e., a discontinuous in response at the point of buckling (ABAQUS®, 2007a)), and (3) a cold-work effect and residual stresses resulting from a manufacturing process.

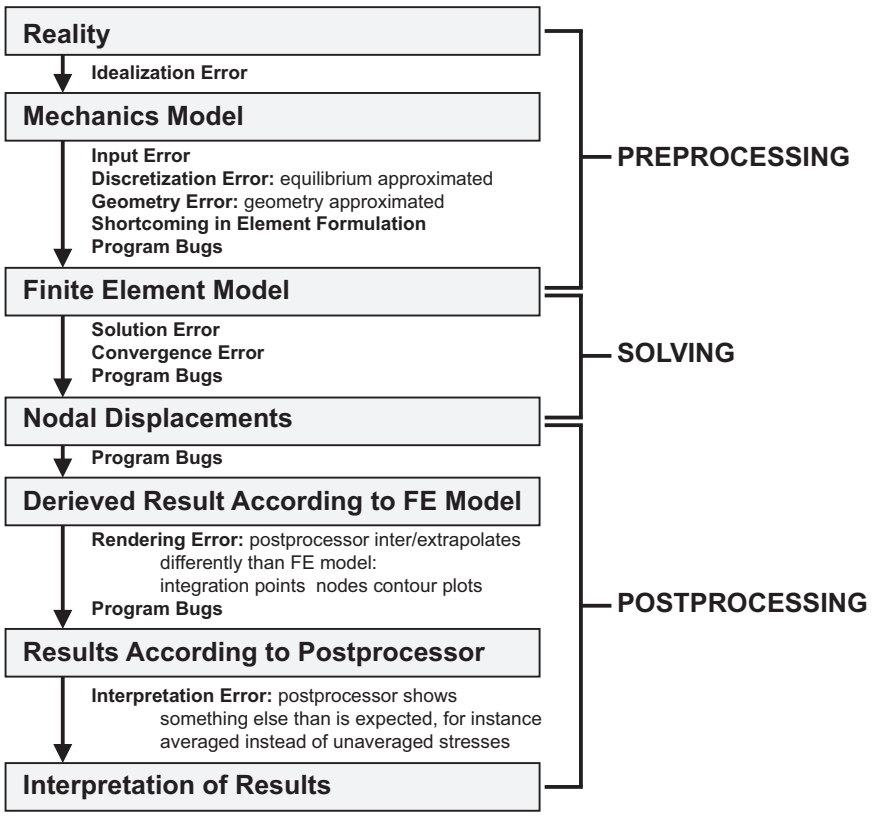


Figure 9: Overview of possible errors in finite-element modeling of thin-walled members (Bakker and Pekoz, 2001).

2.4.1 Inherent Nonlinearities

The nonlinearity sources in structural mechanics include: (1) material nonlinearity due to path- and/or rate-dependent relation(s) at the constitutive stress-strain and/or sectional force-deformation level(s); examples including a bilinear hysteretic and a Ramberg-Osgood model (see Section 2.5), (2) boundary nonlinearity of status-dependent conditions due to a presence of contact elements, and (3) geometric nonlinearity as changes in elemental shapes and orientations resulting in changing of the global stiffness (see Section 2.5 for detail) (ANSYS®, 2009a)). Modeling the buckling response of built-up, cold-formed sections does requires that all of these nonlinearities to be explicitly considered.

A bilinear hysteretic model with an isotropic work hardening assumption coupled with a von Mises yield criteria is well suitable to model steel constitutive relations in large-displacement analyses (Cook, 1995; Cook et al., 2001; ANSYS®, 2009a). The

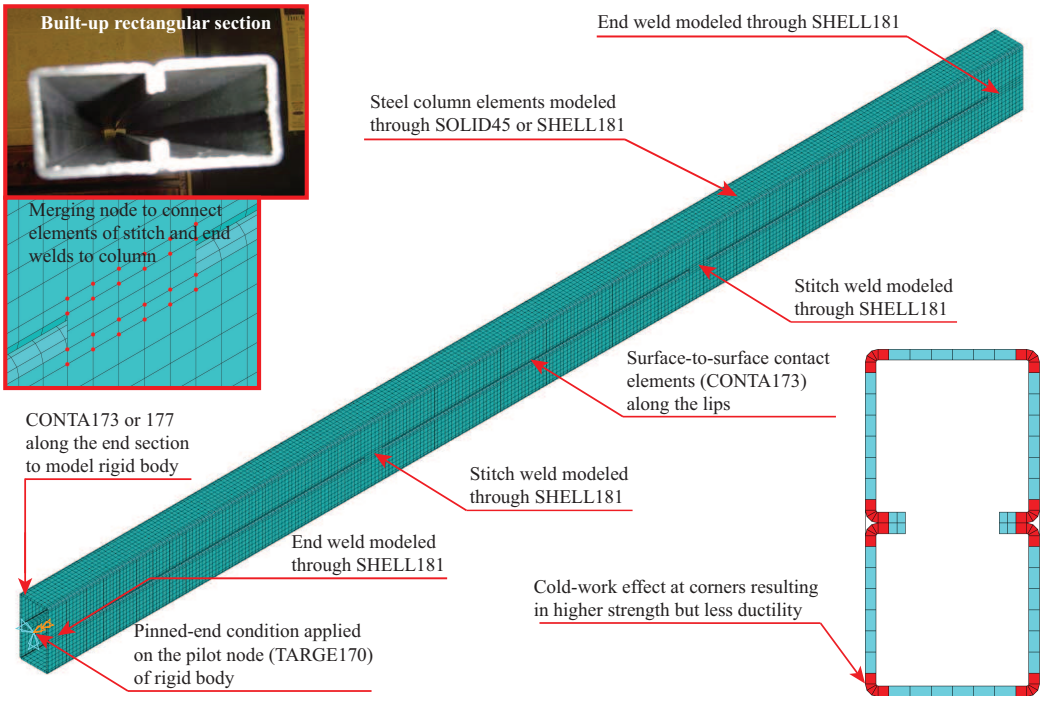


Figure 10: ANSYS implicit-static model of the built-up, *R*-section.

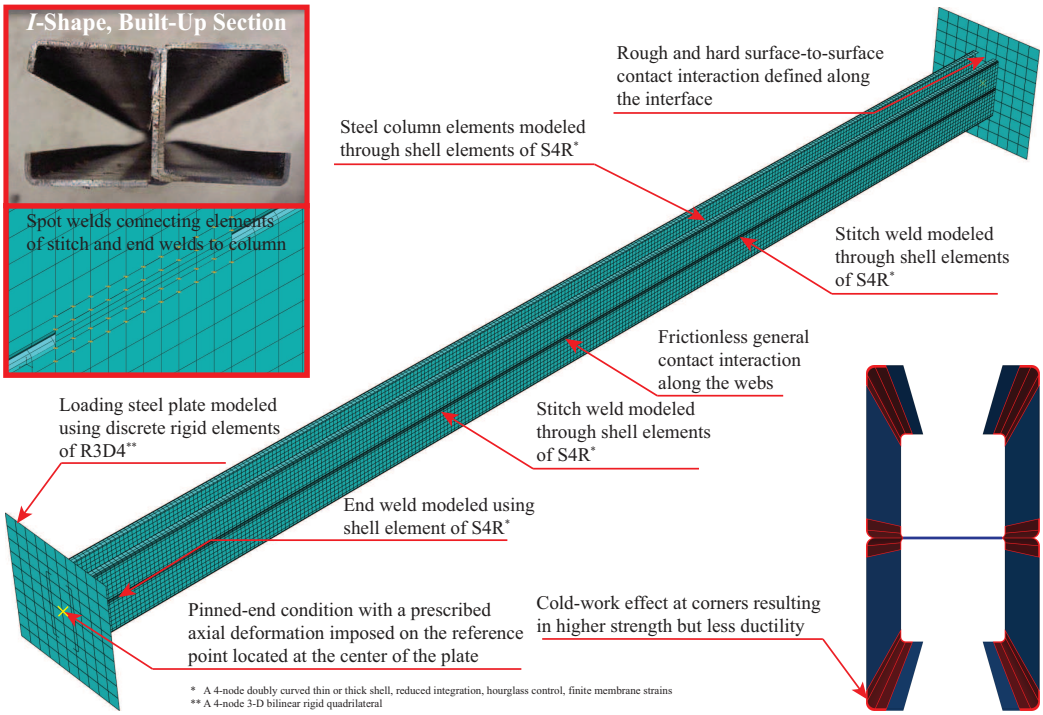


Figure 11: ABAQUS explicit-dynamic model of the built-up, *I*-section.

model is basically a non-degrading and path-dependent with a simplified 0.2% yield stress as a sharp transition dividing the regions of elastic from plastic (Otani, 1974; Piyawat et al., 2008). The strain hardening is incorporated through a positive post-yield stiffness. Upon reversal, an unloading branch with an identical elastic stiffness is preserved if it is within twice of the yield-stress range; otherwise, unloading proceeds with the post-yield stiffness.

In small-strain and/or small-displacement analyses such as simulations of prestressed concrete girders under flexural loadings (Kim et al., 2010), the element geometry is assumed to remain unchanged during the loading history, such that a linear strain-displacement approximation is accurate enough (Bathe, 1996; Boresi and Schmidt, 2003). In large-displacement analysis, the stiffness has to be a function of a deformed configuration where the quadratic strain is significant. The true stress and true (logarithmic) strain (denoted as σ_{true} and ε_{true}) are required to determine the changes in elemental shapes and orientations. The conversion from the engineering format is given as follows: $\sigma_{true} = \sigma(1 + \varepsilon)$ and $\varepsilon_{true} = \ln(1 + \varepsilon)$ (Boresi and Schmidt, 2003). In short, different types of geometrical nonlinear analyses as summarized by Bakker and Pekoz (2001) are listed in Table 1.

Changing in boundary conditions during the analysis due to contact elements between surfaces, e.g., from in contact to not in contact and vice versa, are highly nonlinear and computationally expensive (ANSYS®, 2009a). It commonly occurs when there is a normal and/or tangential interaction(s) between components allowing forces to be transmitted from one to another. A presence of nodal contact pairs consisting of a master surface (target element) and slave nodes defined by contact elements, must be explicitly predefined in advance between possible contacting surfaces for the actual physical contact(s). Misrepresenting these contact pairs results in "no contact" and the elements will simply deform past each other leading to an inaccurate response.

The two types of flexible-to-flexible contacts are: node-to-surface and surface-to-surface. The FEM models shown in Figs. 10 and 11 require surface-to-surface contact.

Type of Analysis	Displacements	Rotations	Strains
First order (linear)	very small	very small	small ($< 5\%$)
Second order (stress stiffening)	small (negligible membrane stresses due to out of plane deflections, displacements smaller than the thickness of the beam/plate/shell	small ($< 10°$)	small ($< 5\%$)
Large displacement	large (significant membrane stresses due to out of plane deflections, displacements larger than the thickness of the beam/plate/shell	small ($< 10°$)	small ($< 5\%$)
Large rotation	large	large	small ($< 5\%$)
Large strain	large	large	large

Table 1: Types of geometric nonlinear analyses by Bakker and Pekoz (2001). Stress stiffening is a coupling phenomena between membrane stresses and lateral displacements induced by bending (Cook, 1995; Cook et al., 2001). A member under a compressive membrane stress will buckle as soon as the membrane stress is large enough to reduce the bending stiffness to zero.

Contact elements are overlaid along the potential surfaces of the lips and the back panels of the *R*- and *I*-sections, respectively. The frictionless interaction property is defined, allowing the surfaces to freely slide past each other with no normal force being transmitted. Careful consideration of the master-surface location is needed to determine whether it should either be double-sided (symmetric contact) or single-sided (asymmetric contact). Nevertheless, if the meshes on the contacting surfaces are identical and sufficiently refined (which is adopted in this investigation), there is not much improvement in accuracy, but it does save time and more computational effort due to shifting from symmetric to asymmetric contact (ANSYS®, 2009a). In this investigation the master surface is defined on the lower member with its slave pair on the upper one.

While it is fairly straight forward to model a fixed-end condition, modeling a pinned end for the ANSYS implicit-static model in Fig. 10 needs a rigid body of a node-to-surface contact type. The rigid body consists of a single pilot (master) node and a slave surface of nodes defined by contact elements. The pilot node governing the motion of the entire

body is placed right at the centroid of the end section representing the swivel pivoting head in the experiment (see Fig. 4). A set of nodes forming a slave surface are defined by surface-to-surface or line-to-surface contact elements depending on whether structural solid or shell elements are used for the column entity. The attachment to the column (a deformable body) is made by overlaying the contact elements onto the end section. The displacement boundary condition is directly imposed on the pilot node. On one end, all translations and an axial rotation are prevented. On the other end, the same constraints are adopted except for the axial translation being either unconstrained under an applied load or controlled by a prescribed deformation as in a force- or a displacement-controlled analysis, respectively. An Eigen-buckling analysis to simulate an imperfection to induce a geometric instability in a displacement-controlled nonlinear counterpart (more detail in the following section) belongs to the former.

The ABAQUS explicit-dynamic model (in Fig. 11) has two extra rigid plates mounted at the column ends to facilitate the inertial effect. The rigid-body pinned end is applied to the plate outer surface. The reference point (pilot node) is located right at the center of the plate which coincides with the center of the end section. The contact elements of a surface-to-surface type is defined at the interface between the section and the inner surface of the plate. The master surface is laid on the plate where coarser meshes are defined (ANSYS®, 2009a; Madenci and Guven, 2006). The interface interaction property is defined as rough-and-hard allowing normal force(s) to be transmitted, while preventing sliding (Narayanan and Mahendran, 2003; Yang and Hancock, 2006; Becque and Rasmussen, 2008).

2.4.2 Geometric Imperfection

An initial imperfection is used to trigger the geometric instability and by doing so bypassing a discontinuous response and a numerical blowout at the bifurcation load. The use of an initial imperfection helps reveal the true buckling response, and is also another

important consideration in the modeling of thin-walled members/structures. Qualitative load-deformation responses of an imperfection-sensitive cylindrical shell demonstrating the importance of using a geometric perturbation is presented in Fig. 12 (Cook et al., 2001). The two types of implementing an initial imperfection are through loading and geometry.

A loading imperfection is incorporated into the model by applying a small fictitious load at a particular location, e.g., at mid-length to force an out-of-straightness resulting in a desired global buckled shape. The magnitude must be sufficiently small not to alter the overall solution. In addition, applying an eccentricity to a prescribed load or displacement in a load- or displacement-controlled analysis is also another means. Nonetheless, a difficulty is in determining and justifying the correct location as well as the magnitude level generally prevents the use of this imperfection type.

A geometric imperfection is implemented through a superposition of a known deformed configuration onto a perfect mesh as illustrated in Fig. 13. Generally, the imperfection can be derived from: (1) an Eigen-buckling analysis (i.e., linear bifurcation analysis), (2) a limit-load analysis (i.e., nonlinear (large-displacement) analysis performed on a perfect configuration (Cook et al., 2001)) and (3) actual imperfections measured from an actual specimen (Becque and Rasmussen, 2008). Among these, seeding a factored Eigen mode(s) is commonly used. Figure 14 shows the first Eigen mode of the *DW-R1* member. Generally, the lowest mode is of interest. Nonetheless, if the first few modes are closely spaced, a single-mode imperfection may over- or underpredict the actual collapse load (ABAQUS®, 2007a; Cook et al., 2001). A combination of (1) the first few modes or (2) the first global and local modes (sometimes overwhelming, especially for a large system, since as many as 12 modes may need to be extracted) may be desired (Ng and Gardner, 2007). It has been confirmed through the numerical buckling series of 360 runs carried out in Section 4.3 that failure to consider the first two-consecutive (closely-spaced) Eigen modes can have severe consequences with an underestimation by as much as 30%. In con-

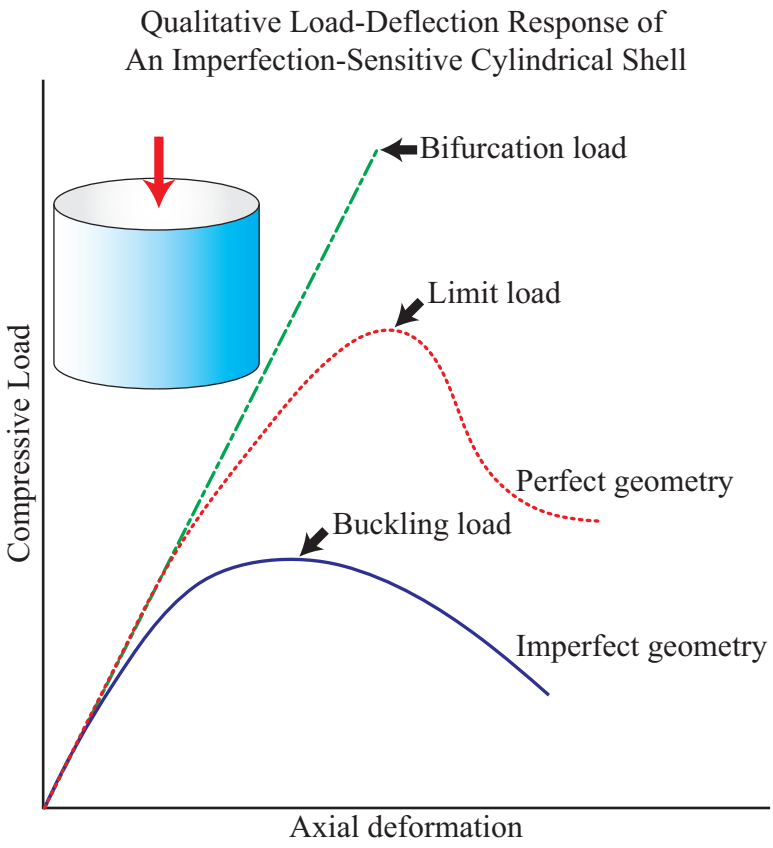


Figure 12: Qualitative load-deformation responses of a cylindrical shell showing an importance of geometric perturbation (Cook et al., 2001).

trast, implementing the first global and local modes simultaneously does not significantly affect the failure load.

A factor to adjust the magnitude of an Eigen-buckling mode(s) is referred to as an imperfection factor and denoted as δ. It is usually defined as a percentage of the section thickness t and as a ratio of the unbraced member length L (for a local and a global imperfection). A ratio of $\frac{L}{2000}$ (a half of the upper limit specified in the AISC design code (AISC, 2005)) is typically adopted as a global factor (Ng and Gardner, 2007). The equations to calculate a local imperfection factor are given in Eq. (27). Among the three expressions, the first one (as proposed by Walker (1975) is widely adopted (Yang and Hancock, 2006). According to Rasmussen and Hasham (2001) and Ng and Gardner (2007), the predicted buckling loads have a relatively low sensitivity to a local imperfection when the ratio of

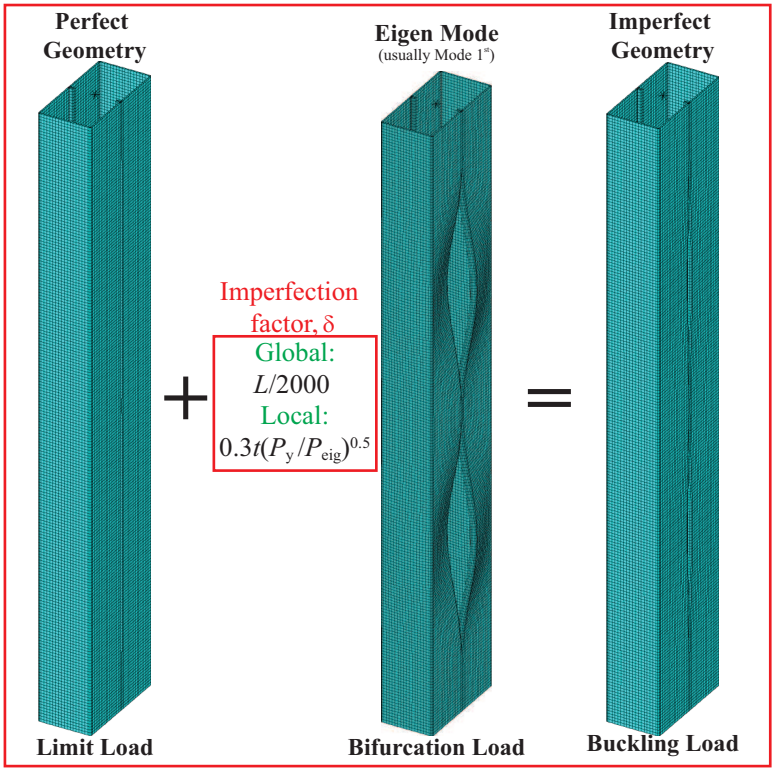


Figure 13: An implementation of geometric imperfection through seeding a known deformed configuration of an Eigen mode onto a perfect configuration. The imperfection factor δ is taken as $\frac{L}{2000}$ (for a global imperfection) or according to the first expression of Eq. (27) (for a local imperfection).

$\left(\frac{\delta}{t}\right)$ exceeds 2.5%.

$$\delta = \begin{cases} 0.3\left(\frac{P_y}{P_{cr}}\right)^{0.5} t & \text{; by Walker (1975)} \\ 0.023\left(\frac{\sigma_y}{\sigma_{cr}}\right) t & \text{; by Gardner and Nethercot (2004)} \\ 0.145\left(\frac{b}{t}\right)\left(\sqrt{\frac{\sigma_y}{E}}\right) t & \text{; by BS 5950 (Talikoti and Bajaria, 2005)} \end{cases} \tag{27}$$

The notations of P_y and P_{cr} denote the squash and the critical (Eigen-buckling) load. The notations of σ_y and σ_{cr} denote the yield and the critical stress. The notation of E denotes the modulus of elasticity and b, the largest of the section width and depth.

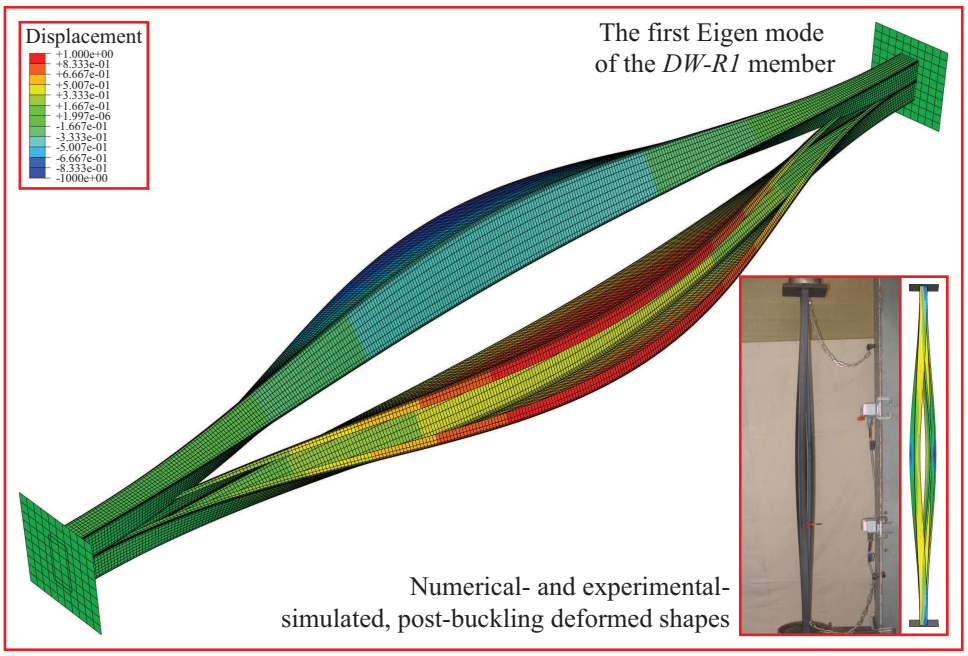


Figure 14: The first Eigen of the *DW-R1* member. A flexural-torsional buckled shape is illustrated on an exaggerated scale for clarity.

2.4.3 Cold-Work Effect and Residual Stresses

The effects of residual stress and cold-working are introduced to cold-formed sections during the manufacturing process of roll-forming and press-breaking. The effect of residual stress causes an early yielding of the steel resulting in a reduction of the member strength. It has been concluded in Gardner and Nethercot (2004) and Ellobody and Young (2005) that this effect can be neglected in finite-element modelings, if the material property is directly derived from the coupons obtained from an actual member, since the residual stress is already inherently embedded. Ignoring residual stress in a member is common is both hot-rolled and cold-formed structural steel design.

The cold-work effect results in a higher strength but less ductility of the steel in the area that is cold worked, in the case of this research around the corners and a thickness-distance neighborhood (the red-shaded regions in Figs. 10 and 11) (Ashraf et al., 2005). A failure to account for in the numerical modeling and design leads to an underestimation in load-carrying capacities (Gardner and Nethercot, 2004).

Based on the concept of (1) strain compatibility, (2) volume-constancy principle of plasticity, and (3) the theory of strain hardening, Karen (1967) arrived at Eqs. (28)-(30) for the strengthening effect of corner yield strength (denoted as σ_{yc}) to virgin yield strength (σ_y).

$$\sigma_{yc} = \left(\frac{\beta}{(a/t)^m}\right)\sigma_y \tag{28}$$

$$\beta = 3.69\left(\frac{\sigma_u}{\sigma_y}\right) - 0.819\left(\frac{\sigma_u}{\sigma_y}\right)^2 - 1.79 \tag{29}$$

$$m = 0.192\left(\frac{\sigma_u}{\sigma_y}\right) - 0.068 \tag{30}$$

The parameters of a and t refer to the geometric properties of the corner inner radius and the section thickness. These equations have been adopted in the AISI specification as Eqs. A7.2-4 with an applicable range applied as follows: (a) an internal radius over a section thickness < 7, (b) $\left(\frac{\sigma_u}{\sigma_y}\right) \geq 1.2$, where σ_u denotes the ultimate strength, and (c) a minimum bending angle of 60° (Hancock et al., 2001). Zhao et al. (2005) recommends an enhancement of 22 % and 16 % for the yield and tensile strengths, respectively. Ashraf et al. (2005) proposed Eqs. (31) and (32) for stainless-steel sections formed using both roll-forming and press-breaking.

$$\sigma_{yc} = \frac{1.881\sigma_y}{\left(\frac{r_i}{t}\right)^{0.194}} \tag{31}$$

$$f_{uc} = 0.75\sigma_c\frac{\sigma_u}{\sigma_y} \tag{32}$$

In this investigation, the cold-work effect is implemented according to the suggestion by Zhao et al. (2005), since some of the material properties adopted from Whittle (2007) fall outside of the applicable range defined for Eq. (28).

2.5 Solution Strategy

The major difference between an implicit and explicit scheme is an equilibrium iteration in the solution process. It is required in the implicit scheme to allow approximate simultaneous solutions of discrete equations (Belytschko et al., 2000). A static analysis which include inertial effects is basically a dynamic analysis and can be carried out implicitly or explicitly (Bathe, 1996). The time integrators of Central-Difference and Newmark methods are an example of these two schemes. In a static analysis, an equilibrium iteration indicating an existence of nonlinearity requires a linearization of the equilibrium equation(s), $[K]\{D\} = \{R\}$. As the stiffness matrix of $[K]$ and/or the load vector of $\{R\}$ become(s) a function of the displacement solution of $\{D\}$, solving requires an iterative process (Cook et al., 2001). The Newton-Raphson method is a commonly used technique to effectively handle hardening behavior, while the continuation methods of Arc-Length and Riks are excellent at tracing snap-back and snap-through behaviors which are exhibited in unstable structures, such as stiffened-plated structures (Riks, 1979; Crisfield, 1998; Bathe, 1996). Possible solution strategies in modeling nonlinear brittle-collapse, post-buckling behaviors of built-up, cold-formed members (as previously shown in Figs. 10 and 11) to ensure the accurate modeling of a structural failure and not a numerical blow out are as follows:

- **Perform the Newton-Raphson iteration with displacement controlled:** This technique can moderately handle a softening descending branch in a brittle-collapse and snap-through behavior. It, however, fails under a snap-back which is not a typical concern for buckling of cold-formed sections. This technique has been mainly adopted for the ANSYS implicit-static models us to validate the experimental results in Fig. 8.

- **Treat a buckling response dynamically using an explicit integrator:** This technique is to approximate the response with inertial effects entirely included at the

beginning or partially after the static solution becomes unstable. An inclusion of geometric and material nonlinearities has little effect on the integrator algorithm (Belytschko et al., 2000). Discontinuous contact conditions are formulated and used on a node-to-node basis resulting in no iteration being required (ABAQUS®, 2007b). This solution technique has been adopted for the ABAQUS explicit-dynamic model to verify the ANSYS implicit-static models.

- **Use an energy stabilizer (i.e., dashpot(s)):** This technique adds an artificial energy to an unstable structure when its load-carrying capacity is reached. The technique works well with a hardening nonlinearity and/or ductile-collapse response with an almost flat plateau after becoming unstable. It ceases under a softening descending branch which is a primary-concerned behavior in cold-formed buckling. Therefore, this technique is not adopted.

- **Use the continuation method of the Arch-Length or Riks scheme:** The algorithm was purposely developed to advance solutions possessing a snap-back and/or snap-through behavior (Riks, 1979). Prior to its introduction, using the aforementioned techniques or literally abandoning equilibrium iterations in the close vicinity of buckling loads or limit points was the common practice (Crisfield, 1998). Unfortunately, the method suffers from an inherent discontinuity due to a presence of contact elements. A numerical difficulty of using the Riks method with surface-to-surface contact elements defined along the back panels of a built-up, *I*-shape section was reported in Becque and Rasmussen (2008). An artificial damping (energy stabilizer) was used to stabilize the solution at the first few substeps. A consideration for the magnitude of the damping factor, as well as the stabilized step size not to alter an overall solution, is very critical. Thus, this technique is adopted exclusively for single, cold-formed sections.

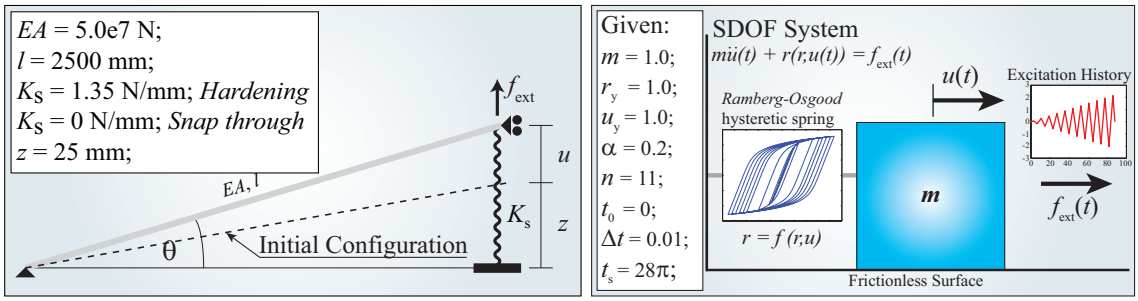


Figure 15: Two nonlinear single-degree-of-freedom systems to review the implicit and explicit numerical schemes available for nonlinear buckling analyses. On the left, a nonlinear-geometric system of an elastic bar attached to a roller and a linear spring on the right end and pinned on the left end (Crisfield, 1998) is implicitly solved under the Newton-Raphson and Arc-Length methods as shown in Figs. 16 and 17. On the right, a nonlinear-hysteretic dynamic system of a unit mass with a Ramberg-Osgood restoring force (Jennings, 1964) is exited under an amplitude-modulated cyclic loading (Piyawat et al., 2008). At a given time step, the solution of the restoring force is iterated under the Newton-Raphson scheme, while the solution of displacement is advanced along the time span using an explicit Central-Difference integration. The implementation flowchart is given in Fig. 18.

Three numerical examples of two nonlinear single-degree-of-freedom (SDOF) systems as shown in Fig. 15 are performed for a thorough review of the adopted solution techniques. The review aspects includes: (1) nonlinear path-dependent and path-independent (i.e., systems with and without memory), (2) limitations of an implicit and an explicit scheme, and (3) a simplicity of an explicit scheme versus a complexity of an implicit scheme. All the presented numerical works are carried out under MATLAB (Harman et al., 2000; Palm, 2001), unless otherwise stated.

The first system on the left in Fig. 15 is an elastic bar attached to a roller and a linear spring on right end and pinned on the other end (Crisfield, 1998). The vertical displacement u of the tip subjected to an upward external force f_{ext} is the unknown of interest. The governing equation as well as the equation of the tangent stiffness K_t (i.e., $\frac{\partial f_{\text{int}}}{\partial u}$, where f_{int} denotes the internal force to equilibrate f_{ext}) are given as a function of u

as follows:

$$f_{\text{ext}} = \underbrace{(EA/l^3)(z^2u + 1.5zu^2 + 0.5u^3) + k_s u}_{f_{\text{int}}} \tag{33}$$

$$K_t = (EA/l^3)(z^2 + 3zu + 0.5u^2) + k_s \tag{34}$$

As indicated in Eq. (34), this system has a geometric nonlinearity with a path-independent feature inferring that its current solution does not require a knowledge of its previous solutions. This system would contain the other nonlinearities in material and boundary if the material stiffness E was a function of u and there was a clearance between the bar and the spring. With a given history of u, f_{ext} can be evaluated trivially. In the opposite, an incremental-iterative approximation of u is needed under a given history of f_{ext}.

The adopted properties of the material and the geometry are as follows: (1) the product of E and the cross-sectional area A equal to 5.0e7 Newtons, (2) the initial bar length l = 2,500 millimeters, and (3) the initial spring length z = 25 millimeters. The SI units of Newton and millimeter are abbreviated as N and mm, hereafter. With the presence of the spring stiffness of k_s = 1.35 N/mm, the system expresses a hardening response in the load-displacement history (see Fig. 16) and a snap-through behavior when k_s = 0 N/mm (see Fig. 17). With the two different values of k_s, the two sets of static solutions are solved iteratively under the implicit schemes of: (1) the Newton-Raphson method with force being controlled and (2) the Arc-Length continuation method, as shown in Figs. 16 and 17, respectively.

In the Newton-Raphson solution process, the incremental equilibrium solution of a nonlinear algebraic equation is advanced through a pseudo time-step (substep) through iterations. Based on the assumption of the existence of the first-order term of the Taylor series and the truncation of the other high-order terms (Hamming, 1986; Mathews and Fink, 2004), the iterative equation at a given substep n is formulated in Eq. (35). The superscript of $\hat{\cdot}$ and the subscript of i denote the approximated solution and the iteration

index starting from zero.

$$\hat{u}_{i+1} = \hat{u}_i - (f_{\text{int}}(\hat{u}_i) - n\Delta f_{\text{ext}})/K_t(\hat{u}_i) \tag{35}$$

With a uniform incremental force Δf_{ext} chosen as 5 N, a total of 17 substeps to trace a hardening response history under f_{ext} of 75 N are carried out. The solution of $\hat{u}$ converging along a referenced load of 25 N is locally shown in the fifth-substep iteration history at the upper-left corner of Fig. 16. The initial value of $\hat{u}$ is taken as zero for the first substep and as the most-recently-converged solution for the rest, i.e., $\hat{u}_{i=0} = u_{n-1}$. The convergence is archived upon the out-of-balance force $f_{\text{int}}(\hat{u}_{i+1}) - n\Delta f_{\text{ext}}$ or $\hat{g}$ less than a tolerance of 10^{-6} N. The localized convergence-history panel at the lower-right corner indicates the largest incremental displacement Δu is in the seventh substep and the largest iteration number in the eighth substep.

Upon a removal of the linear spring, the response under f_{ext} of 15 N changes to a snap-through in behavior as shown in Fig. 17. A total of 19 substeps are carried out under the Arc-Length continuation method to trace the whole response history. An equilibrium iteration under the Newton-Raphson method would have failed at the ninth substep in the vicinity close to the first limit point due to a singularity in the stiffness inversion (see Eq. (35)). Such difficulty motivates the introduction of the continuation method by Riks (1979). The solution of $\hat{u}$ converges along a referenced spherical arc (as locally shown in the 17$^{\text{th}}$ iteration history) instead of a horizontal linear line as previously shown in Fig. 16. The assumption made in the algorithm is that f_{ext} is proportional to a load factor λ, which becomes an additional unknown in return. In specific, the assumption results in: (1) a modification of Eq. (33) to account for λ, and (2) an additional incremental quadratic-constrained equation defining a referenced spherical arc, as given in Eqs. (36) and (37),

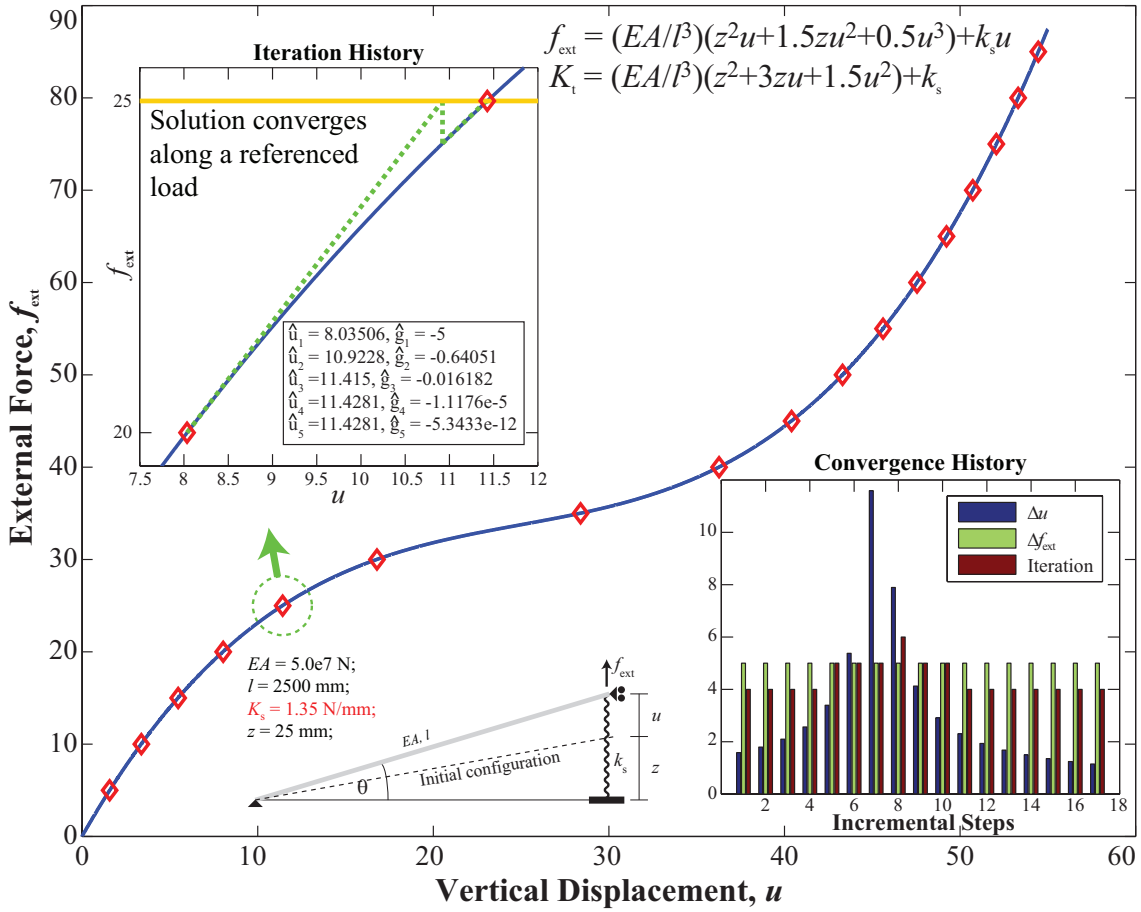


Figure 16: A hardening load-displacement response history of a nonlinear SDOF of an elastic bar resting on a linear spring and subjected to an upward external force f_{ext} of 85 N (Crisfield, 1998). The system has geometric nonlinearity, since the stiffness depends on the deformed configuration, i.e., $K_t = K_t(u)$. The solutions of u are obtained iteratively using the forced-controlled Newton-Raphson method. The solutions converge along referenced forces of a constant increment of 5 N. Convergence is assumed upon an out-of-balance force of $|f_{\text{int}} - f_{\text{ext}}|$ less than 10^{-6} N. The convergence history including the incremental displacements Δu and required iteration number i as well as the iteration history of the fifth substep are also provided.

respectively.

$$\lambda f_{\text{ext}} = \underbrace{(EA/l^3)(z^2u + 1.5zu^2 + 0.5u^3) + k_s u}_{f_{\text{int}}} \tag{36}$$

$$\Delta L^2 = \Delta u^2 + \Delta\lambda^2\psi^2 f_{\text{ext}}^2 \tag{37}$$

The scaling factor of ψ to assure a compatibility in the unit of space is taken as 1.0. A variable of ΔL referred as a radius of a referenced arc and originating at the previous converged solutions of u_{n-1} and $\lambda_{n-1} f_{\text{ext}}$ is given in Eq. (38). ΔL is kept constant during iterations but varied between substeps reflecting in a non-uniform step size. The notation of i_{n-1} denotes as an iteration number required in the previous substep. The notation of n_{max} denotes the permitted maximum substep and is taken as 300.

$$\Delta L_n = \begin{cases} (f_{\text{ext}}^2/n_{\text{max}})\sqrt{1/K_t^2 + \psi^2} & ; \text{if } n = 1 \\ \Delta L_{n-1}\sqrt{3/i_{n-1}} & ; \text{otherwise} \end{cases} \tag{38}$$

The iterative unknowns of Δu and $\Delta\lambda$ denote incremental quantities of u and λ. For a given substep n, they are iterated/updated based on the iterative changes of δu and $\delta\lambda$ as in Eqs. (39) and (40). The initial values of $\Delta\hat{u}_i$ and $\Delta\hat{\lambda}_i$ are taken as zero and $f_{\text{ext}}/n_{\text{max}}$, respectively, for the first substep (i.e., n = 1) and latter as Δu_{n-1} and according to Eq. (37), for other substeps.

$$\Delta\hat{u}_{i+1} = \Delta\hat{u}_i + \delta u \tag{39}$$

$$\Delta\hat{\lambda}_{i+1} = \Delta\hat{\lambda}_i + \delta\lambda \tag{40}$$

The variable of $\delta\lambda$ is determined as a root of the quadratic equation given in Eq. (41). This equation is derived from substituting Eq. (36) into Eq. (37). The variable of δu is a

linear function of $\delta\lambda$ and can be determined according to Eq. (42).

$$a_1\delta\lambda^2 + a_2\delta\lambda + a_3 = 0 \tag{41}$$

$$((f_{\text{int}} - \lambda_i f_{\text{ext}})/K_t) + (f_{\text{ext}}/K_t)\delta\lambda = \delta u \tag{42}$$

The coefficients of a_1, a_2 and a_3 in Eq. (41) and a_4 and a_5 given latter in Eq. (48) are defined in Eqs. (43)-(47). Note that f_{int} and K_t (as previously defined in Eqs. (36) and (37)) contained in Eqs. (42) to (47) are now a function of $\hat{u}_i$ and/or $\hat{\lambda}_i$.

$$a1 = (f_{ext}/K_t)^2 + (\psi f_{ext})^2 \tag{43}$$

$$a2 = 2(f_{ext}/K_t)(\Delta u_i + (f_{\text{int}} - \lambda_i f_{\text{ext}})/K_t) + 2\Delta\lambda_i(\psi f_{\text{ext}})^2 \tag{44}$$

$$a3 = (\Delta u_i + (f_{\text{int}} - \lambda_i f_{\text{ext}})/K_t)^2 + (\Delta\lambda_i \psi f_{\text{ext}})^2 \tag{45}$$

$$a_4 = \Delta u_i((f_{\text{int}} - \lambda_i f_{\text{ext}})/K_t) + \Delta u_i^2 \tag{46}$$

$$a_5 = (f_{\text{ext}}/K_t)\Delta u_i \tag{47}$$

Only one of the two distinctive real roots (denoted as $\delta\lambda_1$ and $\delta\lambda_2$) of Eq. (41) is taken as $\delta\lambda$. The imaginary root(s) is invalid indicating a reduction of ΔL or a failure of the algorithm. The criterion to choose $\delta\lambda$ is as follows:

$$\delta\lambda = \begin{cases} \delta\lambda_1 & \text{; if } (a_4 + a_5\delta\lambda_1) > (a4 + a5\delta\lambda_2) \\ \delta\lambda_2 & \text{; otherwise} \end{cases} \tag{48}$$

The converged $\Delta\lambda_n$ can possibly be positive or negative with magnitude less than or equal to a unit depending on whether an ascending or descending branch of the response is being traced as evidenced in the local panel of the convergence history. Convergence is assumed upon satisfying the condition of $|f_{\text{int}} - \lambda f_{\text{ext}}| < 10^{-6}$ N, same as in the former method. Solution updating is ceased once the magnitude of λ_n exceeding a unit indicating the desired loading magnitude has been achieved; otherwise, u_n and λ_n are kept updated

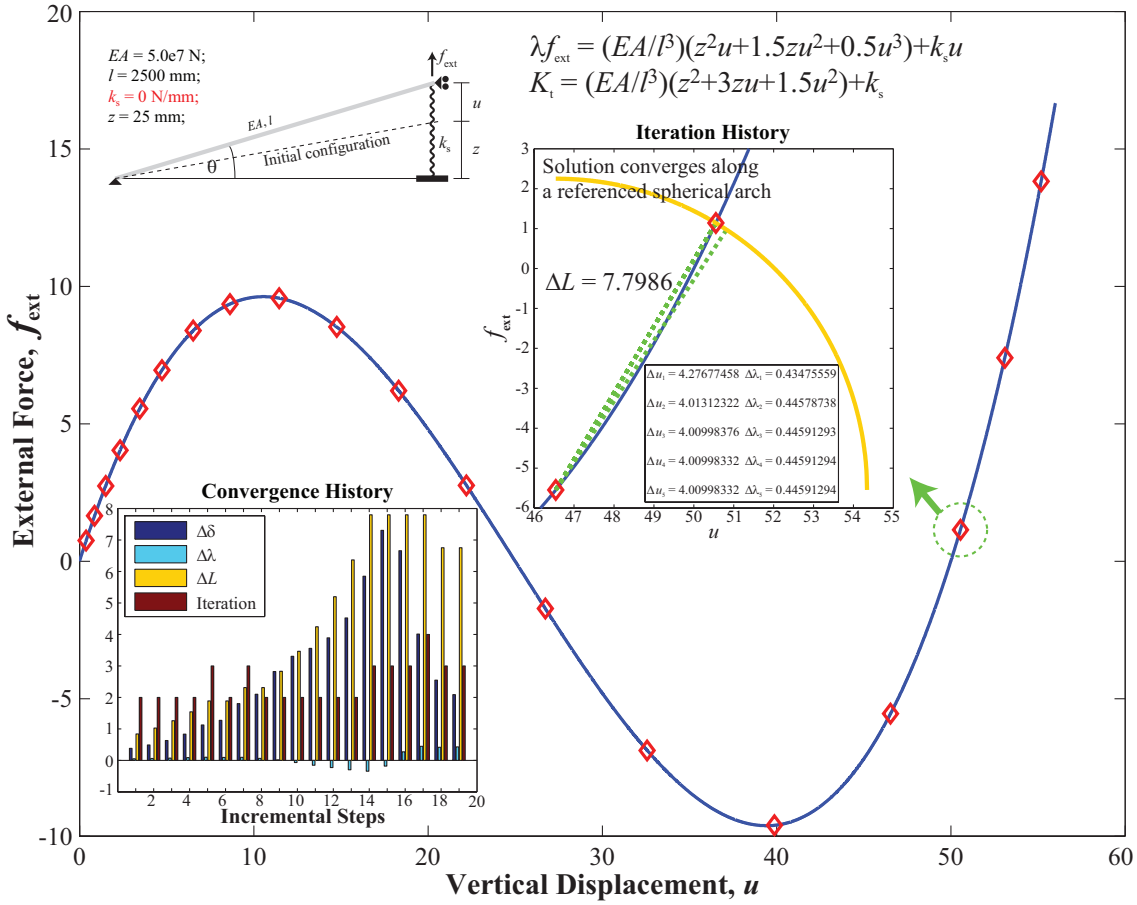


Figure 17: A snap-through response history of the first SDOF system shown in Fig. 15. Basically, the system is identical with the one in Fig. 16 except no linear spring supporting at the bar tip, i.e., $k_s = 0$. The spherical Arc-Length scheme is used to trace the solutions of the displacement u and the load proportional factor λ converging along referenced spherical arcs instead of linear referenced loads as in Fig. 16. Various convergence histories including the incremental displacement $\Delta\delta$, the incremental load factor $\Delta\lambda$, the arc radius ΔL, and the iteration history at 17$^{\text{th}}$ substep are also included.

until $n_{\max}$ is reached. The associated recorded histories show the maximum iteration number of five is required in the 17$^{\text{th}}$ substep, while the 15$^{\text{th}}$ substep is the largest in step size, i.e., the largest in ΔL and $\Delta\lambda$. To facilitate insightful detail, the graphical implementation under LabVIEW (LabVIEW™, 2000) is included in Appendix A. The linearized version of the method (known as the Riks method) has a linear constrained equation, which bypasses the issues of quadratic equations and choice of roots, but is less stable and slower to converge (Crisfield, 1998).

The second SDOF system (on the right of Fig. 15) to review an explicit dynamic integration of the Central-Difference method is a chain-like system consisting of a unit lumped mass m attached to a nonlinear-hysteretic spring featuring the Ramberg-Osgood model (Jennings, 1964; Chopra, 2000; Piyawat et al., 2008). The system is excited under an amplitude-modulated cyclic load $f_{\text{ext}}(t)$ of 28π-second long and 0.75-Hz frequency. The equation of motion along with the governing equations of the restoring force on: (1) the virgin (skeleton) curve, and (2) the reloading and unloading curves are given in Eqs. (49), (50), and (51), respectively.

$$m\ddot{u}(t) + r(r, u(t)) = f_{\text{ext}}(t) \tag{49}$$

$$\frac{r}{r_y} + \kappa \left(\frac{r}{r_y}\right)^{\eta} = \frac{u}{u_y} \tag{50}$$

$$\frac{r - r_p}{2r_y} + \kappa \left(\frac{r - r_p}{2r_y}\right)^{\eta} = \frac{u - u_p}{2u_y} \tag{51}$$

The restoring force $r = r(r, r_p, u, u_p)$ is highly nonlinear path-dependent as a function of itself, displacement u and selectively, the most recent reversal (denoted as u_p and r_p) in the displacement vs. restoring force history (see Fig. 18, the lower-left corner). The variables of u_p and r_p are kept constant during the unloading and reloading process (as long as the sign of an incremental displacement Δu remains unchanged) and altered once Δu changes in sign at a reversal. They are considered as local minima (i.e., valleys), if $\Delta u > 0$, otherwise; local maxima (i.e., peaks). The parameters of u_y and r_y (both taken as 1.0) are referred as the yield displacement and yield restoring force. The parameters of κ and η (taken as 0.2 and 11, respectively) are parameters controlling the hysteretic profile and the smoothness on an elastic-to-plastic transition. The value of n must be a positive odd integer greater than one (Jennings, 1964). As $\eta \to \infty$, the model approaches elastic, ideally plastic behavior.

With the presence of the Ramberg-Osgood model, an explicit (on the green background of Fig. 18) and implicit (on the red background) algorithms can be brought to-

gether enabling a side-by-side qualitative visualization favoring the former simplicity and the latter complexity. The price of avoiding equilibrium iteration results in a conditional stability, which is the opposite to the adopted implicit integrator (will be discussed shortly). With a second-order truncation error as same as in the Newton-Raphson scheme, a stable time step Δt needs to be smaller than a critical time step Δt_{cr} defined as a function of the maximum natural frequency; otherwise, an unboundedly-growing solution (Bathe, 1996; Belytschko et al., 2000; ABAQUS®, 2007b). Such restriction is not as much of a concern in an implicit scheme, and thus, allowing larger time steps. With a uniform Δt of 0.01 seconds, nearly 8,800 time steps to complete the whole loading history are carried out. The most computational work is spent on the approximation of the restoring force. That is, at a given time step t_n, the Newton-Raphson algorithm (as shown on the red background) approximates r_n upon the known value of u_n from: (1) the initial condition specified at t = 0, and (2) the Central-Difference integration, thereafter. The iterative equation along with the characteristic equation $F(\hat{u}_i)$ and its first derivative with respect to $\hat{u}_i$ (denoted as $F'(\hat{u}_i)$) are given in Eqs. (52)-(54), respectively (Nakamura, 1991). Again, the subscript i denotes an iteration index. Convergence is assumed upon satisfying the condition of $(\hat{r}_{i+1} - \hat{r}_i)/\hat{r}_i < 10^{-6}$. The being-approximated $\hat{r}_{i+1}$ is then taken as the restoring force solution at time t_n (i.e., r_n). To facilitate the discussion, the combined schematic of the integration and the iteration is summarized on the left hand-side of Fig. 18.

$$\hat{r}_{i+1} = \hat{r}_i - F(\hat{r}_i)/F'(\hat{r}_i) \tag{52}$$

$$F = \begin{cases} u_y(\frac{\hat{r}_i}{r_y} - \kappa\left(\frac{\hat{r}_i}{r_y}\right)^{\eta}) - u_n & \text{; virgin curve} \\ 2u_y(\frac{\hat{r}_i - r_p}{2r_y} + \kappa\left(\frac{\hat{r}_i - r_p}{2r_y}\right))^{\eta} - (u_n - u_p) & \text{; reloading curves} \end{cases} \tag{53}$$

$$F' = \begin{cases} u_y(\frac{1}{r_y} + \kappa\eta\left(\frac{1}{r_y}\right))\left(\frac{\hat{r}_i}{r_y}\right)^{(\eta-1)} & \text{; virgin curve} \\ \left(\frac{u_y}{r_y}\right)(1+\kappa\eta)\left(\frac{\hat{r}_i - r_p}{2r_y}\right)^{(\eta-1)} & \text{; reloading curves} \end{cases} \tag{54}$$

The solution of u_n is then updated along the time span to the next time step of $n+1$ upon the committed value of r_n through the Central-Difference integration according to Eqs. (55)-(57) (the algorithm shown on the green background). In contrast to the implicit algorithm, no iteration but only algebraic evaluation is needed here, which highlights the beauty of the explicit scheme.

$$\ddot{u}_{n+1} = \frac{(f_{\text{ext}}(t_n) - r_n)}{m} \tag{55}$$

$$\dot{u}_{n+1} = \begin{cases} \dot{u}_n + \frac{1}{2}\Delta t \ddot{u}_n & ; t = 0 \\ \dot{u}_n + \Delta t \ddot{u}_n & ; \text{otherwise} \end{cases} \tag{56}$$

$$u_{n+1} = u_n + \Delta t \dot{u}_n \tag{57}$$

OpenSees (Fenves et al., 2002) is adopted as a numerical framework to perform an implicit integration of the Newmark method as the verification. The availability of the source code enables the implementation of the Ramberg-Osgood model as a subclass of the *UniaxialMaterial* class (Piyawat, 2005; Piyawat et al., 2008; Piyawat and Pei, 2009). A unit nodal mass attached to a nonlinear zero-length element of one end fixed and axially free in translation on the other end is constructed in the two-dimensional modeling domain. The newly-implemented model defining the elemental response at the force-deformation level is specified. With a uniform Δt of 0.1 seconds, which is 10 times greater the Δt of the explicit scheme, the validation is made through comparing the restoring force vs. the displacement history, as shown on the lower left corner of Fig. 18.

Under a linear transient analysis, the Newmark integrator is unconditionally stable. This points out its advantage over the explicit integrator (Belytschko et al., 2000). With the parameters of γ and β controlling the accuracy, numerical stability, and algorithmic damping chosen as 0.5 and 0.25, respectively, an unconditional stability is obtained under the current nonlinear analysis (Cook et al., 2001). Nevertheless, the major drawback of adding the algorithmic damping via using $\gamma > 0.5$ to suspend the high-frequency-noise

is that the accuracy of the solution drops significantly (Belytschko et al., 2000). Under this circumstance, the Hilbert α-method is capable of providing the numerical dissipation without as much loss of accuracy (Hilbert et al., 1977).

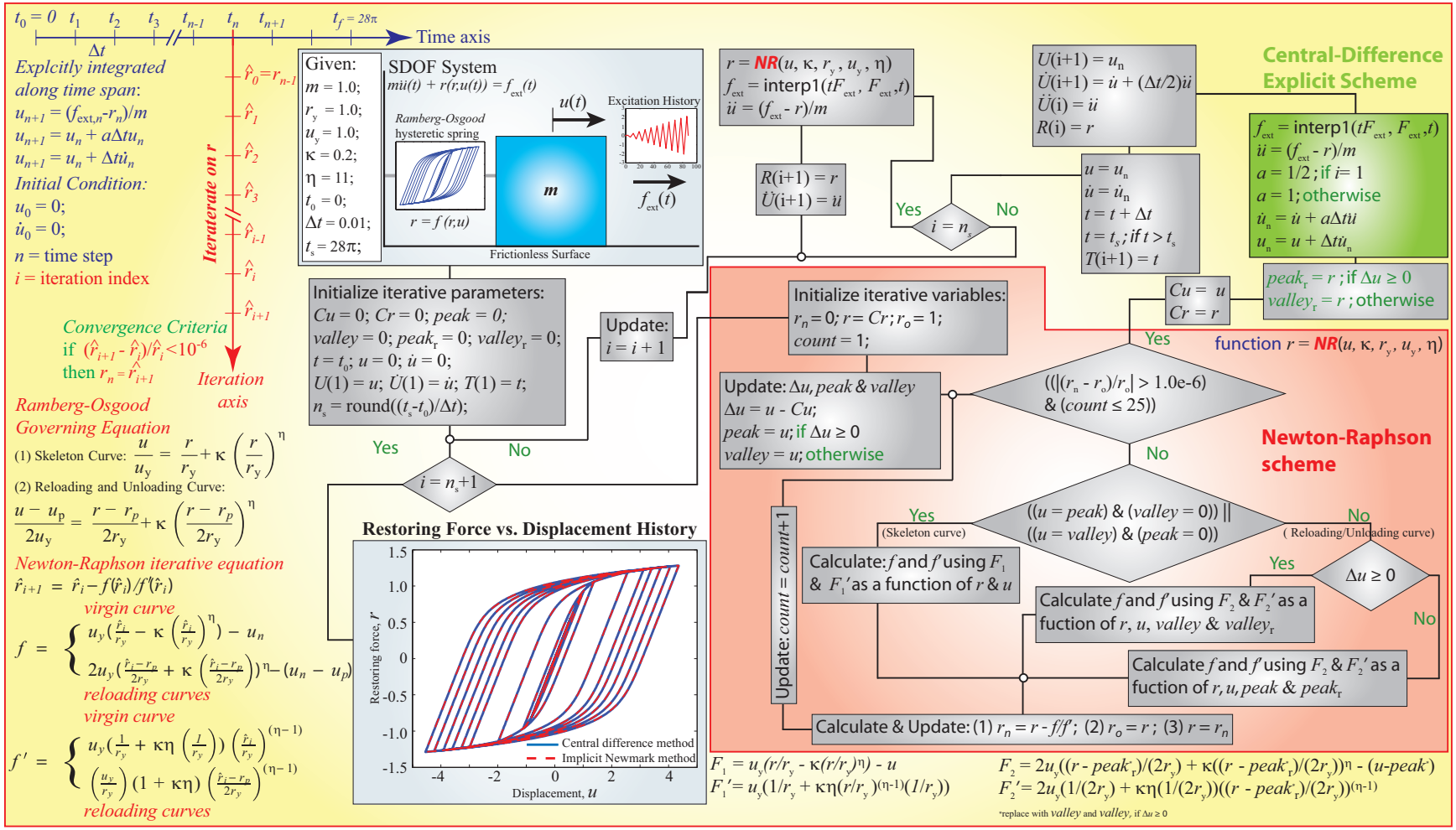


Figure 18: An implementation flowchart of a nonlinear-hysteretic SDOF system under an amplitude-modulated excitation. The restoring force r of the Ramberg-Osgood feature (Jennings, 1964) is iterated under the Newton-Raphson scheme. The displacement u is explicitly integrated along the time span using the Central-Difference integrator.

3 PHASE I: ANSYS VALIDATION AND ABAQUS VERIFICATION[1]

3.1 Overview of *Phase I*

In this study, calibration of a state-of-the-art modeling strategy for a nonlinear large-displacement buckling analysis is carried out. Two nonlinear finite-element packages of ANSYS and ABAQUS are used to validate and verify over 265 experimental buckling tests (previously reviewed in Section 2.3). ANSYS is designated to validate the experimental results, and the ANSYS results are then verified by ABAQUS. Two different numerical schemes of implicit-static and explicit-dynamic are adopted. Also, a variety of iterative and non-iterative solution techniques are incorporated including: (1) the Newton-Raphson method, (2) the Arc-Length method, (3) the Riks method, and (4) the Central-Difference integration method. The ANSYS structural solid (brick) element of SOLID45 is thoroughly examined in comparison with its shell element counterpart of SHELL181 for modeling a critical state of buckling and a softening response in the post-buckling regime to assure a true structural failure (not a numerical-induced one). Finally, quantitative and qualitative comparisons between the experimental and numerical analyses are presented, which include:

- Axial load versus displacement histories along with ultimate axial load capacities
- Reaction and energy time histories before and after low-pass filtering
- Deformed shapes along with von-Mises stress contours

[1]This section is designed to be independent and self-contained to facilitate submission as a journal article. Therefore, some materials previously presented in Chapter 2 is repeated.

3.2 Numerical Simulation of Buckling in Built-up, Cold-Formed Sections

The modeling procedure as summarized in Fig. 19 consists of: (1) *Preprocessing Phase* where the problem (i.e., stiffness matrix) is formulated, (2) *Solution Phase* where the solution vector is solved either implicitly through iterations or explicitly through central-difference time integration, and (3) *Postprocessing Phase* where the solutions of interest are interpreted, e.g., the buckling capacities and their corresponding deformed shapes.

3.2.1 Preprocessing Phase

The key details of the ANSYS implicit-static and the ABAQUS explicit-dynamic modelings are summarized in Fig. 20. Their representative finite-element (FEM) models are shown in Figs. 21 and 22. The models contain all the sources of nonlinearity in material, geometry, and boundary (ABAQUS®, 2007a). The use of a path-dependent, bilinear-isotropic constitutive model causes the material nonlinearity. A large-displacement analysis, where the stiffness is a direct function of a deformed configuration, yields the geometric nonlinearity. A presence of contact elements along the lips and the back panels of the *R*- and *I*-shape orientations contributes in the boundary nonlinearity. The cold-work effect from the forming process usually results in a higher strength, but less ductility of the steel around the corners and in vicinity of a thickness distance (as shaded under the red regions) (Ashraf et al., 2005). The yield and ultimate strengths are to be increased by 22% and 17%, respectively, while the ultimate strain is to be decreased by half (Hancock et al., 2001). The residual stress is neglected, as the material properties were experimentally derived directly from the coupon tests performed on specimens of the actual members (Yang and Hancock, 2004; Yang et al., 2004; Ng and Gardner, 2007). The material characteristics of the modulus of elasticity (E), Poisson's ratio (ν), the yield stress and strain (σ_y and ε_y), and the ultimate stress and strain (σ_u and ε_u) are listed in Table 2.

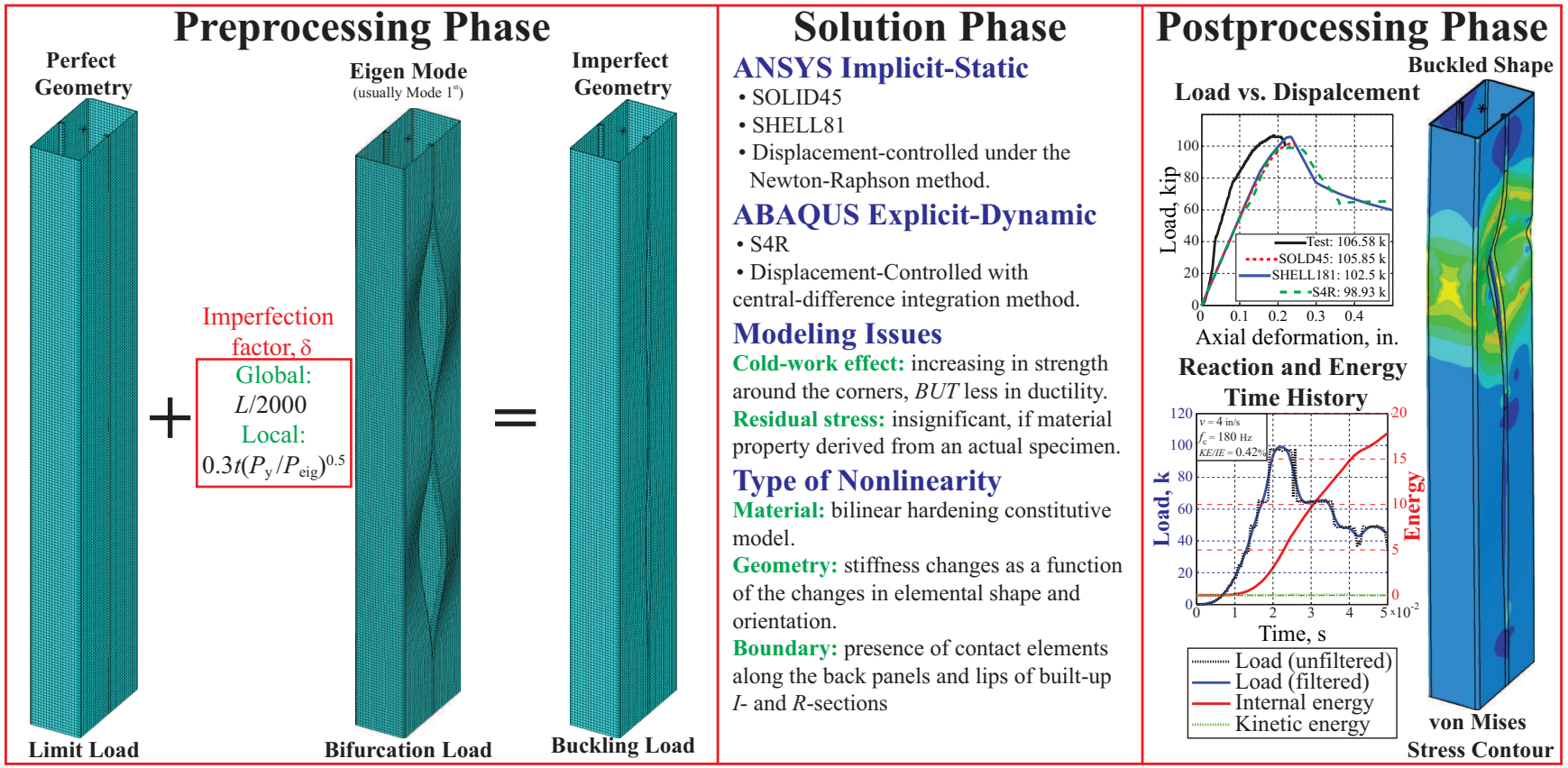


Figure 19: The modeling procedure to perform a nonlinear (large-displacement) buckling analysis.

Nominal Thickness(in.)	Measured Thickness(in.)	E (ksi)	ν (%)	Stress(ksi)		Strain(in./in.)	
				σ_y	σ_u	ε_y	ε_u
0.064	0.06073	29.5e3	0.3	71.1	81.3	2.41e-3	2.68e-1
0.080	0.07530	29.5e3	0.3	61.6	81.0	2.09e-3	2.66e-1
0.100	0.10010	29.5e3	0.3	71.8	81.1	2.43e-3	2.68e-1

Table 2: Material characteristics obtained from coupon tests performed on specimens of 0.5-in width and 2-in. length, cut from actual members (Whittle, 2007). The averaged values of three identical tests for each thickness are listed in an engineering format. ANSYS requires material stress-strain relation in this format, while the logarithmic format is required in ABAQUS. The relation between the two formats is: $\varepsilon_{\text{true}} = \ln(1+\varepsilon)$ and $\sigma_{\text{true}} = \sigma(1+\varepsilon)$.

In the first panel of Fig. 19, an Eigen-buckling mode is seeded onto a perfect mesh to trigger a geometric instability to avoid an exaggerated bifurcation load (see Fig. 12), where both perfect and infinitesimally-close buckled configurations and a numerical blowout are possible (Yang and Hancock, 2004; Yang et al., 2004; Gardner and Nethercot, 2004; Ashraf et al., 2005; Ng and Gardner, 2007). The first Eigen mode is commonly preferred, unless, the first two-consecutive modes are closely spaced having magnitudes less than 0.5 kips. Then, the second mode is also required. Failure of this may result in an underestimation of the ultimate load-carrying capacity as much as 30% (see Section 4.3). The degree of imperfection (denoted as δ), as suggested by Walker (1975), is adopted toward a member expressing distortional or local failure. It is incorporated into the first mode, and a magnitude of one-tenth the thickness is applied to the second mode, if applicable. For a flexural and a flexural-torsional buckling member, δ is taken as a fraction of the unbraced length. The imperfection factor is summarized as follows:

$$\delta = \begin{cases} \frac{L}{2000} & \text{; flexural (Euler) buckling} \\ 0.3t\sqrt{\frac{P_y}{P_{eig}}} & \text{; distortional and local buckling} \end{cases} \tag{58}$$

Where L and t denote an unbraced column length and a section thickness. The notations of P_y and P_{eig} denote a squash load (causing a yielding failure of an entire member) and an Eigen-buckling load. Alternatively, a non-Eigen-based perturbation using an imperfection

degree measured from an actual member was carried in Becque and Rasmussen (2008), which is time-consuming and believed not to yield any significant differences in accuracy as long as δ exceeds a certain threshold. According to Rasmussen and Hasham (2001) and Ng and Gardner (2007), the predicted buckling loads have a relatively low sensitivity to a local imperfection when the ratio of $\left(\frac{\delta}{t}\right)$ exceeds 2.5%. No loading eccentricity is considered in the modeling to reflect a condition of the pure-compression test. In short, for a given nonlinear buckling analysis, an additional linear analysis of Eigen buckling is required in advance with at least two modes extracted.

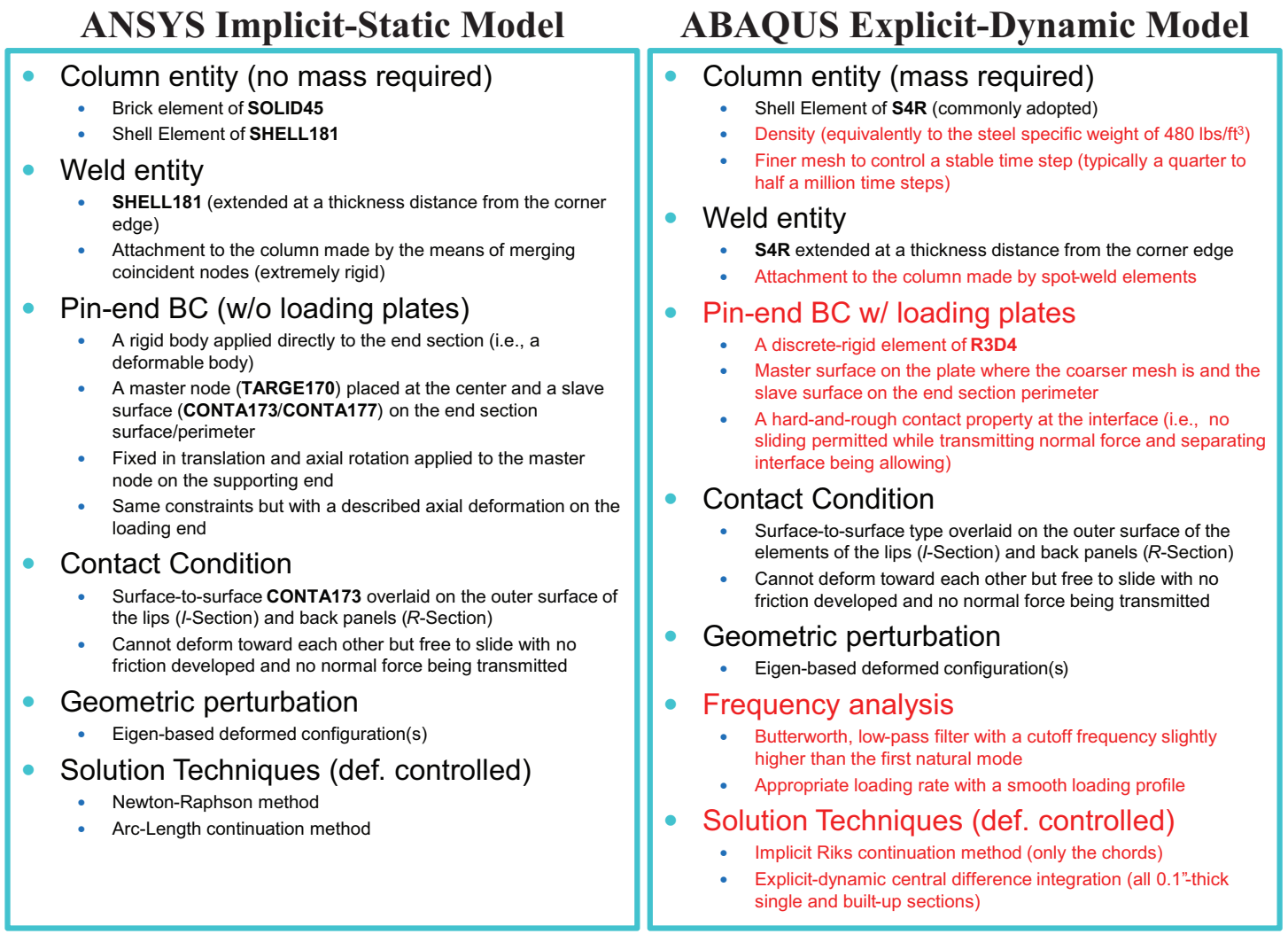


Figure 20: The key details of the ANSYS implicit-static and the ABAQUS explicit-dynamic modelings. The differences between the two modeling schemes are highlighted in red.

ANSYS Implicit-Static FEM model

ANSYS implicit-static modeling is adopted as the main package to validate the 265 tests. The representative finite-element model of the built-up, *R*-section is shown in Fig. 21. Two separate sets of modeling the column entity using a structural shell element of SHELL181 (a commonly-used element in the modeling discipline of thin-walled structures) and a structural solid element of SOLID45 are carried out to examine the modeling advantages in: (1) advancing through a critical state of being buckled, (2) tracing a softening response of the post-buckling regime, and (3) assuring a truly structural failure (not a numerical blowout). According to Bakker and Pekoz (2001) (Fig. 9), the SOLID45 is supposed to be better (disregarding the demanding relatively refined meshes) due to less errors in discretization and geometric approximation, e.g., mid-surface contact location as commonly adopted in shell elements.

The pinned-end condition is modeled according to a rigid-body concept consisting of a target element and a set of nodes defined by contact elements. A single pilot (master) node of TARGE170 governing the motion of the entire rigid body is placed coincidentally at the center of the end section, representing the swivel pivoting head in the experiment (see Fig. 4). A set of rigid-body nodes forming a slave surface is defined by surface-to-surface CONTA173 or line-to-surface CONTA177 depending on whether SOLID45 or SHELL181 is being used for the column elements. The rigid body is attached to the (deformable) column by directly overlaying the slave surface on the end section. A displacement boundary condition is directly imposed on the master node. On one end, all translations and axial rotation are prevented. On the other end, the same constraints are applied but with a prescribed axial deformation to perform a displacement-controlled analysis.

For the built-up members, CONTA173 are overlaid on the lips and the back panels of the *I*- and *R*-sections to prevent them from deforming toward each other. The contact behavior is assumed as frictionless, i.e., free to slide without normal force being transmit-

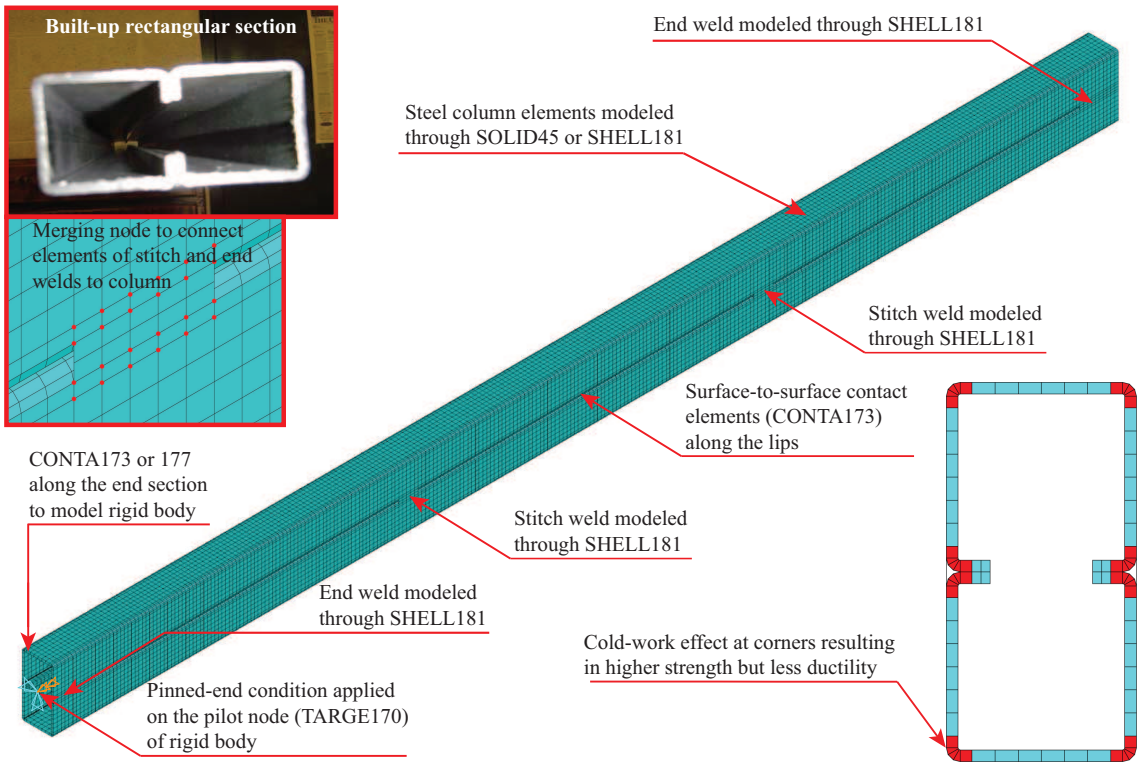


Figure 21: ANSYS SOLID45/SHELL181 implicit-static model of the built-up, *R*-section.

ted. The elements of the welds are accounted for using SHELL181. They are attached to the column by means of merging coincident nodes. The width of the weld is assumed to extend beyond the corners at a distance of the section thickness. Therefore, there are four merged nodes at a given cross section of the weld. The largest mesh sizes across the width and along the length are kept as 0.20 in. consistently throughout this work.

The errors inherent to running these numerous numerical tasks of 322 simulations are compromised through a sequential, batch-feeding mode using a collection of ANSYS-Parametric-Design-Language (APDL) macros (Madenci and Guven, 2006; ANSYS®, 2009b) to create and execute the models and retrieve the solutions of interest. With the varying section properties (Fig. 5), stitch-weld patterns (Fig. 6), and material characteristics (Table 3) taken as the input arguments, these macros are called selectively, sequentially, and repetitively by a unique global driver file to handle different specimen configurations.

ABAQUS Explicit-Dynamic FEM Model

The ABAQUS explicit-dynamic model of the built-up, *I*-section is shown in Fig. 22. A commonly-used shell element of S4R is adopted for the components of the column and welds. The connections between these components are made rigidly through spot-weld elements, instead of merging the coincident nodes as in the ANSYS modeling. A discrete-rigid element of R3D4 is used to model the two square loading plates of 1.0-in thick and 8.0-in. width. These plates, in contrast to the ANSYS implicit-static modeling, are included to facilitate the inertial effect. The column mass is incorporated through a common steel specific weight of 480 lbs/ft^3. A lumped rotational mass of the plate located at the centroid is taken as 4.7e-05 kip.s^2/in. No translational mass is required due to the axial deformation being controlled.

A contact interaction of surface-to-surface type is defined at the interface of the plate and the column's end section. The master surface is laid on the plate where the coarser mesh is, and the slave surface is laid on the end section. A hard-and-rough behavior is defined as the contact property, meaning that no sliding is permitted, while transmitting normal force and separating interface is being allowed. The pinned-end condition is directly applied to a reference point of the plate, located at the center. Fixed in translation and in axial rotation is imposed to the supporting plate. The same constraint, but with a prescribed axial deformation under a smooth loading profile, is imposed at the reference point of the loading plate. A frictionless-general-contact interaction is included along the lips and the back panels of the *R*- and *I*-sections. These surfaces are not allowed to deform toward each other, but can freely slide pass with no friction developed.

3.2.2 Solution Phase

All the numerical buckling analyses are carried out with an axial deformation being controlled under a large-displacement assumption to consider geometrical nonlinearity. The solutions are not unique and strongly dependent on the incorporated geometric imperfec-

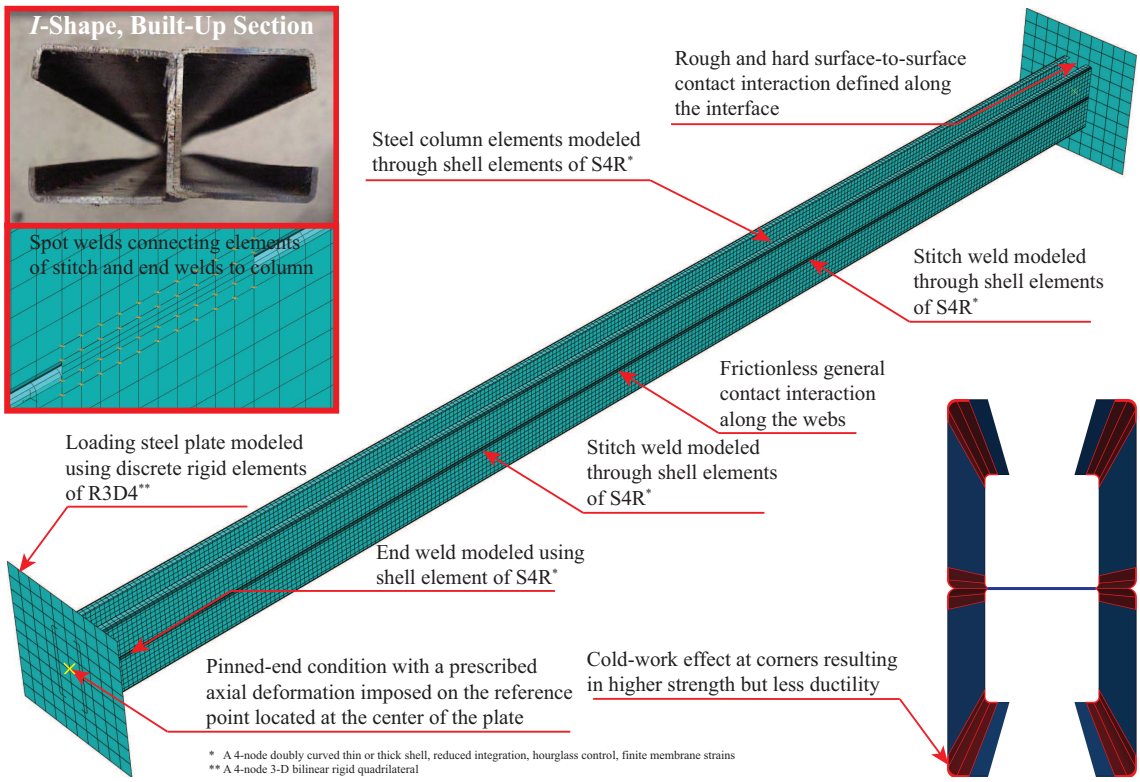


Figure 22: The ABAQUS explicit-dynamic model of the built-up, *I*-section.

tion (Mish et al., 2000). The solutions are obtained implicitly under ANSYS and explicitly under ABAQUS. An overview of the Solution Phase (previously reviewed in Section 2.5 through numerical exercises) is illustrated in the second panel of Fig. 19. The three possible solution techniques to handle a ductile- and a brittle-collapse failure mechanism in built-up, cold-formed sections are described as follows:

- *Using the Newton-Raphson method with displacement-controlled as the solution technique*. The scheme under force-controlled (i.e., given force to iterate on displacement) is very effective for a nonlinear problem with a hardening and ductile-collapse, load-deformation relation (Kim et al., 2010), but fails under a softening one, such as in a snap-through and a brittle-collapse failure. Termination as approaching a critical buckling state due to a singularity in the stiffness-matrix inversion is typical. This can be sometimes insufficient to justify a true structural failure from a numerical blowout, resulting in a misleading load-carrying capac-

ity. Alternatively, using the displacement-controlled scheme may trace a solution of the post-buckling regime, but with no guarantee. It depends on several factors, e.g., how the stiffness matrix is formulated, how large the incremental substep is (using the smaller ones does not always assure a convergence), and how tight the tolerance being used is. This technique is fully adopted during the ANSYS implicit-static solution process to validate both single and built-up sections. The tolerances on an out-of-balance force and moment are left to defaults as 0.1% with a minimum reference value of 1.0 kip and 0.01 kips-in. The initial, minimum, and maximum substeps for a load step are taken as 25, 5, and 3,200, respectively. Bisection is activated once the predicted successful iteration for a given substep exceeds 25 iterations. A convergence history is monitored and recorded for the loosening purpose when the divergence in advancing through the buckling state is encountered. The tolerance on the out-of-balance force and moment are loosened as 0.5% with a minimum reference value of 50 kips and 0.1 kips-in., respectively. These, thus, raise the tolerance to 0.25 kips and 5e-4 kips-in, respectively.

- *Using the method of continuation as the solution technique*. The method of continuation was originally developed under a proportional loading assumption to trace a snap-through solution (Riks, 1979). The assumption, in return, leads to an additional quadratic equation as in the ANSYS Arc-Length method and an additional linear equation as in the ABAQUS Riks method. In contrast to the Newton-Raphson method, instead of converging along a referenced horizontal load (see Fig. 16), the Arc-Length solution converges along a referenced spherical arc centering at the previous converged solution (see Fig. 17). This circumvents the singularity issue in the stiffness matrix inversion, and thus, enables the post-buckling solution. The Arc-Length method converges faster (at a cost of solving a quadratic equation at each iteration) but has a hard time iterating a post-buckling, descending response, whereas the Riks method is relatively good at solving a snap-through behavior.

The continuation method suffers from a presence of contact elements (discontinuity) in a built-up section (theoretically, due to a violation of smoothness in behavior (Crisfield, 1998)). The contact formulation cannot be established properly. To overcome the difficulty, the (static) Riks method was used in series with an energy stabilizer (a pseudo dashpot to dissipate energy) as in Becque and Rasmussen (2008). In all, the Riks method is partially adopted in the ABAQUS solution process exclusively for the single sections of the channels and the chords. All the controlling parameters, including a minimum and a maximum load multiplier, are left to defaults. The solution step size cannot be explicitly controlled and entirely depends on the previous ones.

- *Using the explicit Central-Difference time integration method as the solution technique*. Treating a nonlinear quasi-static problem dynamically is another means to overcoming the difficulty in the contact formulation. No iteration required during the solution process highlights the beauty of the explicit scheme. Nevertheless, significantly small increments and finer meshes for a stable and reliable solution are a tradeoff. An uncertainty in loading rate is also a critical issue and will be discussed later in Section 3.2.3. For a given run, all these considerations literally lead to a quarter or half a million time steps to achieve the required load-displacement history. The solution of such a high-frequency simulation is inevitably noisy. The behavior of the first mode is of interest, and the other high-frequency components need to be suspended using a Butterworth, low-pass filter having a cutoff frequency slightly higher than the first natural mode (Mitra, 2005). In short, for a given explicit run, one additional frequency analysis to determine a proper cutoff frequency is required in advance. This solution technique is fully adopted during the ABAQUS solution process for the verification.

3.2.3 Postprocessing Phase

The overview of the Postprocessing Phase is summarized in the third panel of Fig. 19. Using different ANSYS structural elements of SHELL181 and SOLID45 yields almost identical histories of axial load versus deformation responses as shown Fig. 23 (see Appendix B for other histories of the adopted configurations). The latter, however, has a convergent advantage enabling post-buckling solutions for most analyses without loosening the default tolerances. This is particularly so for members prone to distortional buckling (i.e., all the series of *I3*- and *R3*-sections). In contrast, SHELL181 nearly always terminates prior to buckling. Moreover, it is significantly more sensitive to loading eccentricity, specifically in the series of single-sided, *R1*-sections (*SW-R1*). A relatively small eccentricity (introduced) may cause the numerically simulated shape to deviate from the experimentally deformed shape. Therefore, only the results of SOLID45 are processed and presented hereafter. The numerical validation is performed for the ultimate buckling capacities (see Figs. 24 and 25) and for the deformed shapes along with von-Mises stress contours (Figs. 27-31 and Appendix C). The load-carrying verification under ABAQUS explicit-dynamic selectively performed on the thickest sections are presented in Fig. 32. The corresponding time histories of filtered and unfiltered reactions as well as kinetic and internal energy are presented in Figs. 33-35.

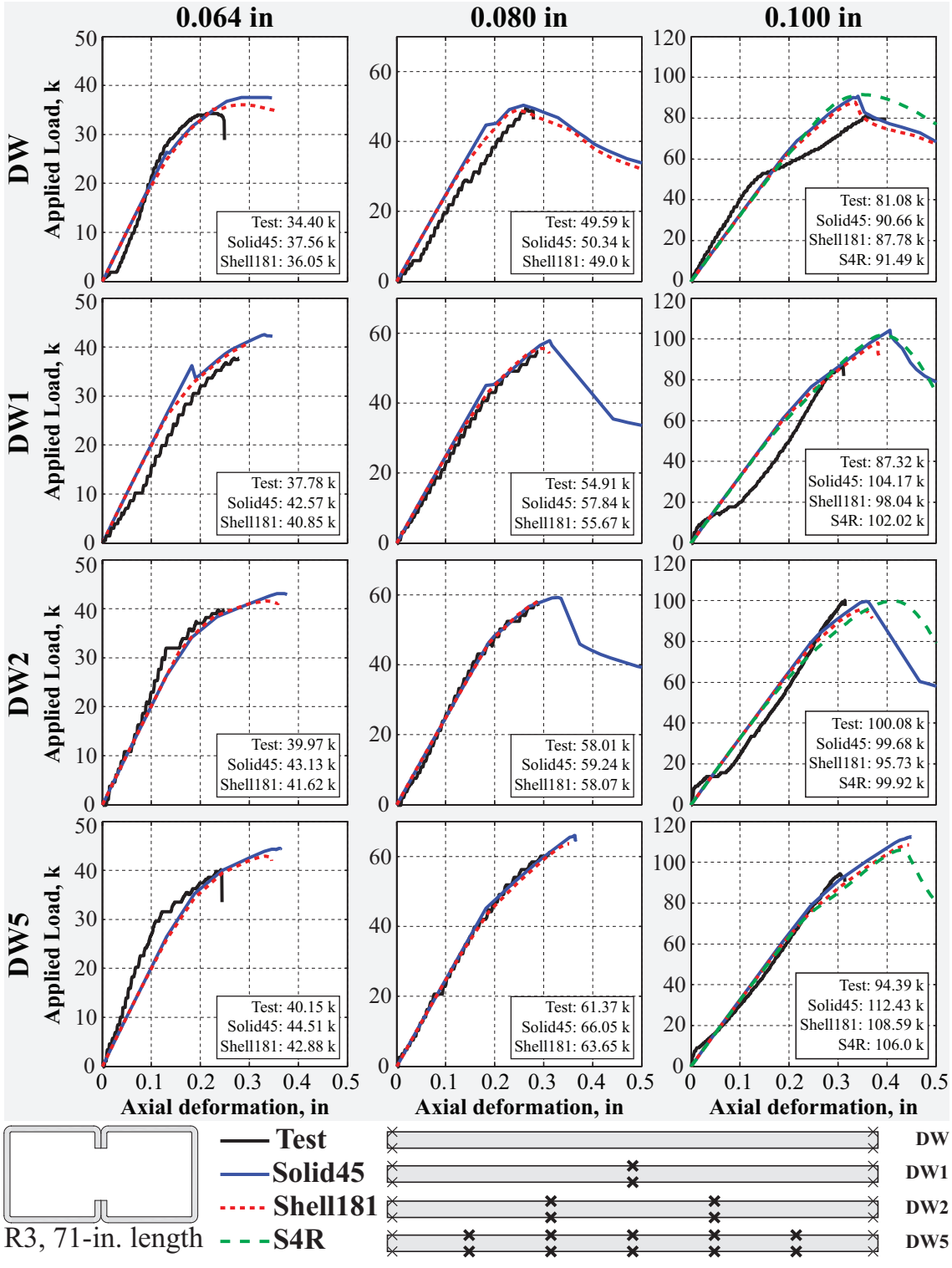


Figure 23: Load vs. deformation history of the 71”-long, *R3*-sections.

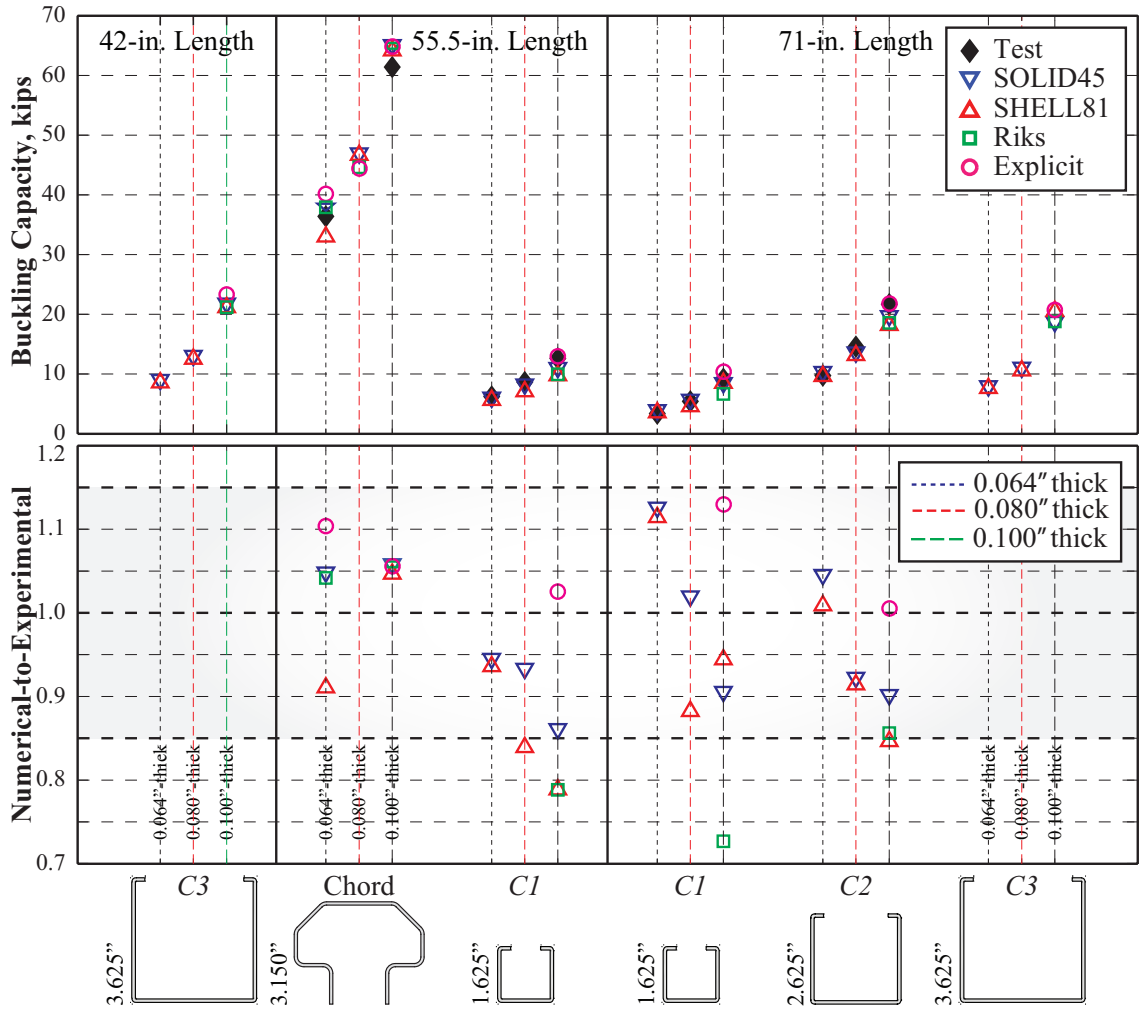


Figure 24: Compressive load-carrying validation and verification of the single sections under ANSYS implicit-static and ABAQUS explicit-dynamic.

Overall, the numerical modelings of ANSYS implicit-static and ABAQUS explicit-dynamic closely predict the compressive strengths of the single sections, approximately within 15% difference as shown in Fig. 24. A noticeable discrepancy among the adopted solution techniques is only found on the 0.1”-thick and 71”-long, *C1*-section where the solution of the Riks method is underestimated by nearly 30%. A careful examination is paid to the preprocessing and the solution phases of the ABAQUS static model, but nothing wrong is found. A flexural-torsional mode common in slender channels and its non-stitched, built-up counterparts are precisely replicated as depicted in Fig. 26. Numerical challenges were encountered during the solution process of the chords. The default

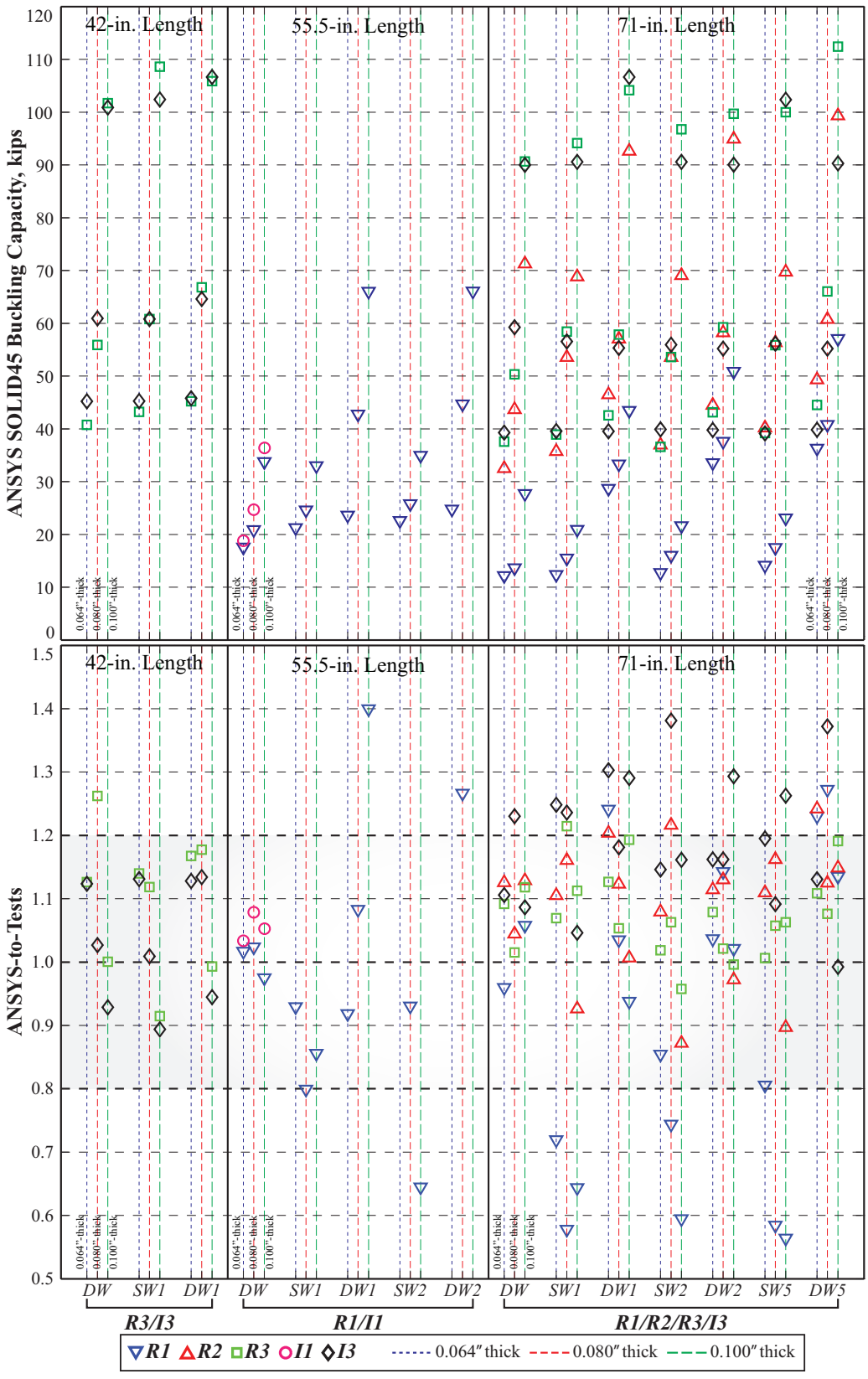


Figure 25: Compressive load-carrying validation of the built-up, *I*- and *R*-sections under the ANSYS implicit-static modeling. The ANSYS model is found inapplicable for asymmetrical, single-sided members prone to flexural or flexural-torsional buckling.



Figure 26: Flexural-torsional buckling of the 71”-long *C1* and *DW-R1* members.

tolerance became too tight as the members buckled and could not be satisfied for both out-of-balance force and moment. Loosening was done, and only the thickest section was able to go into the post-buckling regime. The ANSYS Arc-Length method was activated instead of the Newton-Raphson method, yet the difficulty was not properly handled. On the other hand, the implicit-static Riks method in ABAQUS (as commonly used in Yang and Hancock (2004), Yang et al. (2004), and Ng and Gardner (2007)) could smoothly advance the whole loading history. Figure 27 shows a local buckling of the rippling lips simulated in the chord section.

The degree of accuracy has dropped in the modeling of the built-up sections as ranging from the largest to smallest sections. The numerical modeling overestimates the majority of the measured capacities by as large as 40%. Two of the main factors toward the discrepancy appear to be the experimental loading offset and the improper setup of the pinned-end condition, particularly so for the *I3*-sections, where only one experimental repetition was conducted for each individual configuration. This results in a suspicious data quality. Such an imperfection was totaly excluded in the modeling as having the pre-

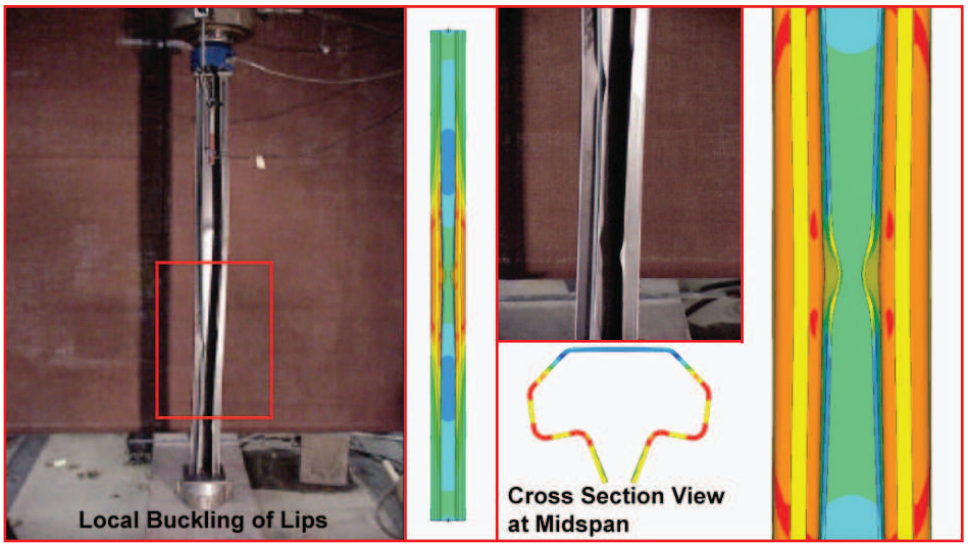


Figure 27: Local buckling of the lips in the 55.5”-long chord.

scribed deformation placed right at the section centroid. Better approximations are on the *R*-section series as the distribution of the capacity comparisons is narrower. The lower bound of the upper-limit compressive strength has been reached with the *DW1* pattern (see Fig. 6). In addition, the post-buckling, deformed shapes of this pattern in Figs. 28 and 29 also representatively reflect their experimental counterparts. Overall, the numerical analysis overestimated the experimental results by 12% on average. Thus, to account for accidentally introduced eccentricity of the axial load in the experiment, an adjustment factor of 0.88 could be applied to the numerical simulation data obtained for the axial load capacity for built-up, cold-formed sections subject to pure compression. Similar adjustment has been done in the AISI standard (see Section 2.2). In Section 4.4, the factor will be implemented to the proposed distortional-buckling equation.

An exception aside from the above observation is made on the series of *SW1*-, *SW2*-, and *SW5*-*R1* (denoted as *SW*-*R1* hereafter). The simulated strengths are surprisingly low, but despite this, the failure pattern of the channels prying about the mid-length is very well captured as illustrated in Figs. 30 and 31. On the other hand, the larger sections of these welding patterns, although having distortional buckling, were closely predicted. Debugging to increase the weld thickness and strength to delay the prying was attempted.

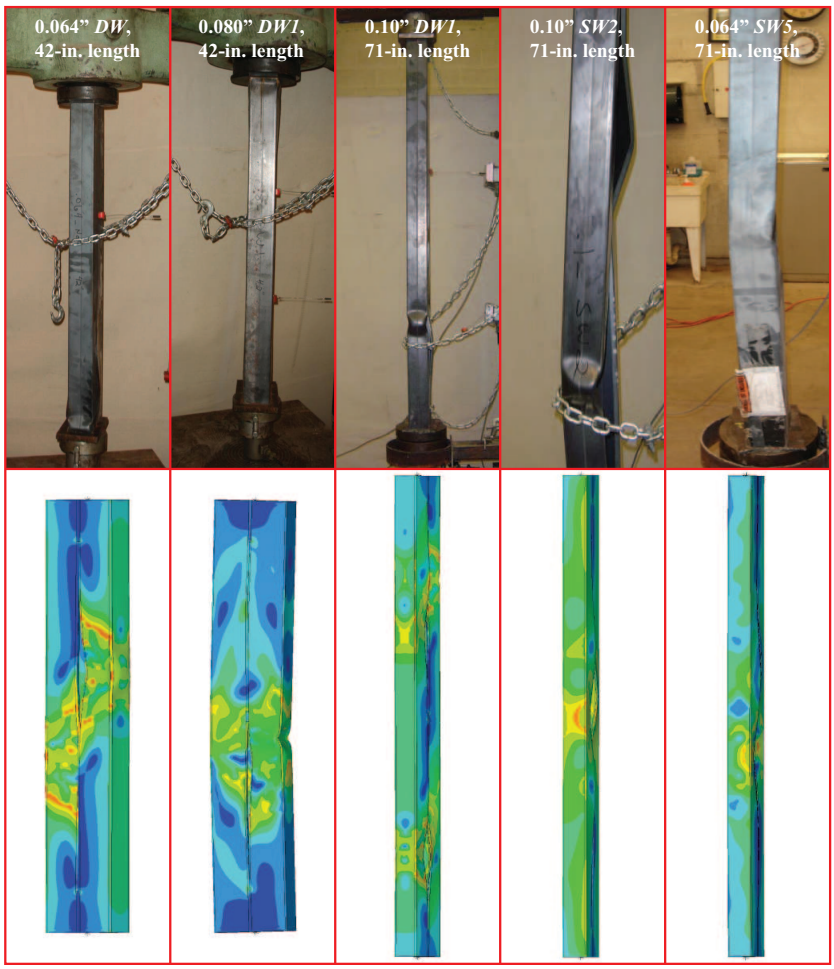


Figure 28: Distortional deformed shapes of 42”- and 71”-long *R3*-sections.

Nonetheless, the results remained unchanged. Thus, it is concluded that the ANSYS implicit-static model is inapplicable for asymmetrical, single-sided members prone to flexural or flexural-torsional buckling. In this case, the ABAQUS explicit-dynamic model can be adopted.

The buckling-capacity verification under the ABAQUS explicit-dynamic modeling is summarized in Fig. 32. The corresponding time histories of (1) filtered and unfiltered reaction forces and (2) kinetic and internal energies are presented in Figs. 33 to 35. The verification is selectively performed on the thickest sections, where the ANSYS modeling provides the most reliable reference as less difficulty in the post-buckling convergence was encountered. In general, the buckling capacities of the explicit-dynamic simulations

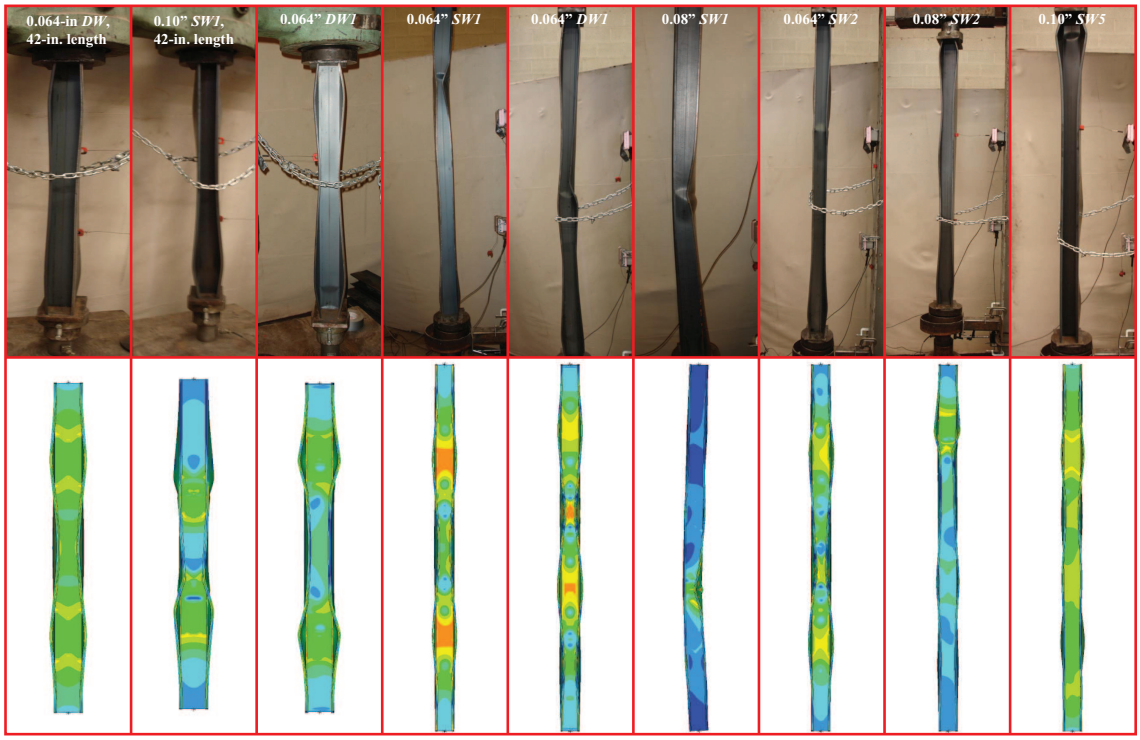


Figure 29: Distortional deformed shapes of 42”- and 71”-long *I*3-sections.

well validate those of the implicit-static counterparts. First, a parametric study to determine a proper rotational mass and loading rate was conducted on the chords, where less complexity was encountered, while an insight has already been gained from the static solution of the Riks method. The study was initially focused more on the strength aspect regardless of minimizing a kinetic energy to dynamically approach a quasi-static simulation. While trying various loading rates by fixing the prescribed axial deformation and shortening the duration, the following combination was found suitable for the chords: (1) 1.0 in./s loading rate of applying a 0.2-in. prescribed deformation within a duration of 0.2 seconds (almost 19 times longer than the first fundamental frequency of 93.64 Hz), and (2) 4.7e-05 kip.s^2/in. rotational mass of the top and bottom plates. Nonetheless, applying the same loading rate to the channels and its built-up counterparts satisfies the energy aspect, but not the strength. Rather, a faster loading rate of 4.0 in./s is generally found compatible for most built-up sections. A proper loading rate seems to be section-dependent. Applying a slower rate to minimize the inertial effect is not as promising as thought. A

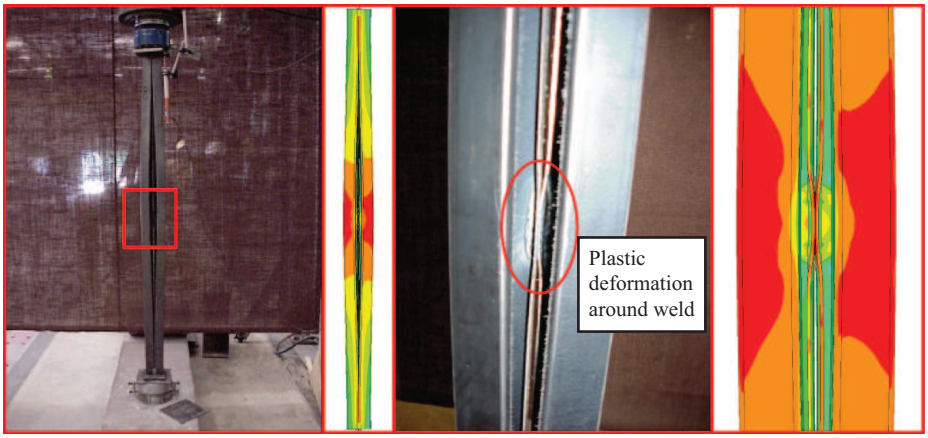


Figure 30: Plastic deformation around the weld of the 55.5”-long, *SW1-064R1* members.

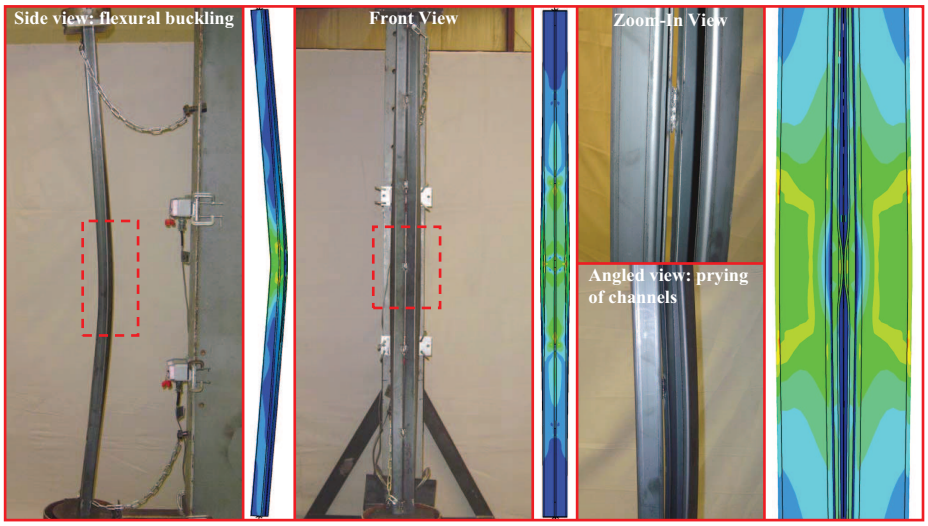


Figure 31: Buckled shape of the 71”-long, *SW5-064R1* member.

Butterworth, low-pass filter with a cutoff frequency slightly higher than the first natural mode effectively cancels out the noise and higher-mode components, revealing the true buckling behavior (ABAQUS®, 2007b).

In Fig. 32 where kinetic-to-internal energy ratios are shown, two distinctive regions divided upon a 10% ratio (with a transition on the *R2*-sections) establish an energy criterion. A justified loading rate should yield a kinetic-to-internal ratio less than 10% and between 10%-30% for the built-up members prone to distortional and flexural buckling, respectively. As mentioned previously, the implicit-static limitation on the *SW-R1* members has been exceeded. Unfortunately, these members are excluded from the preceding

observation due to a violation of the no-sliding interaction property resulting in a suspicious simulation. Right before buckling, the members start to slide on and completely off the plates.

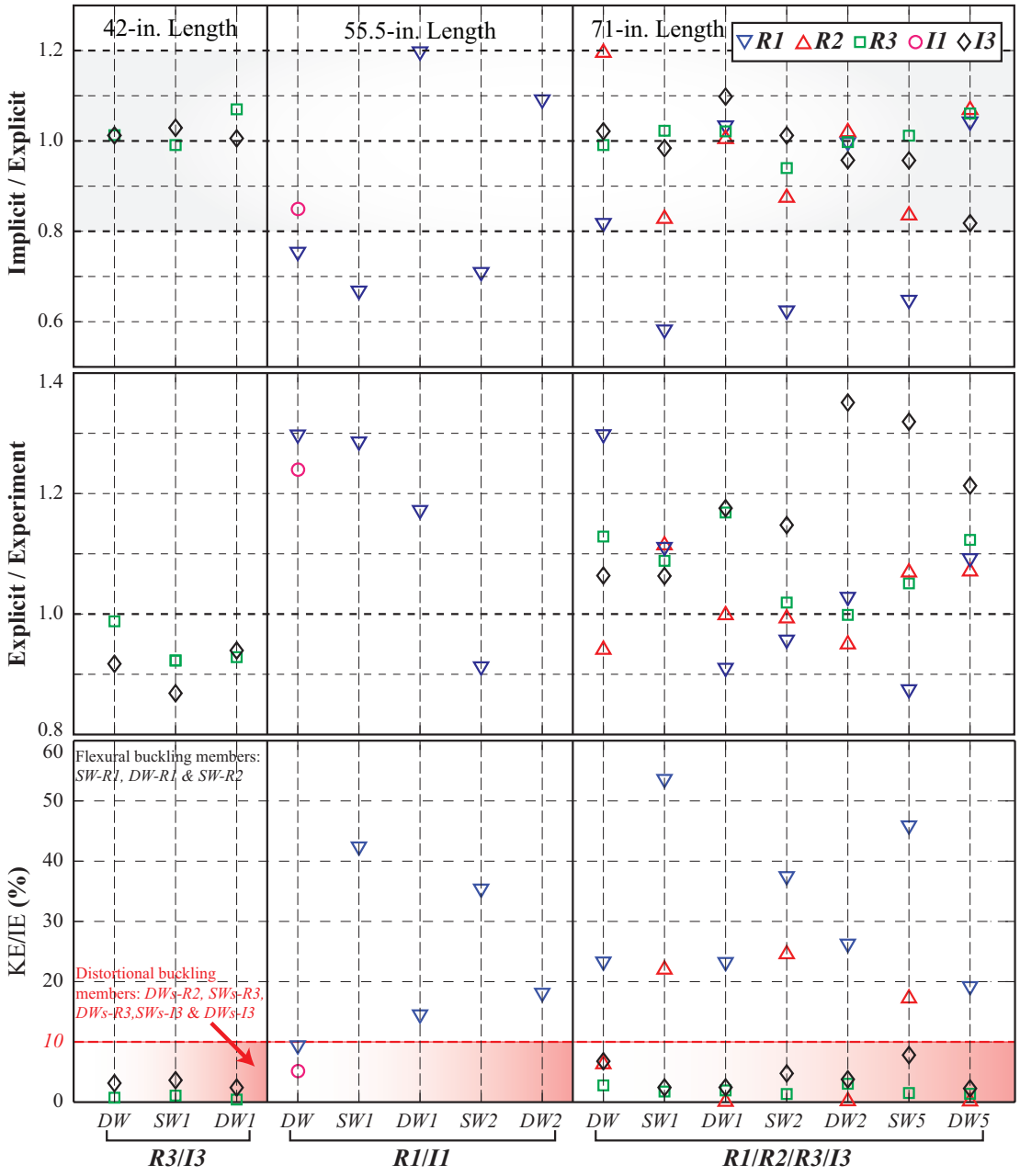


Figure 32: Verification of the ANSYS implicit-static results under the ABAQUS explicit-dynamic simulation.

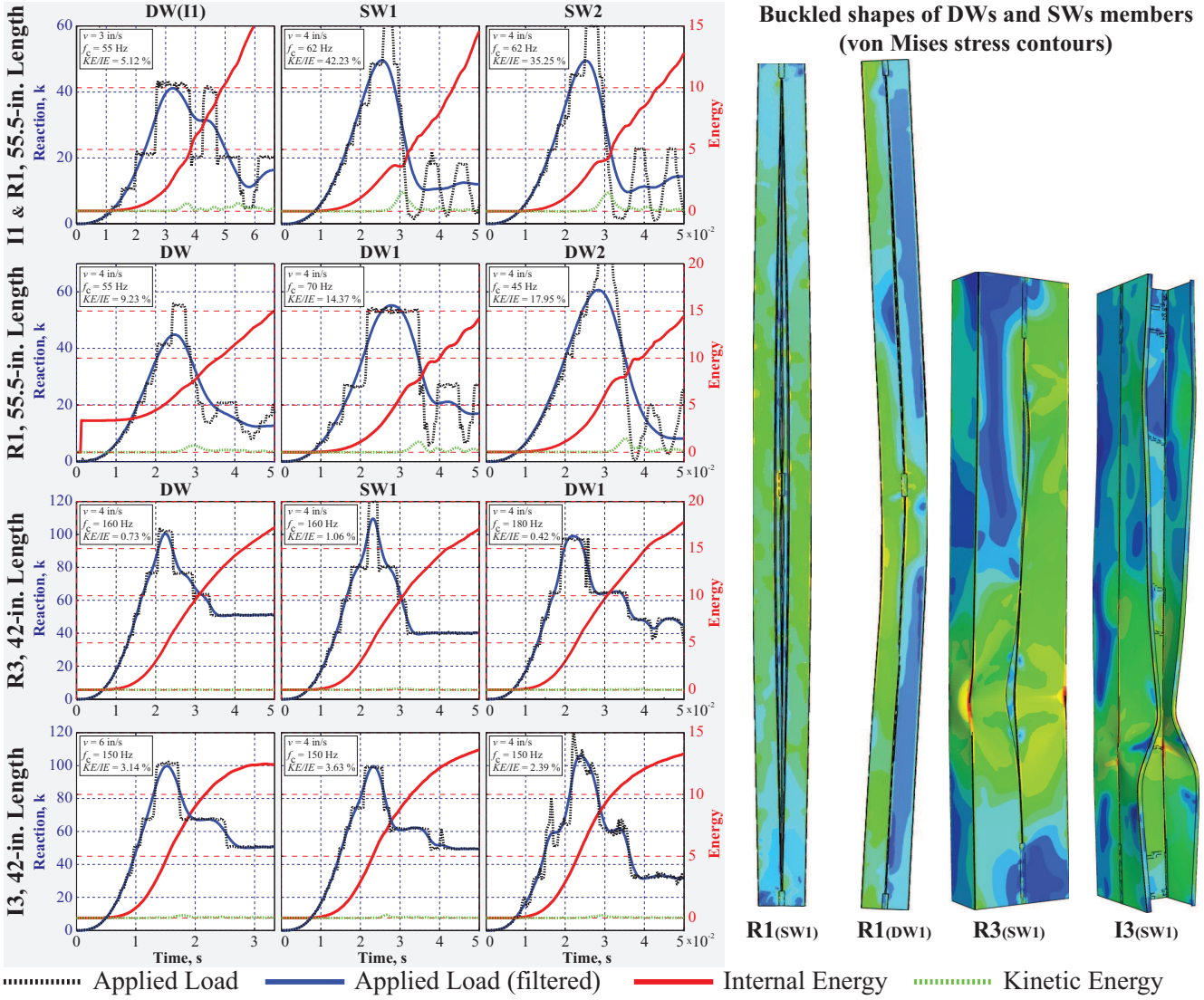


Figure 33: Reaction and energy time histories of 42.0”- and 55.5”-long, built-up sections.

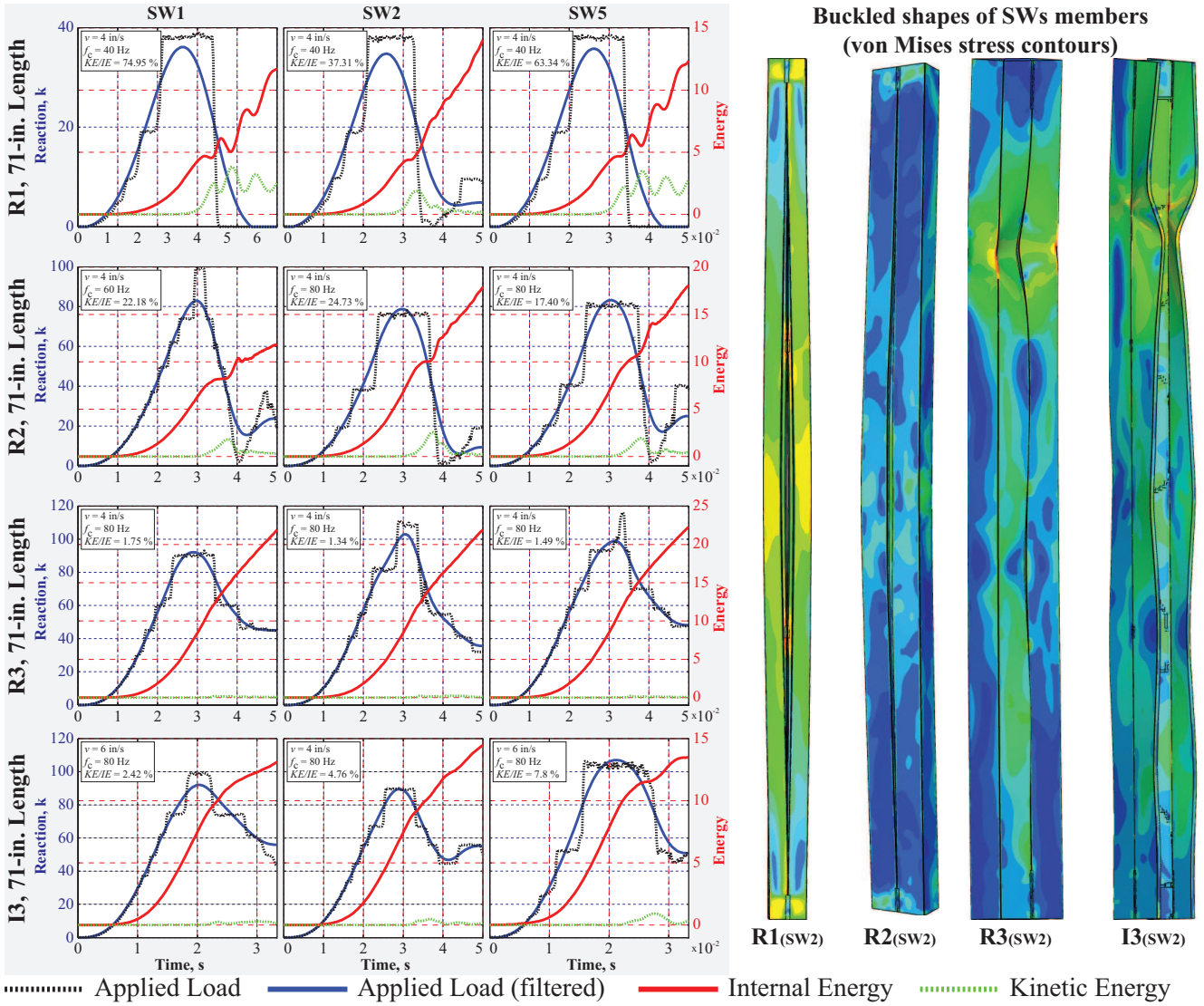


Figure 34: Reaction and energy time history of the 71”-long, single-sided welding sections.

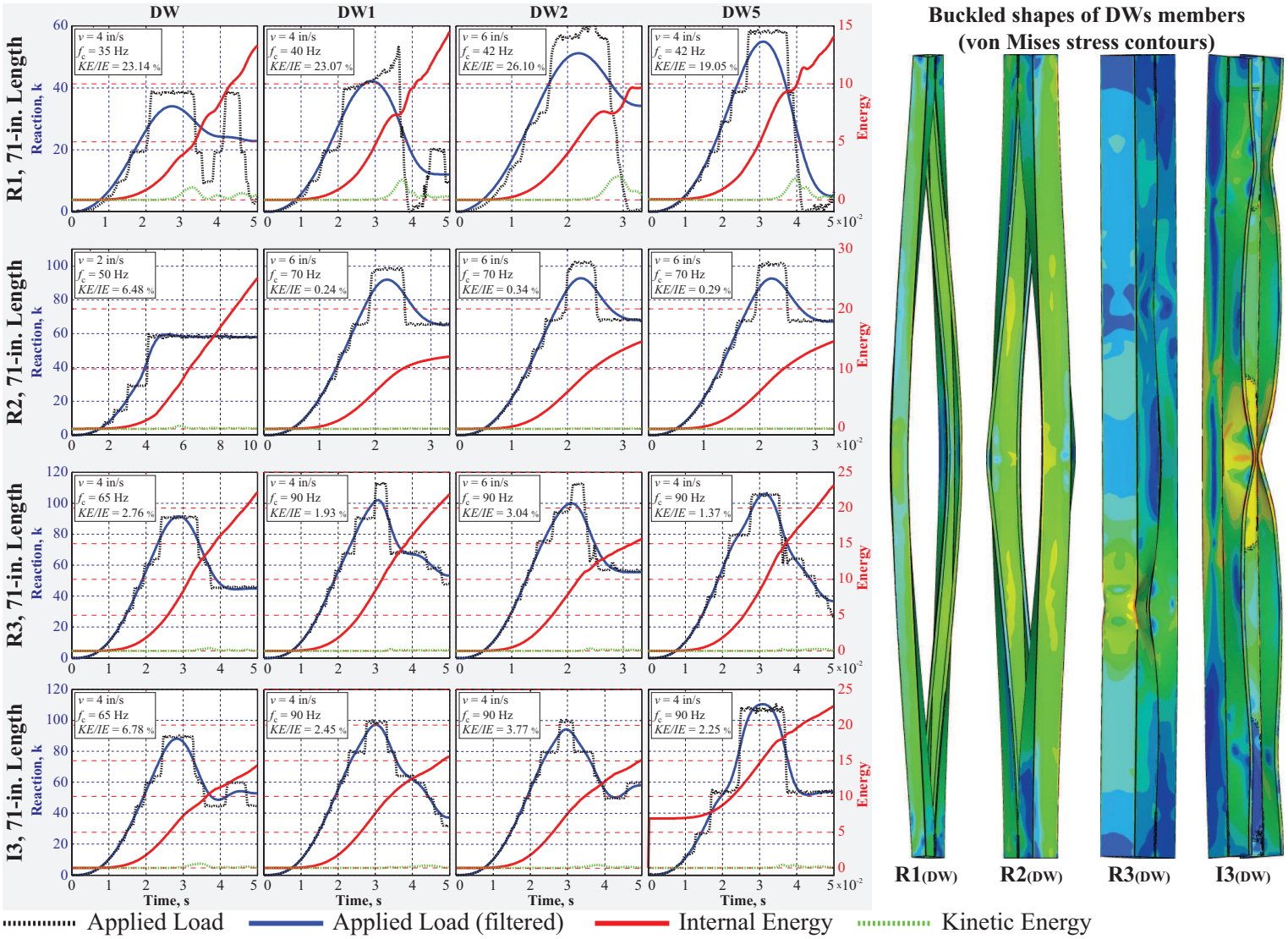


Figure 35: Reaction and energy time history of 71”-long, double-sided welding sections.

3.3 Conclusion

The study in this section presents a state-of-the-art modeling strategy to handle nonlinear buckling behaviors of built-up, cold-formed sections with geometrically unstable configurations. Over 265 experimental buckling tests are used to numerically validate the ANSYS implicit-static model and ABAQUS explicit-dynamic model is used for verification. The ABAQUS model complements the ANSYS model by offering features it lacks. The ANSYS model generally ensures a satisfactory buckling capacity prediction, but leaves an uncertainty in the post-buckling response, particularly for members that are likely to fail in flexural buckling. This sometimes results in a difficulty in judging a true structural failure from a numerical blowout. In contrast, the ABAQUS explicit-dynamic model is capable of tracing unstable descending loading histories, although a proper loading rate is still questionable. Furthermore, a variety of iterative and non-iterative solution techniques, including Newton-Raphson, Arc-Length, Riks, and Central-Difference integration methods, are adopted for obtaining reliable solutions. Overall, the numerical analysis overestimated the experimental results by an average of 12%. This is due to an accidentally introduced eccentricity and an improper setup of the pinned-end condition in the experiment. Therefore, an adjustment factor of 0.88 shall be applied to each numerical simulation to determine axial load capacity of a built-up, cold-formed section under pure compression.

3.4 Discussion

Use of the first Eigen-mode is preserved for a member prone to distortional buckling, unless the first two Eigen loads are closely spaced less than 0.5 kips in magnitude; otherwise, they both should be incorporated in the geometric perturbation. Failure to do this may result in a severe underestimation of the member strength. When dealing with a flexural-buckling member, even though only the first mode about the weak-bending axis is theoretically possible, the strong-axis bending mode may be practical due to improperness

in fabrication and/or boundary condition. According to the experimental deformed shapes of the double-sided, *R1*-sections, a strong-axis buckling is observed requiring seeding the latter mode onto a perfect mesh.

Incorporating the end-plate condition in the ANSYS implicit-static modeling was also examined. The same principal of applying the contact and boundary conditions as in the ABAQUS explicit-dynamic model was repeated. Identical results to the adopted modeling strategy upon using a rigid-body concept were yielded in the channels. Nonetheless, a numerical blowout due to too much penetration of the elements of columns and plates and rigid-body motion of the column due to improper contact constraints are encountered when modeling the chords and the built-up sections. Modeling the weld connections, as extremely rigid by directly merging column-to-column nodes instead of through the weld entities, was also examined and found fairly good for the symmetrical double-sided members. Exceedingly conservative and totally misleading deformed shapes were an outcome in the single-sided welding sections.

4 PHASE II: FORMULATION OF THE PROPOSED DISTORTIONAL EQUATION[2]

4.1 Overview of *Phase II*

An extensive numerical analysis of over 265 pure-compression buckling tests is carried out using ANSYS implicit-static and ABAQUS explicit-dynamic simulations (Chapter 3). The state-of-the-art modeling procedure has been proven to accurately predict the geometrically unstable behavior of built-up, cold-formed sections. This work aims to assess the aforementioned experimentally identified deficiency and address it by developing a new axial load capacity equation for built-up sections prone to distortional buckling. Through a systematic parametric study, investigations are made on the correlation between the ultimate capacities and the geometrically induced failure modes as influenced by the out-of-flatness along the section perimeter and the out-of-straightness along the member length. A total of 360 ANSYS runs over 20 unbraced lengths and 2 built-up orientations, each associated with a set of three section widths and three thicknesses (identical to those adopted in the tests), are compared with the AISI design curves (see Section 2.2). The correlation between the distortional-buckling data and their design values is analyzed to develop an equation that addresses the deficiency using a least-square regression analysis of a three-dimensional surface fitting.

4.2 Computational Modeling of Buckling in Built-up, Cold-formed Sections

The state-of-the-art modeling strategy previously calibrated in *Phase I* (Chapter 3) through the ANSYS implicit-static validation and the ABAQUS explicit-dynamic verification over the 265 experimental tests (Section 2.3) is strictly followed. The representative FEM

[2]This section is designed to be independent and self-contained to facilitate submission as a journal article. Therefore, some materials previously presented in Chapter 2 is repeated.

models of the built-up, *I*- and *R*-sections are presented in Figs. 36 and 37. The brick element of SOLID45 is adopted for the elements of the column and the nonlinear shell element of SHELL181 for the weld entities of 3/16 in. in thickness (Whittle, 2007). The largest mesh sizes across the width and along the length are kept consistently close to 0.20 in. throughout the parametric study (Section 4.3). The numbers of elements vary from 5,000 elements in the smallest and shortest member to 500,000 elements in the largest and longest member. One-sided contact elements consisting of the master and the slave surfaces are overlaid on the lips of the *R*-section and on the back panels of the *I*-section. The interaction of these surfaces is defined as frictionless indicating that they can freely slide pass and be apart from each other with neither tangential nor normal forces being developed. Once in contact, no force is transmitted from one surface to the other. The pinned-end condition is simulated through a rigid body consisting of a master (target) node and a slave surface. The target node of TARGE170 element is located right at the end-section centroid, reflecting the pure compression of no eccentricity being considered. The slave surface of CONTA173 is overlaid on the entire area of the end section. A fully-fixed in translation and axially-fixed in rotation are imposed to the target node on the supporting end. The same constraint, but with a prescribed axial deformation to perform a displacement-controlled analysis, is applied at the other loading end. The magnitudes of the prescribed deformations to pass the critical buckling point into the post-buckling regime vary from 0.15 - 0.50 in., depending on the length and size of the member being simulated.

An Eigen buckling mode is seeded onto a perfect configuration to trigger the geometric instability to bypass the (exaggerated) bifurcation load (see Fig. 12). The first mode is usually of interest, unless the first two consecutive modes are closely spaced less than 0.5 kips in magnitude; otherwise, the second mode is also taken. Failure to do this may result in an severe underestimation of the ultimate capacity (more discussion in Section 4.3). The degree of an imperfection (denoted as δ), taken as a percentage of the thickness as

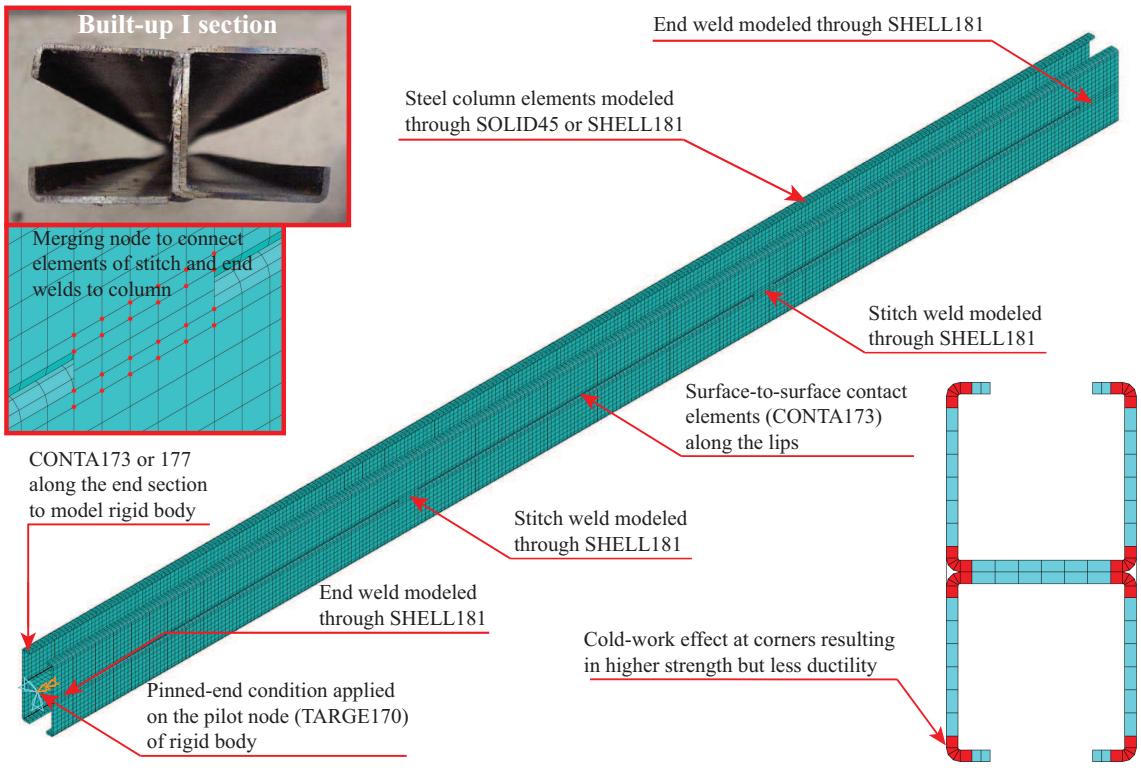


Figure 36: ANSYS SOLID45 FEM model of the built-up, *I*-section.

suggested by Walker (1975), is adopted toward a distortional or a local mode. For a global-buckling member, δ is taken as a fraction of an unbraced length L. The imperfection factor δ (in Eq. (59)) is incorporated to factor the first Eigen mode and one-tenth of thickness is applied toward the second mode, if needed.

$$\delta = \begin{cases} \frac{L}{2000} & ; \text{global (Euler) buckling} \\ 0.3t\sqrt{\frac{P_y}{P_{eig}}} & ; \text{distortional and local buckling} \end{cases} \tag{59}$$

The notations of L and t denote an unbraced column length and a member thickness. The notations of P_y and P_{eig} refer to a squash and an Eigen-buckling load.

An isotropic bilinear model with kinematic strain hardening is assumed for the constitutive model. The material characteristics of the modulus of elasticity (E), the Poisson's ratio (ν), the 0.2% yield stress and strain (σ_y and ε_y), and the ultimate stress and strain (σ_u and ε_u), are experimentally determined according to the ASTM coupon tests and summa-

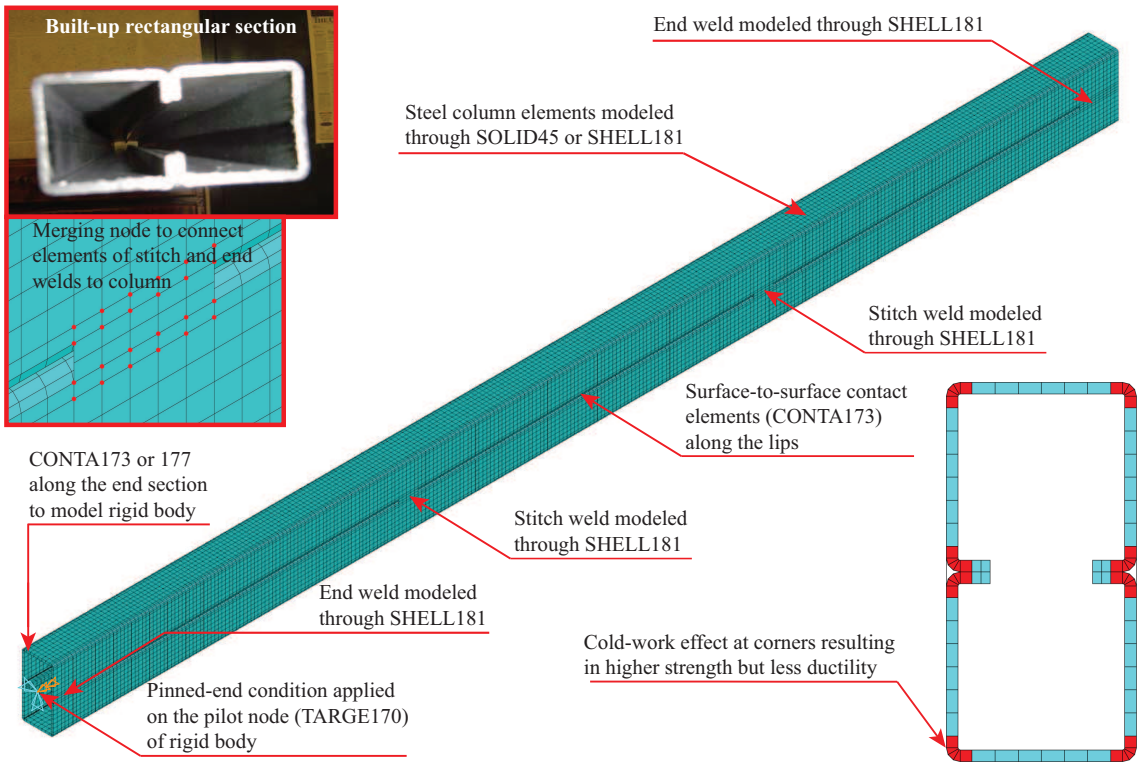


Figure 37: ANSYS SOLID45 FEM model of the built-up, *R*-section.

rized in Table 2. The cold-work effect, as commonly found in cold-formed steel due to a substantial plastic deformation around the bend during the manufacturing process, results in a raise in strength but decreasing in ductility. The effect is incorporated to the corner elements and its thickness-distance neighborhood (see Figs. 36 and 37) by a 22% and 17% increase of σ_y and σ_u, respectively. The yield strain of ε_y remains the same, while ε_u is divided by half resulting in a steeper slope of the tangent modulus. The effect of residual stress is neglected, as it is inherently embedded in the material properties experimentally derived from actual members (Yang and Hancock, 2004; Yang et al., 2004; Ng and Gardner, 2007).

The solutions of a large-displacement assumption are obtained implicitly under the Newton-Raphson method with the axial deformation of the master node being controlled. The tolerances on the out-of-balance force and moment are left to defaults as 0.1% with a minimum reference value of 1.0 kip and 0.01 kip-in., respectively. The initial, minimum

and maximum substeps per a load step are taken as 25, 5 and 3,200. Bisection is activated, once the predicted successful iteration for a given substep exceeds 25 iterations. A convergence history is monitored and recorded for the loosening purpose as needed when the divergence in advancing through the buckling state is encountered. The tolerance on the residual force and moment are loosened as 0.5% with the minimum reference value of 50 kips and 0.1 kips-in., respectively. These raise the tolerances to 0.25 kips and $5(10^{-4})$ kips-in. Nonetheless, the post-buckling solution may still not be possible with the loosened tolerances. At this stage, the ABAQUS explicit-dynamic model (Section 3.2.1) is brought in to assure a true structural failure.

4.3 Parametric Study to Numerically Expand the Buckling-Capacity Archive

A total of 18 built-up configurations of the *I*- and *R*-sections are considered in the parametric study. The same widths and thicknesses chosen in the experimental tests are used for each configuration. For a given configuration, 20 different unbraced lengths varying from 15 to 140 in. are examined. An increment of 5 in. in unbraced length is adopted up to the length of 80 in., with a 10-in. increment for the rest. A double-sided stitch pattern of two intermediate welds at third-points (*DW2*) is chosen to comply with the upper limit of the fastener spacing. Table 3 summarizes the section properties including: (1) the full unreduced and its effective cross-sectional areas (A and A_e), (2) the smallest radius of gyration of an individual channel (r_i) and its built-up counterpart (r), and (3) the ratio of the fastening modification factor $\left(\frac{a}{r_i}\right)$ to the unmodified slenderness $\left(\frac{kL}{r}\right)_o$. The errors inherent in running about 360 numerical parametric tests are compromised through a sequential batch feed mode using a collection of ANSYS Parametric Design Language (APDL) macros (Madenci and Guven, 2006), which create and execute the models and retrieve the solutions of interest.

The aforementioned 18 series of numerical-simulated capacities are presented in Figs. 38-

	I1 & *R1*, b_o = 1.625”			*I2* & *R2*, b_o = 2.625”			*I3* & *R3*, b_o = 3.625”		
	0.064”	0.08”	0.1”	0.064”	0.08”	0.1”	0.064”	0.08”	0.1”
A	0.6432	0.7869	1.0219	1.0076	1.2387	1.6225	1.3720	1.6905	2.2231
A_e	0.6207	0.7869	1.0219	0.6991	0.9902	1.4150	0.6827	1.0160	1.5264
r_i	0.5954	0.5888	0.5777	0.9395	0.9453	0.9554	1.2741	1.2684	1.2587
r	0.6794	0.6733	0.6630	1.1278	1.1339	1.1442	1.5711	1.5652	1.5552
$\frac{\left(\frac{a}{r_i}\right)}{\left(\frac{kL}{r}\right)_o}$	0.3805	0.3813	0.3828	0.4002	0.4010	0.4023	0.4101	0.4108	0.4119

Table 3: The built-up characteristics of the 18 configurations. The fastening spacing a is taken as one third of an unbraced length for the *DW2* pattern to comply with the upper limit of the modified slenderness ratio, as the factor of $\left(\frac{a}{ri}\right)$ does not exceed $0.5\left(\frac{kL}{r}\right)_o$.

40 and Figs. 41-43 as compared to the corresponding experimental capacities and to the AISI specification. Each figure presents the results of both orientations (*I* and *R*) for a given width and given three different thicknesses. Throughout all the series, it is demonstrated that the *DW2* welding pattern adequately holds the two individual channels together so as to interact as a whole member.

In Figs. 41 and 42, a transition of numerical failure modes from distortional to flexural buckling is observed in the smallest (*I1* and *R1*) and intermediate (*I2* and *R2*) sections. For the largest section, one failure mode of distortional buckling governs. The boundary of a transition from distortional to flexural is the same for both *I*- and *R*-orientations, except for the 0.08”-thick, *I2*- and *R2*-sections. The transition boundaries are at the unbraced lengths of 40, 35, and 25 in. for the *I1*- or *R1*-sections with 0.064, 0.08, and 0.1 in. thickness, respectively. On the other hand, the boundaries are formed at the lengths of 110, 90 (for *I2*), or 100 (for *R2*), and 75 in. for the intermediate sections with 0.064, 0.08, and 0.1 in. thickness, respectively. A smooth transition of the failure mode is observed in the former (*I1* and *R1*), whereas a noticeable sudden jump is obvious in the latter (*I2* and *R2*). There is no significant difference in the ultimate capacities between the two built-up shapes. No difference is seen for the members that fail in flexural buckling, as their out-of-straightness totally governs. A small discrepancy is noticed for the members prone to distortional buckling, and the discrepancy is increased as the members become thicker and longer. The experimentally measured capacities of the *I*-sections are lower than those

of the *R*-sections in the small and intermediate sections, but the opposite is the case for the largest section. However, the numerical results indicate that the impact of the built-up orientations on the maximum capacities is minimal as opposed to the experimental results. A ductile-collapse mechanism is observed from *I1* and *R1*-sections with lengths longer than about 100 in., exhibiting a nearly flat plateau in the load-displacement curve right after flexural buckling. A brittle failure is typical for the rest of the members failing in both flexural and distortional modes. The post-buckling solution of a ductile member is faster in convergence. As the member that fails in flexural buckling becomes shorter, the tolerance on the out-of-balance force is exceeded right at or after reaching a buckling state, and thus, it results in a difficulty in differentiating a true structural failure from a numerical blowout. At this stage, the ABAQUS explicit-dynamic model is brought in to resolve the concern.

As mentioned previously, special attention should be paid when dealing with the first two closely-spaced Eigen modes with the difference in the magnitude of less than 0.5 kips. For the largest section of *I3* and *R3*, both the first and second modes would have to be simultaneously incorporated in the geometric perturbation. Failure to consider both might underestimate the true capacity by as much as 30%. For instance, the axial capacity for the 0.1”-thick and 75”-long, *DW2-I3* specimen jumps out of the trend (from 104.7 to 87.8 kips) when implementing only the first mode.

Overall, the AISI Sections C4.1.1, C4.1.2 and C4.2(b) for the applicable failure modes of flexural, flexural-torsional, and distortional buckling, respectively, are conservative for all the 18 numerical-simulated series, but are overly conservative for the thicker and larger sections, especially for those prone to distortional buckling. An identical conclusion was drawn in the experimental study. Section C4.1.1 is efficient for those smallest and intermediate sections that mainly fail in flexural buckling, as their capacities are in good agreement with the proposed design curves (the parabolic segments of the blue-dotted lines presented in Figs. 41 and 43). Thus, there is no compelling reason to update this

provision and its related provisions of slenderness modification factor (Section D1.2). One of the reasons enabling the exceedingly conservative specification is due to considering a flexural-torsional mode (AISI Section C4.1.2), as its nominal strength tends to govern for most of the loner lengths after the flat plateau of the distortional provisions (Section C4.2(b)). As evidenced throughout the 18 numerical series that no specimen buckled in flexural-torsional mode (only either in flexural or distortional), Section C4.1.2 shall be excluded from the design consideration of the adopted *I*- and *R*-sections with the *DW2* welding configuration. For the 228 distortional-buckling members, the out-of-flatness has significantly more influence than the slenderness as their capacity versus length relationship is nearly linear (not parabolic) (see Figs. 42 and 43). However, the provision of distortional buckling (Section C4.2(b)) does not reflect this regard, as its predicted strength becomes a constant after the member length exceeds the critical length of L_{cr} (defined in Eq. (16)).

4.4 Formulation of the Distortional Equation

The formulation of the proposed equation for distortional built-up sections is presented. The correlation between the ultimate buckling capacities and their geometrical and material characteristics is analyzed using a least-square regression analysis of a three-dimensional surface fitting (Harman et al., 2000; MATLAB®, 2010). The complexities of the distortional buckling as resulted from the interaction between the flexural and the local buckling (accounted through the out-of-straightness of $\left(\frac{kL}{r}\right)_m$ and the out-of-flatness of $\left(\frac{t}{b_o}\right)$ in Eq. (1)) are lumped into the fitting coefficients.

A total of 114 data points are retrieved from the 228 exceedingly-conservative distortional members. Only the lower capacity between the two orientations is selected for each data point. One data point represents three dimensionless quantities of (1) the actual thickness-to-largest width ratio $\left(\frac{t}{b_o}\right)$, (2) modified slenderness ratio $\left(\frac{kL}{r}\right)_m$, and (3) buckling-to-yield strength $\left(\frac{P_n}{P_y}\right)$. The meshgrid surface shown in Fig. 44 is achieved by using a quadratic polynomial regression function. The sum of squares due to the fitting error, root mean square error, and square of the correlation between the measured and predicted values are 0.206, 0.043, and 0.922, respectively. When the first two values are close to zero and the third value is close to one, it is considered that the fitting is highly significant with a greater proportion of the variance (Mathews and Fink, 2004). The resulting distortional buckling equation is given as follows:

$$P_n = 0.877 P_y \underbrace{\left\{ 36.5 \left(\frac{t}{b_o}\right) - 326.5 \left(\frac{t}{b_o}\right)^2 - \frac{1}{638} \left(\frac{kL}{r}\right)_m \right\}}_{\leq 1.0} \tag{60}$$

A factor of 0.877 is applied to compensate for an initial crookedness in the experimental simulations, e.g., due to eccentricity and boundary condition. The factor (as previously determined at 0.88 in Chapter 3) is adjusted according to Eq. (2) to simplify its application. The justification as well as the above definitions of the parameters are given in Section 4.5.

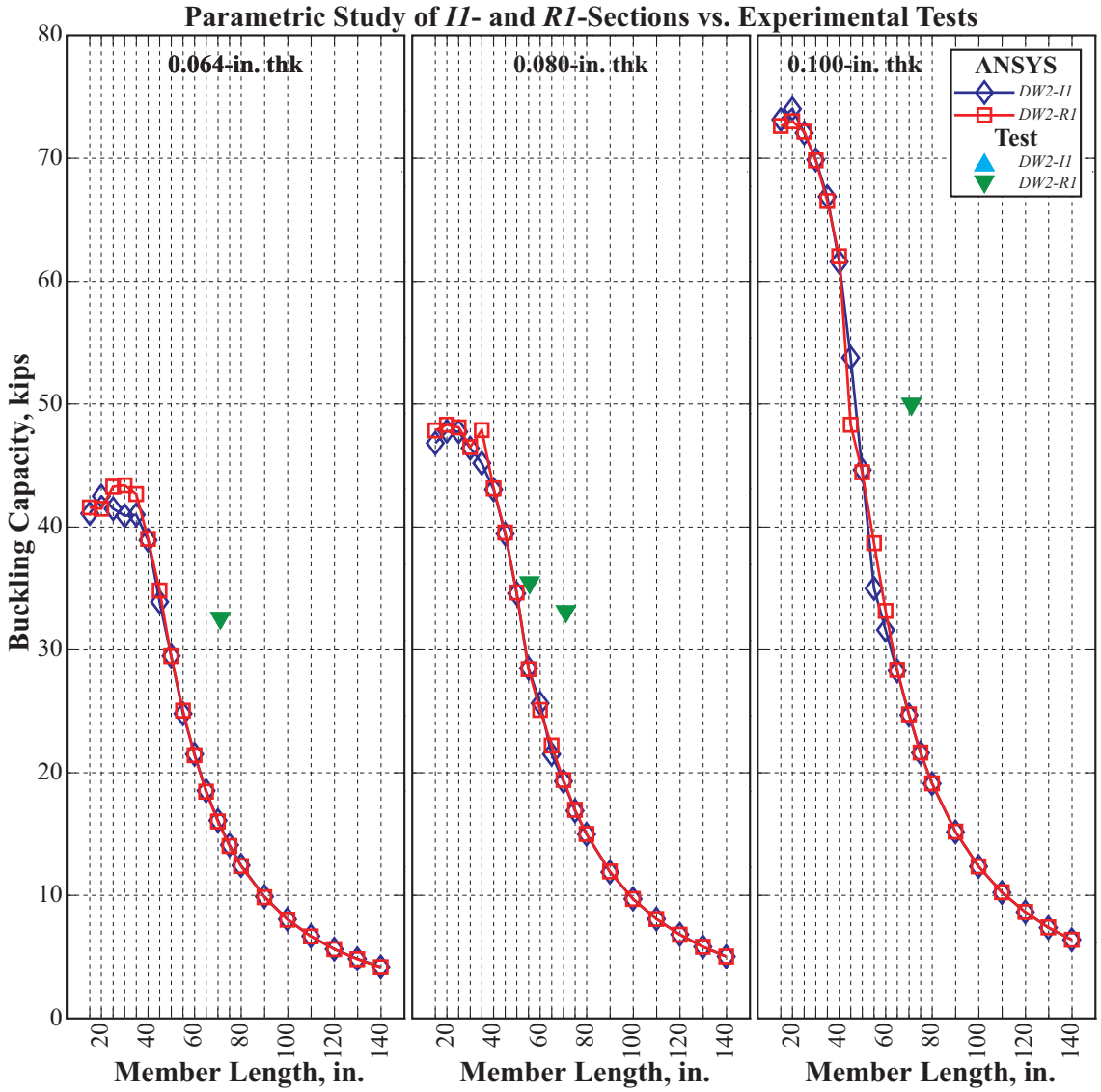


Figure 38: Parametric study of Members *DW2-I1* and *-R1* over varying unbraced lengths. A comparison to their corresponding experimental counterparts is made.

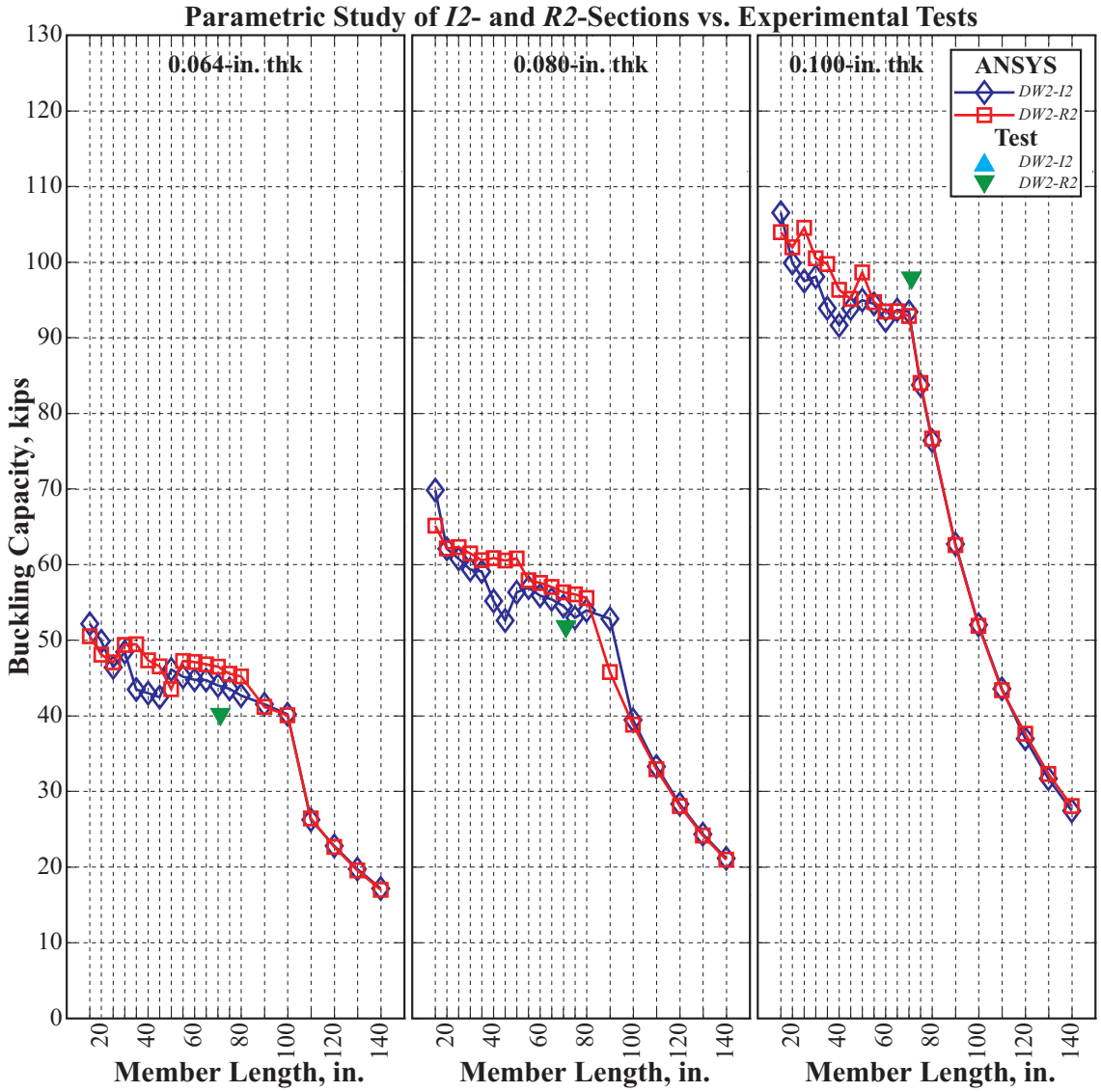


Figure 39: Parametric study of Members *DW2-I2* and -*R2* over varying unbraced lengths. A comparison to their corresponding experimental counterparts is made.

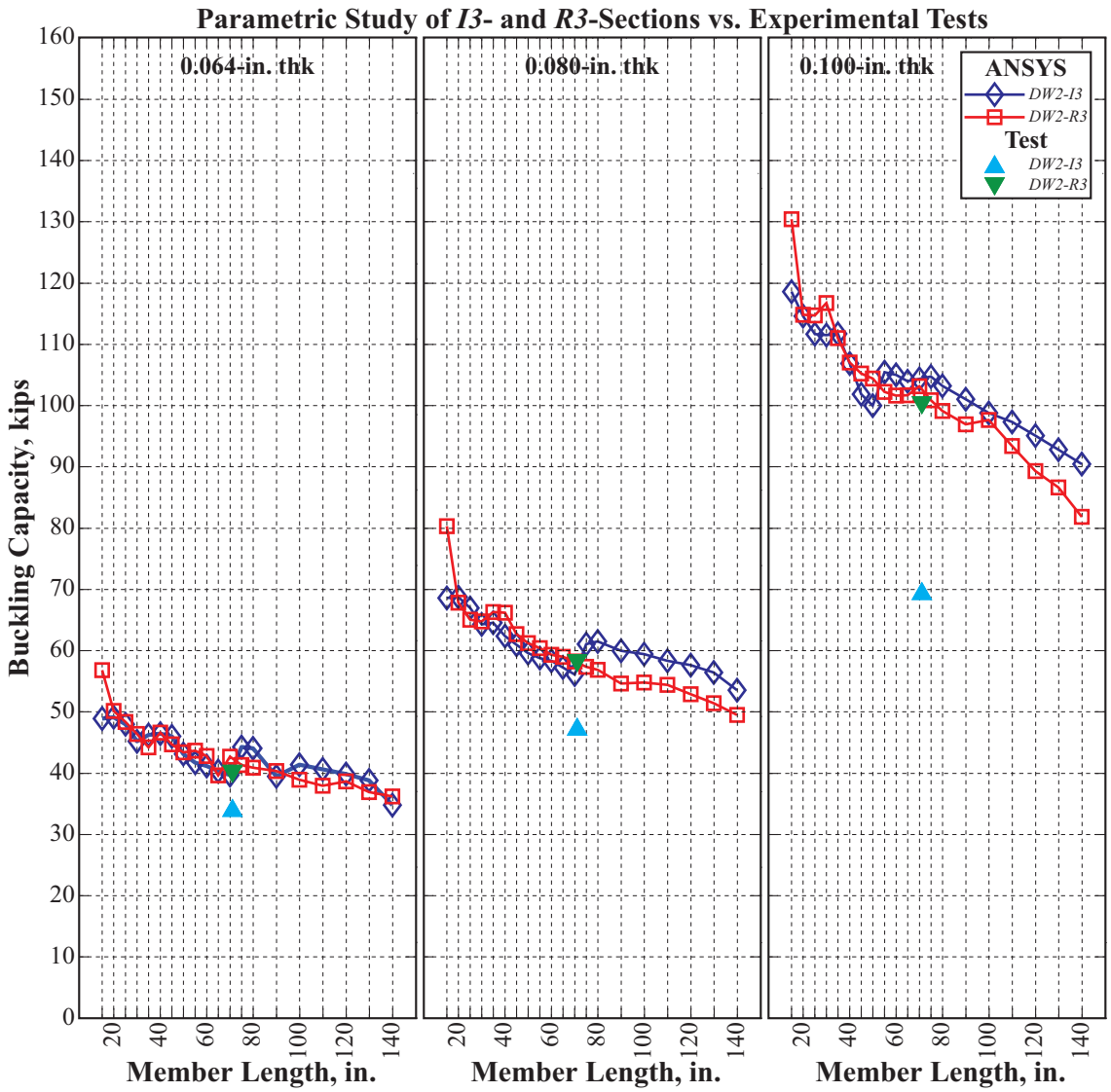


Figure 40: Parametric study of Members *DW2-I3* and *-R3* over varying unbraced lengths. A comparison to their corresponding experimental counterparts is made.

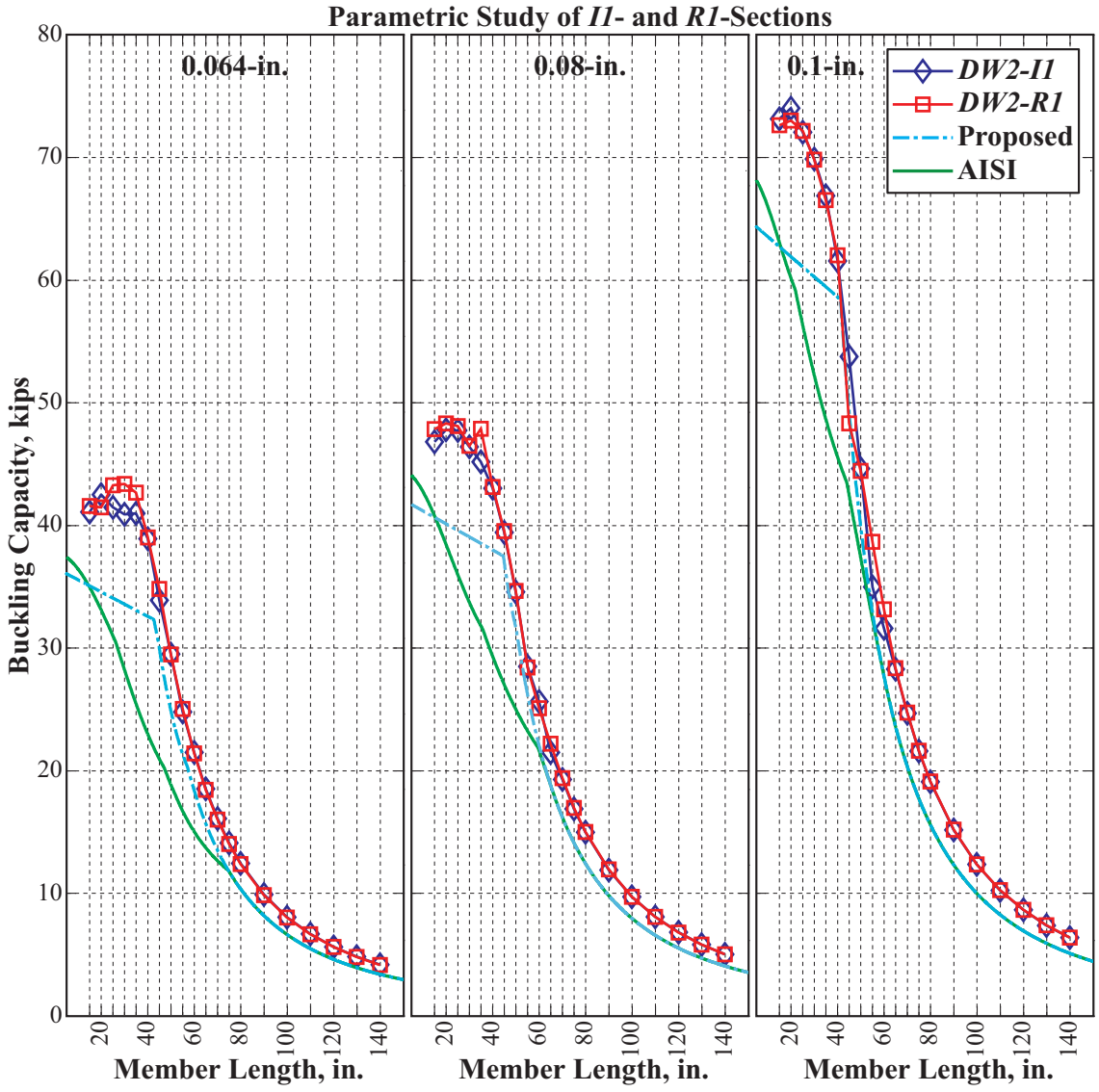


Figure 41: Parametric study of Members *DW2-I1* and -*R1* over varying unbraced lengths. A comparison to the nominal compressive strengths of the 2007 AISI specification and the proposed distortional equation (Eq. (61)) is made.

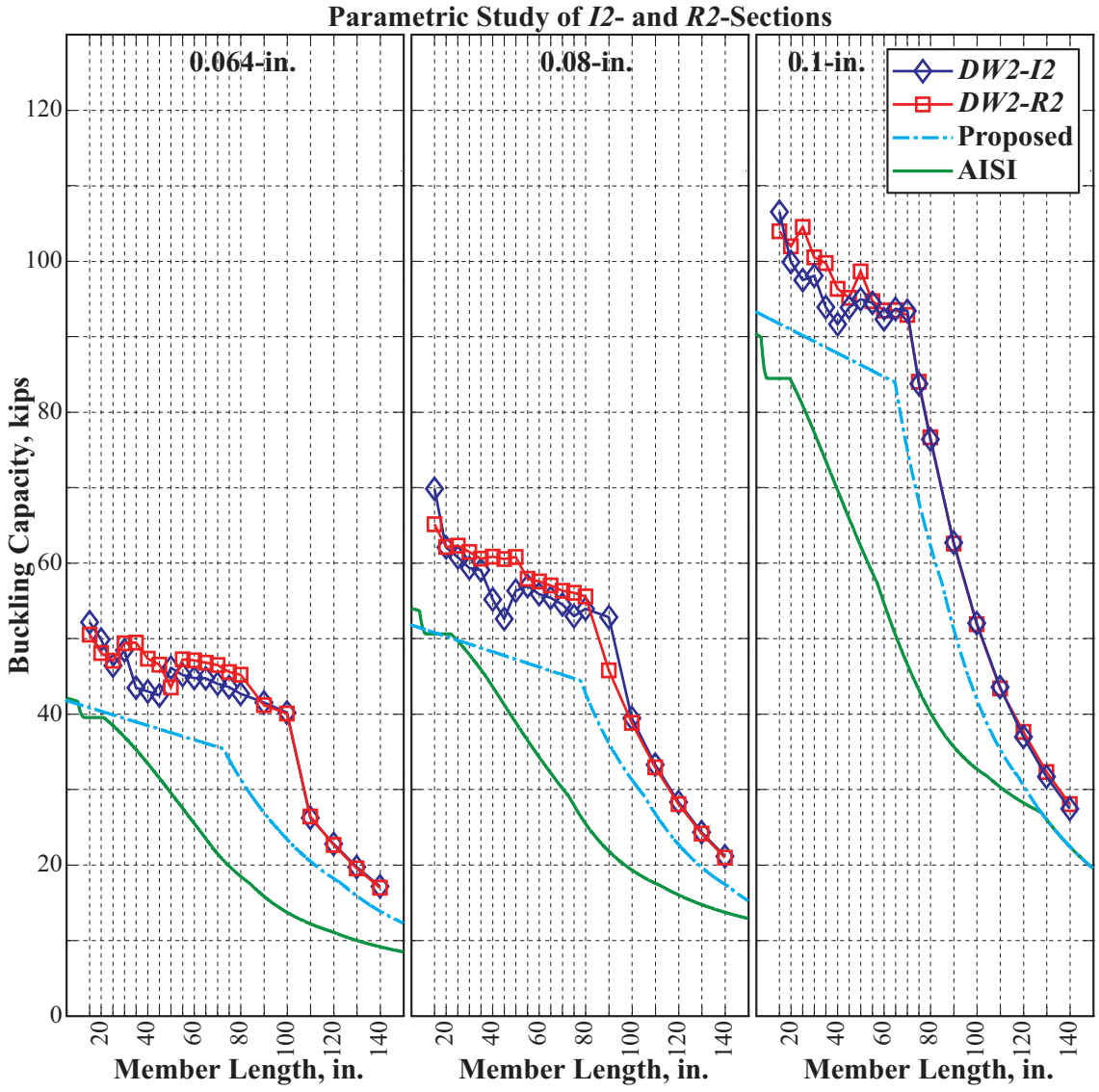


Figure 42: Parametric study of Members *DW2-I2* and *-R2* over varying unbraced lengths. A comparison to the nominal compressive strengths of the 2007 AISI specification and the proposed distortional equation (Eq. (61)) is made.

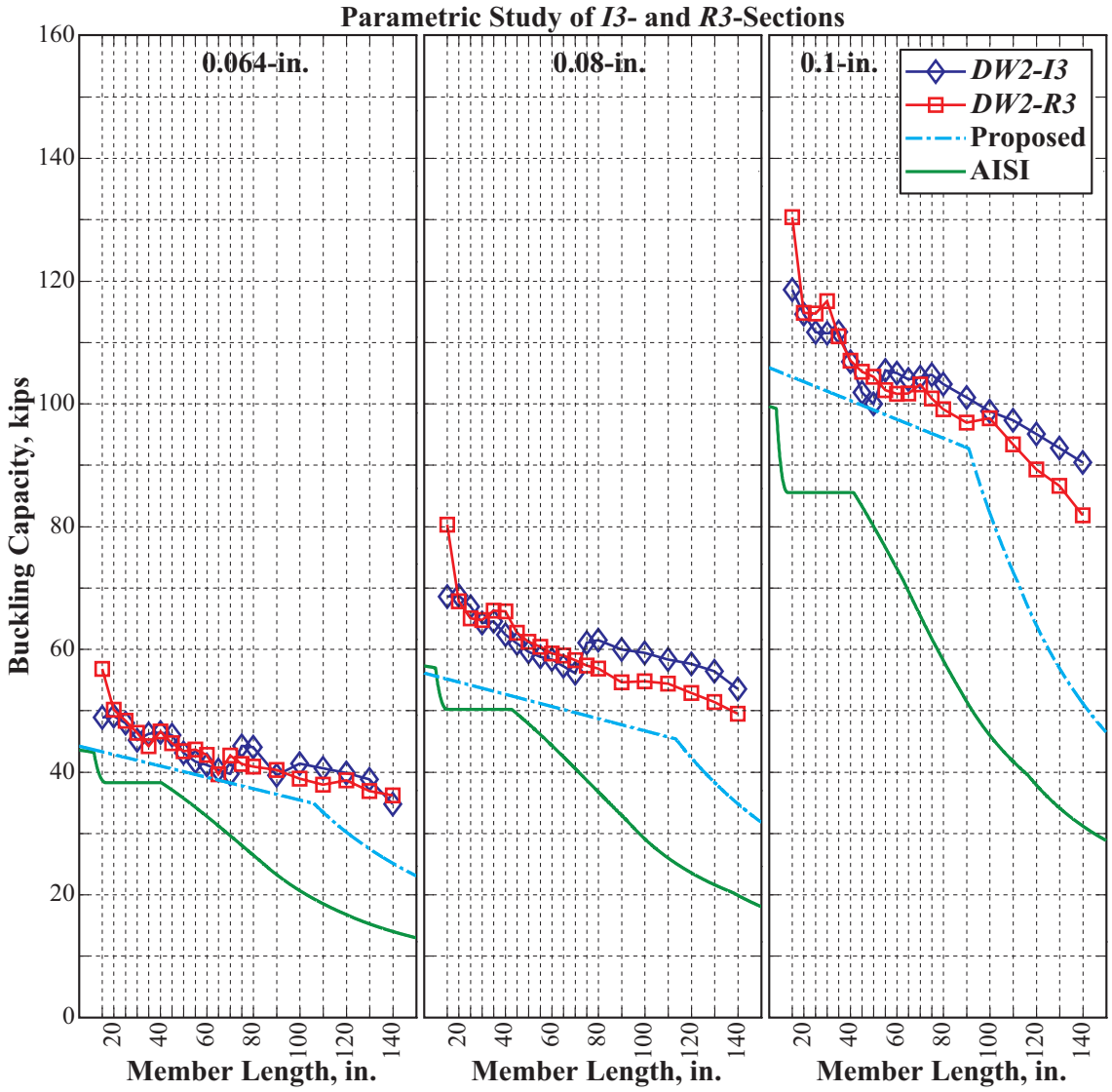


Figure 43: Parametric study of Members *DW2-I3* and -*R3* over varying unbraced lengths. A comparison to the nominal compressive strengths of the 2007 AISI specification and the proposed distortional equation (Eq. (61)) is made.

4.5 Evaluation of the Proposed Distortional Equation

Through the parametric study carried out in Section 4.3, it is justified that there are no compelling reasons to (1) update the flexural built-up provision (AISI Sections C4.1.1 and D1.2) or (2) consider the flexural-torsional provision (AISI Section C4.2), as all the specimens fail due to either flexural or distortional buckling. Thus, the proper design consideration for a symmetrical built-up section shall only take into account for the flexural provision and the proposed distortional equation (Eq. (60)). The buckling-strength calculation is simplified accordingly as follows:

$$P_n = \begin{cases} 0.877 \left(\frac{\pi^2 E}{\left(\frac{kL}{r}\right)_m^2} \right) A_e, \text{ elastic flexural buckling (AISI Section C4.1.1)} \\ 0.877 P_y \underbrace{\left\{ 36.5 \left(\frac{t}{b_o}\right) - 326.5 \left(\frac{t}{b_o}\right)^2 - \frac{1}{638} \left(\frac{kL}{r}\right)_m \right\}}_{\leq 1.0}, \text{ distortional buckling} \end{cases} \tag{61}$$

The material property of the modulus of elasticity is denoted as E, while the parameters of b_o and t refer to the section characteristics of the out-to-out largest width and thickness. The parameters of A_e and P_y denote the effective cross-sectional area of uniform compression and a squash load (simply taken as a product of the yield strength σ_y and the full unreduced cross-sectional area A). The modified stiffness ratio of $\left(\frac{kL}{r}\right)_m$ is defined as $\sqrt{\left(\frac{kL}{r}\right)_o^2 + \left(\frac{a}{r_i}\right)^2}$, where $\left(\frac{a}{r_i}\right) \leq 0.5 \left(\frac{kL}{r}\right)_o$. The first term in the square root refers to the unmodified (overall) slenderness ratio, and the second term refers to the fastening modification factor to account for a relative deformation-induced shear force in the welds. The parameters of k, L, and r are the effective length factor (taken as 1.0 for a pinned-end support), the unbraced member length, and the weak-axis radius of gyration, respectively. The parameters of a and r_i denote the weld spacing (taken as $\frac{L}{3}$ for the *DW2* welding pattern) and the weak-axis radius of gyration of an individual channel.

The evaluations of Eq. (61) to the experimental and the AISI design curves are pre-

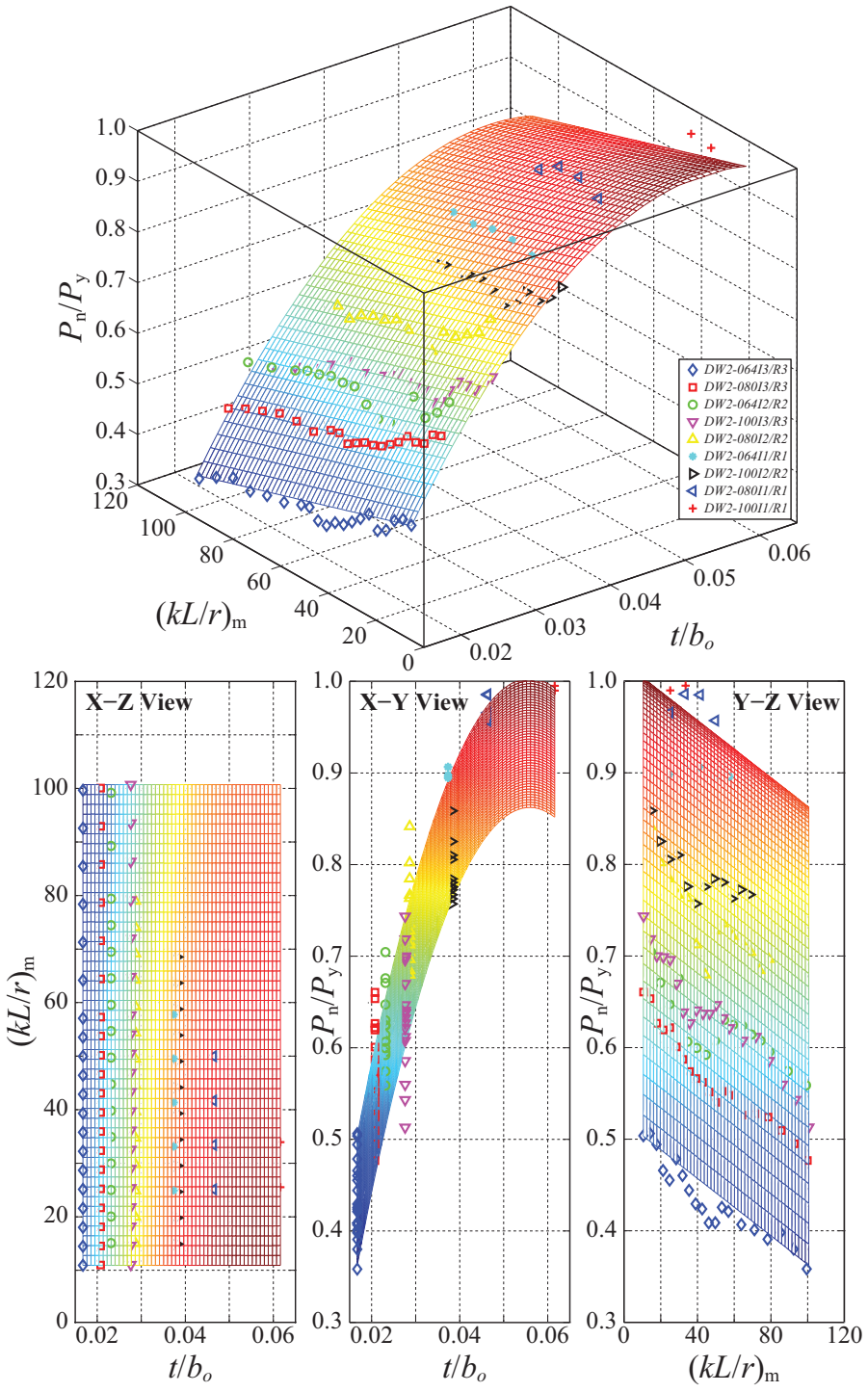


Figure 44: A three-dimensional surface fitting of 114 distortional-buckling data retrieved from Figs. 41-43.

sented in Figs. 45-47. The entire experimental set containing both compliant and non-compliant welding patterns (according to the preceding two equations from AISI Section D1.2) are adopted. The compliant patterns include *DW2* and *DW5*. Overall, for the compliant patterns, the proposed design curves are more accurate and less conservative, in particular for a thicker and larger distortional member. Nonetheless, the *DW2*- and *DW5-I3* members (shown in Fig. 47) are excluded from the preceding observation due to their unreliable experimental quality. They are suspected of being severely prone to an eccentricity and/or a defective setup of the pinned-end condition due to only one experimental repetition conducted for each individual configuration. For instance, the measured strength unexpectedly decreases from 100 kips in the *DW2-100R3* member to about 70 kips in the *DW2-100I3* member. In short, a further validation against more reliable data of other widths and thicknesses is crucial for the justification of Eq. (61).

4.6 Conclusion

The current AISI specification for the axial load capacity of built-up, cold-formed sections have been experimentally identified as being exceedingly conservative for longer members and thicker sections that are likely to fail in distortional buckling. The accuracy of the specification using the modified slenderness ratio is adequate for built-up members that are likely to fail in flexural buckling. But attention must be paid to the coexisting distortional failure mode. Consequently, a regression-based axial load capacity equation is developed for distortional members. The evaluation shows strong correlation with the experimentally measured capacities. However, more pure compression tests on other practical, built-up configurations and section properties are needed for further calibration of the developed equation.

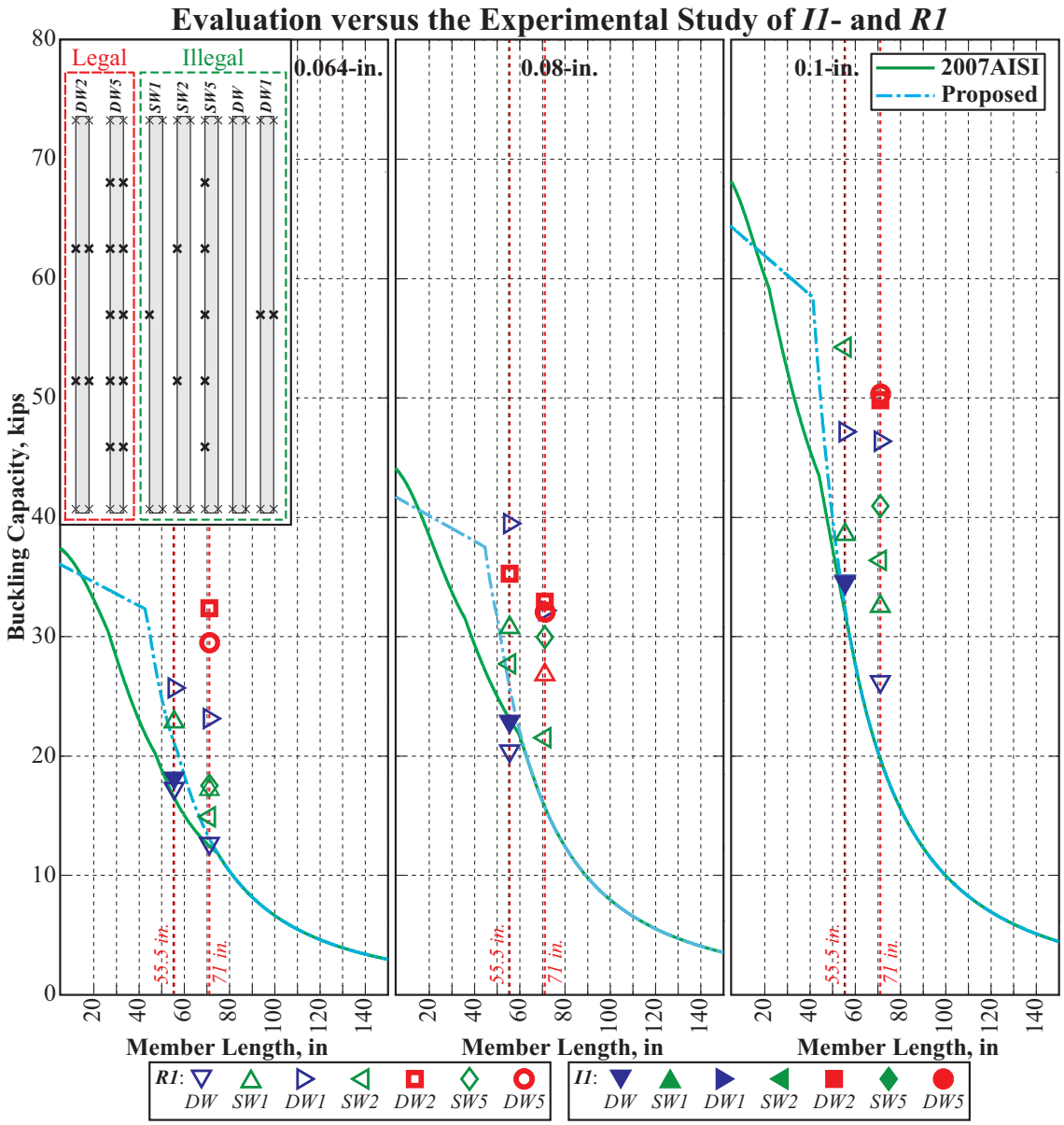


Figure 45: Experimental compressive strength of *I1*- and *R1*-sections versus the corresponding proposed nominal strengths.

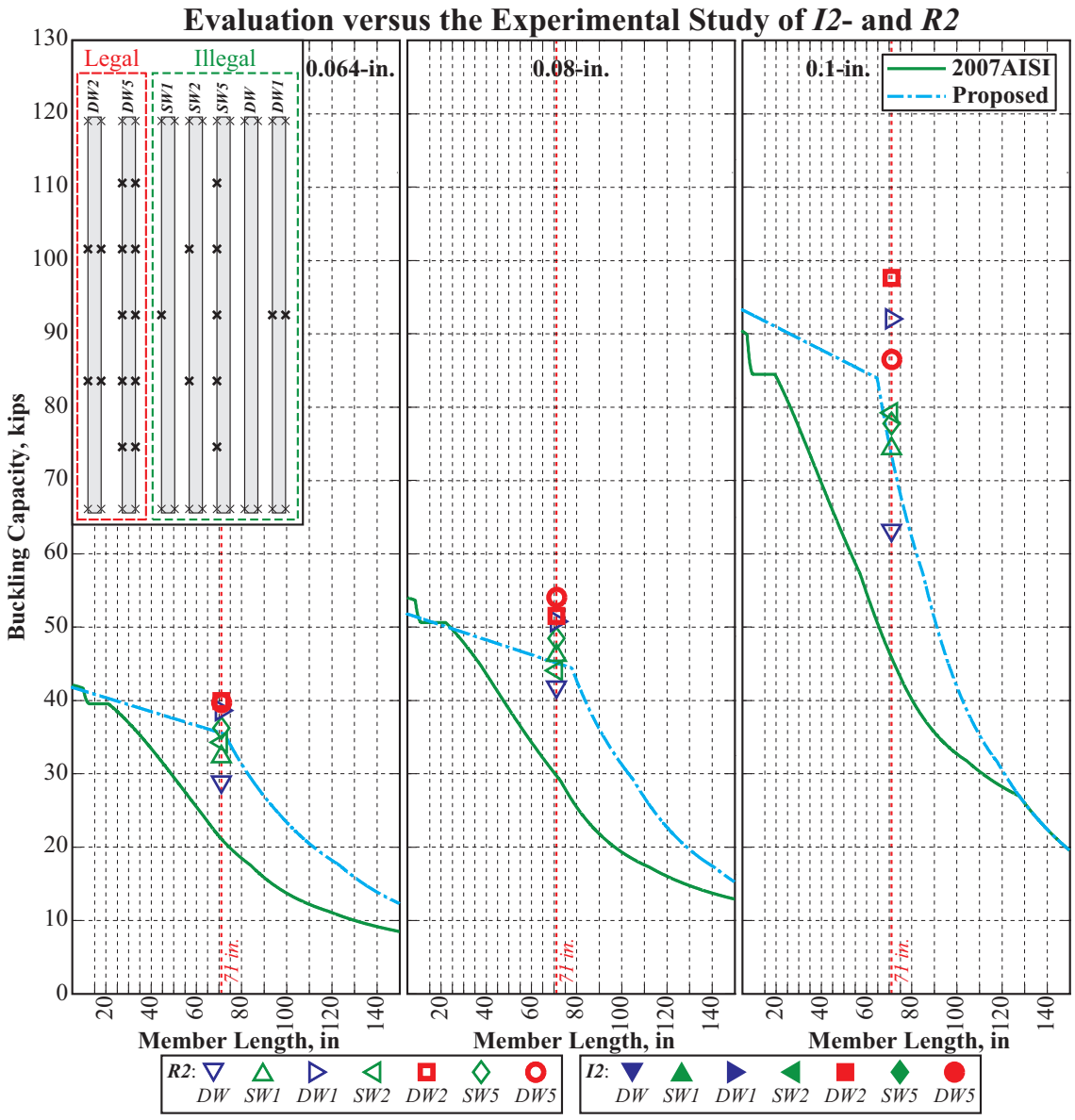


Figure 46: Experimental compressive strength of *I2*- and *R2*-sections versus the corresponding proposed nominal strengths.

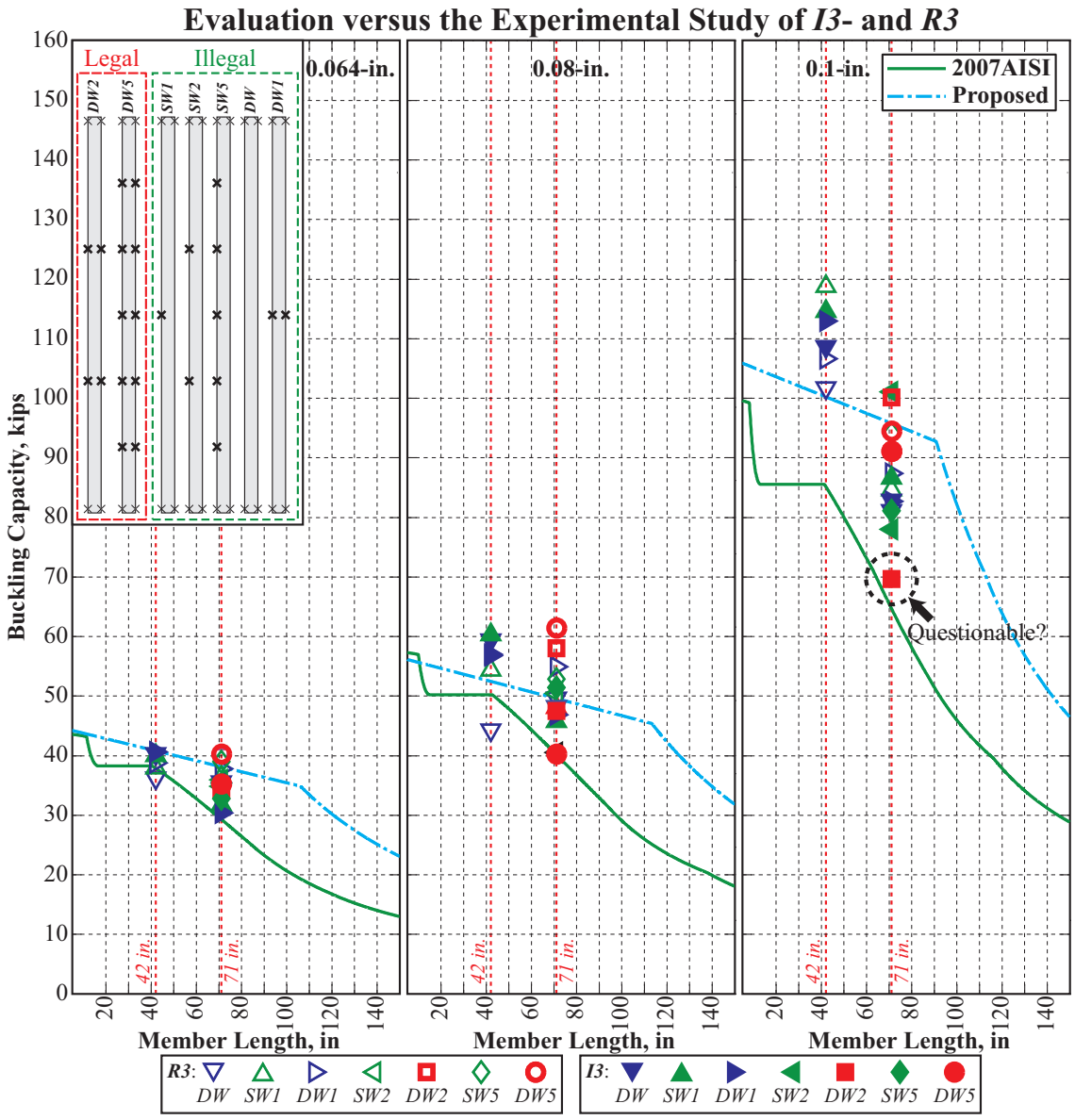


Figure 47: Experimental compressive strength of *I3*- and *R3*-sections versus the corresponding proposed nominal strengths.

5 CONCLUSIONS

Section C4 of the 2007 AISI specification for the axial load capacity of built-up, cold-formed columns has been experimentally identified as being conservative for longer and thicker sections that are likely to fail in distortional buckling. This analytical research used nearly 1,000 highly nonlinear FEM analyses under ANSYS implicit-static and ABAQUS explicit-dynamic modelings to: (1) evaluate the existing experimental data, (2) validate a finite element model, (3) expand the understanding of cold formed built up columns using analytical methods, and (4) propose a simpler more accurate distortional-buckling equation and its corresponding design approach for symmetrical built-up, cold-formed columns.

This modeling strategy to handle nonlinear buckling behaviors of built-up, cold-formed sections with geometrically unstable configurations has been carefully validated against 265 existing experimental tests. The ABAQUS explicit model complements the ANSYS implicit counterpart by offering features ANSYS lacks. The ANSYS model generally ensures a satisfactory buckling capacity prediction but leaves an uncertainty in the post-buckling response, particularly for members that are likely to fail in a brittle manner in flexural buckling. This sometimes results in a difficulty in judging a true structural failure from a numerical blowout, and thus, misrepresenting the actual capacity. In contrast, the ABAQUS explicit-dynamic model is capable of tracing unstable descending loading paths, although a proper loading rate for this scheme is still questionable. Furthermore, a variety of iterative and non-iterative solution techniques, including Newton-Raphson, Arc-Length, Riks, and Central-Difference integration methods, are adopted for obtaining reliable solutions.

The parametric study of 18 built-up configurations of 20 uninvestigated lengths shows the accuracy of the flexural provision. But this investigation also points out that attention must be paid to the distortional provision. To simplify the calculations while improving the accuracy the proposed distortional design equation is proposed. It has been formu-

lated using the numerically simulated distortional-buckling data and using a least-square regression analysis of a three-dimensional surface fitting. The proposed equation and design approach are more accurate and simpler, making hand calculations possible, than the present AISI specification. This work includes:

- *Validation:* Over 265 pure-compression buckling tests are used to validate the ANSYS implicit-static modeling;
- *Verification:* The ANSYS static results are verified by a totally different numerical scheme, ABAQUS using explicit-dynamic modeling;
- *Justification:* The experimentally-identified inaccuracy of the buckling provisions in the 2007 AISI standard is numerically justified or confirmed;
- *Rectification:* The correlation between the distortional-buckling data and their design values is analyzed to develop an equation that addresses the inaccuracy using a least-square regression analysis of a three-dimensional surface fitting;
- *Evaluation:* The proposed design approach is evaluated and compared to the experimental capacities and the AISI design curves.

This study results in a better understanding of buckling in built-up, cold-formed columns. Assemblages, including trusses and wall struts can be made more efficient by following the suggested design approach. Recommendations for future research include: (1) further validation of the proposed equation against more reliable experimental data of other section widths and thickness under both pinned- and fixed-end condition (i.e., varying the degrees of out-of-flatness and out-of-straightness), (2) further investigation/justification on the explicit-dynamic characteristics of a proper loading rate and an acceptable mode-dependent minimum energy ratio, and (3) better static modeling strategy that effectively and certainly handles unstable softening descending paths of the post-buckling regimes.

References

ABAQUS® (2007a). *ABAQUS/Standard User Manual*. Habbitt, Karlsson & Sorenson (HKS) Inc., version 6.7 edition.

ABAQUS® (2007b). *Getting Started with Abaqus: Interactive Edition*. Habbitt, Karlsson & Sorenson (HKS) Inc., version 6.7 edition.

AISC (2005). *Sttel Constrction Manual*. American Institute of Steel Construction (AISC), Inc., Chicago, IL, 13th edition.

AISI (2001). *North American Specification for the Design of Cold-Formed Steel Structural Members*. American Iron and Steel Institute, 1140 Connecticut Avenue NW Washington DC 20036, 2001 edition.

AISI (2007). *North American Specification for the Design of Cold-Formed Steel Structural Members*. American Iron and Steel Institute, 1140 Connecticut Avenue NW Washington DC 20036, 2007 edition.

AISI (2008). *AISI MANUAL: Cold-Formed Steel Design*. American Iron and Steel Institute, 1140 Connecticut Avenue NW Washington DC 20036, 2008 edition.

ANSYS® (2009a). *Help System, ANSYS Structural Guide*. ANSYS Inc., 275 Technology Drive Canonsburg, PA 15317, release 11.0 edition.

ANSYS® (2009b). *Help System, Programmer's Manual for Mechanical APDL*. ANSYS Inc., 275 Technology Drive Canonsburg, PA 15317, release 12.0 edition.

Ashraf, M., Gardner, L., and Nethercot, D. (2005). "Strength enhancement of corners regions of stainless steel cross sections." *Journal of Constructional Steel Research*, 61(1), 37–52.

Bacque, J. and K.J., R. (2009a). "Experimental investigation of local-overall interaction buckling of stainless steel lipped channel columns." *Journal of Construction Steel Research*, 65, 1677–1684.

Bacque, J. and K.J., R. (2009b). "A numerical investigation of local-overall interaction buckling of stainless steel lipped channel columns." *Journal of Construction Steel Research*, 65, 1685–1693.

Bakker, M. and Pekoz, T. (2001). "The finite element method for thin-walled members - basic principles." *Third International Conferences on Thin-Walled Structures*, J. Zaras, K. Kowal-Michalska, and J. Rhodes, eds. Elsevier, 427–36.

Bathe, K. (1996). *Finite Element Procedures*. Prentic Hall, Upper Saddle River, New Jersey 07458.

Becque, J. and Rasmussen, K. (2008). "Numerical investigation and design methods for stainless steel columns failing by interaction of local and overall buckling." *Report No. R888*, School of Civil Engineering, the University of Sydney.

Belytschko, T., Liu, W., and Moran, B. (2000). *Nonlinear Finite Elements for Continua Structures*. John Wiley & Sons Ltd., 605 third Avenue, New York, NY 10158-0012, USA.

Biggs, K. (2008). "Axial load capacity cold-formed built-up members. Master's thesis, the University of Oklahoma.

Boresi, A. and Schmidt, R. (2003). *Advanced Mechanics of Materials*. John Wiley & Sons, Inc., 6 edition.

Brueggen, B. and Ramseyer, C. (2003). "Cold-formed steel joist member buckling capacity testing." *Report no.*, Fears Structural Engineering Laboratory, the University of Oklahoma.

Chopra, A. (2000). *Dynamics of Structures: theory and applications to earthquake engineering*. Prentice Hall.

Cook, R. (1995). *Finite Element Modeling for Stress Analysis*. John Wiley & Sons, Inc., New York.

Cook, R., Malkus, D., Plesha, M., and Witt, R. (2001). *Concepts and Applcations of Finite Element Analysis*. John Wiley & Sons, Inc., 4th edition.

Crisfield, M. (1998). *Non-Linear Finite Element Analysis of Solids and Structures, Volume 1: Essentials*, Vol. 1. John Wiley & Sons.

Ellobody, E. and Young, B. (2005). "Structural performance of cold-formed high strength stainless steel columns." *ournal of Constructional Steel Research*, 61(12), 1631–49.

Fenves, G., Mazzoni, S., McKenna, F., and Scott, M. (2002). *Open System for Earthquake Engineering Simulation (OPENSEES): User Manual*. Pacific Earthquake Engineering Research Center (PEER), the University of California, Berkeley, 1.6.0 edition.

Gardner, L. and Nethercot, D. (2004). "Numerical modeling of stainless steel structural components - a consistent approach." *Journal of Structural Engineering, ASCE*, 130(10), 1586–601.

Hamming, R. (1986). *Numerical Methods for Scientists and Engineers*. Dover Publications, Inc., 31 East 2nd Street, Mineola, N.Y. 11501, 2 edition.

Hancock, G., Murray, T., and Ellifritt, D. (2001). *Cold-Formed Steel Structures to the AISI Specification*. Marcel Dekker, Inc.

Harman, T., Dabney, J., and Richert, N. (2000). *Advanced Engineering Mathematics with MATLAB®*. Brooks/Cole, 2 edition.

Hilbert, H., Hughes, T., and Taylor, R. (1977). "Improved numerical dissipation for time integration algorithms in structural dynamics." *Earthquake Engineering and Structural Dynamics*, 5, 283–292.

Jennings, P. (1964). "Periodic response of a general yielding structure." *Journal of the Engineering Mechanics Division, Proceedings of the American Society of Civil Engineers*, 90(EM2), 131–166.

Karen, K. (1967). "Corner properties of cold-formed steel shapes." *Journal of Structural Division, ASCE,* 93(1), 401–32.

Kim, W., Piyawat, K., Ramseyer, C., and Kang, T. (2010). "Experimental and numerical simulations of pre-stressed self-consolidating-concrete structures subjected to nonlinear deformations." *Int. J. Theoretical and Applied Multiscale Mechanics,* 1(4), 319–338.

LabVIEW™ (2000). *LabVIEW Measurements Manual*. National Instruments Corporation, 11500 N Mopac Expwy, Austin, TX 78759-3504, 2000 edition.

Madenci, E. and Guven, I. (2006). *The Finite Element Method and Applications in Engineering Using ANSYS*. Springer Science + Business Media, LLC, 233 Spring Street, New York, NY 10013, USA.

Mathews, J. and Fink, K. (2004). *Numerical Methods Using MATLAB*. Pearson Prentice Hall, 4 edition.

MATLAB® (2010). *User's Guide: Curve Fitting Toolbox™ 3*. The MathWorks, Inc., 3 Apple Hill Drive, Natick, MA 01760-2098, r2010b edition.

Mish, K., Herrmann, L., and Haws, L. (2000). *Finite Element Procedures in Applied Mechanics*. UCD/ECI 212A/W2000.

Mitra, S. (2005). *Digital Signal Processing*. McGraw-Hill, 3rd edition.

Nakamura, S. (1991). *Applied Numerical Methods with Software*. Prentice Hall, Inc.

Narayanan, S. and Mahendran, M. (2003). "Ultimate capacity of innovative cold-formed steel columns." *Journal of Constructional Steel Research*, 59(4), 489–508.

Ng, L. and Gardner, L. (2007). "Buckling of stainless steel columns and beams in fire." *Engineering Structures*, 29, 717–30.

Otani, S. (1974). "Inelastic analysis of r/c frame structures." *Journal of the Structural Division, ASCE,* 100(ST7).

Palm, W. (2001). *Introduction to Matlab 6 for Engineers*. McGraw-Hill.

Piyawat, K. (2005). "Understanding nonlinear dynamic simulation using opensees. Master's thesis, The University of Oklahoma.

Piyawat, K. and Pei, J. (2009). "Linking nonlinear system identification with nonlinear dynamic simulation under opensees: Some justification and implementations." *ASCE Journal of Engineering Mechanics*, 135(11), 1213–1226.

Piyawat, K., Pei, J., and Wright, J. (2008). "A two-state-variable approach for sdof systems with piecewise strong-form restoring force." *Proceedings of the 26th International Modal Analysis Conference (IMAC XXVI)*, Society for Experimental Mechanics, Inc., Orlando, FL.

Rasmussen, K. and Hasham, A. (2001). "Nonlinear analysis of locally buckled i-section steel beam-columns." *Third International Conferences on Thin-Walled Structures*, J. Zaras, K. Kowal-Michalska, and J. Rhodes, eds. Elsevier, 427–36.

Riks, E. (1979). "An incremental approach to the solution of snapping and buckling problems." *International Journal of Solids and Structures*, 15, 529–551.

Talikoti, R. and Bajaria, K. (2005). "New approach to improving distortional strength of intermediate length thin-walled open section columns." *Electronic Journal of Structural Engineering*, 5, 69–79.

Walker, A. (1975). *Design and Analysis of Cold-Formed Sections*. International Textbook Company Limited.

Whittle, J. (2007). "Buckling capacities of axial loaded cold-formed built-up members. Master's thesis, the University of Oklahoma.

Whittle, J. and Ramseyer, C. (2009). "Buckling capacities of axially loaded, cold-formed, built-up c-channels." *Thin-Walled Structures*, 47, 190–201.

Yang, D. and Hancock, G. (2004). "Compression tests of cold-reduced high strength steel sections, i: Stub columns." *Journal of Structural Engineering ASCE*, 130(11), 1772–1781.

Yang, D. and Hancock, G. (2006). "Numerical simulation of high-strength steel box-shaped columns falling in local and overall buckling modes." *Journal of Structural Engineering*, 132(4), 541–549.

Yang, D., Hancock, G., and Rasmussen, K. (2004). "Compression tests of cold-reduced high strength steel sections, ii: Long columns." *Journal of Structural Engineering ASCE*, 130(11), 1782–1788.

Yu, W. and LaBoube, R. (2010). *Cold-Formed Steel Design*. John Wiley & Sons, Inc., 4 edition.

Zhao, X., Wilkinson, T., and J., H. G. (2005). *Cold-Formed Tubular Members and Connections*. Elsevier, Elsevier Inc. 525 B Street, Suite 1900, San Diego, CA 92101-4495, USA.

A LABVIEWS IMPLEMENTATION OF ARC-LENGTH METHOD

Implementation of Arc-Length method as described in Crisfield (1998) under LabView to approximate a snap-through behavior of a nonlinear SDOF system in Fig. 17. Figure 48 shows the flowchart of the driver VI and the subVIs are presented in Figs. 49 and 50.

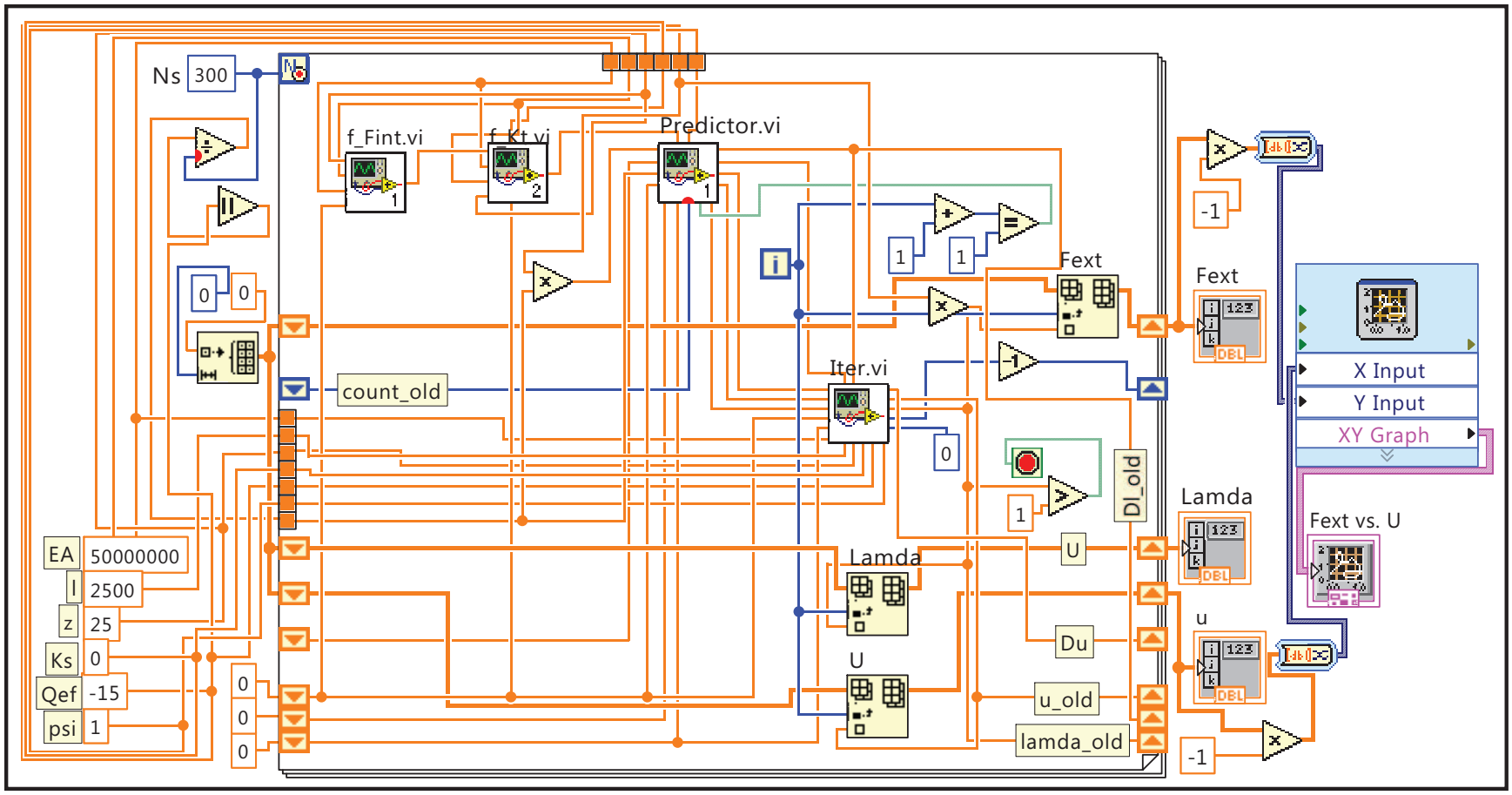


Figure 48: LabView implementation of spherical Arc-Length method to approximate a snap-through behavior of a nonlinear-geometric SDOF elastic bar as shown in Fig. 17. This VI is a driver containing subVIs as shown in Figs. 49 and 50.

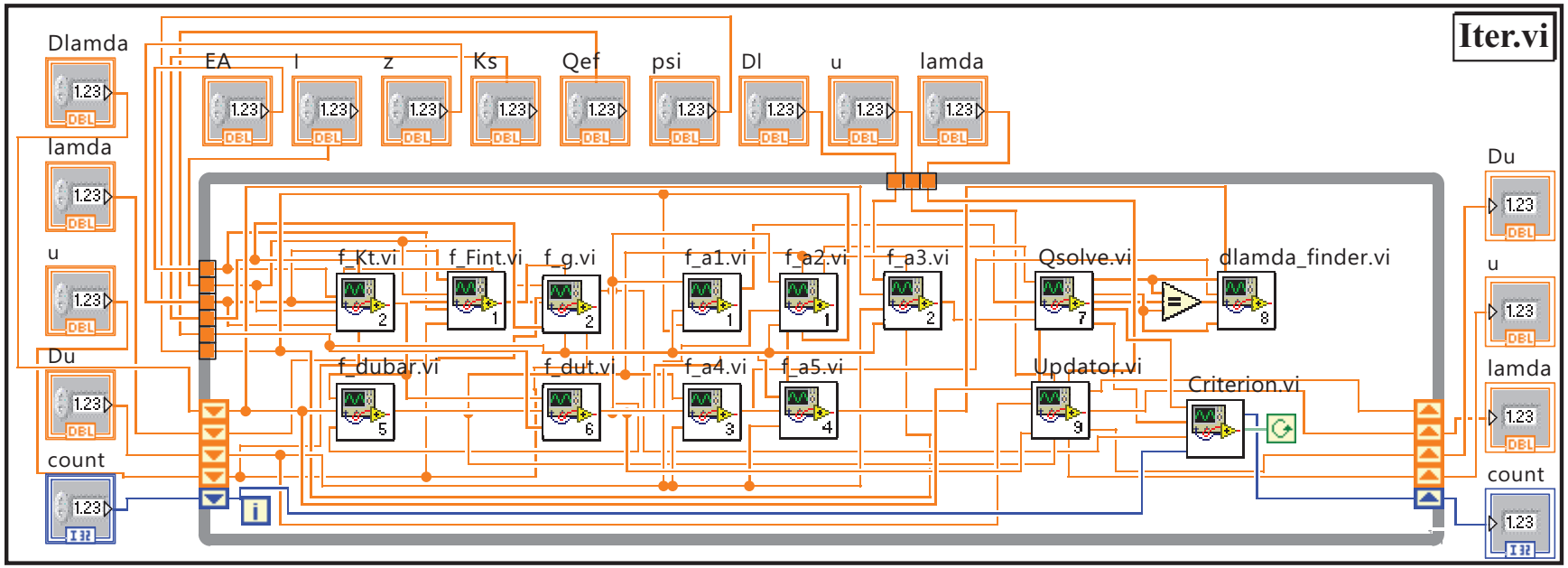


Figure 49: A subVI of Iter.vi to perform iteration. This subVI is called by the driver VI in Fig. 48.

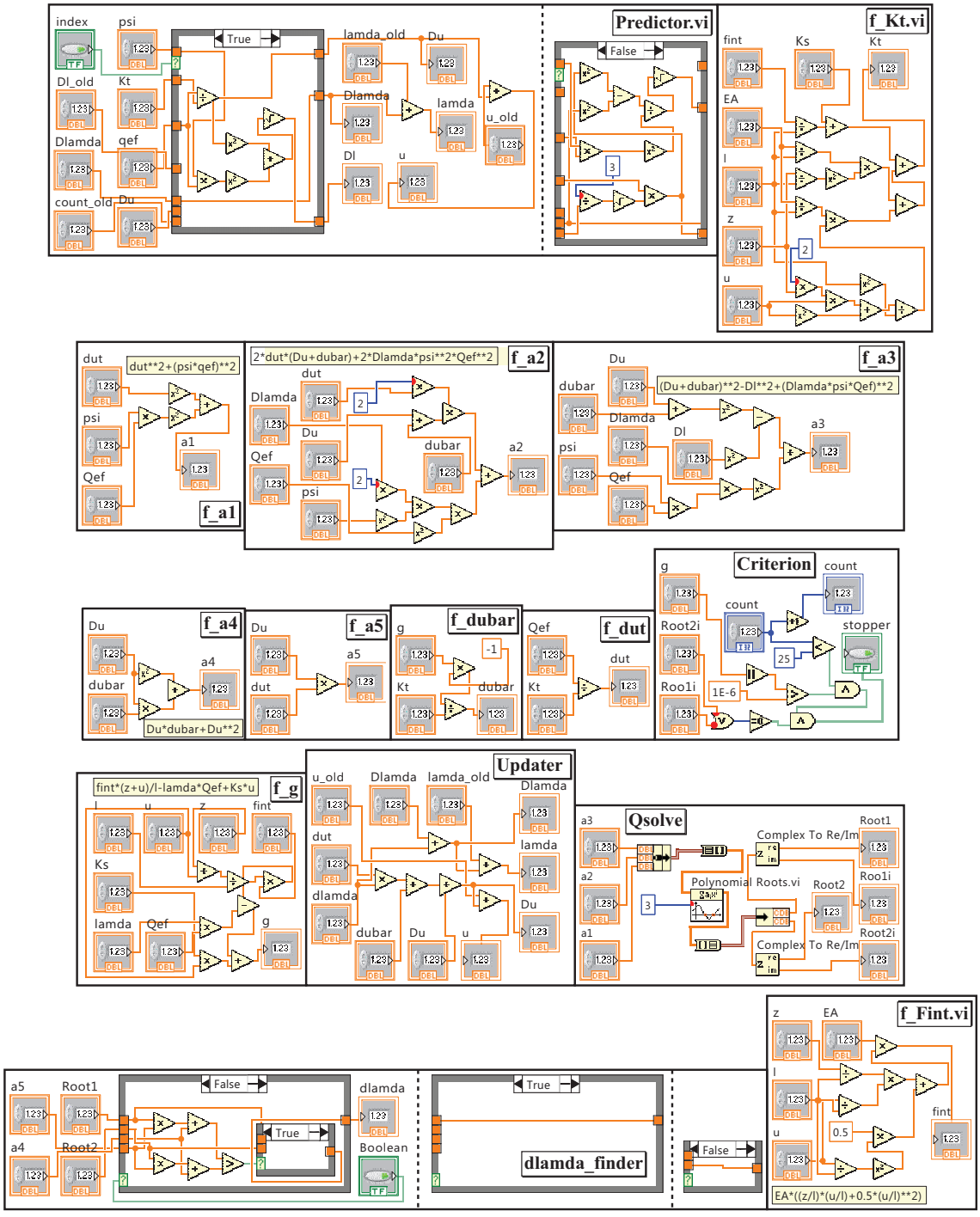
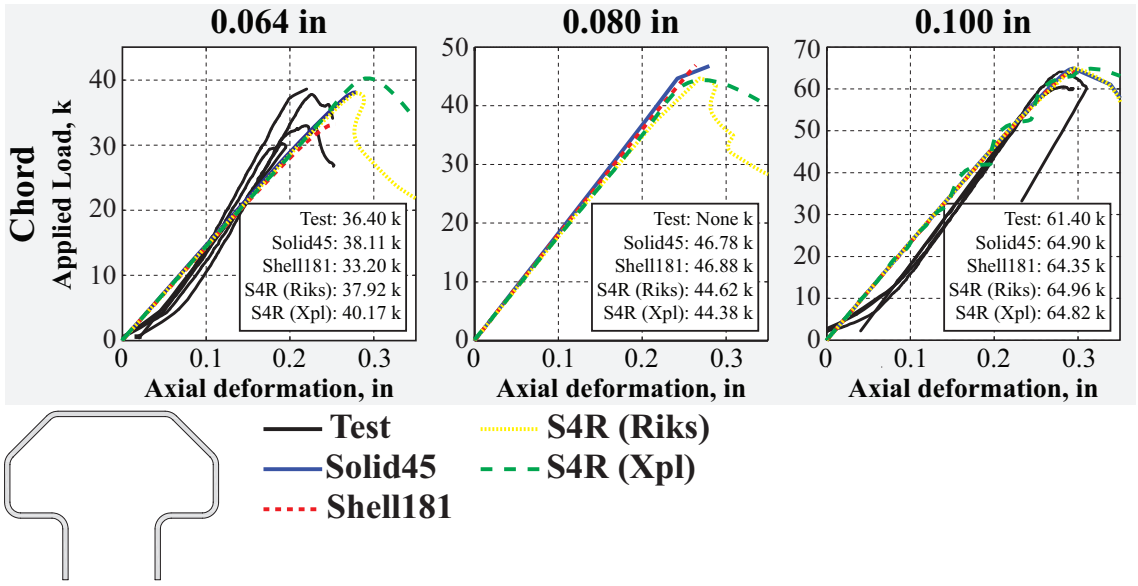


Figure 50: SubVIs of the driver VI in Fig. 48.

B LOAD VS. DISPLACEMENT HISTORY

Experimental and numerical simulated load vs. displacement histories of the adopted cold-formed sections are presented in Figs. 51-178. Implicit static and explicit dynamic solution techniques of Newton-Raphson scheme, Riks method and central-difference scheme, are applied in the numerical analyses. Notation of Solid45 and Shell181 indicates ANSYS solutions of using structural solid and shell elements to model column members. S4R (4-node shell element with reduced integration) with Riks and Xpl refer to ABAQUS solutions of Riks method and central-difference scheme, respectively. The presentation order ranges from single to built-up members, member lengths, section sizes and weld orientations. The format for each figure adopts three columns indicating three different section thicknesses of 0.064, 0.08, and 0.1 in. Different welding patterns, e.g., *DW* and *SW1*, are categorized row-wise.



Chord, 55.5-in. length

Figure 51: Overview of load vs. deformation history of *Chord*-sections presented in Figs. 52-54.

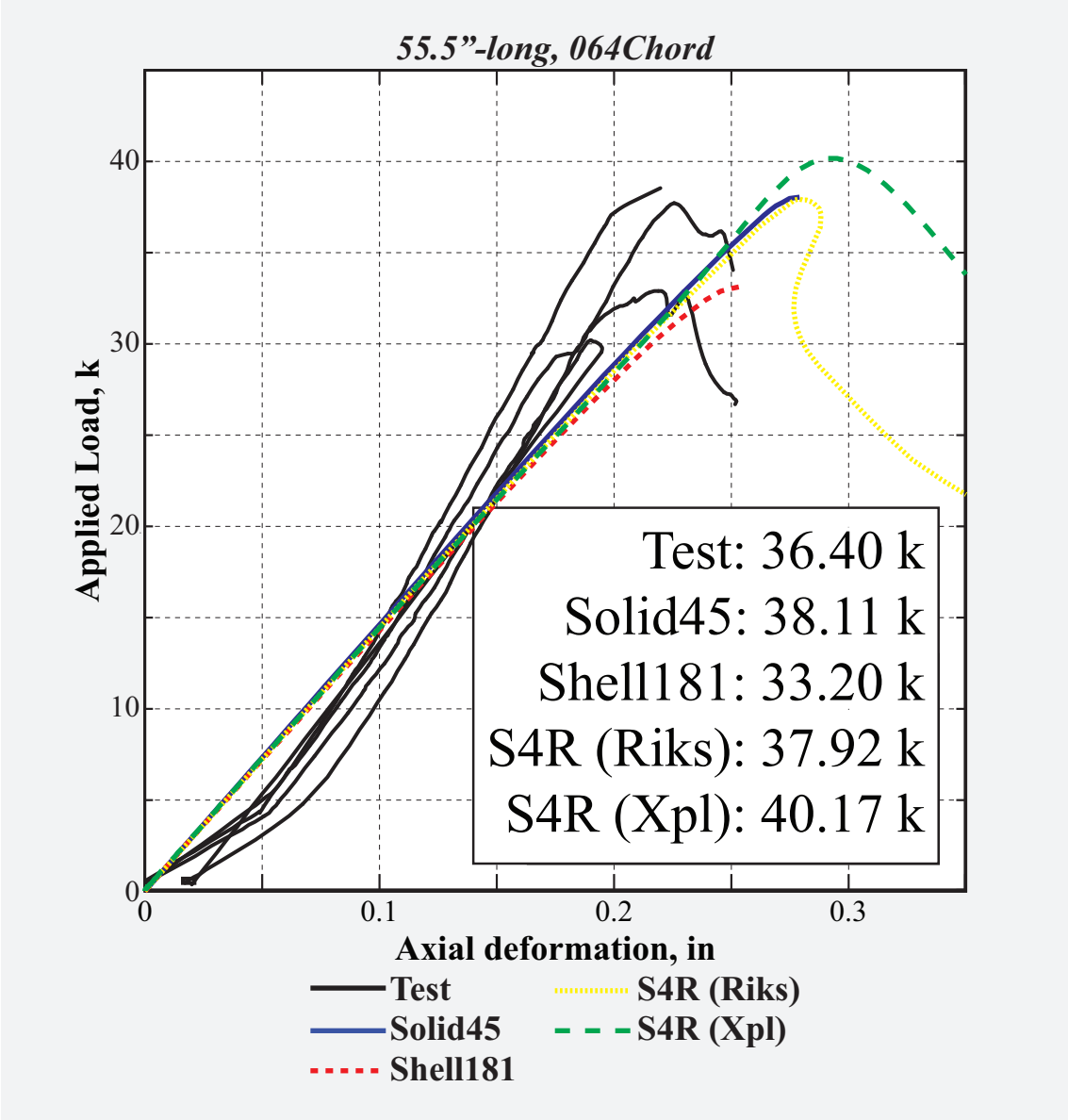


Figure 52: Load vs. deformation history of chord members

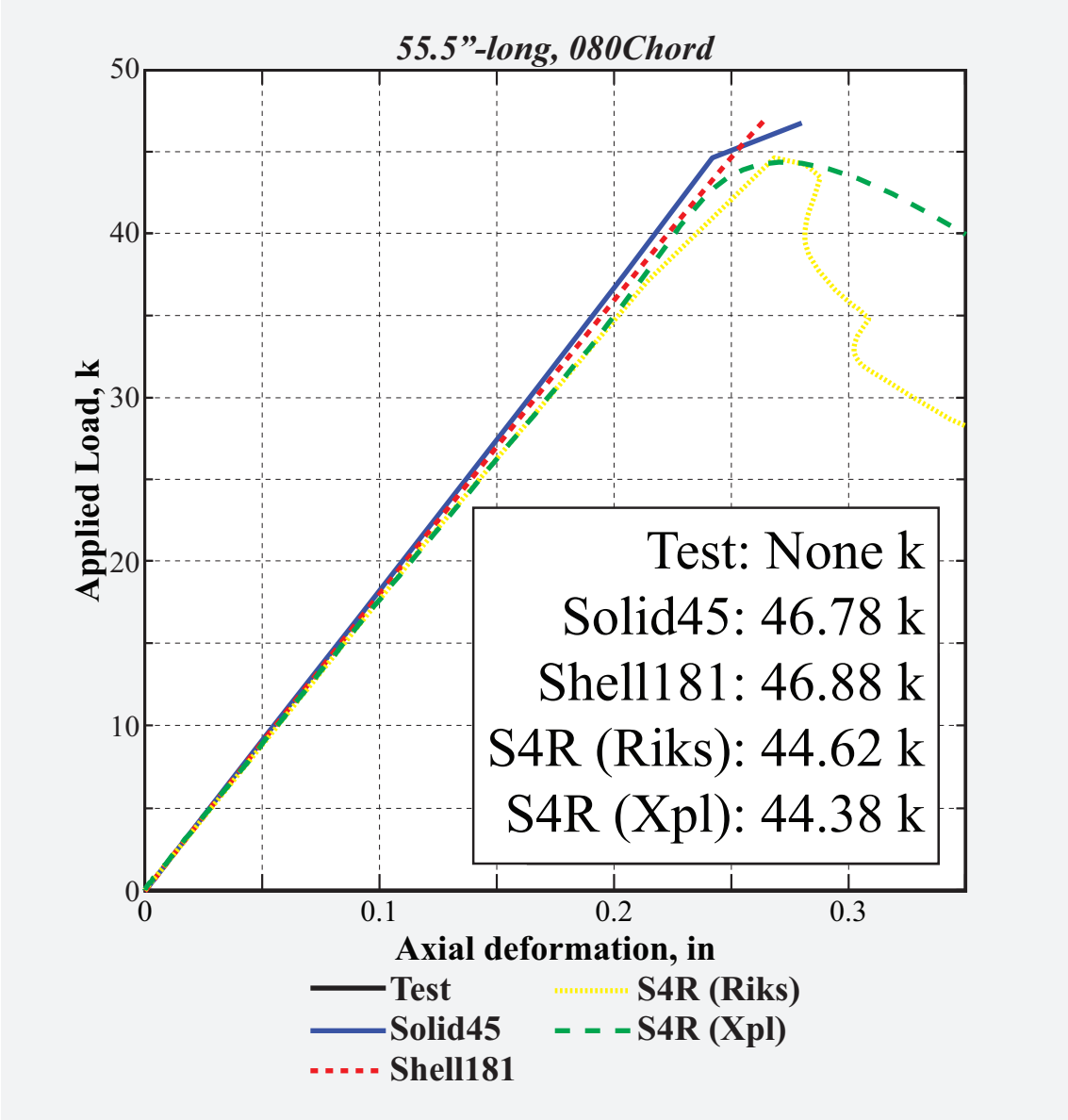


Figure 53: Load vs. deformation history of chord members

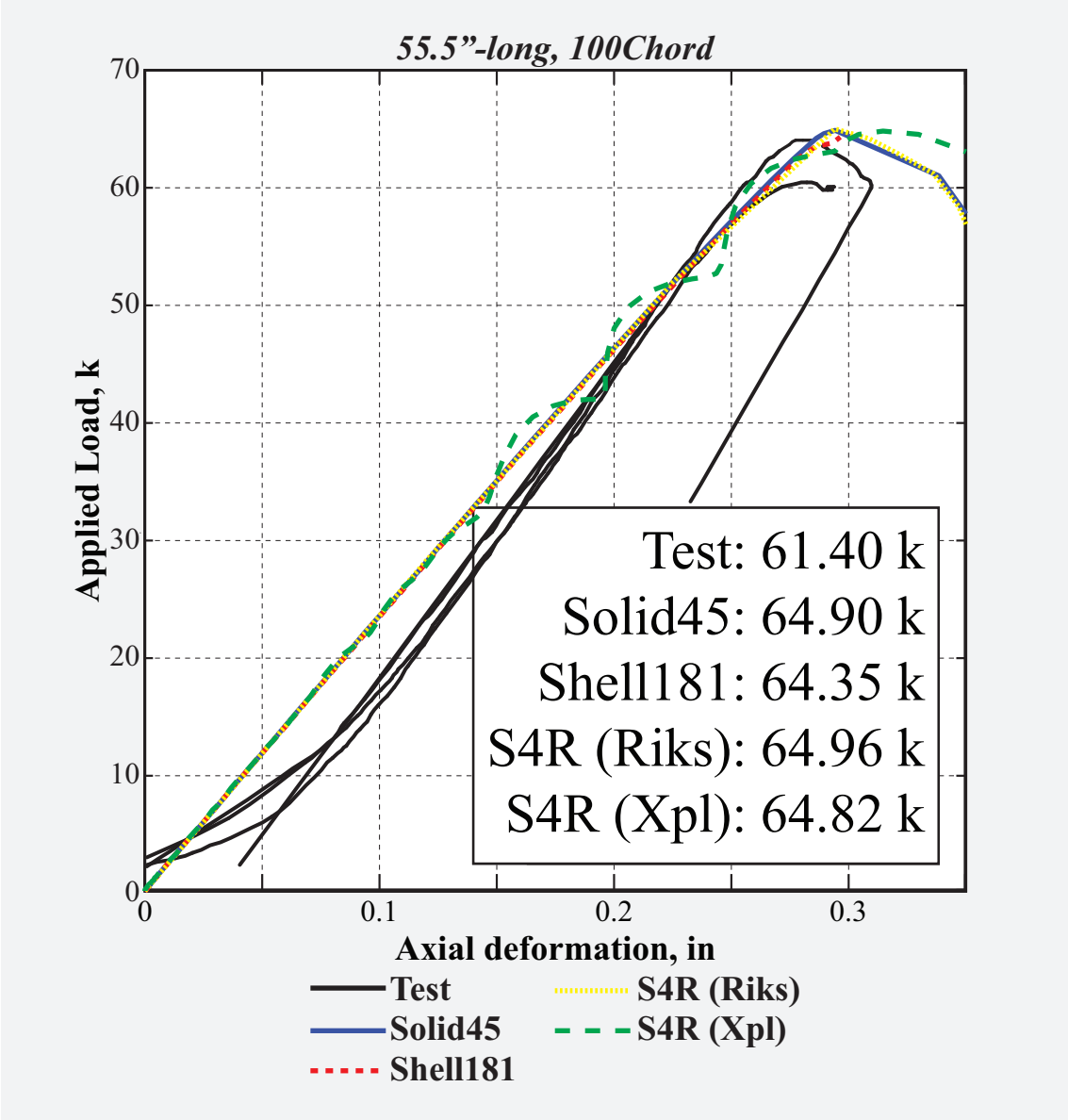


Figure 54: Load vs. deformation history of chord members

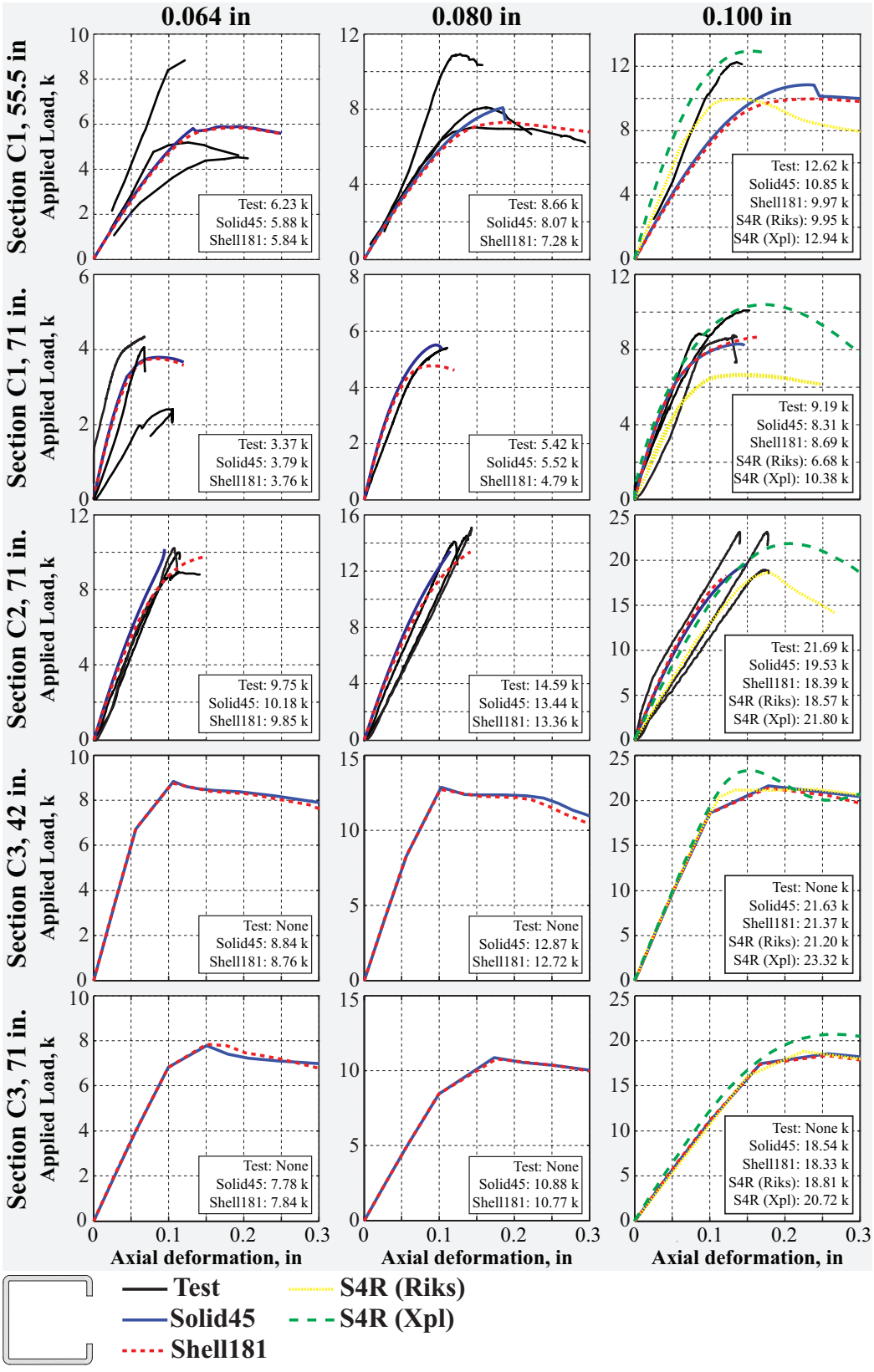


Figure 55: Overview of load vs. deformation history of *C*-sections presented in Figs. 56-70.

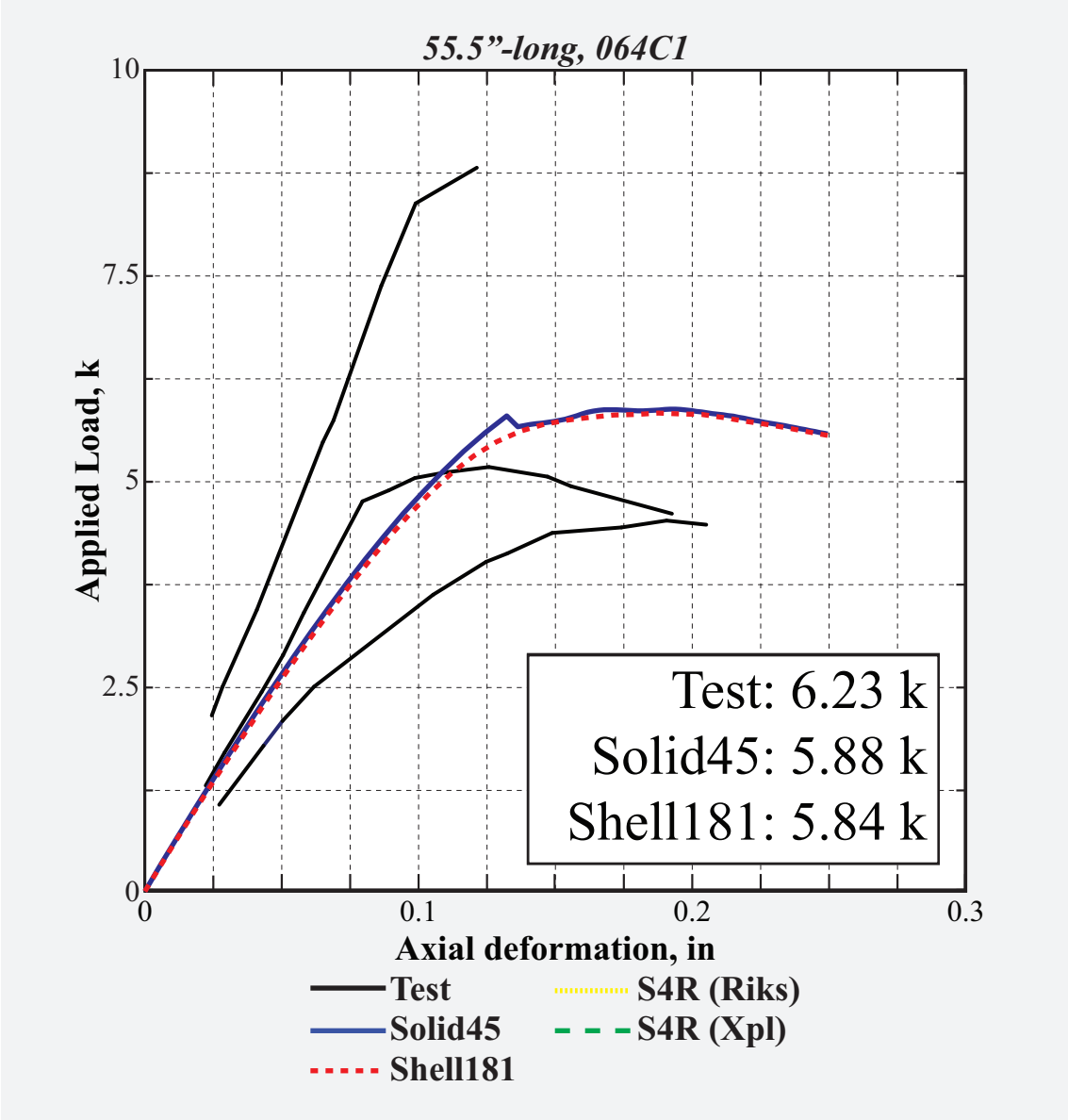


Figure 56: Load vs. deformation history of 55.5”-long, 0.064”-thick *C1*

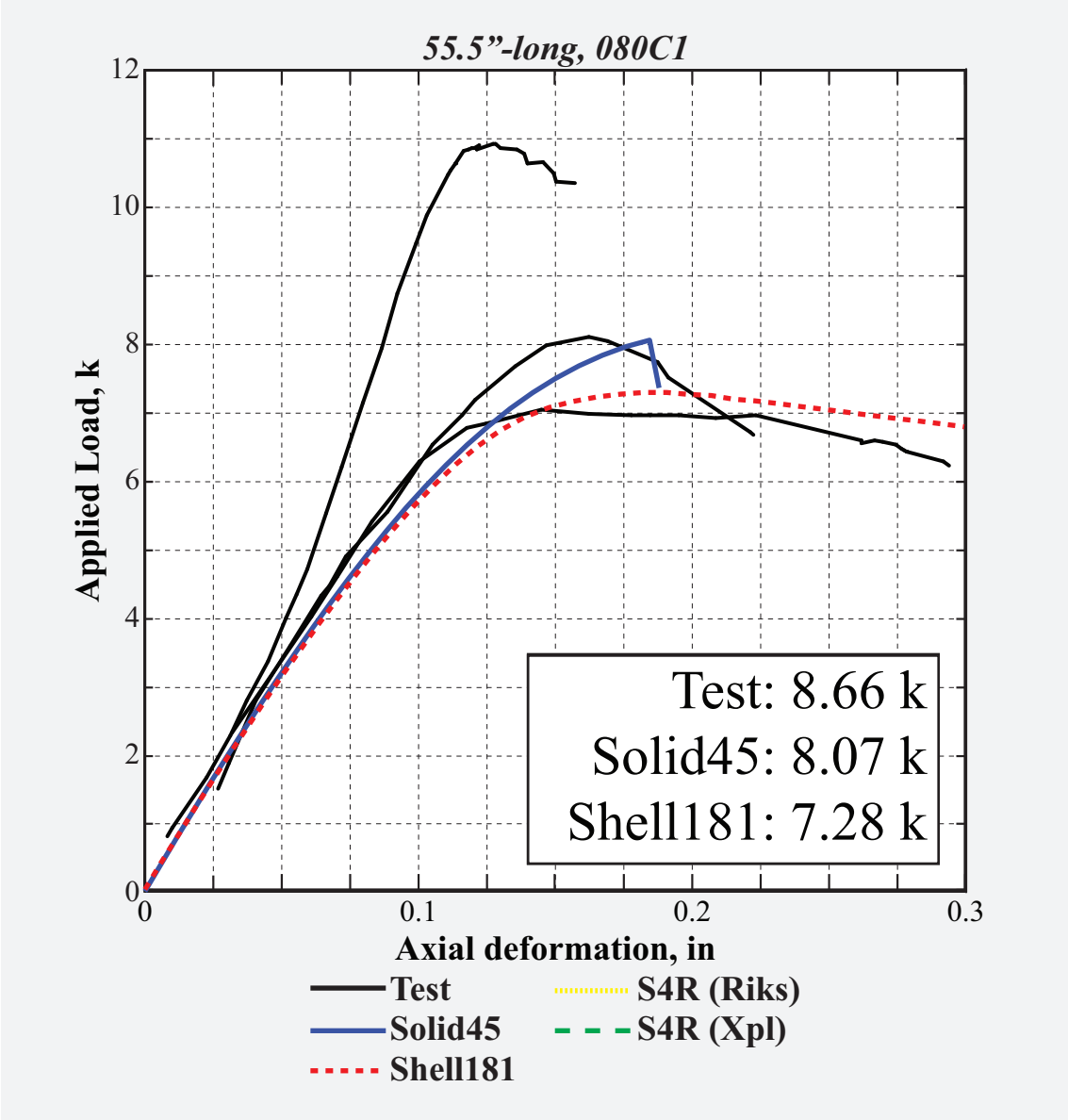


Figure 57: Load vs. deformation history of 55.5”-long, 0.08”-thick *C1*

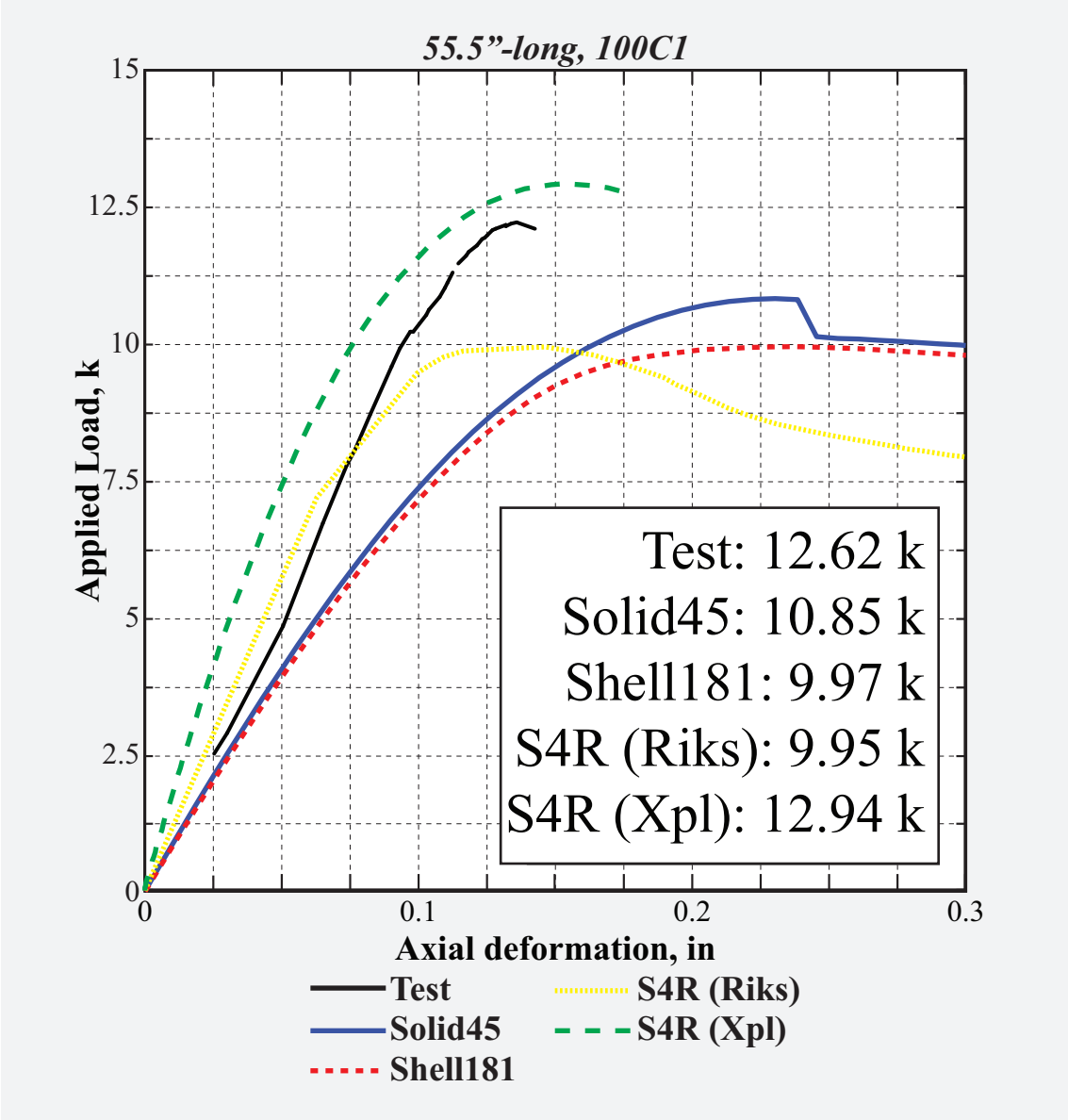


Figure 58: Load vs. deformation history of 55.5”-long, 0.1”-thick *C1*

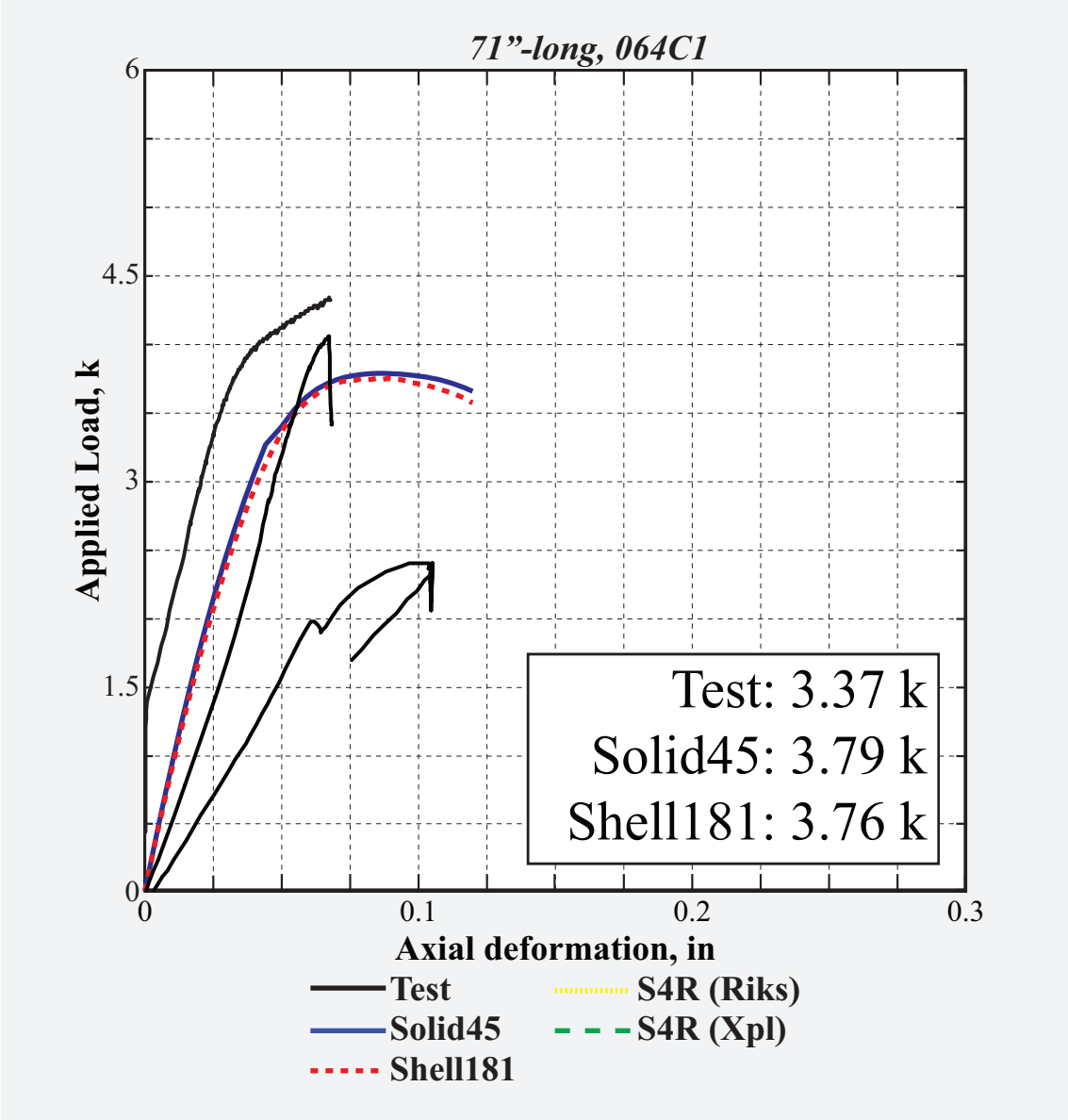


Figure 59: Load vs. deformation history of 71”-long, 0.064”-thick *C1*

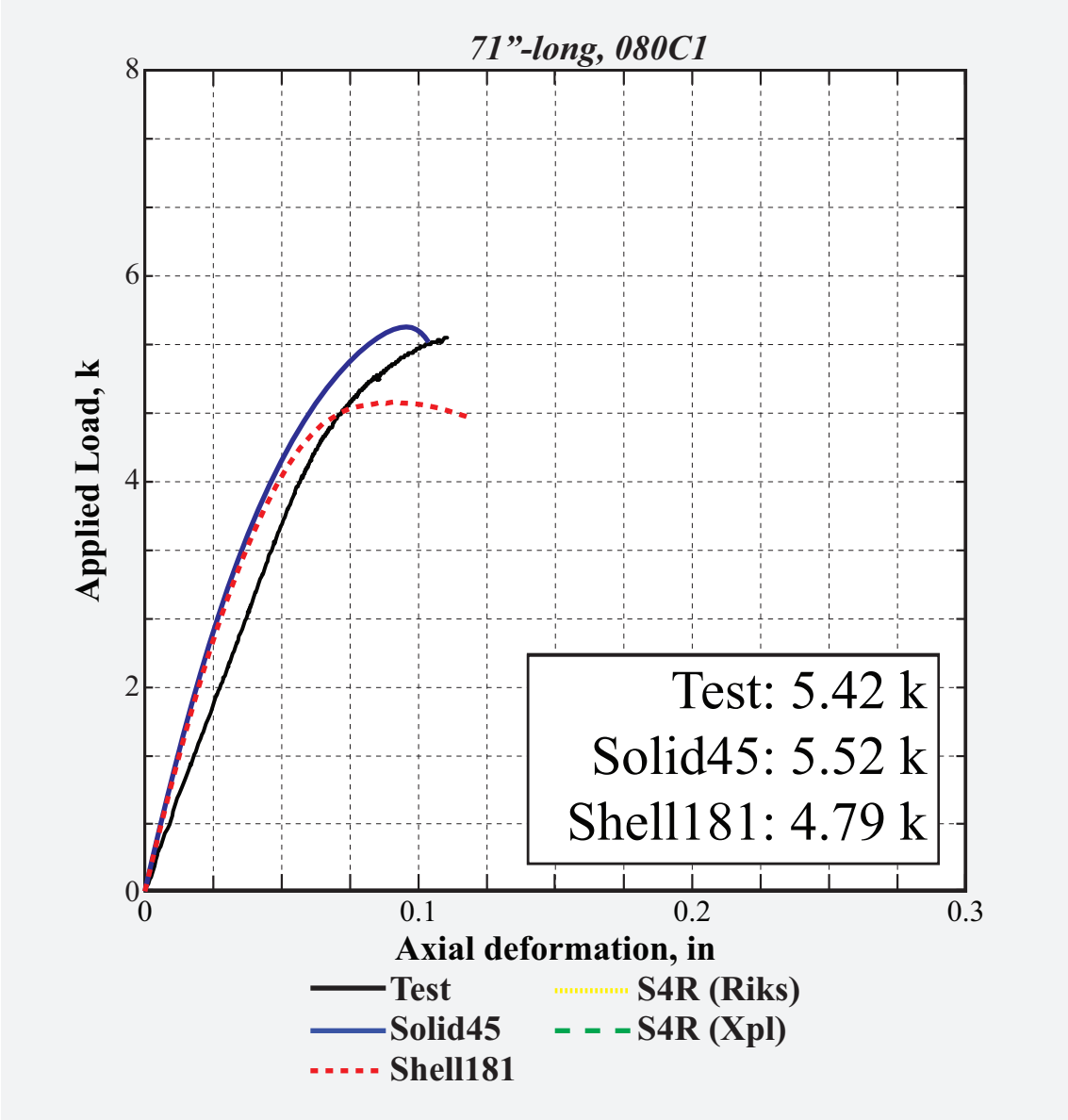


Figure 60: Load vs. deformation history of 71”-long, 0.08”-thick *C1*

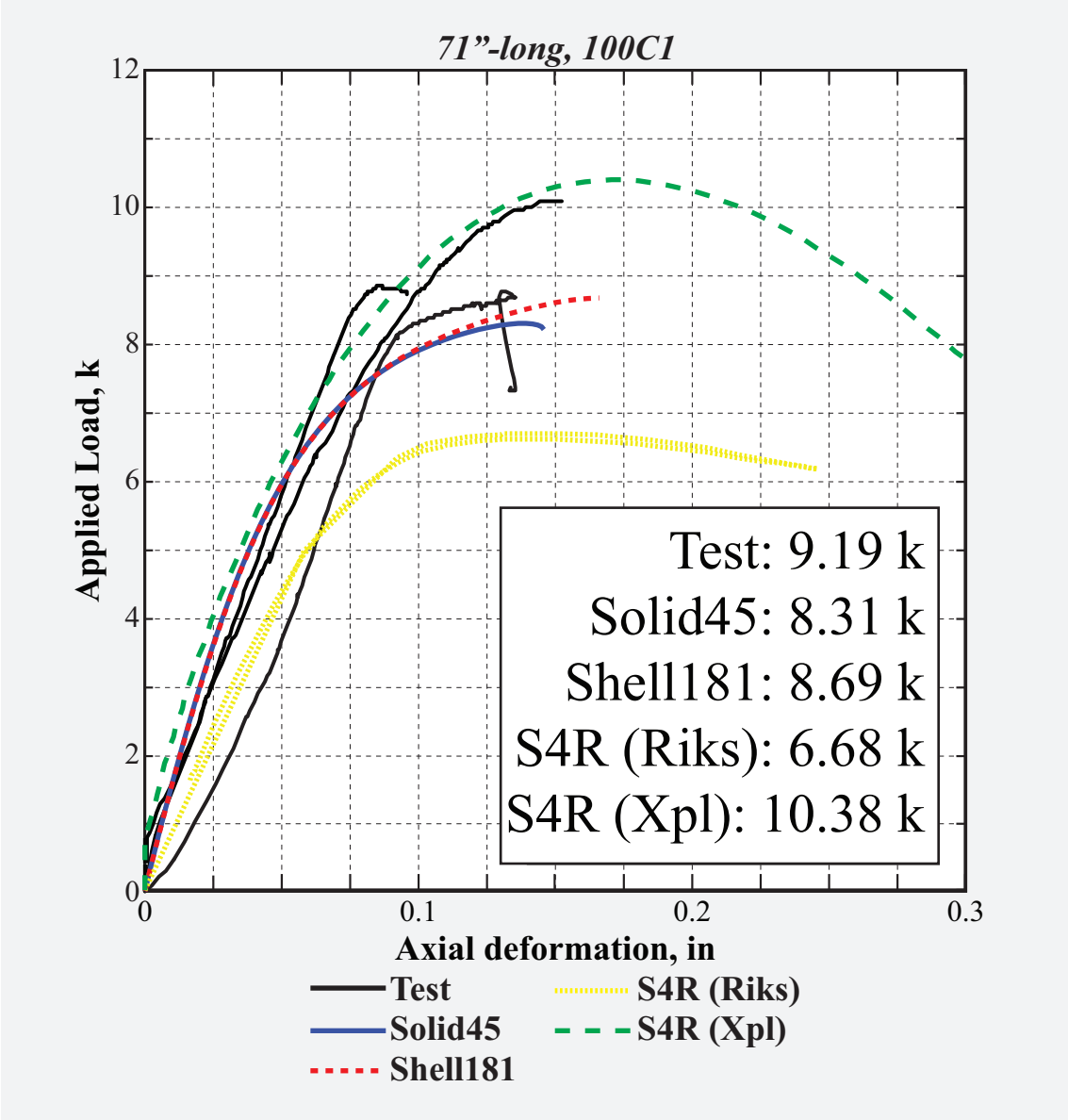


Figure 61: Load vs. deformation history of 71”-long, 0.1”-thick *C1*

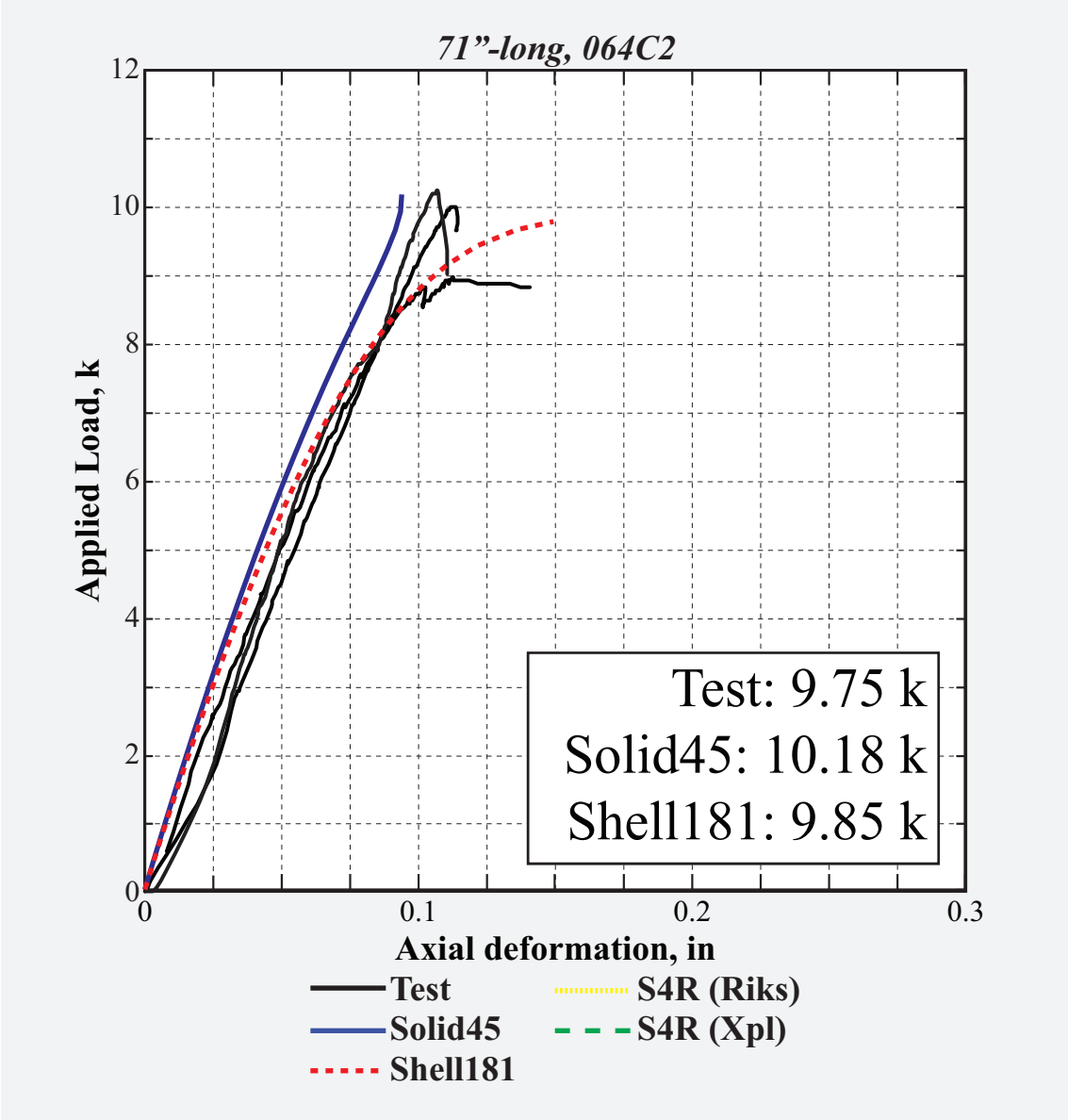


Figure 62: Load vs. deformation history of 71”-long, 0.064”-thick *C2*

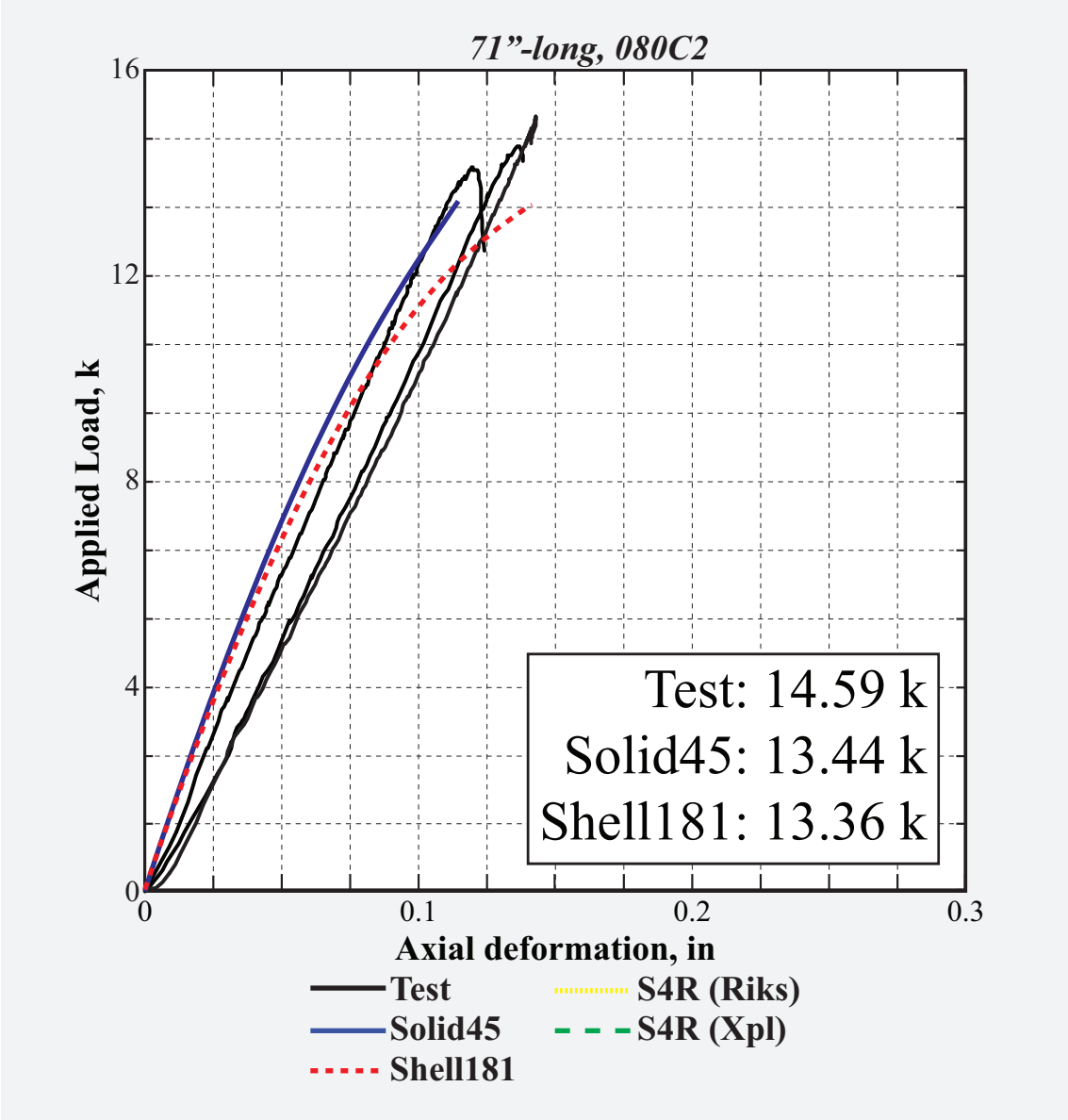


Figure 63: Load vs. deformation history of 71”-long, 0.08”-thick *C2*

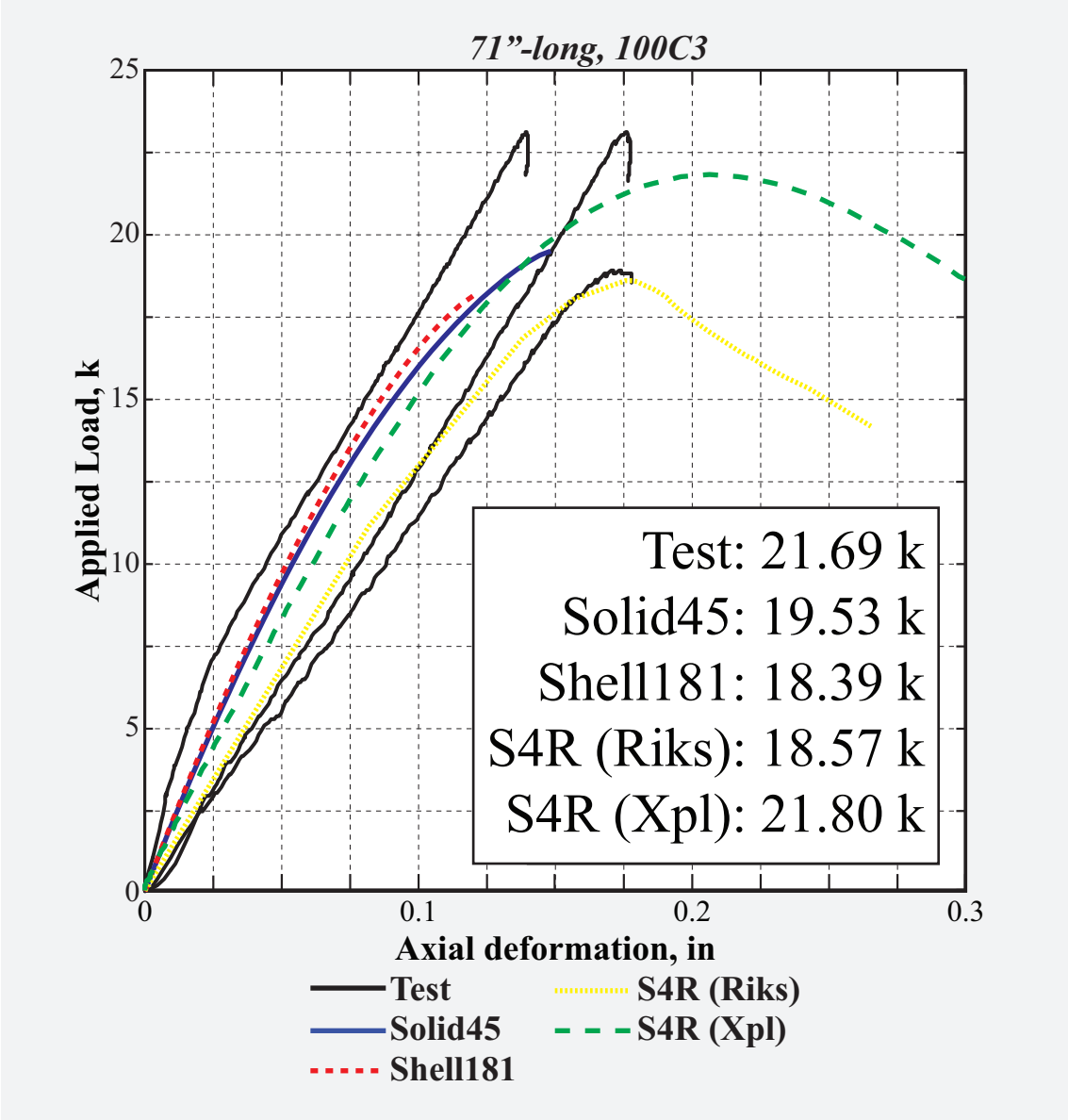


Figure 64: Load vs. deformation history of 71”-long, 0.1”-thick *C2*

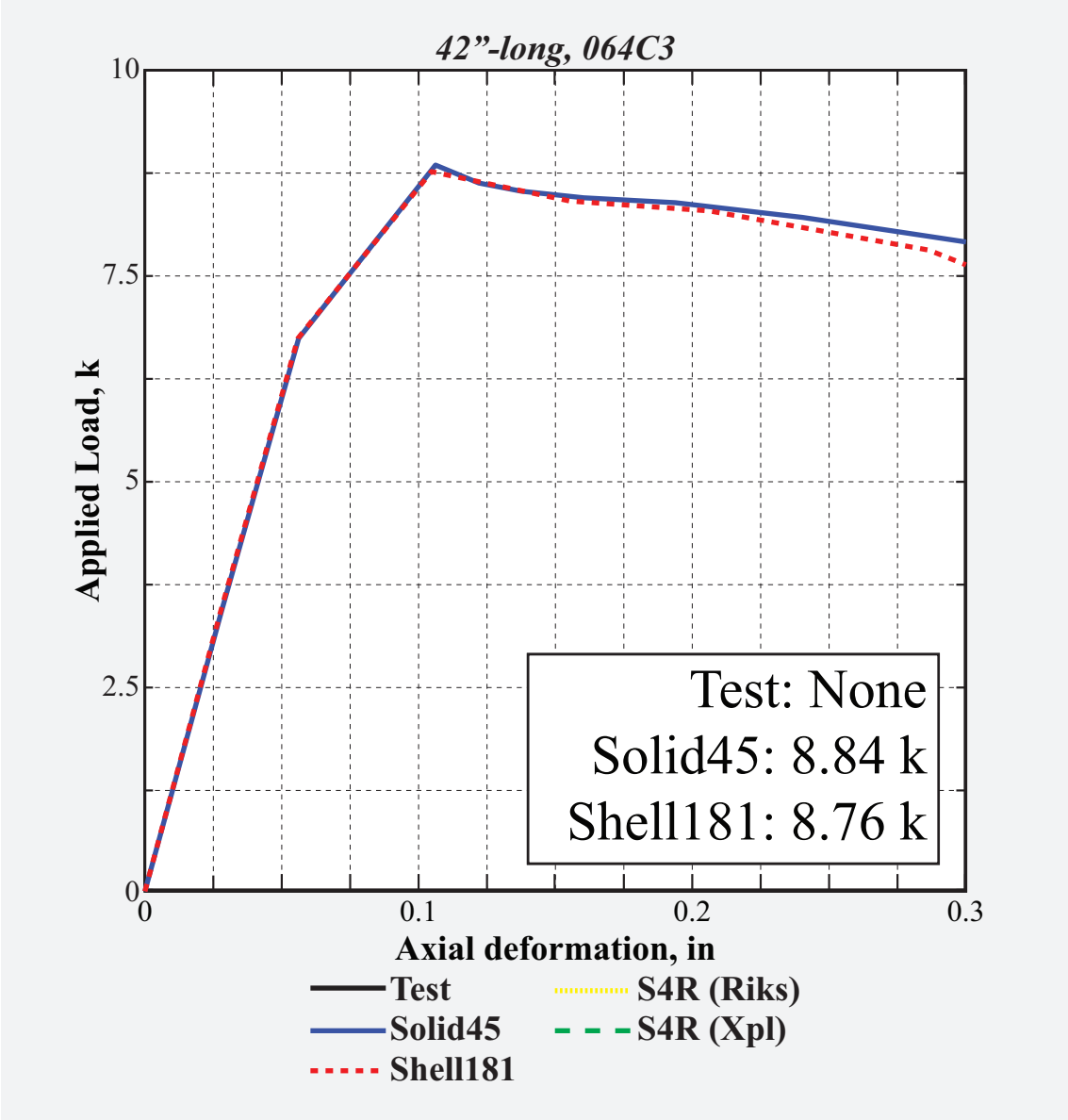


Figure 65: Load vs. deformation history of 42”-long, 0.064”-thick *C3*

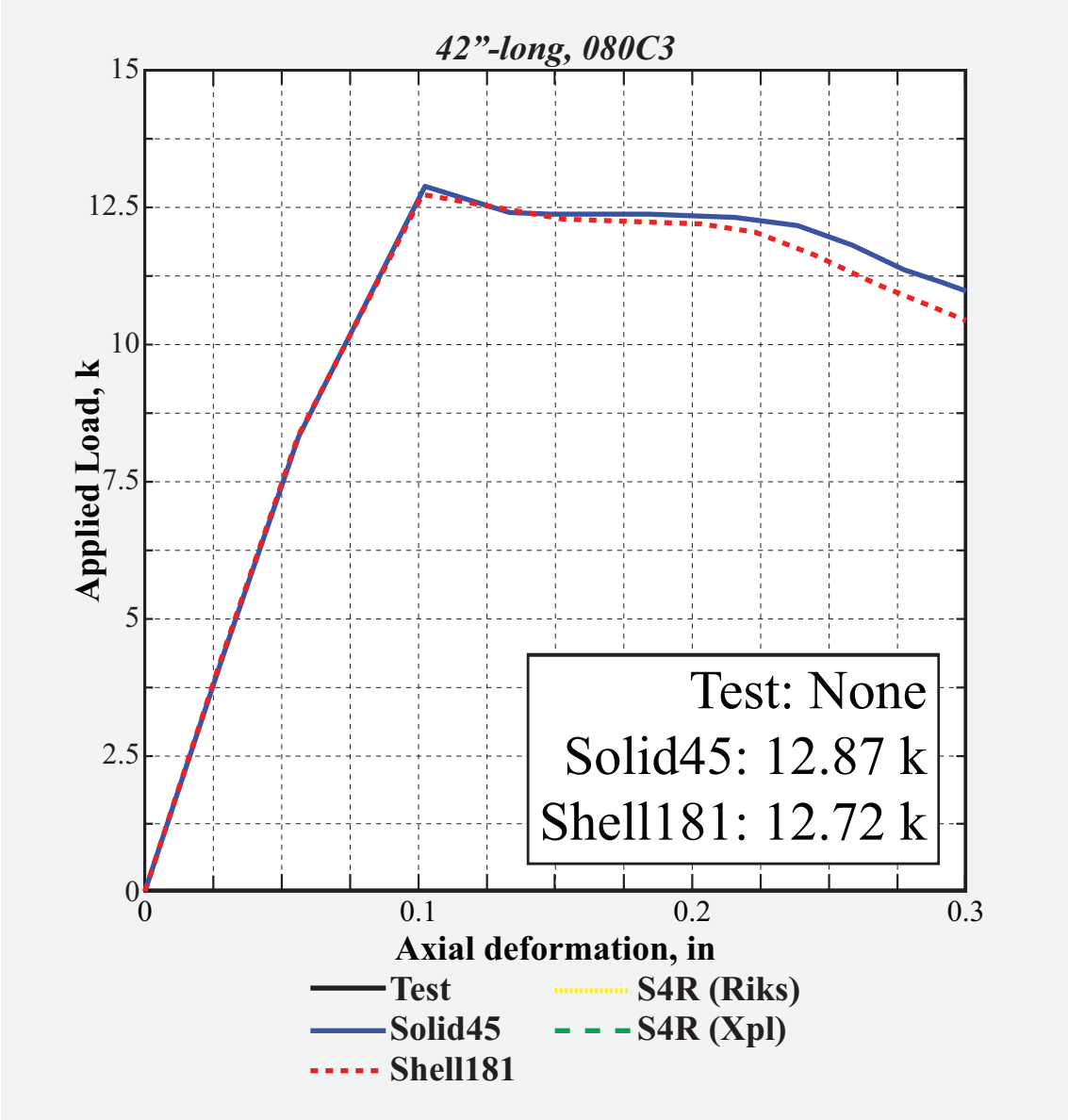


Figure 66: Load vs. deformation history of 42”-long, 0.08”-thick *C3*

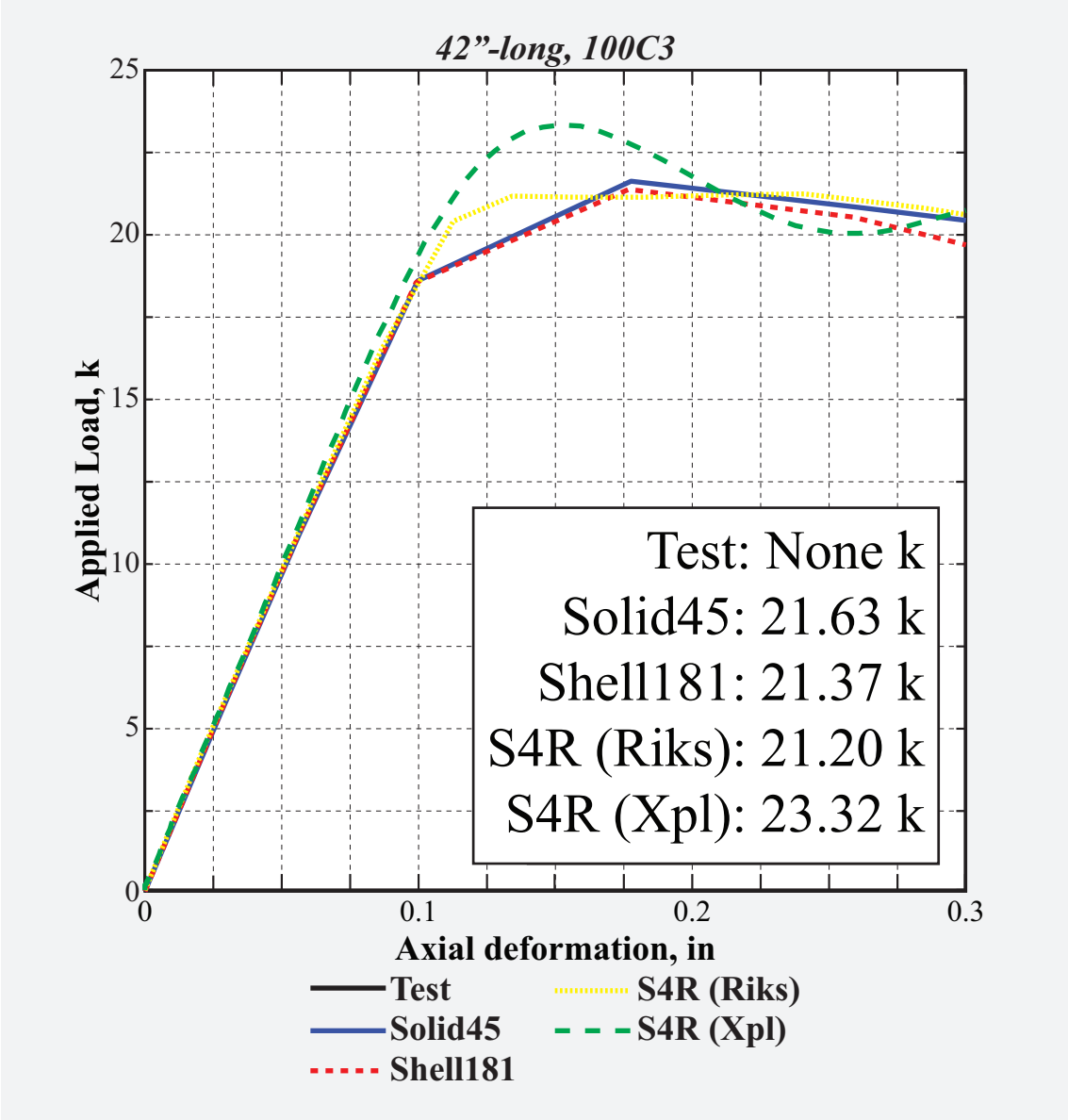


Figure 67: Load vs. deformation history of 42”-long, 0.1”-thick *C3*

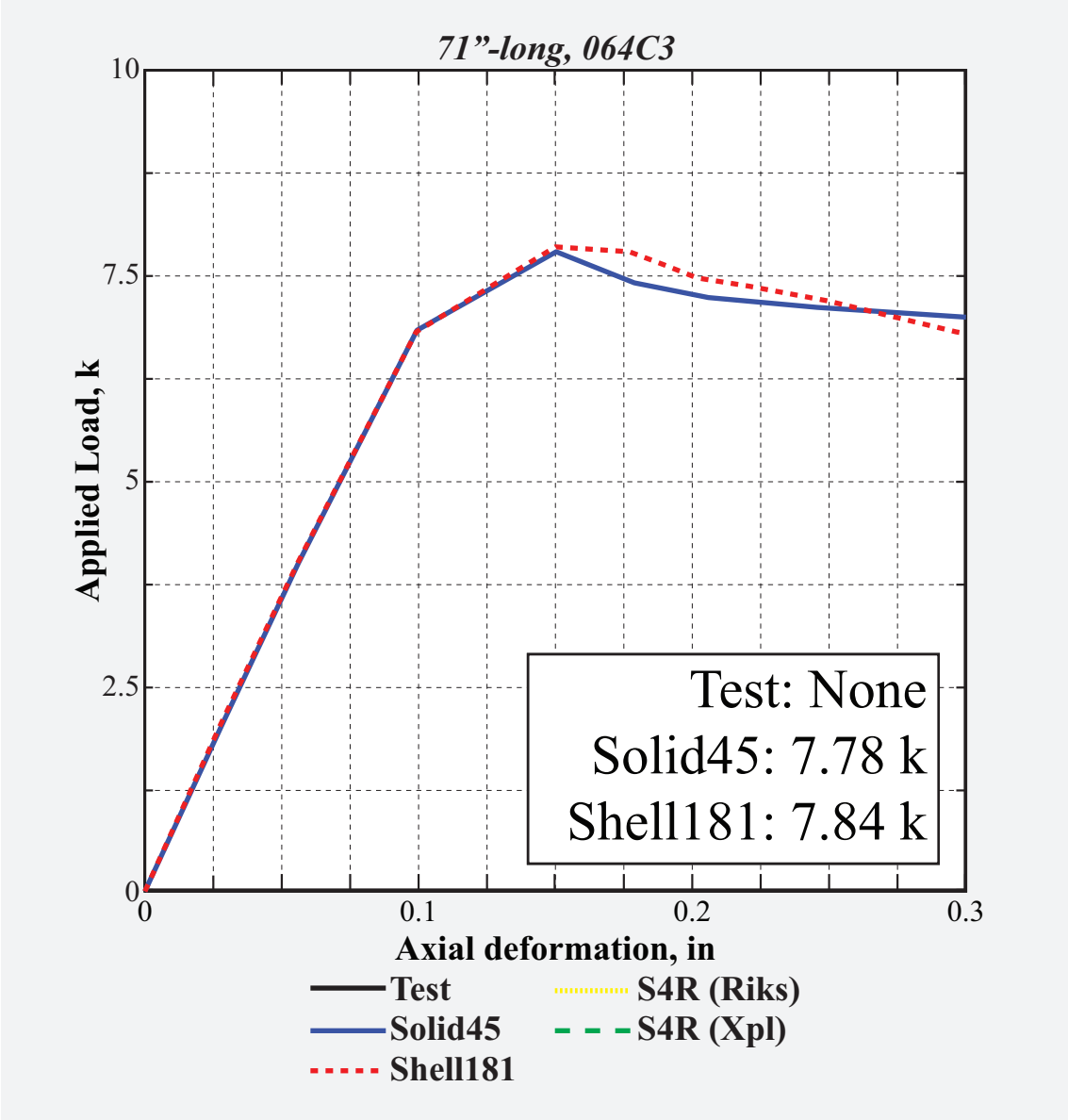


Figure 68: Load vs. deformation history of 71”-long, 0.064”-thick *C3*

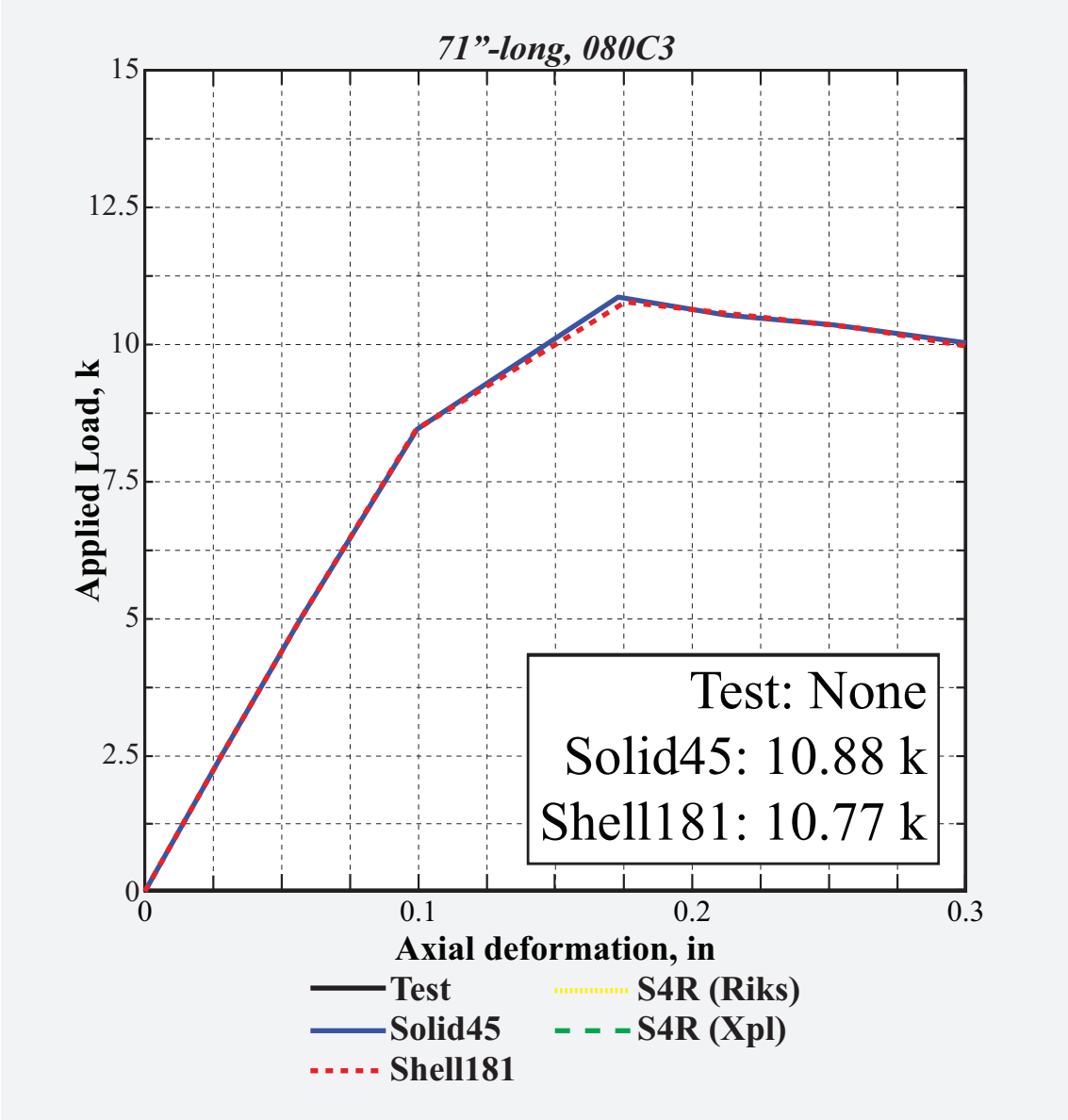


Figure 69: Load vs. deformation history of 71”-long, 0.08”-thick *C3*

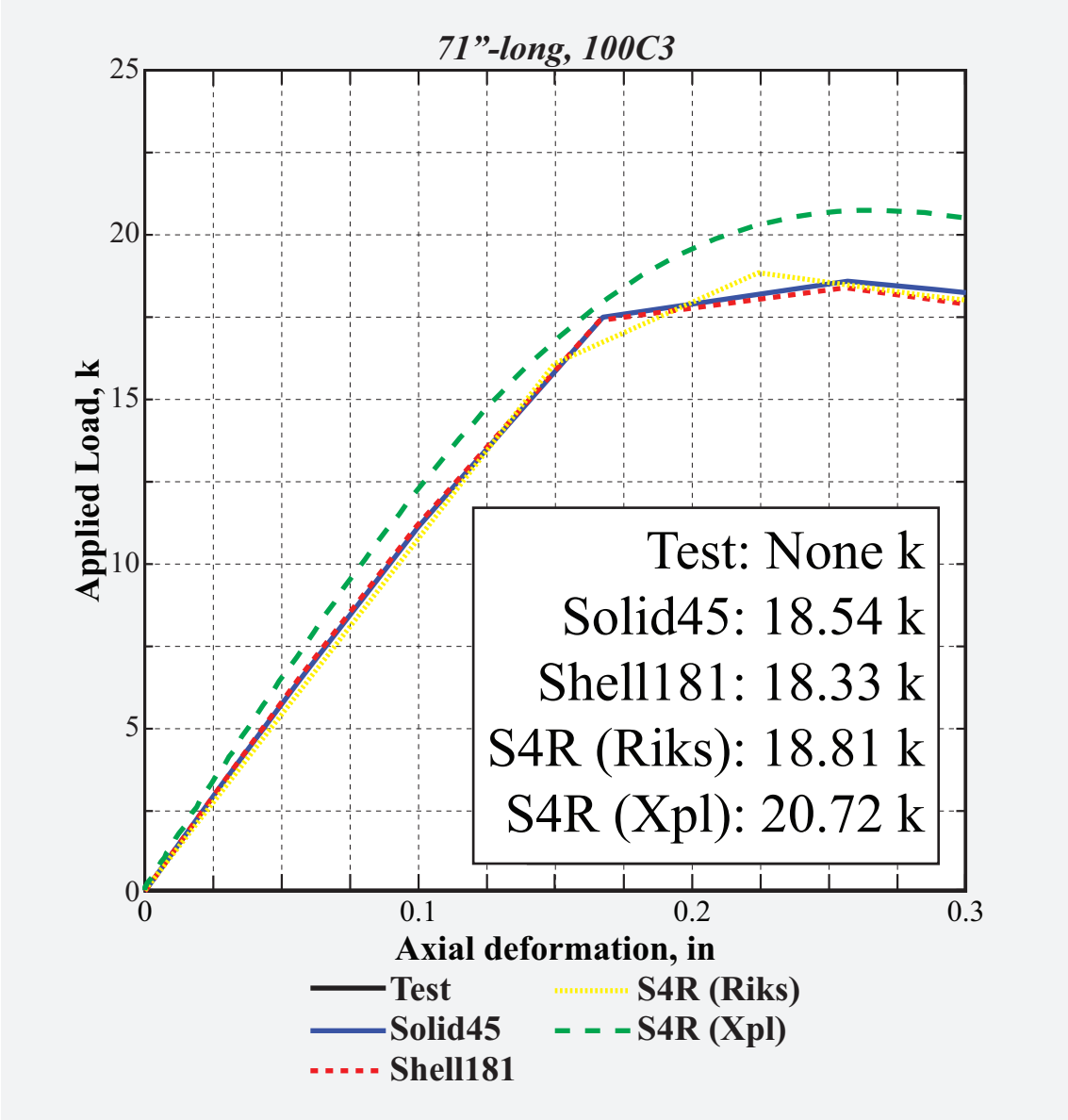


Figure 70: Load vs. deformation history of 71”-long, 0.1”-thick *C3*

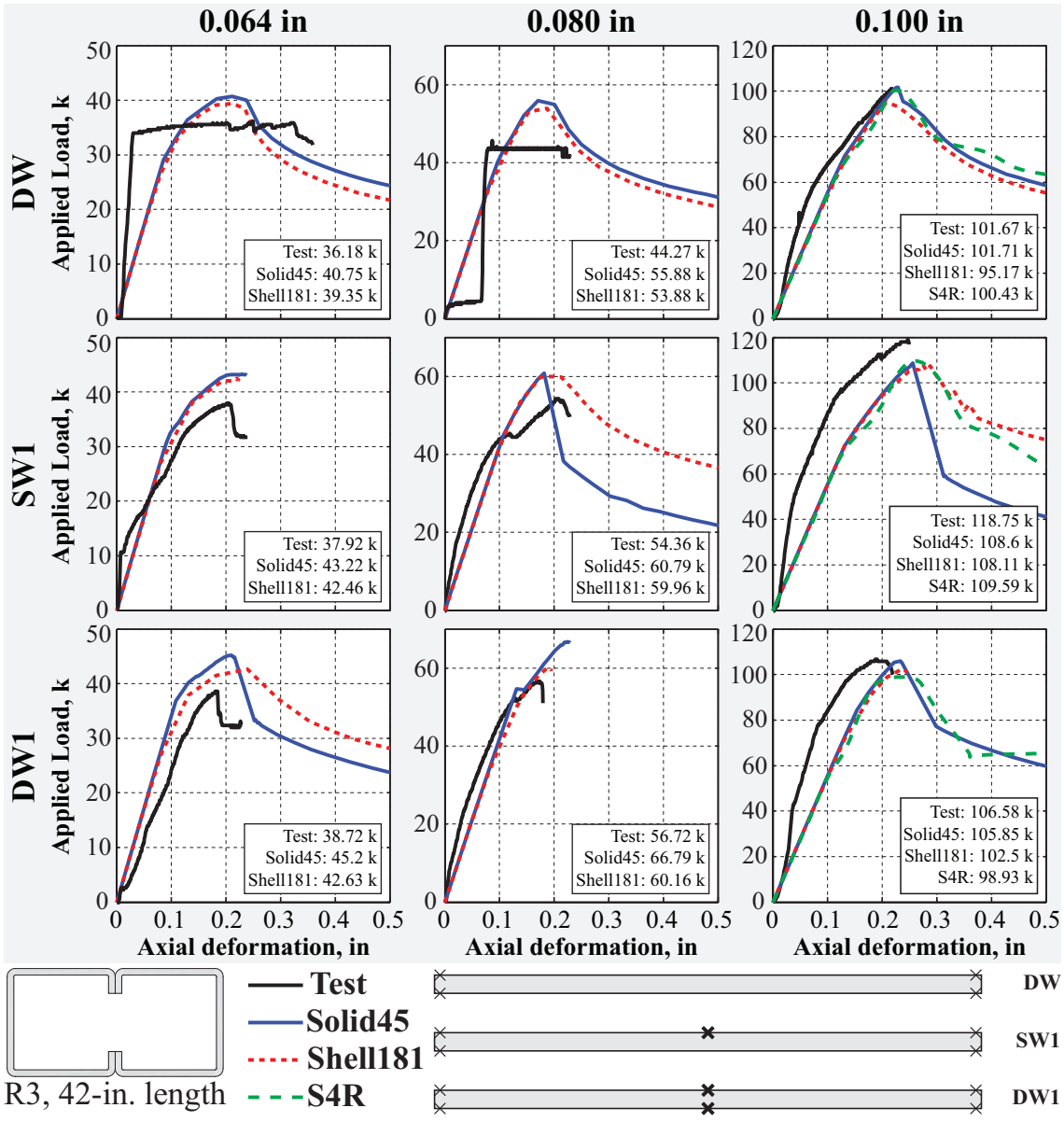


Figure 71: Overview of load vs. deformation history of 42”-long *R3*-sections presented in Figs. 72-80.

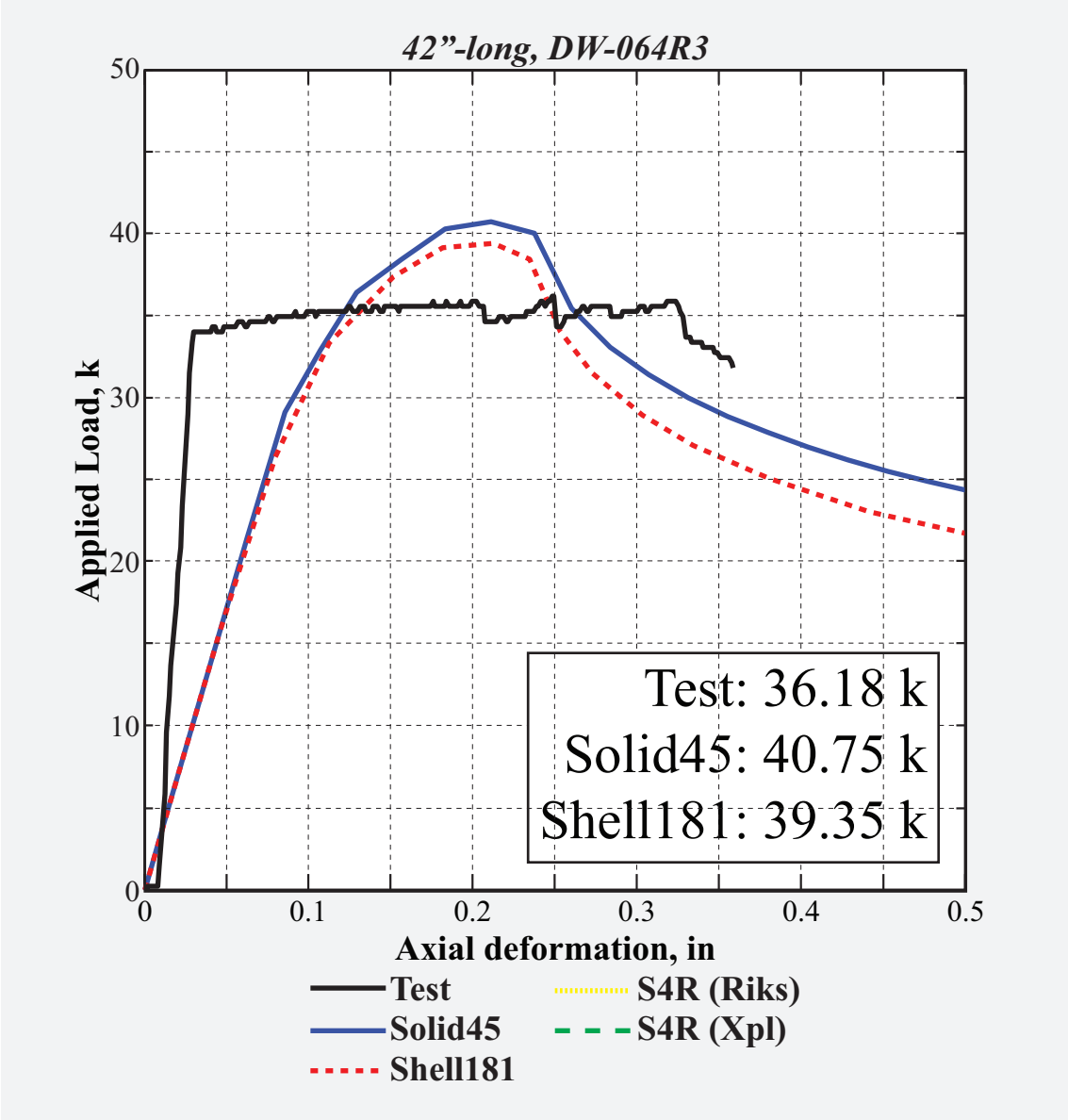


Figure 72: Load vs. deformation history of 42”-long, 0.064”-thick *DW-R3*

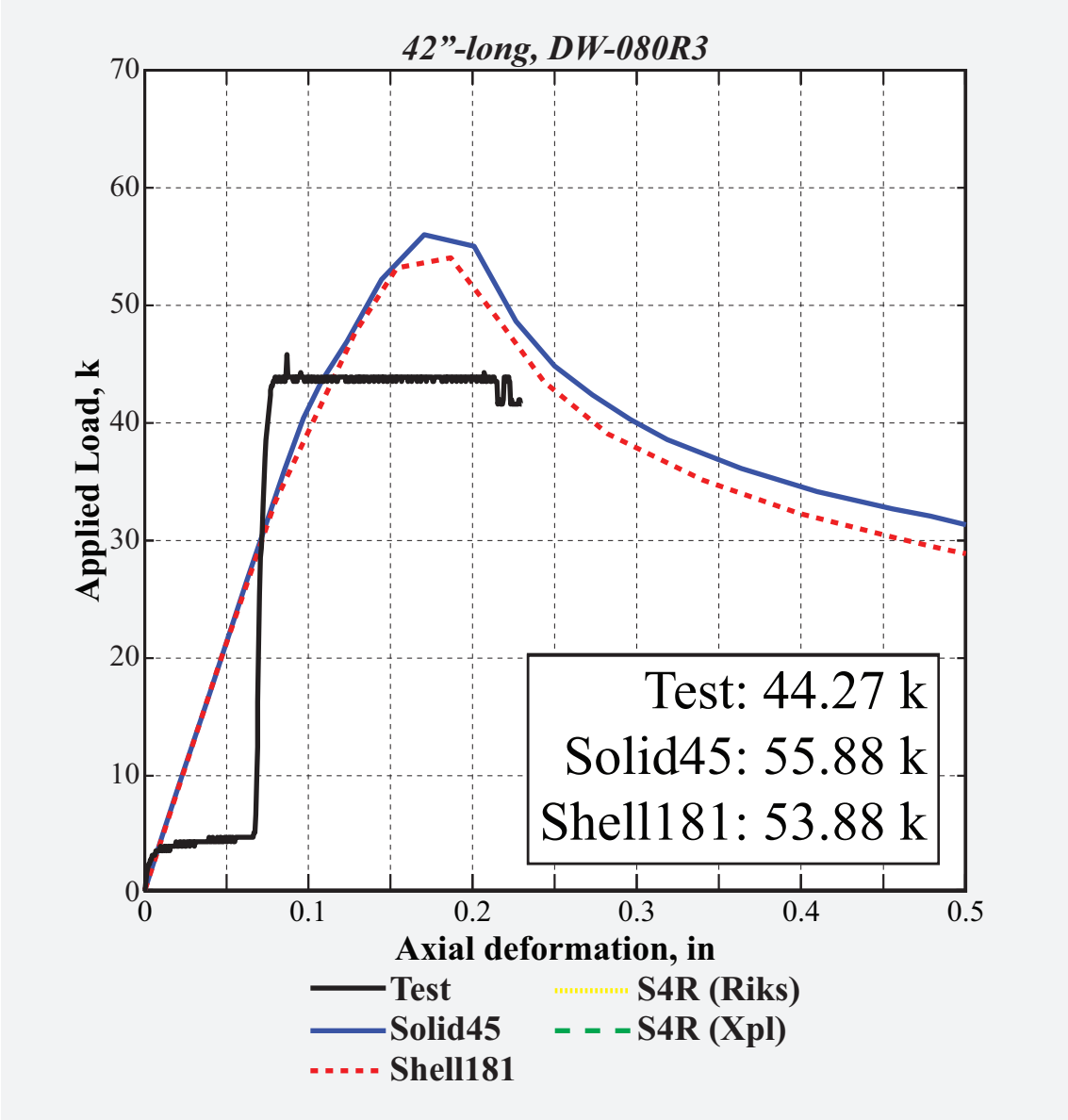


Figure 73: Load vs. deformation history of 42”-long, 0.08”-thick *DW-R3*

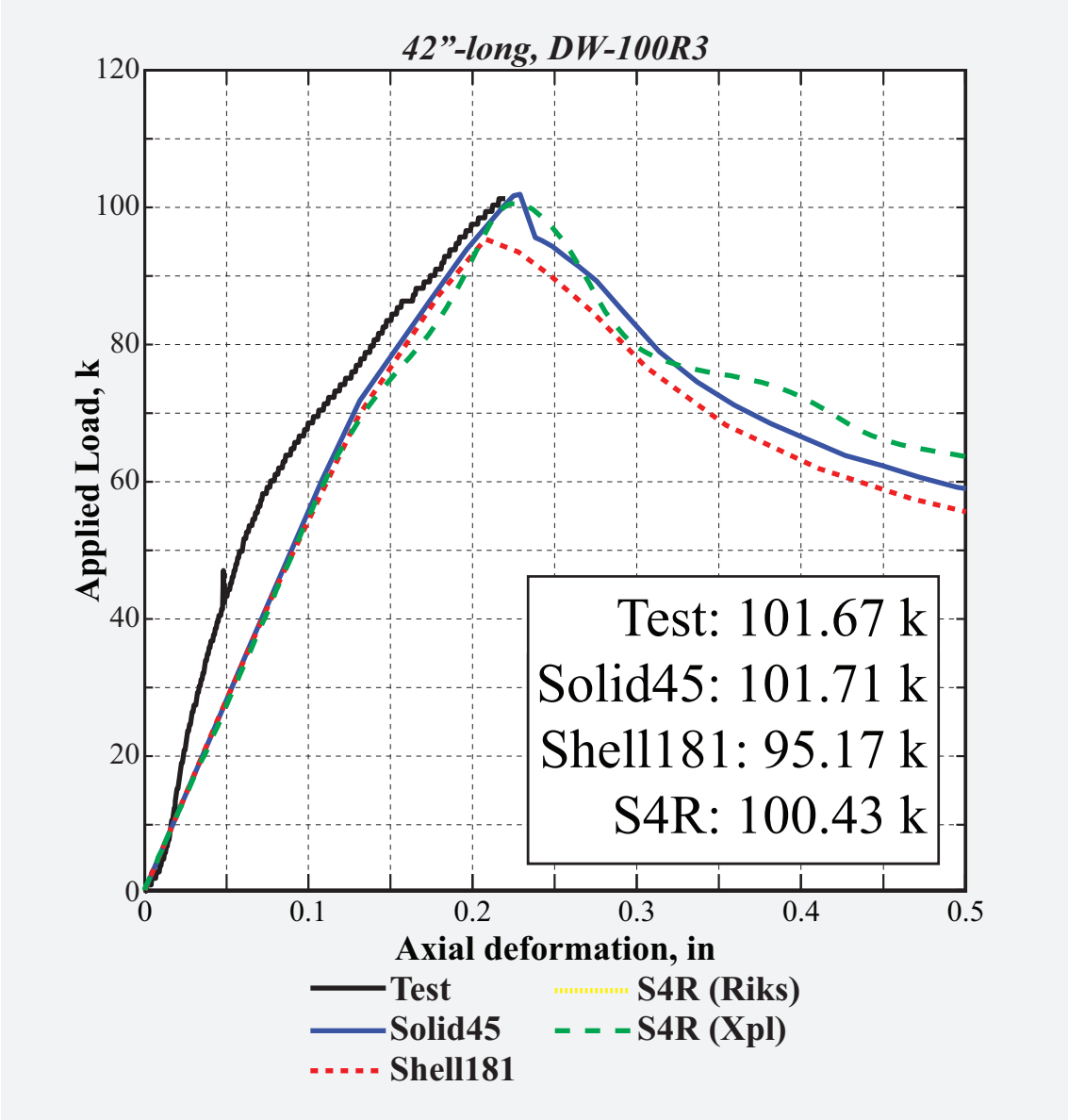


Figure 74: Load vs. deformation history of 42”-long, 0.1”-thick *DW-R3*

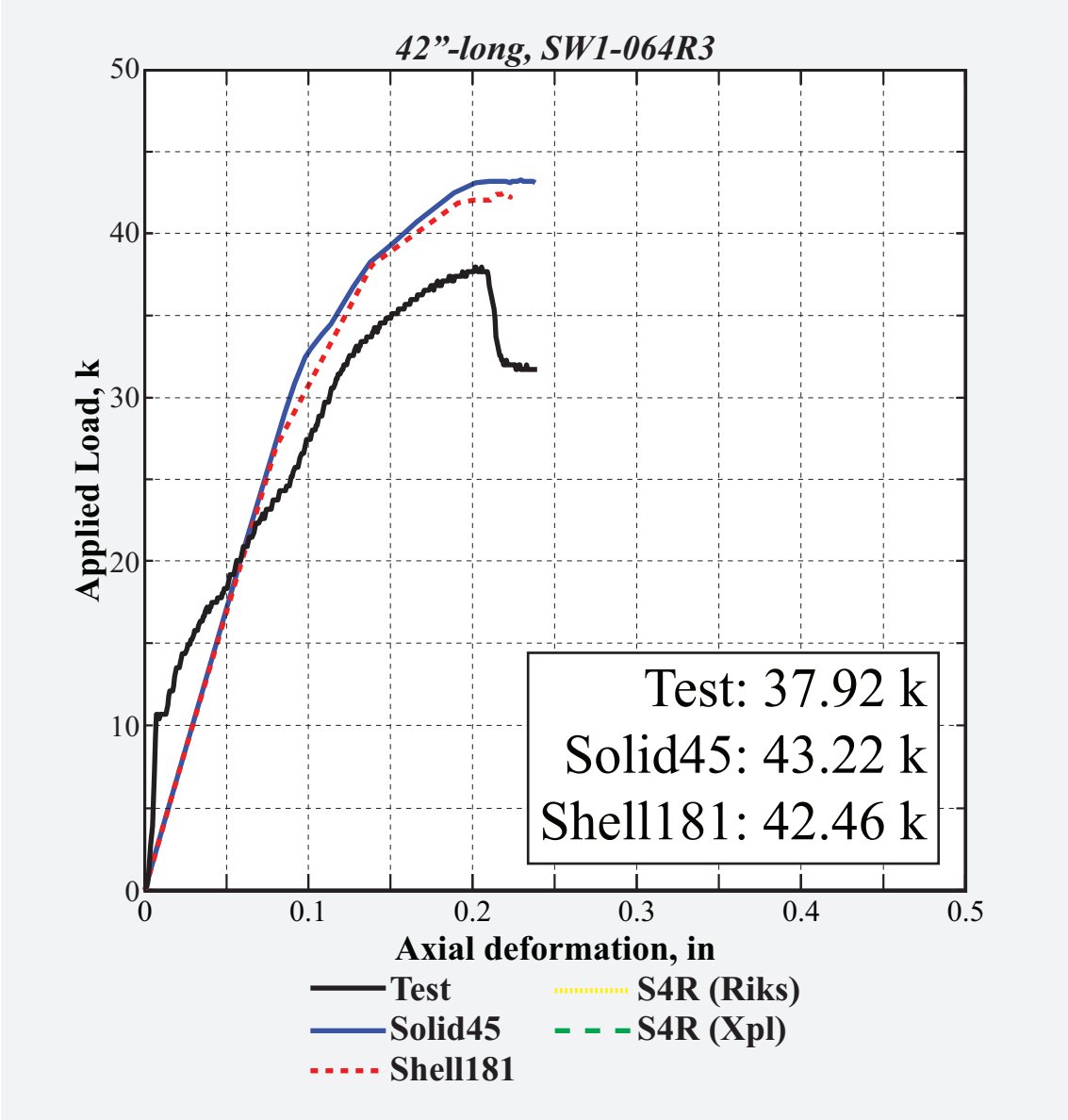


Figure 75: Load vs. deformation history of 42”-long, 0.064”-thick *SW1-R3*

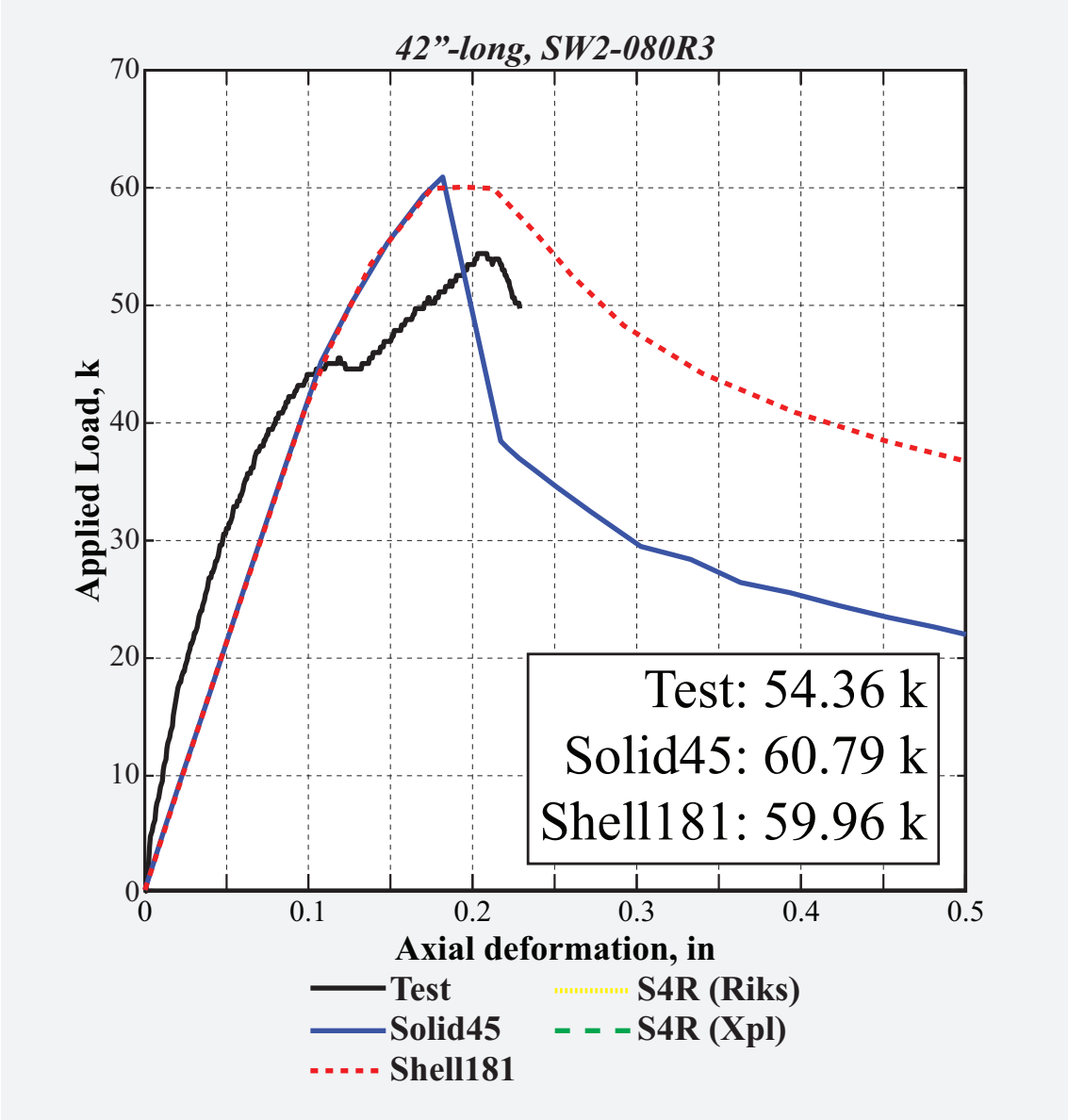


Figure 76: Load vs. deformation history of 42”-long, 0.08”-thick *SW1-R3*

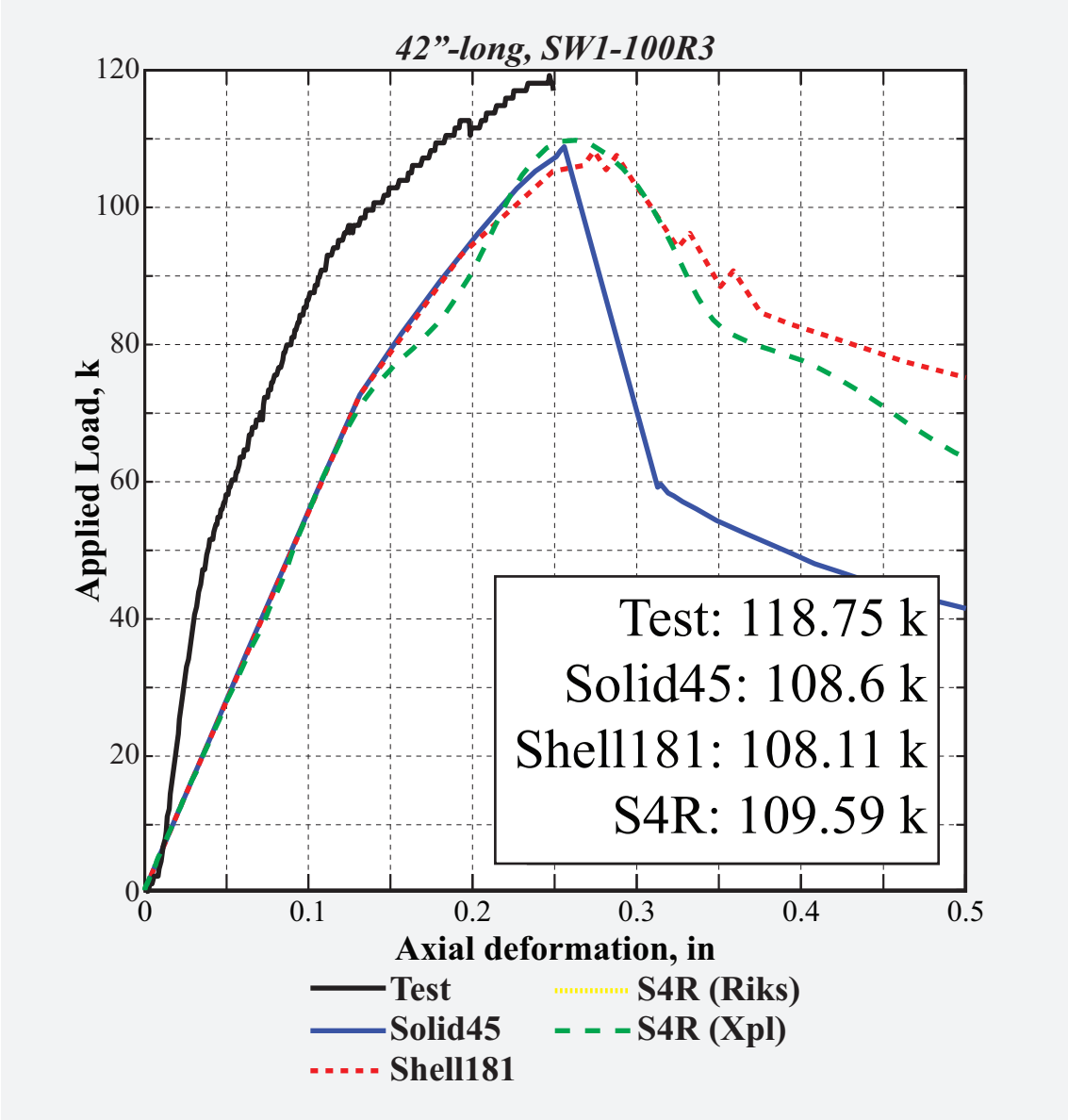


Figure 77: Load vs. deformation history of 42”-long, 0.1”-thick *SW1-R3*

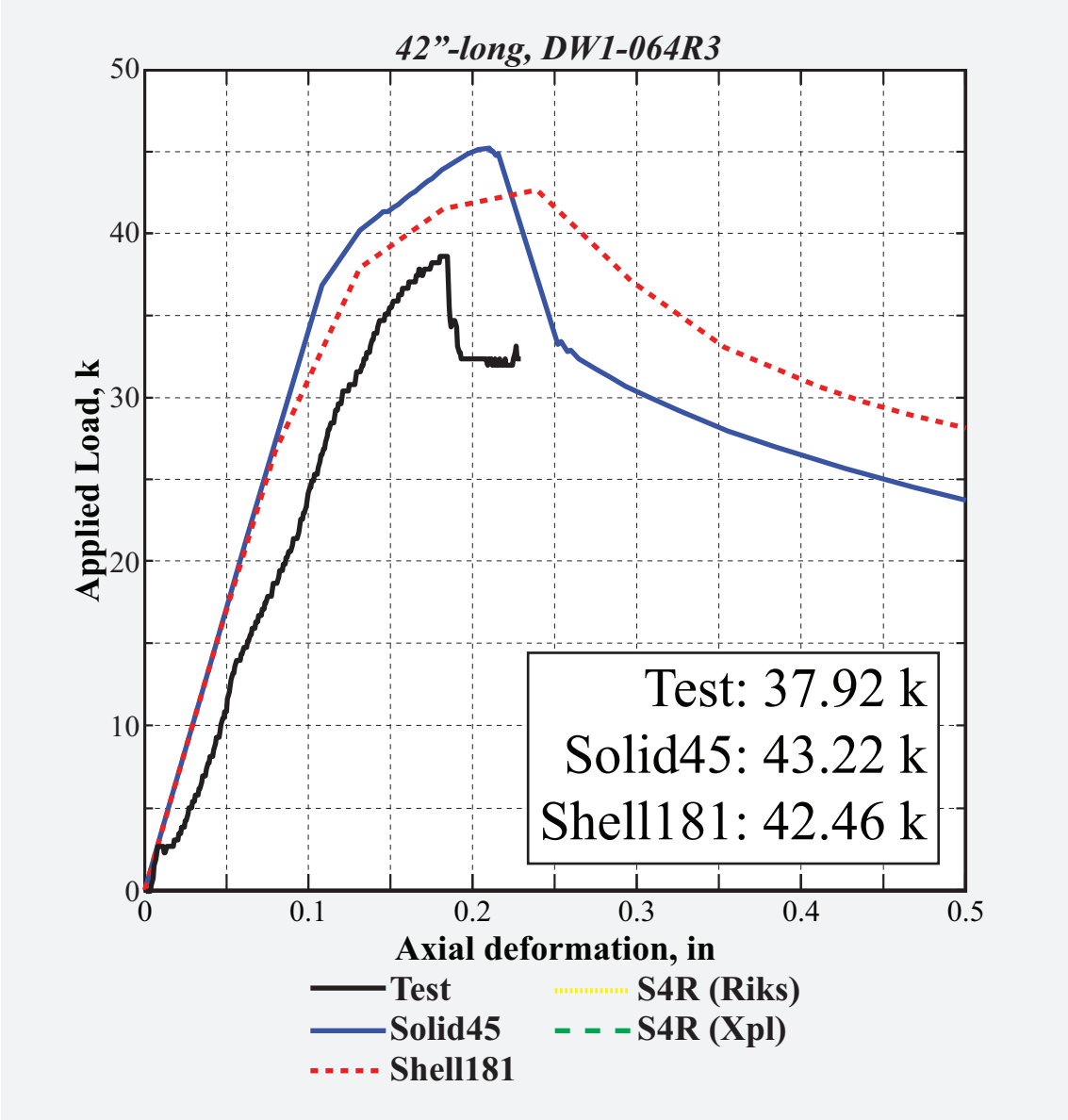


Figure 78: Load vs. deformation history of 42”-long, 0.064”-thick *DW1-R3*

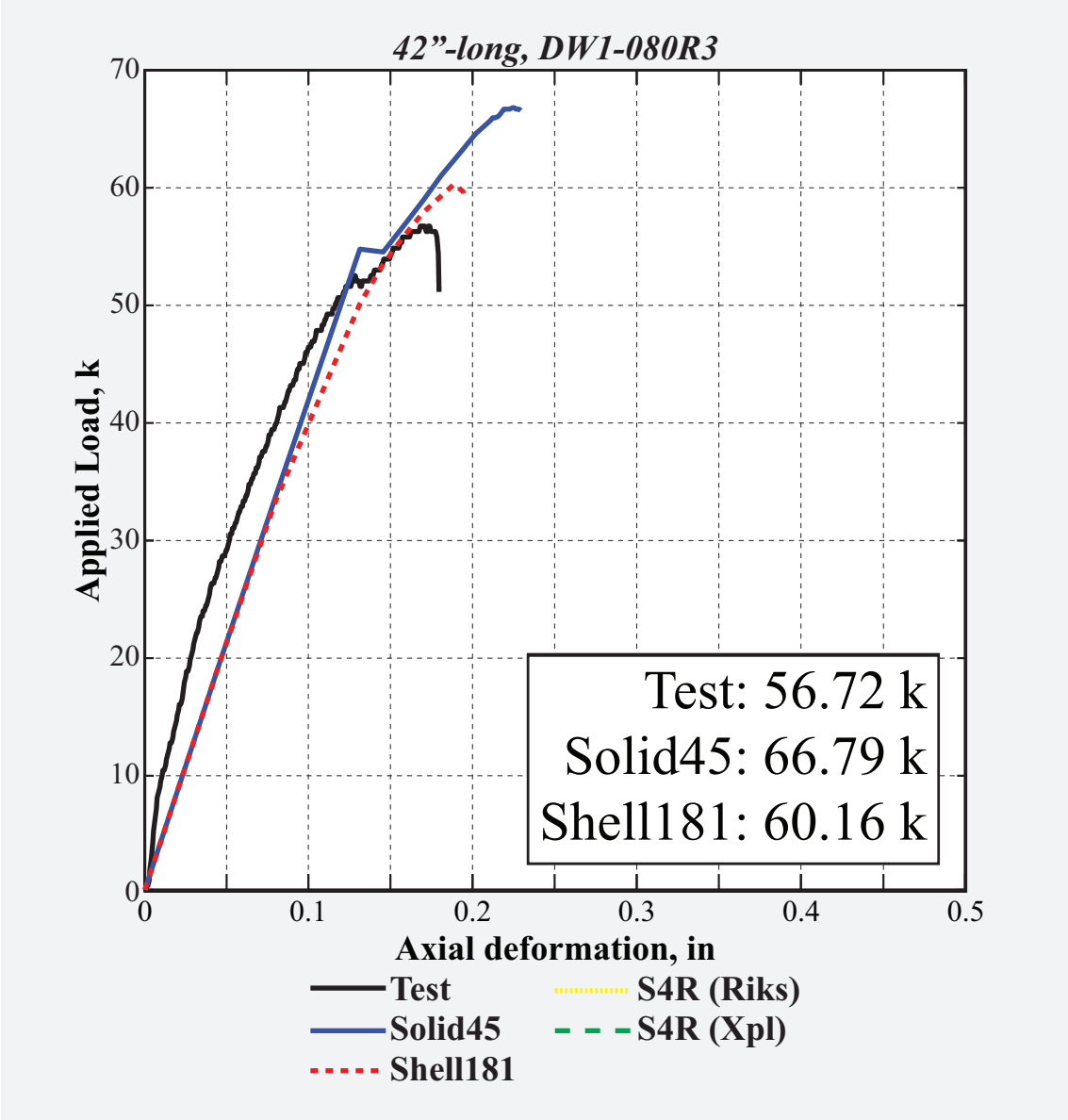


Figure 79: Load vs. deformation history of 42”-long, 0.08”-thick *DW1-R3*

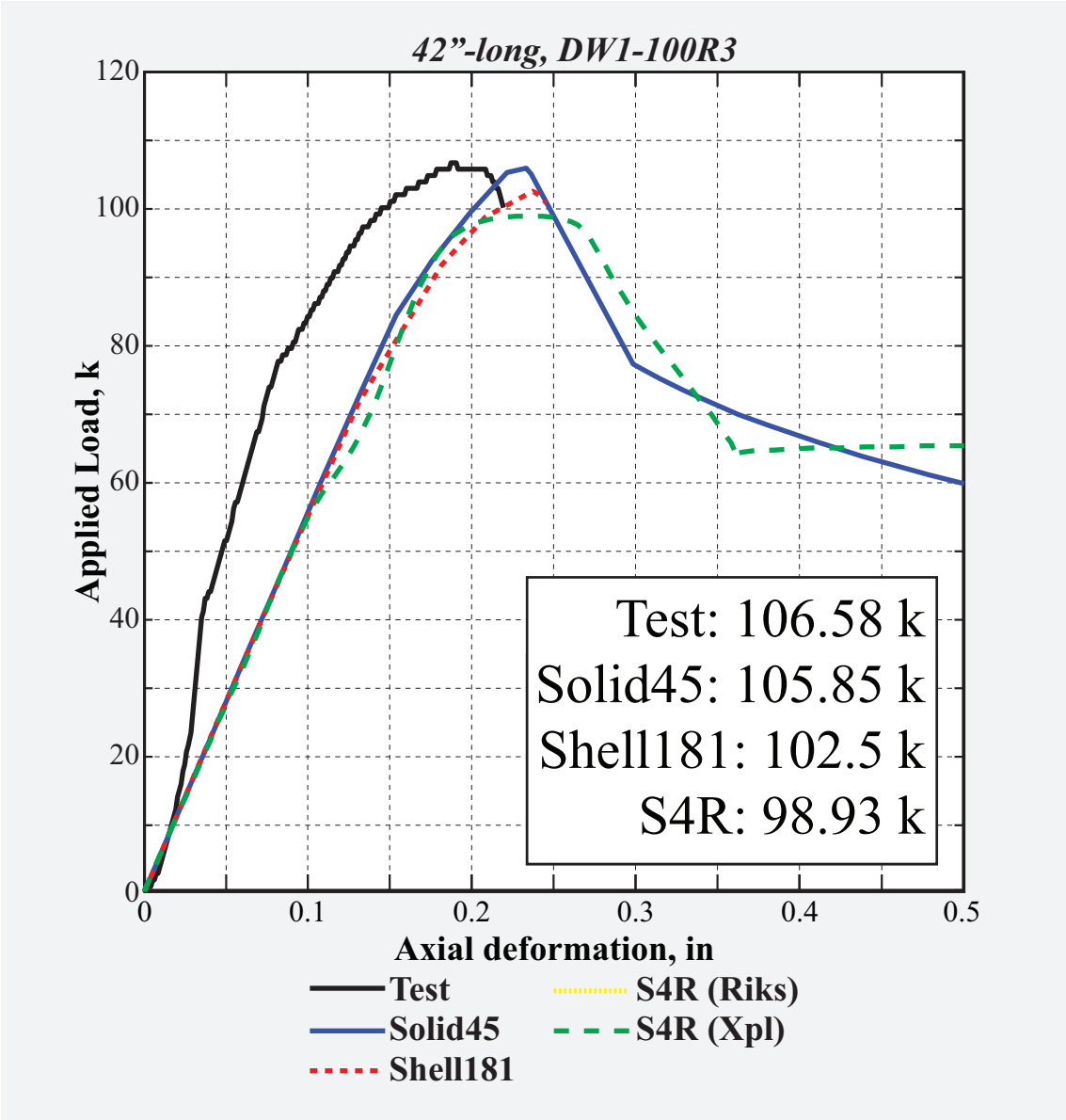


Figure 80: Load vs. deformation history of 42”-long, 0.1”-thick *DW1-R3*

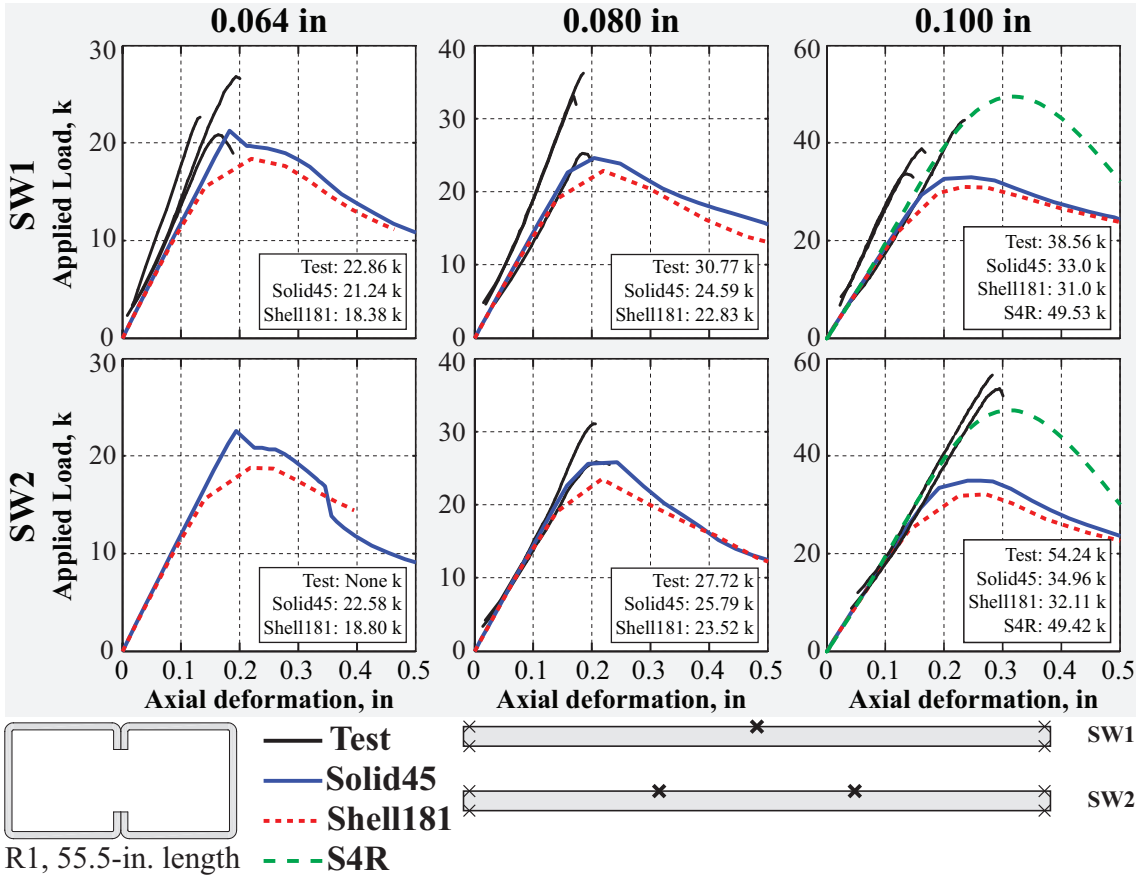


Figure 81: Overview of load vs. deformation history of 55.5”-long, single-sided *R1*-sections presented in Figs. 82-87.

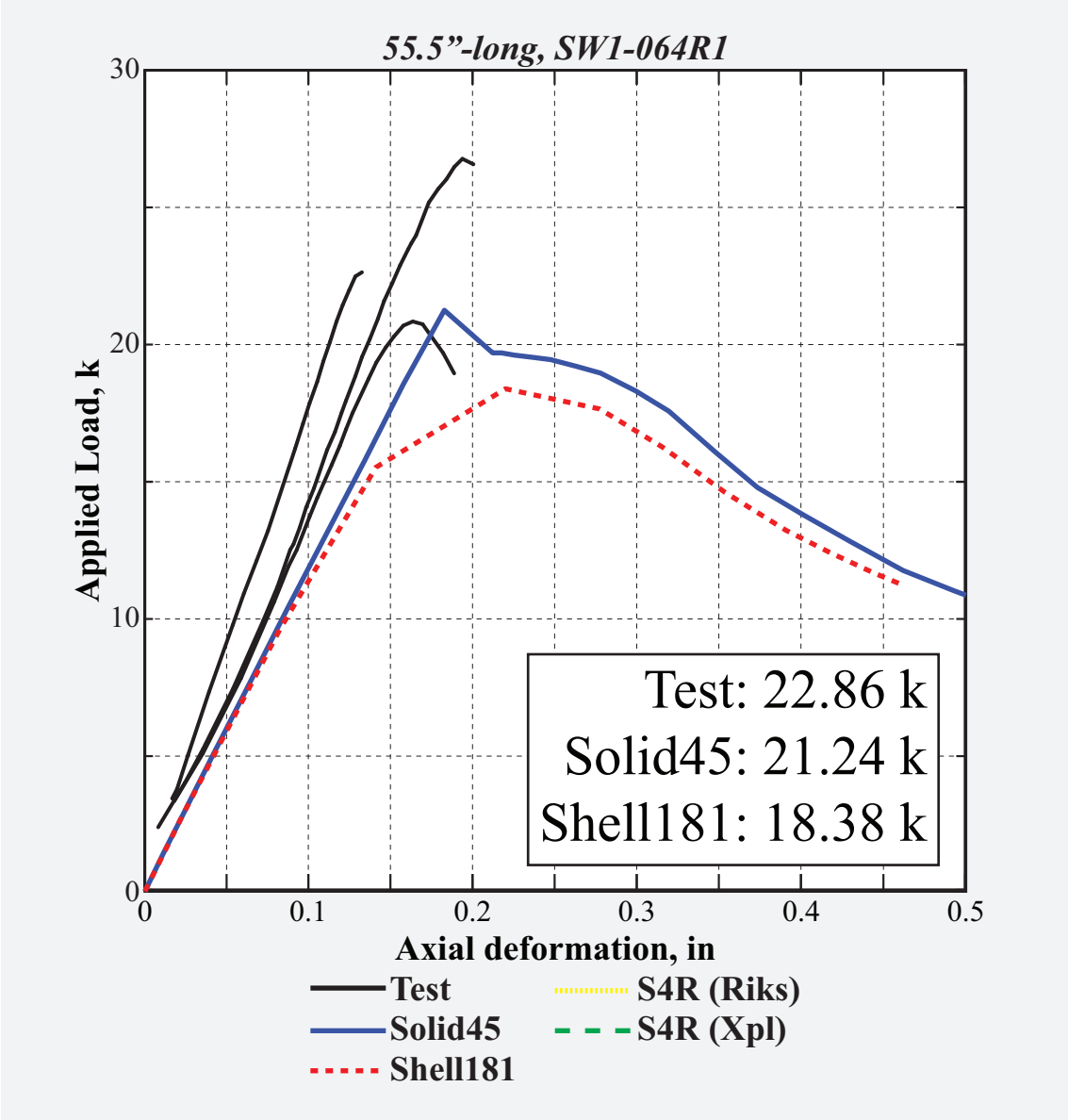


Figure 82: Load vs. deformation history of 55.5”-long, 0.064”-thick *SW1-R1*.

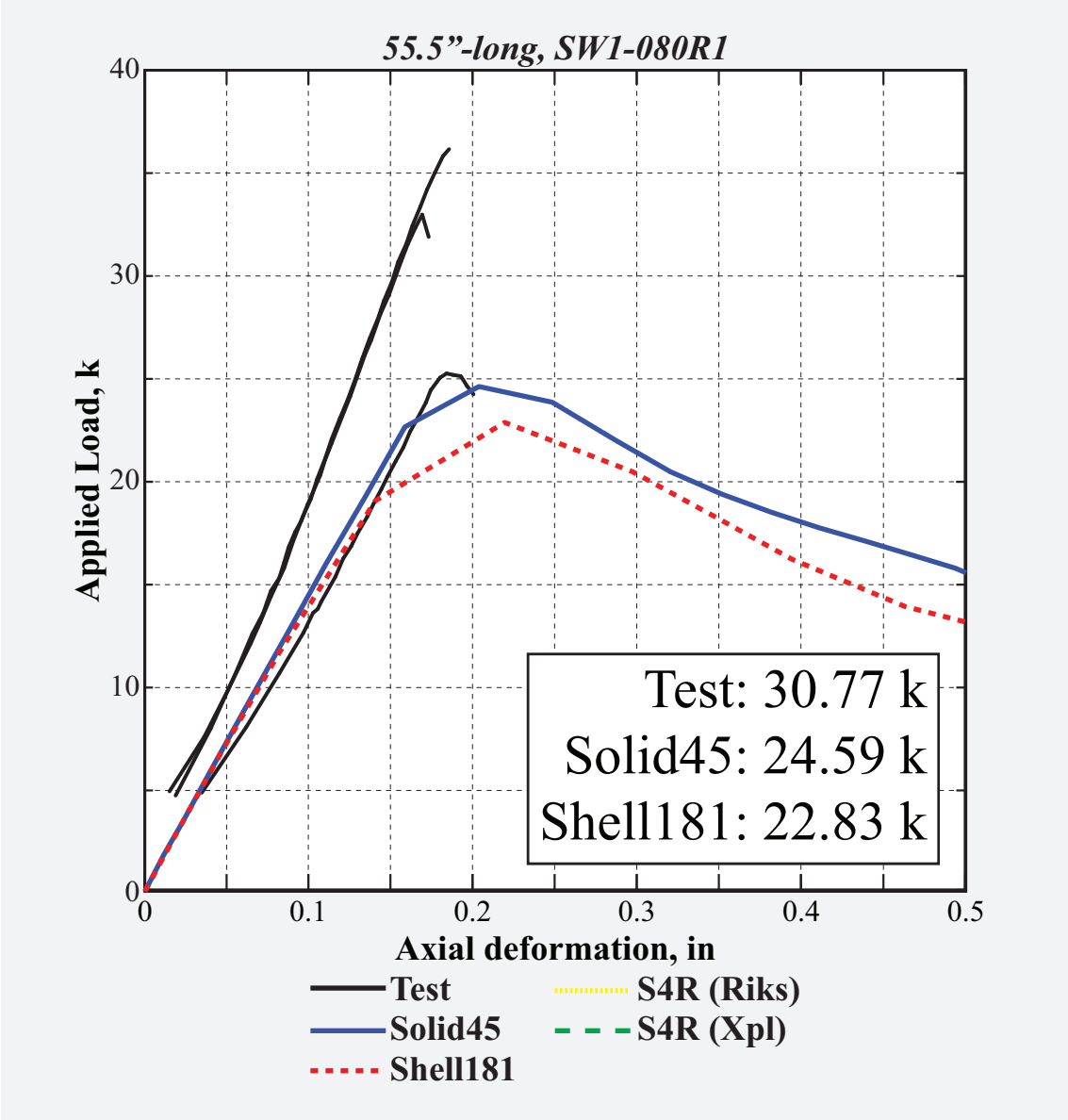


Figure 83: Load vs. deformation history of 55.5”-long, 0.08”-thick *SW1-R1*.

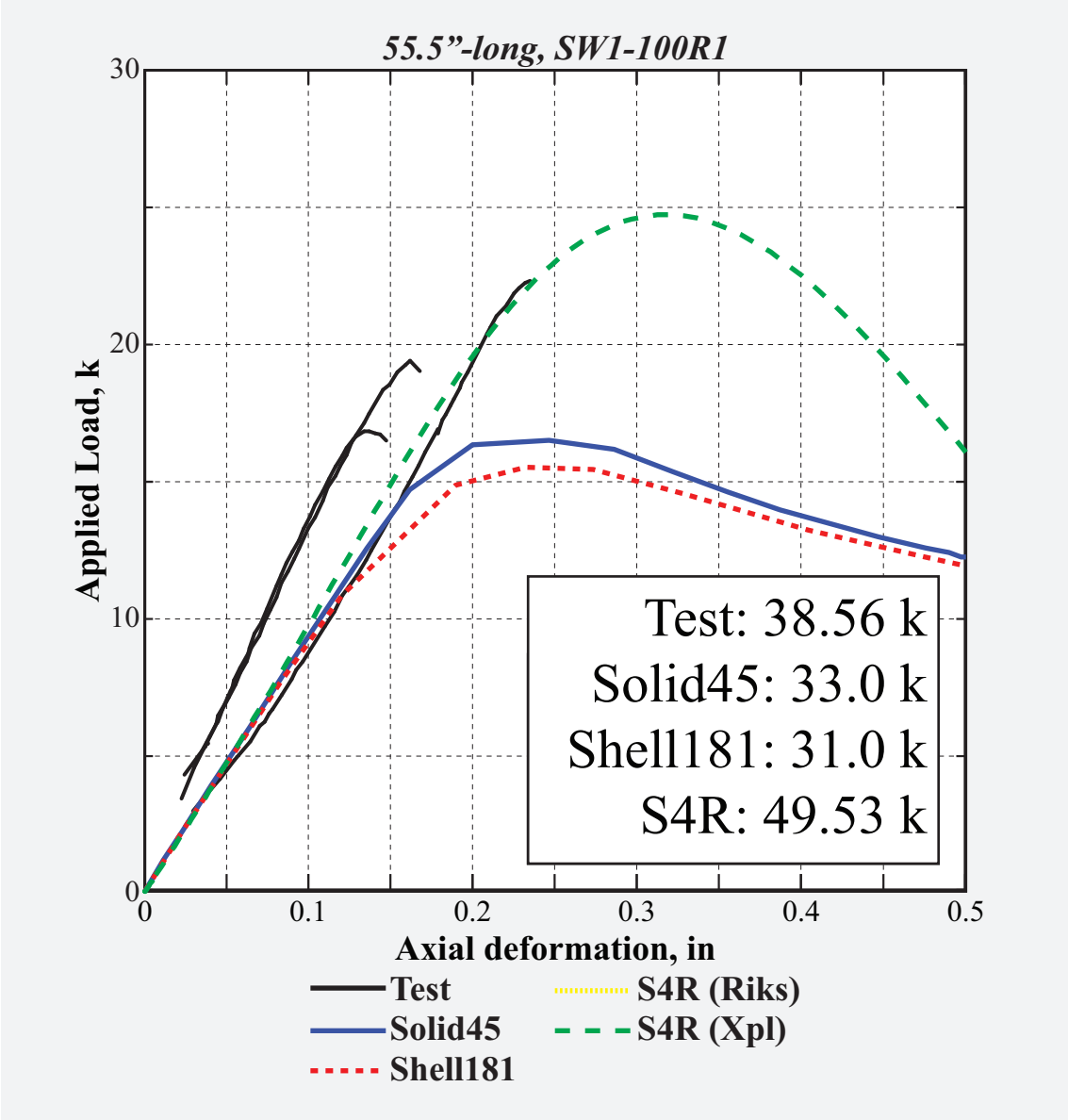


Figure 84: Load vs. deformation history of 55.5”-long, 0.1”-thick *SW1-R1*.

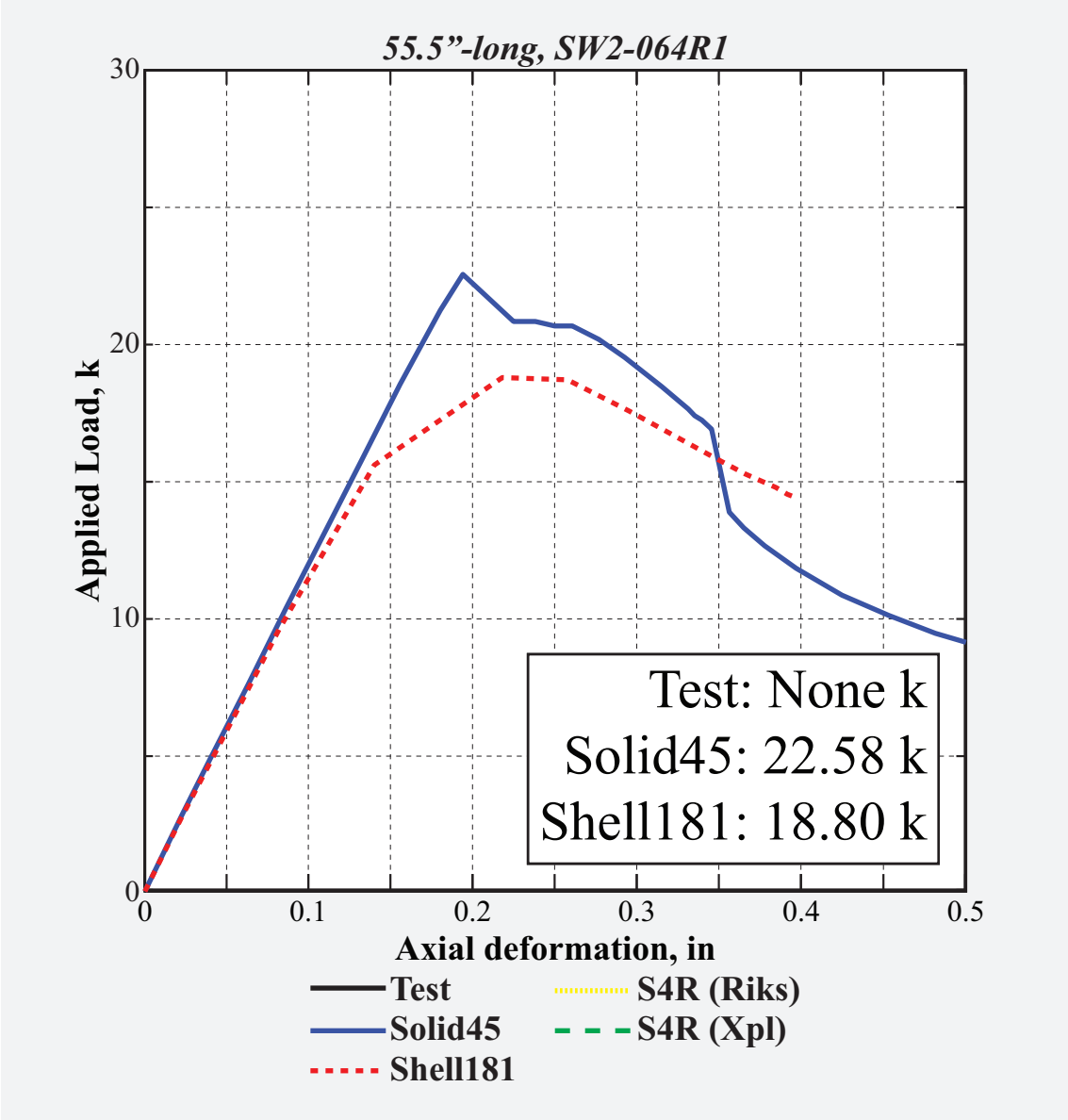


Figure 85: Load vs. deformation history of 55.5”-long, 0.064”-thick *SW2-R1*.

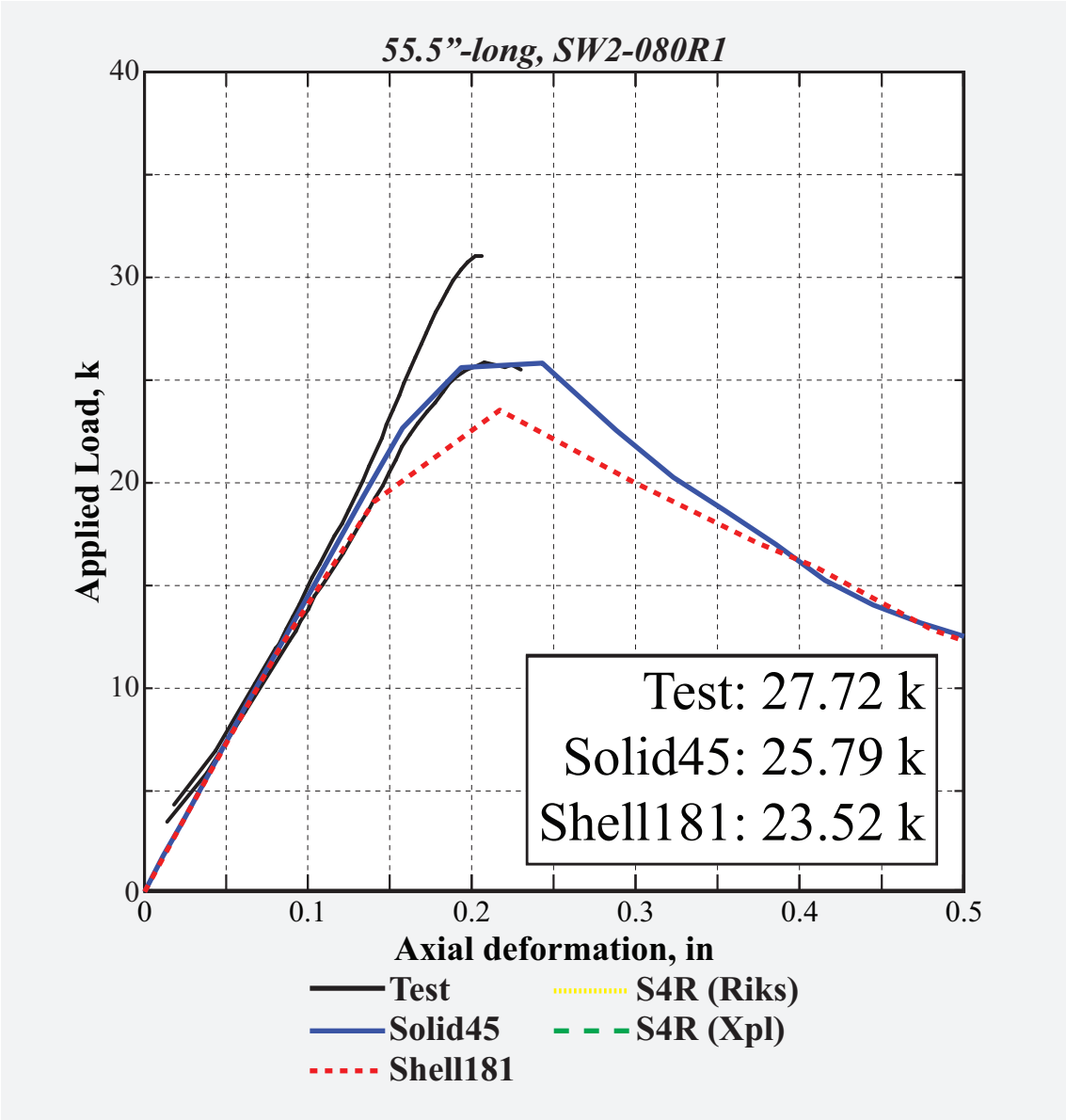


Figure 86: Load vs. deformation history of 55.5”-long, 0.08”-thick *SW2-R1*.

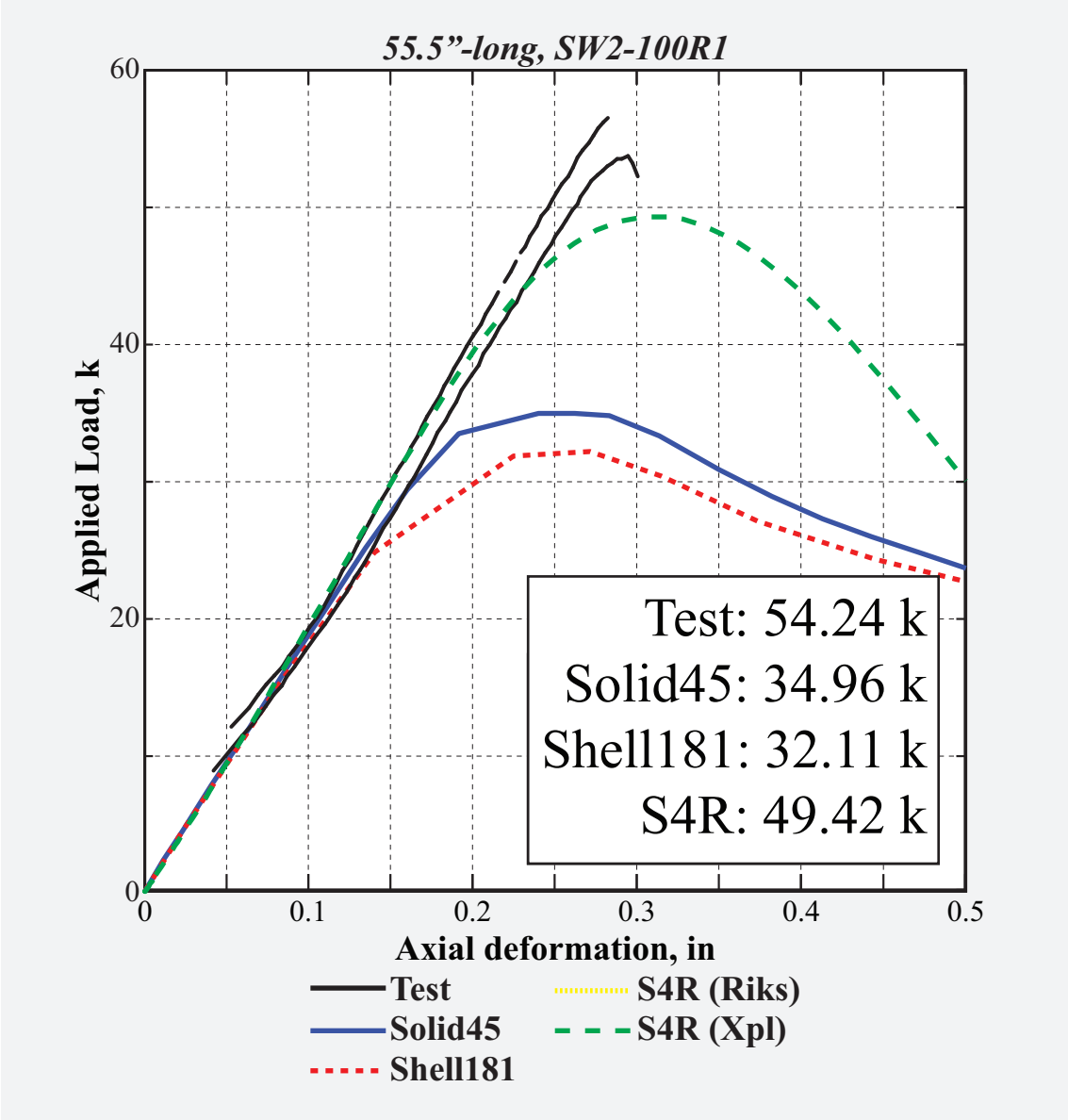


Figure 87: Load vs. deformation history of 55.5”-long, 0.1”-thick *SW2-R1*.

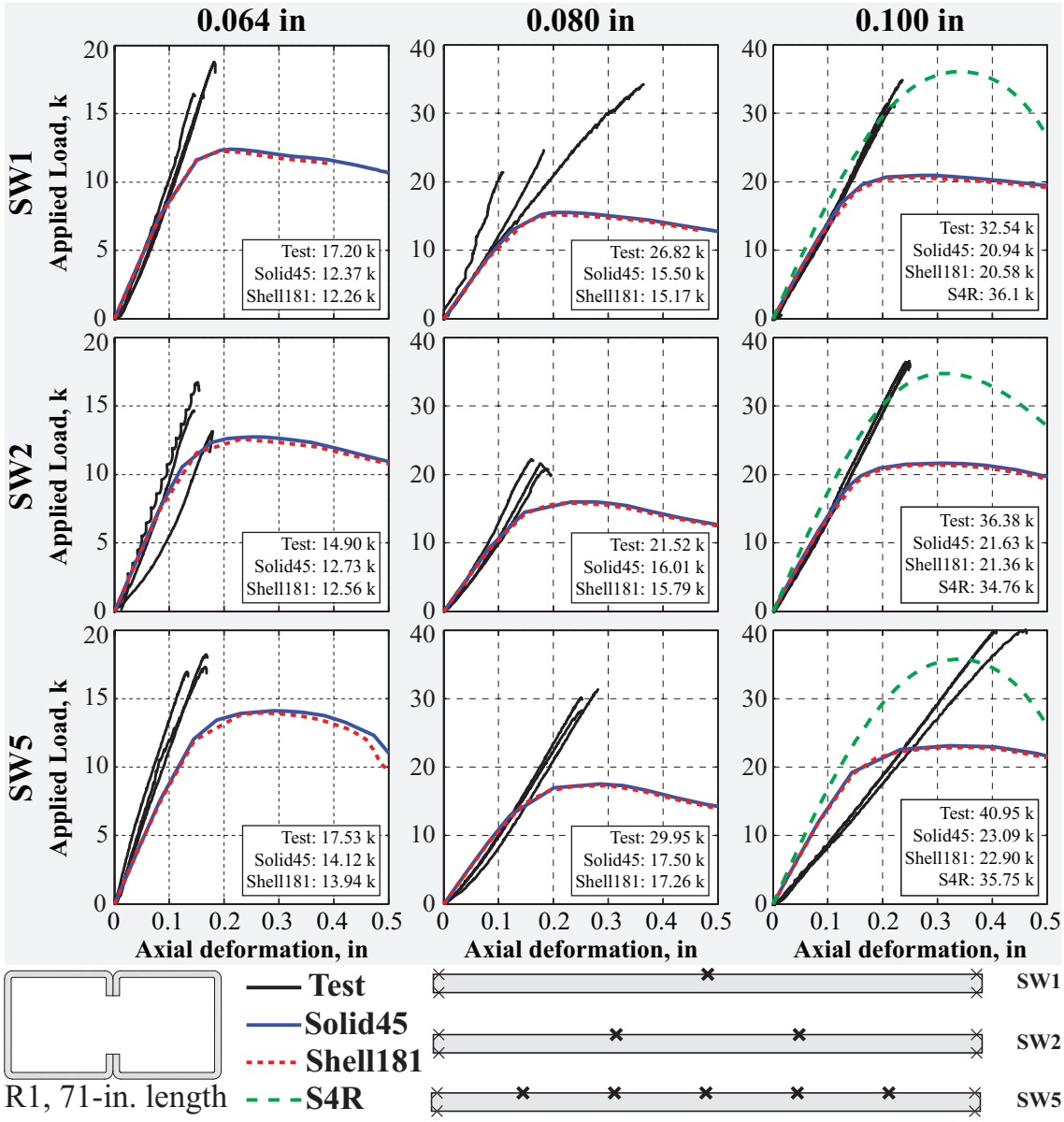


Figure 88: Overview of load vs. deformation history of 71”-long, single-sided *R1*-sections presented in Figs. 89-97.

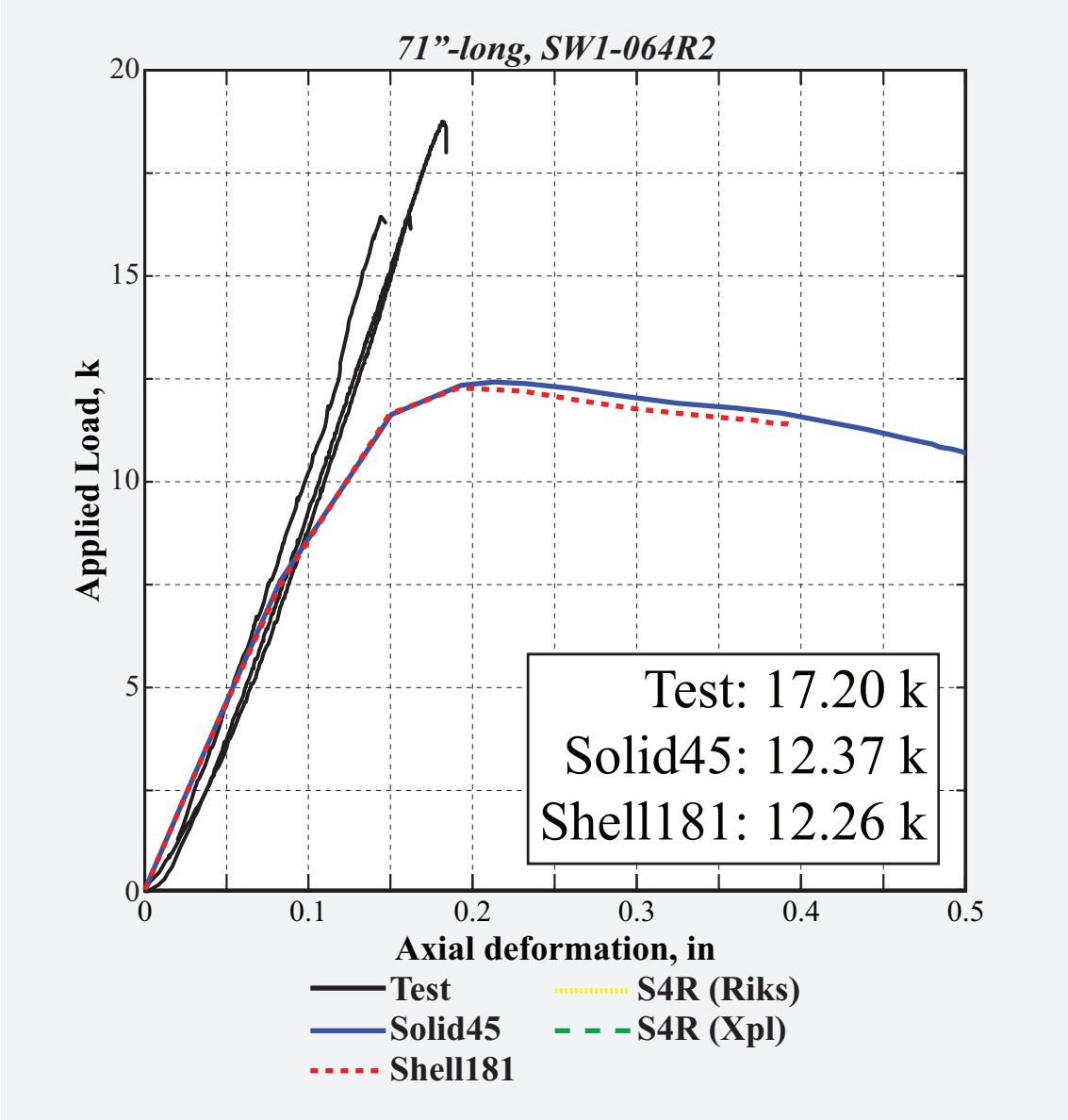


Figure 89: Load vs. deformation history of 71”-long, 0.064”-thick *SW1-R1*.

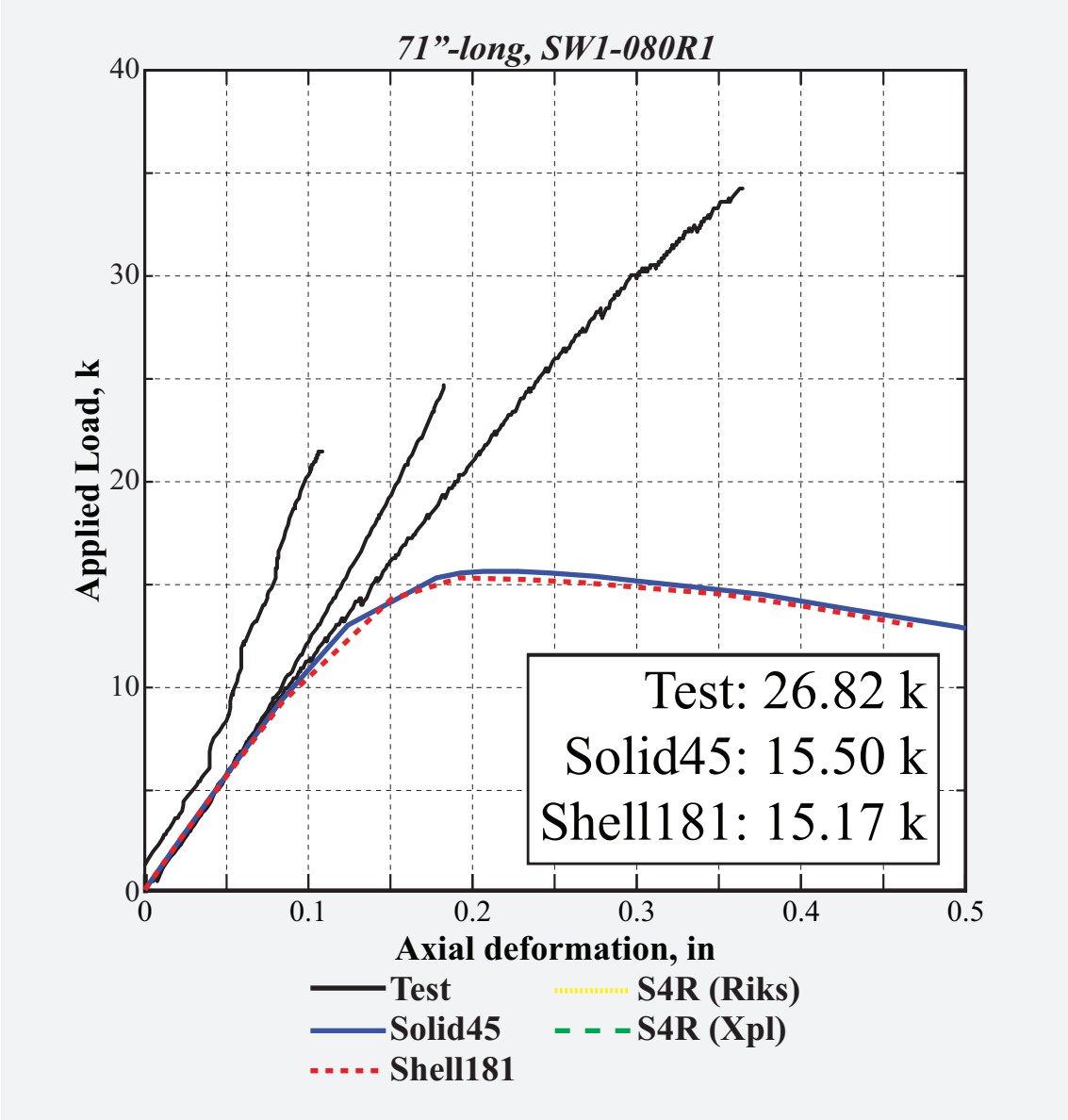


Figure 90: Load vs. deformation history of 71”-long, 0.08”-thick *SW1-R1*.

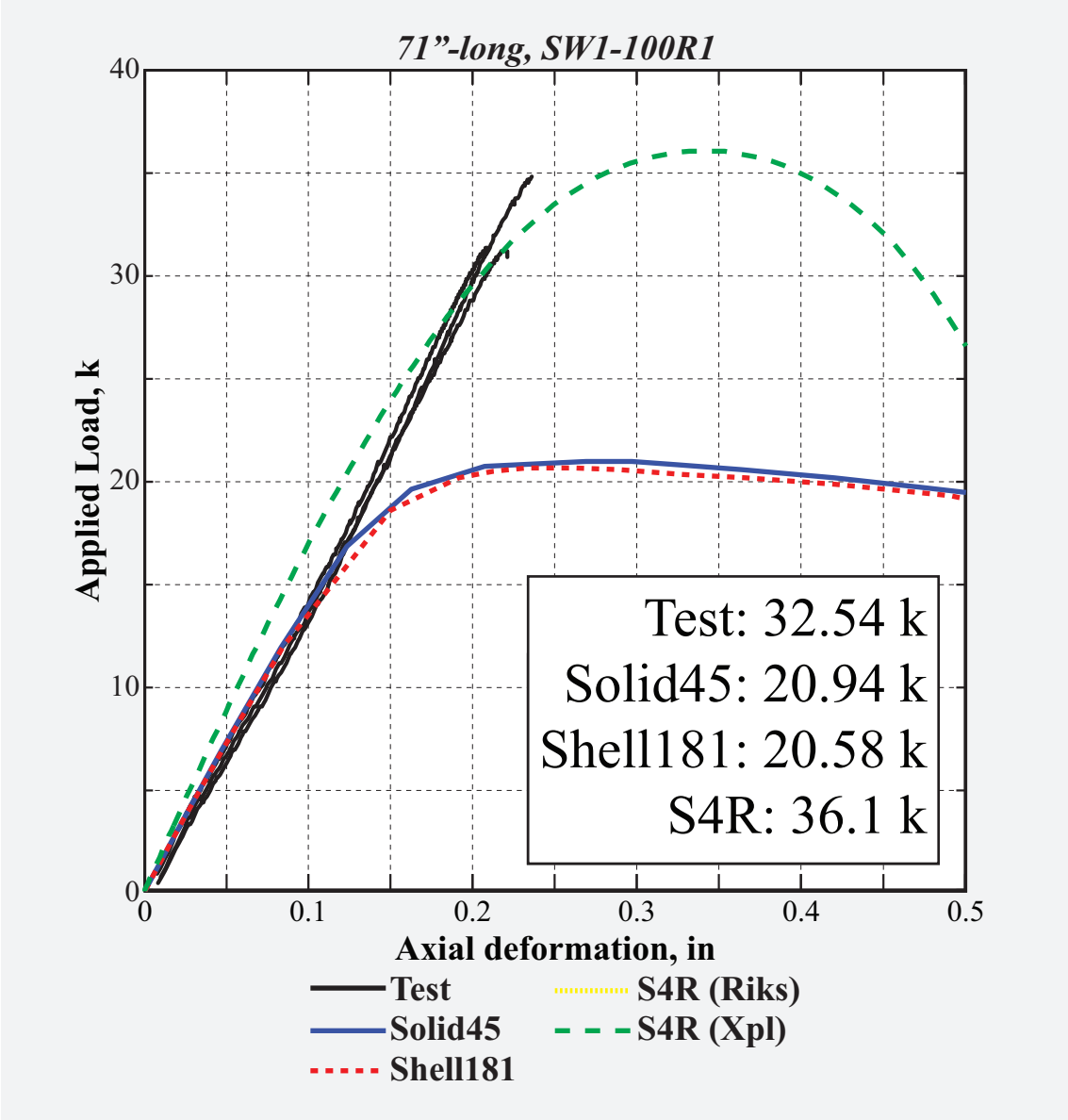


Figure 91: Load vs. deformation history of 71”-long, 0.1”-thick *SW1-R1*.

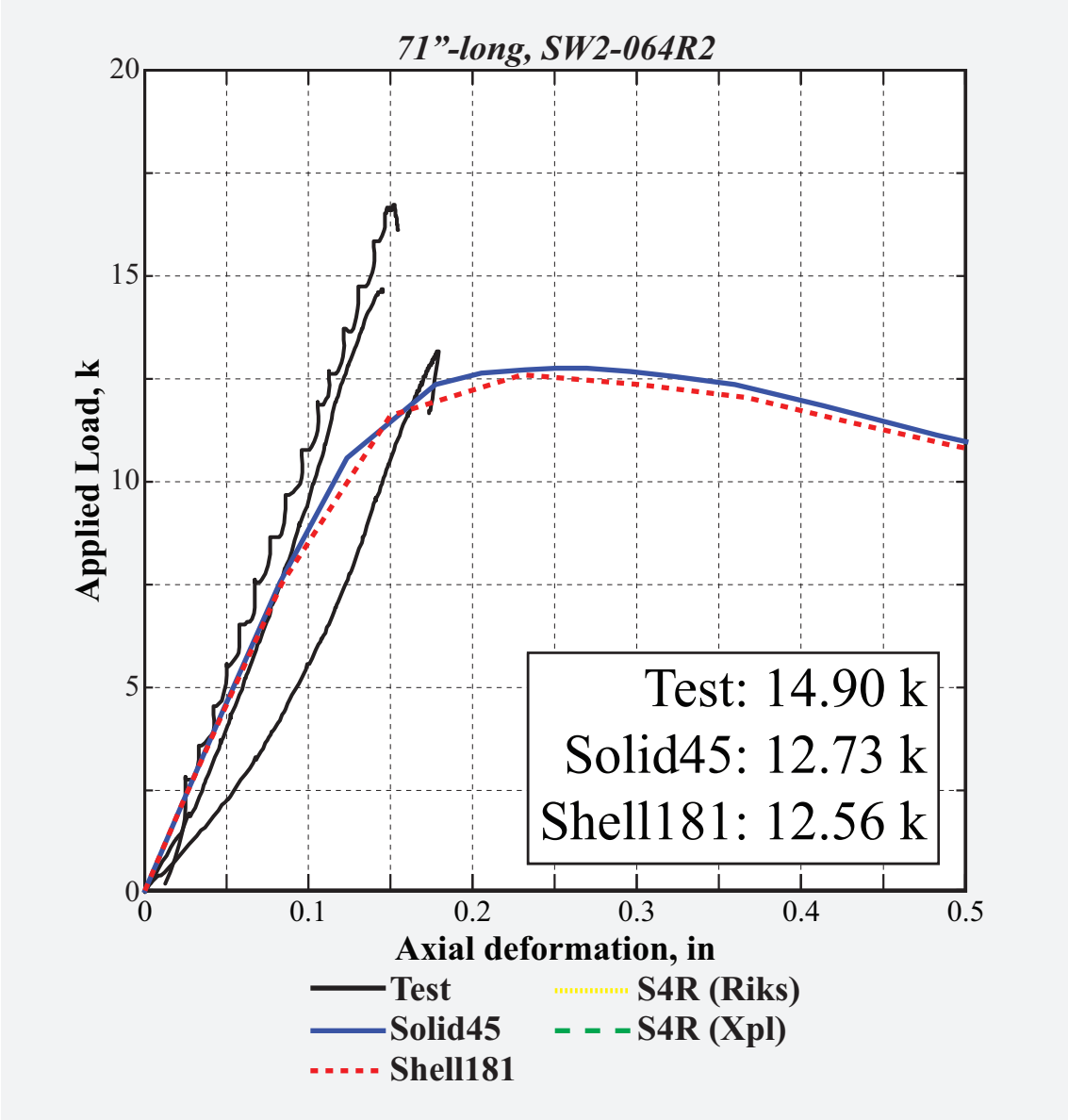


Figure 92: Load vs. deformation history of 71”-long, 0.064”-thick *SW2-R1*.

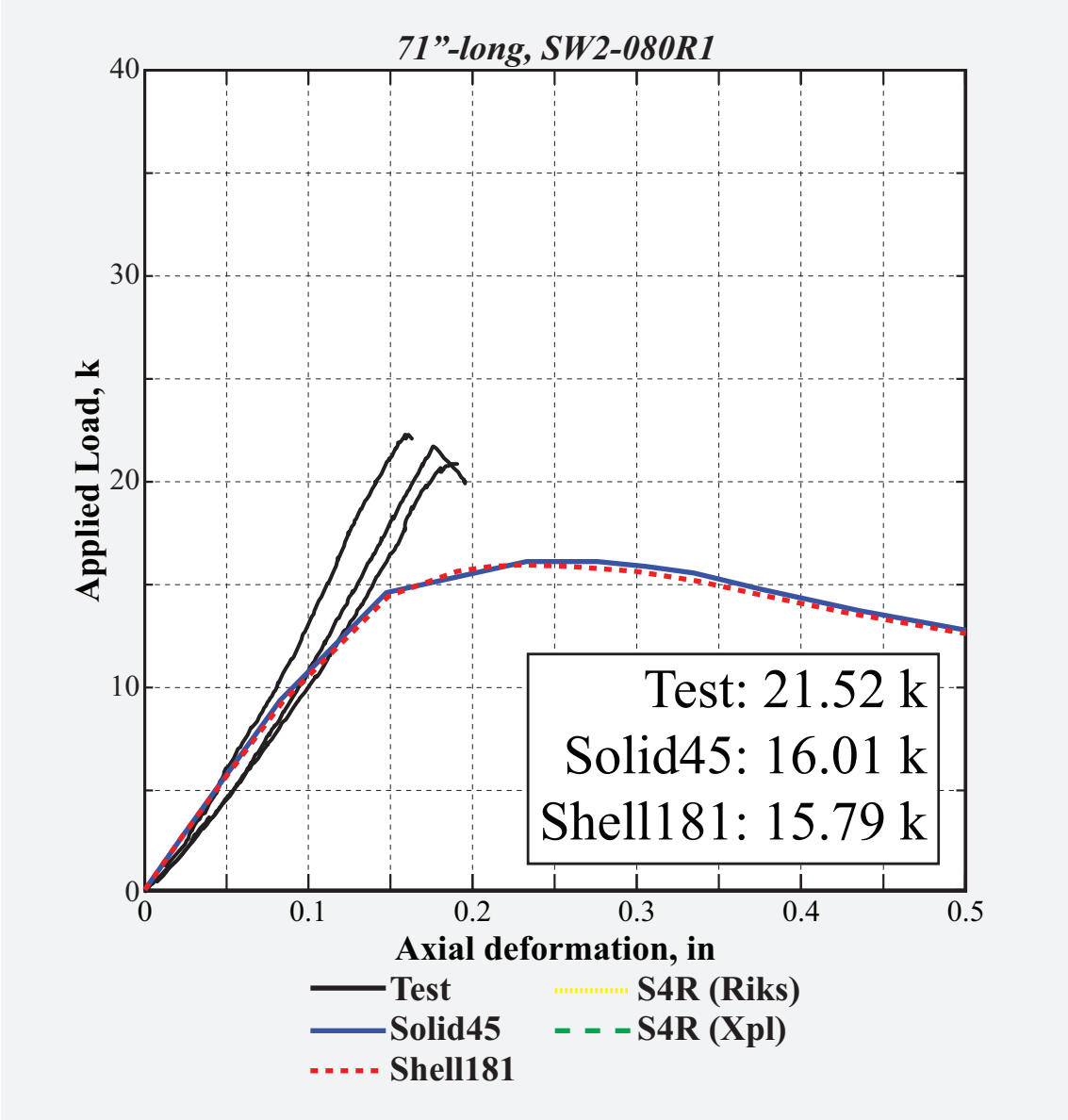


Figure 93: Load vs. deformation history of 71”-long, 0.08”-thick *SW2-R1*.

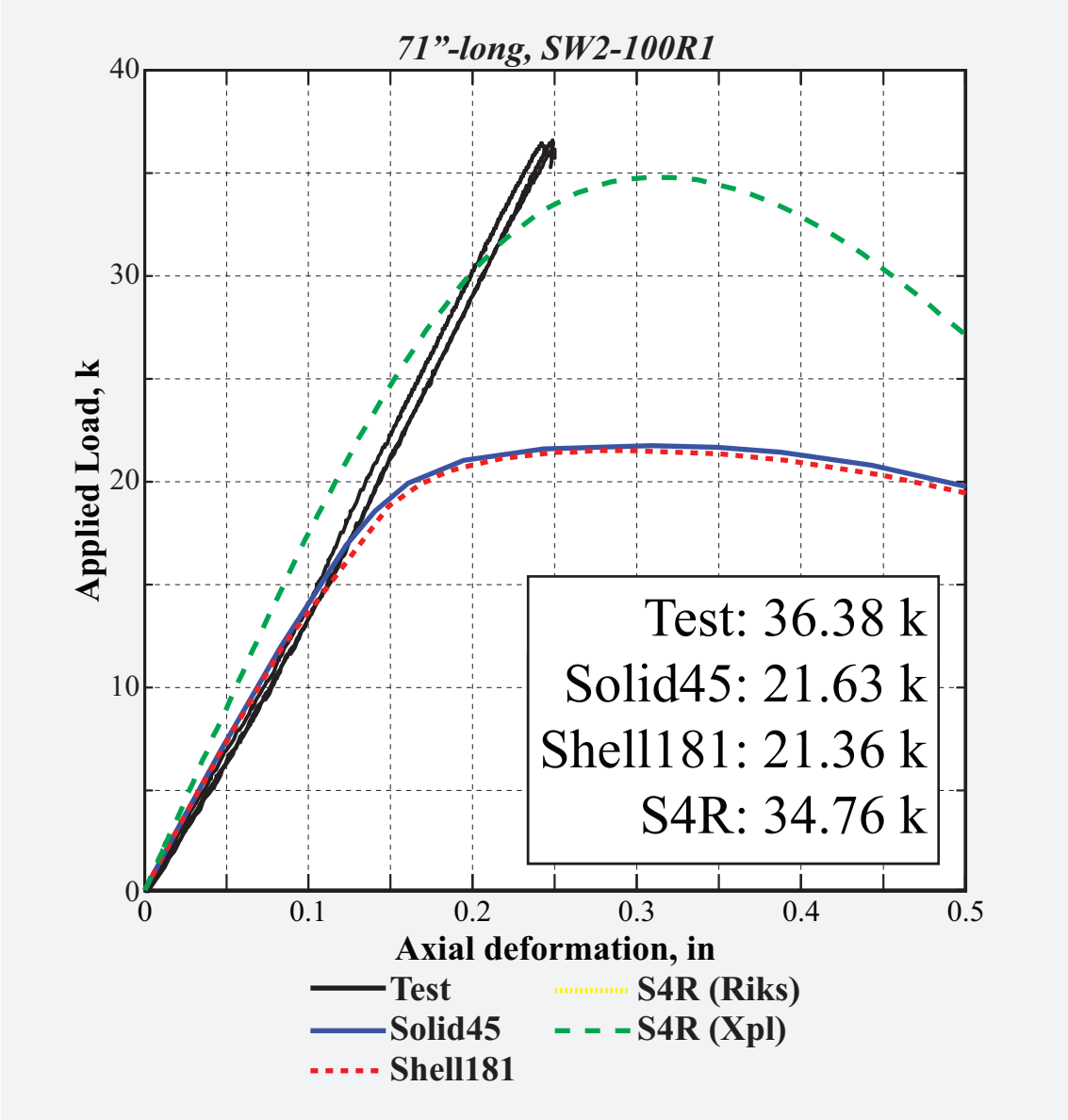


Figure 94: Load vs. deformation history of 71”-long, 0.1”-thick *SW2-R1*.

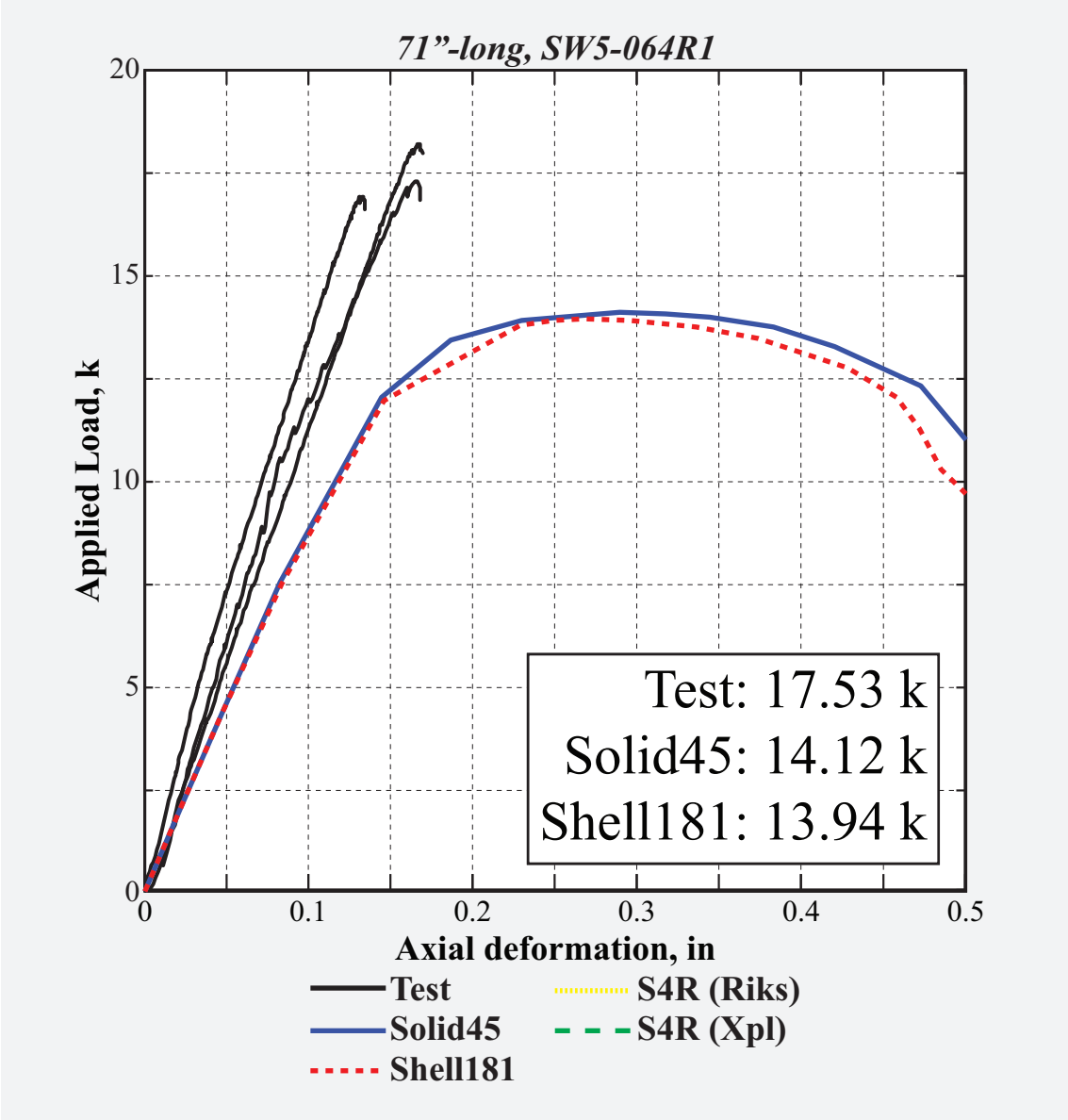


Figure 95: Load vs. deformation history of 71”-long, 0.064”-thick *SW5-R1*.

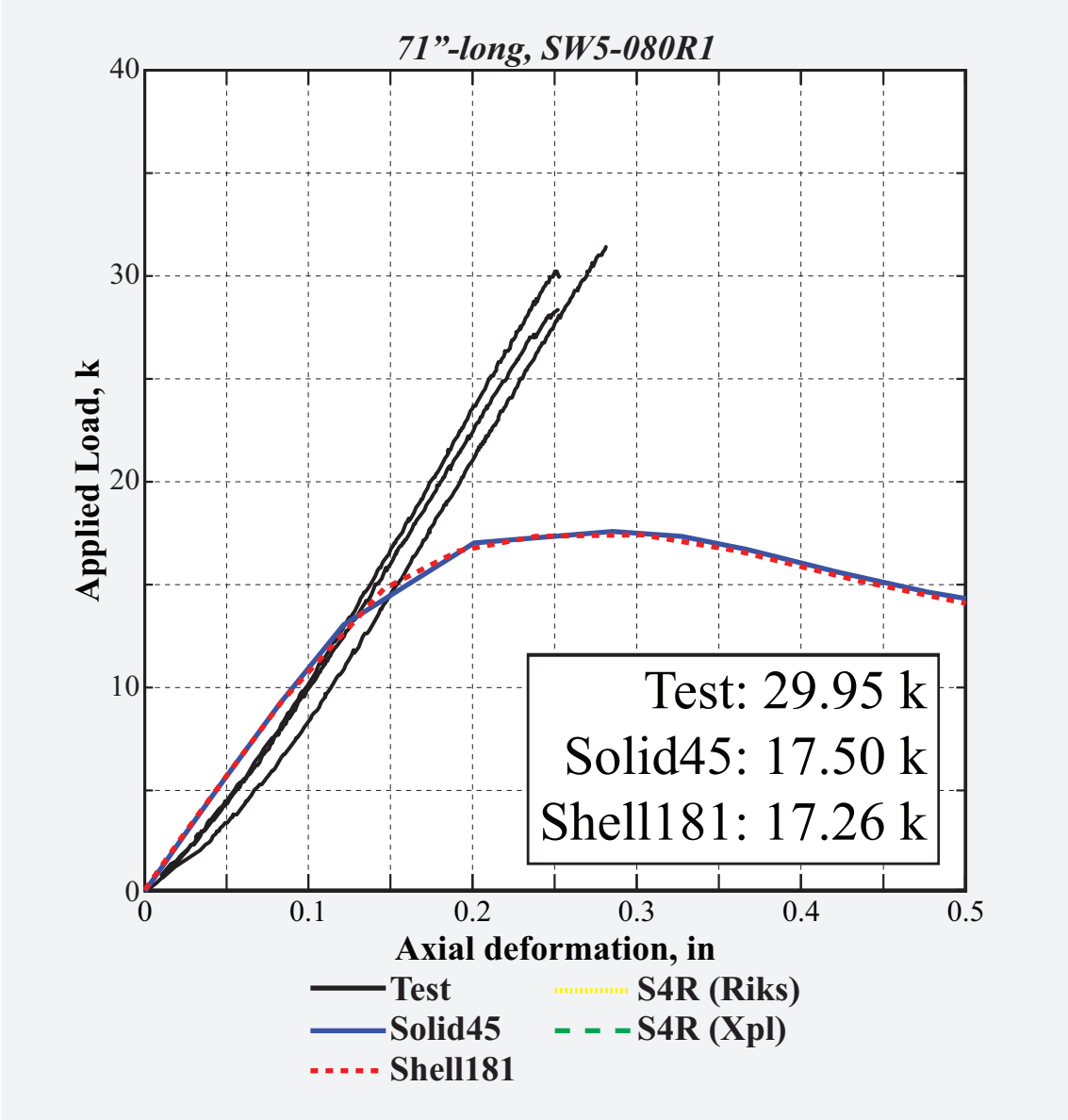


Figure 96: Load vs. deformation history of 71”-long, 0.08”-thick *SW5-R1*.

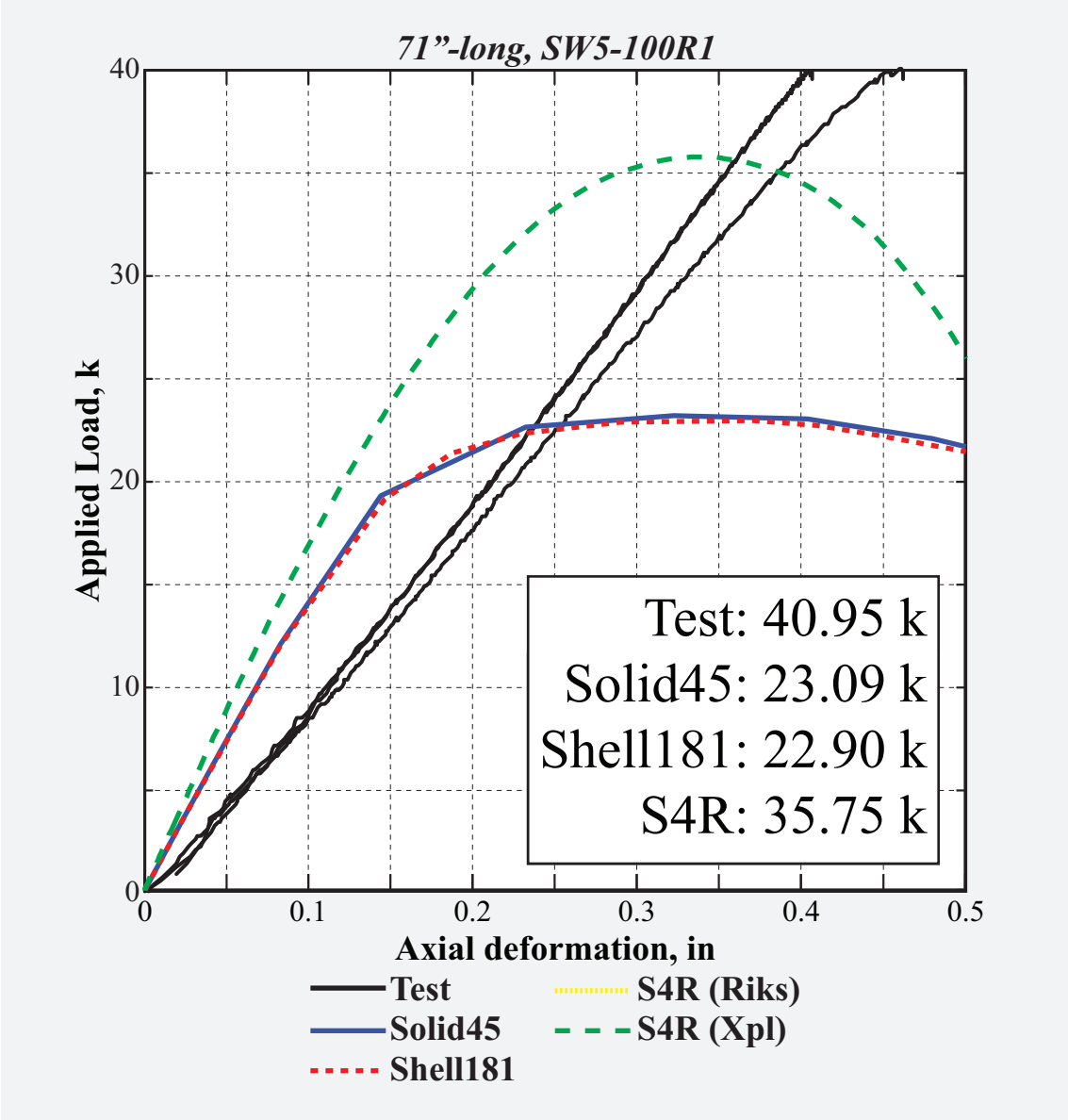


Figure 97: Load vs. deformation history of 71”-long, 0.1”-thick *SW5-R1*.

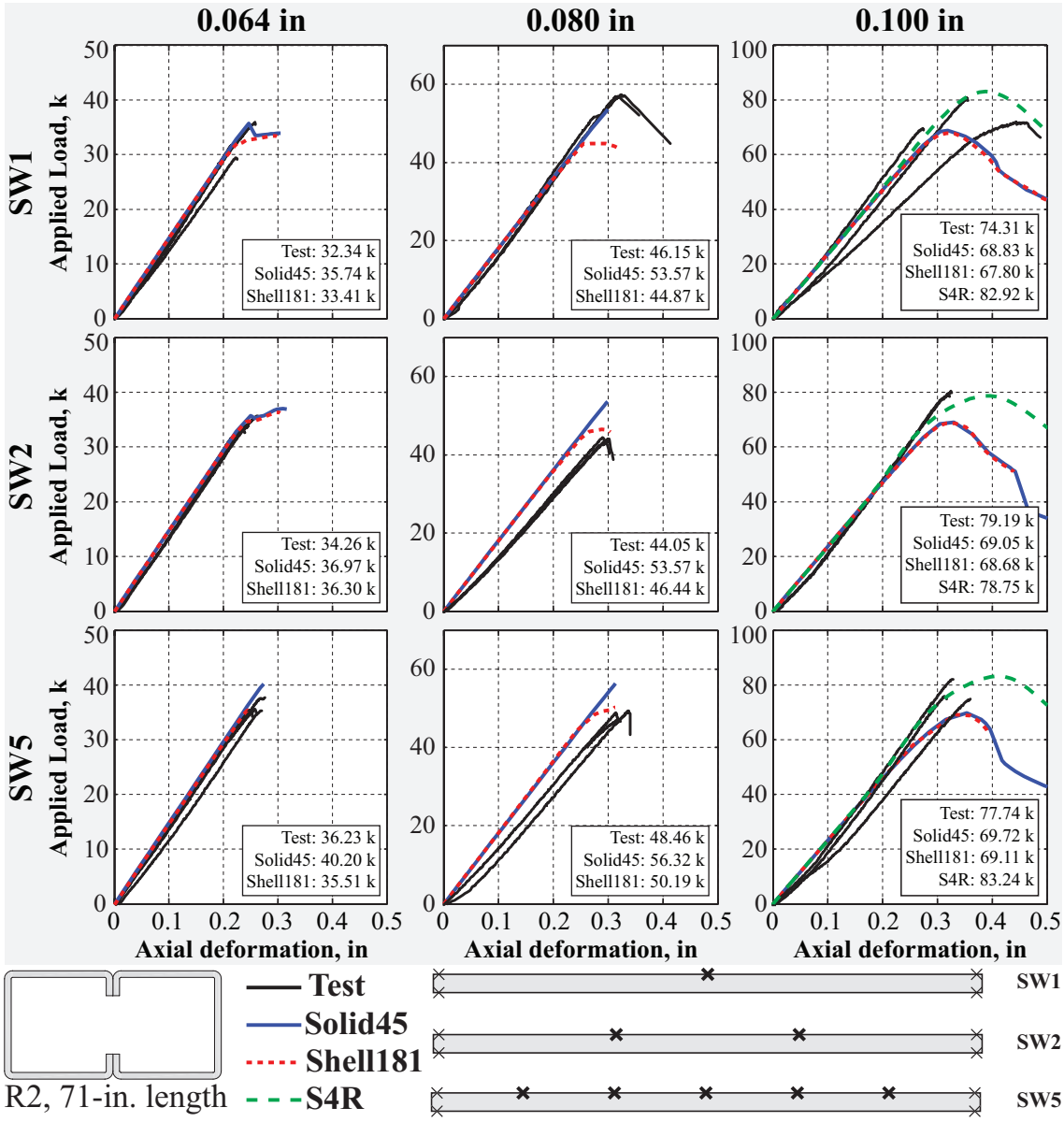


Figure 98: Overview of load vs. deformation history of 71”-long, single-sided *R2*-sections presented in Figs 99-107.

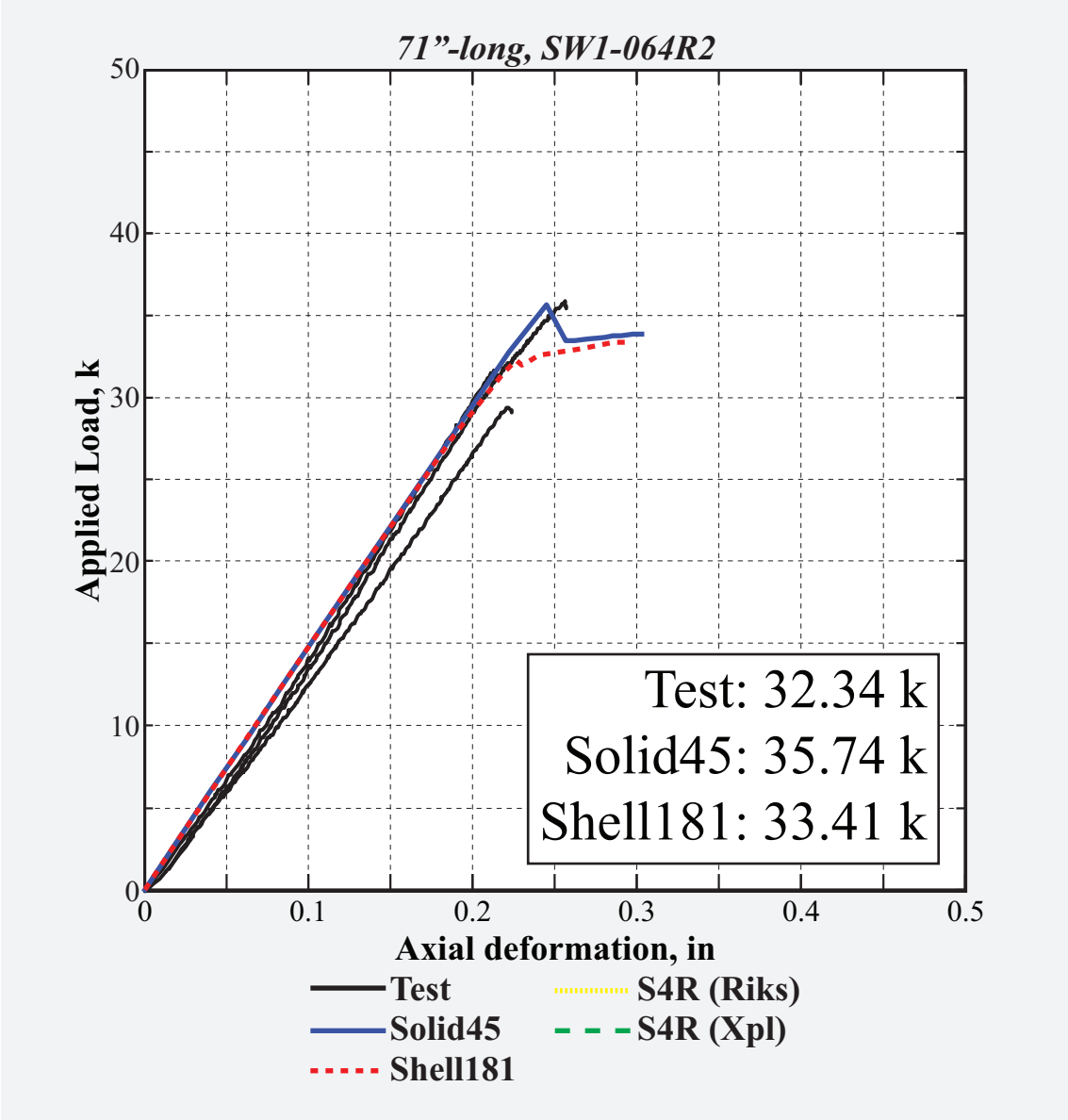


Figure 99: Load vs. deformation history of 71”-long, 0.064”-thick *SW1-R2*.

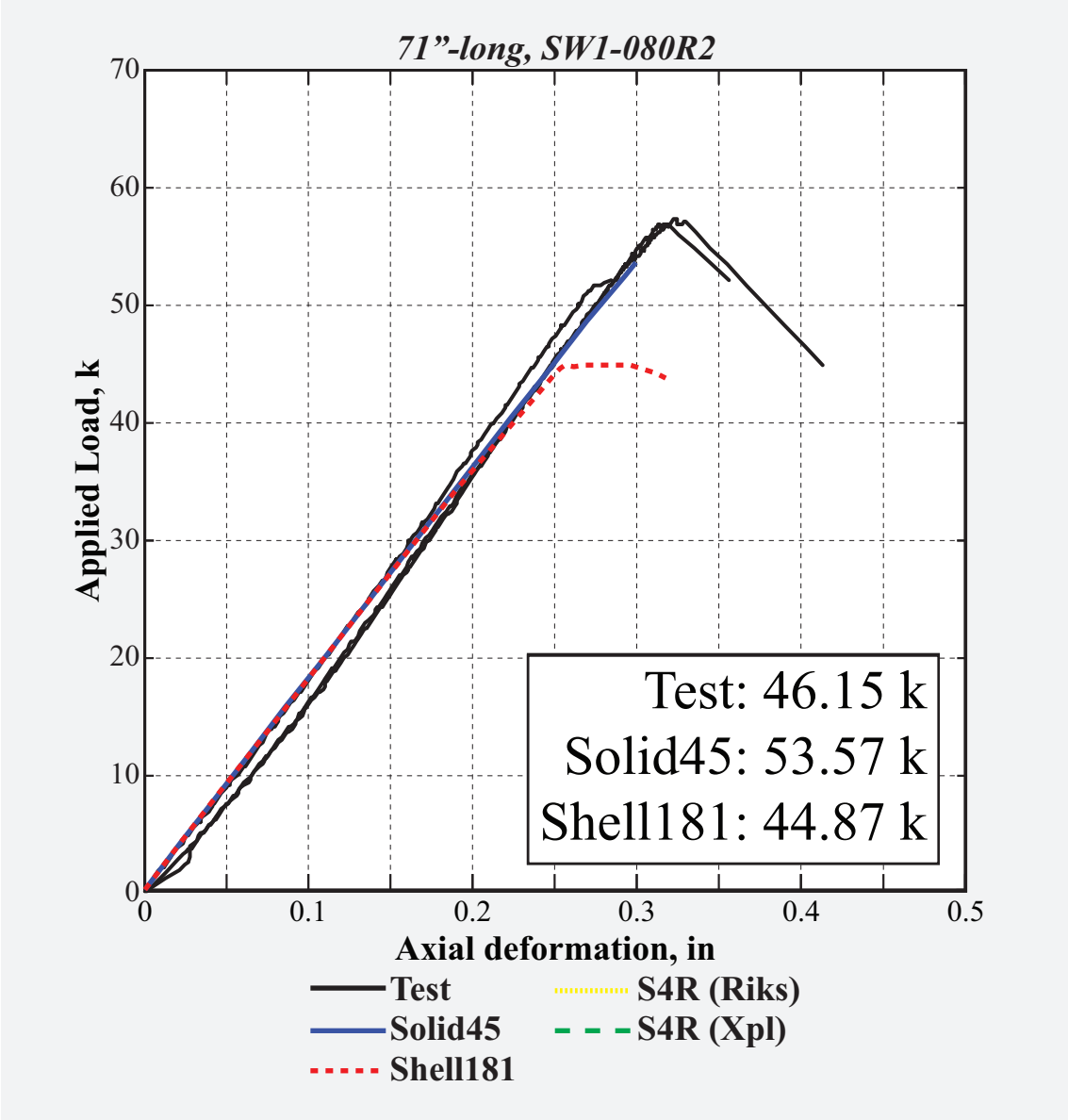


Figure 100: Load vs. deformation history of 71”-long, 0.08”-thick *SW1-R2*.

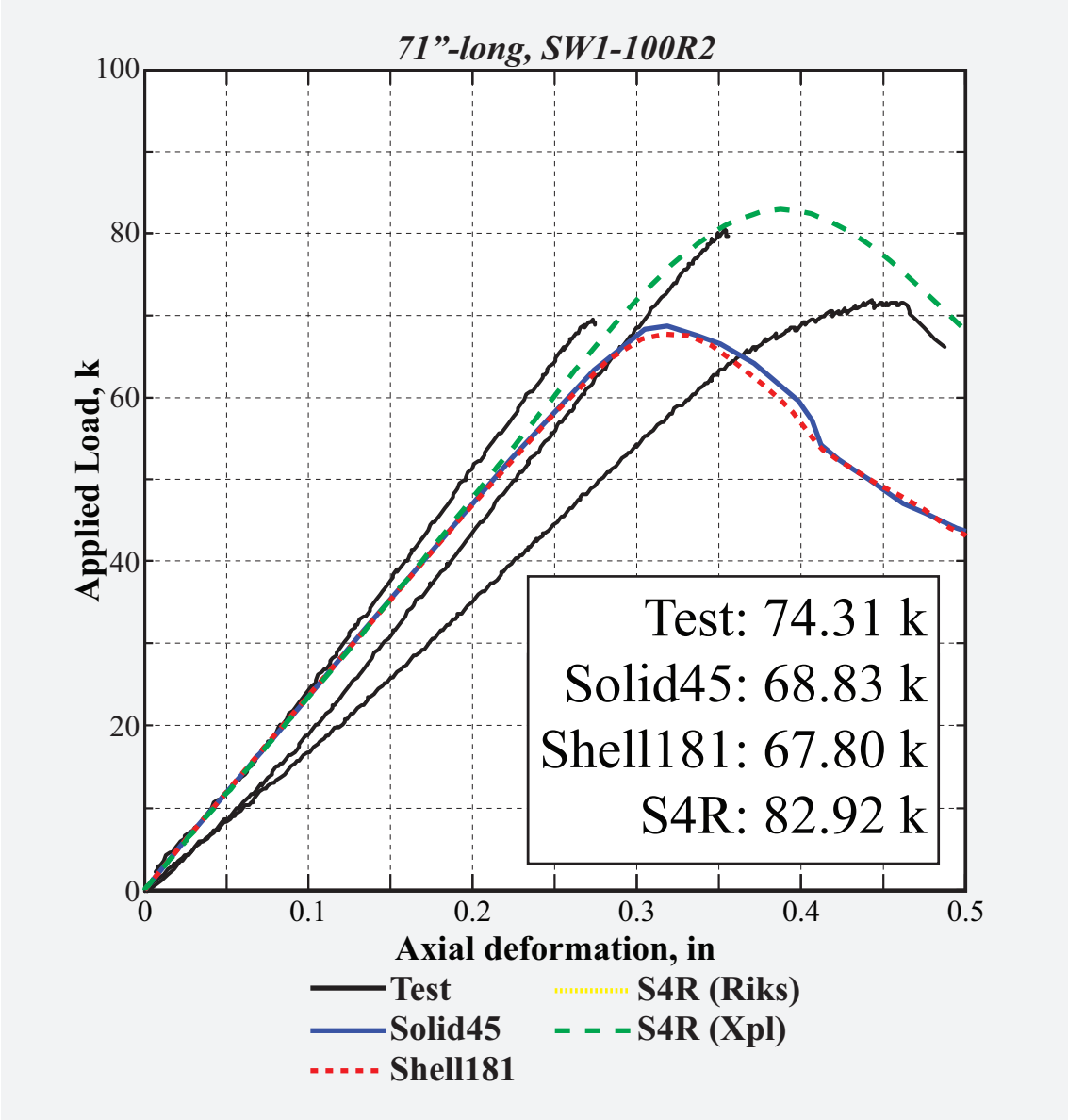


Figure 101: Load vs. deformation history of 71”-long, 0.1”-thick *SW1-R2*.

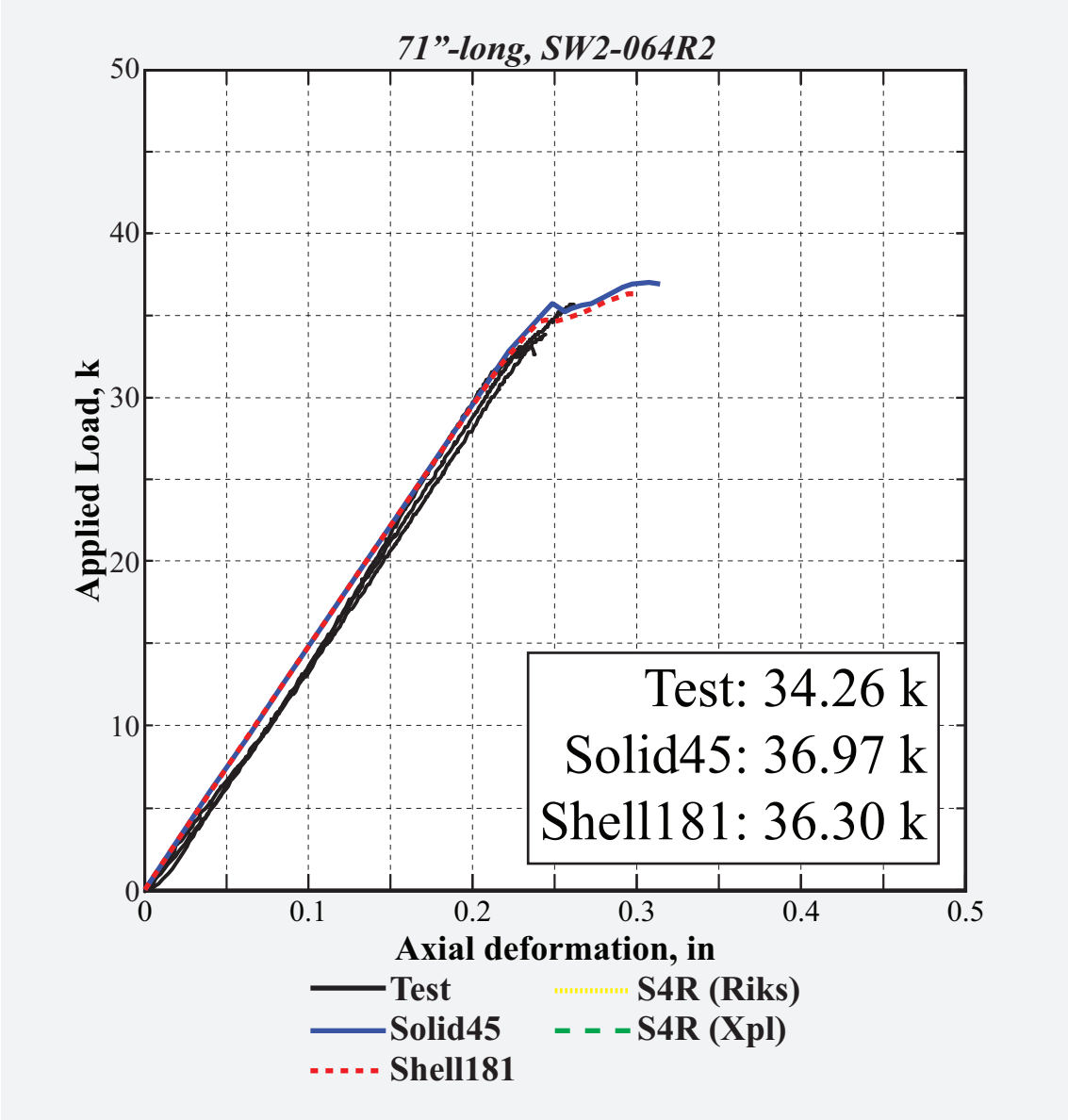


Figure 102: Load vs. deformation history of 71”-long, 0.064”-thick *SW2-R2*.

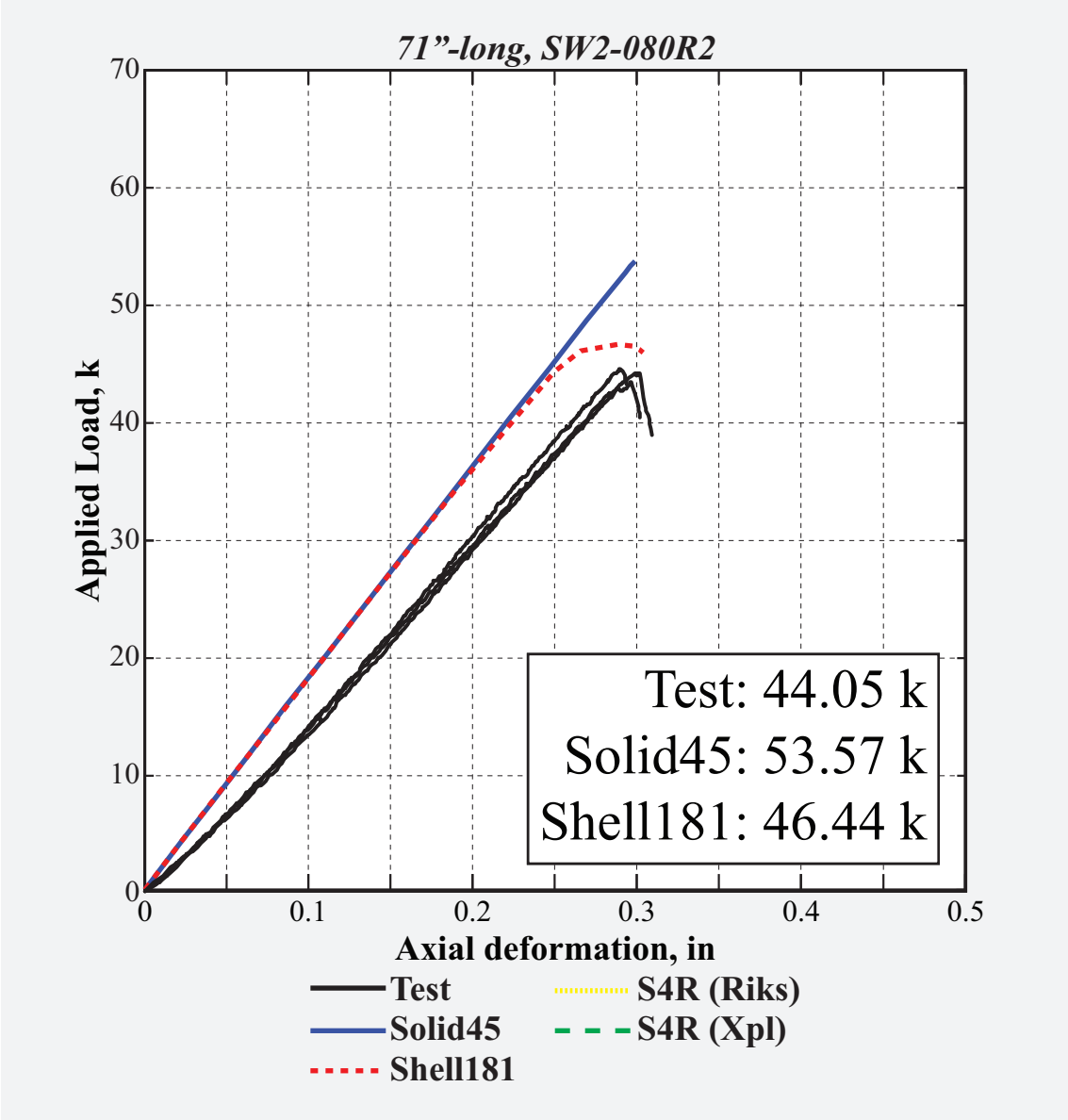


Figure 103: Load vs. deformation history of 71”-long, 0.08”-thick *SW2-R2*.

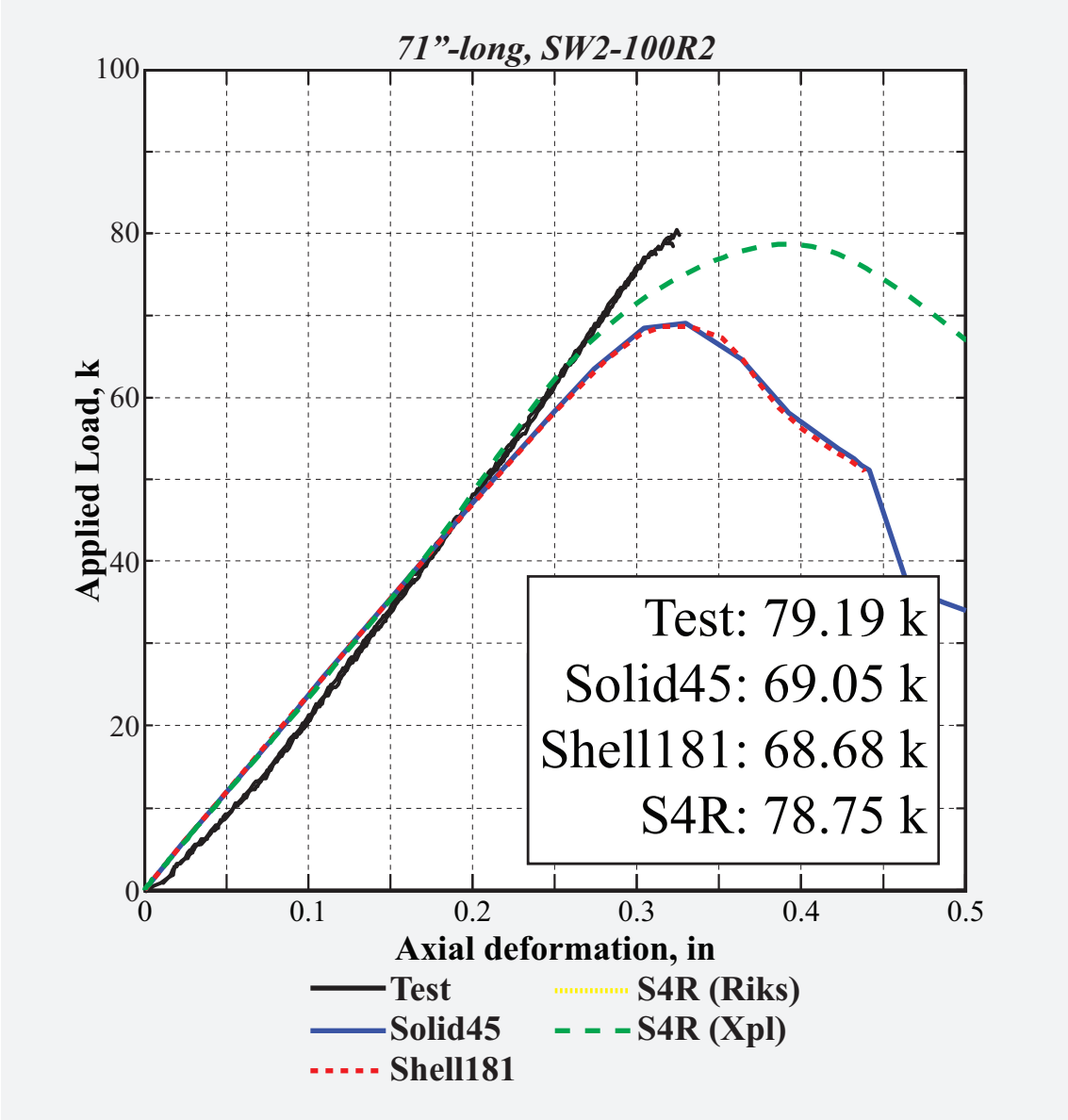


Figure 104: Load vs. deformation history of 71”-long, 0.1”-thick *SW2-R2*.

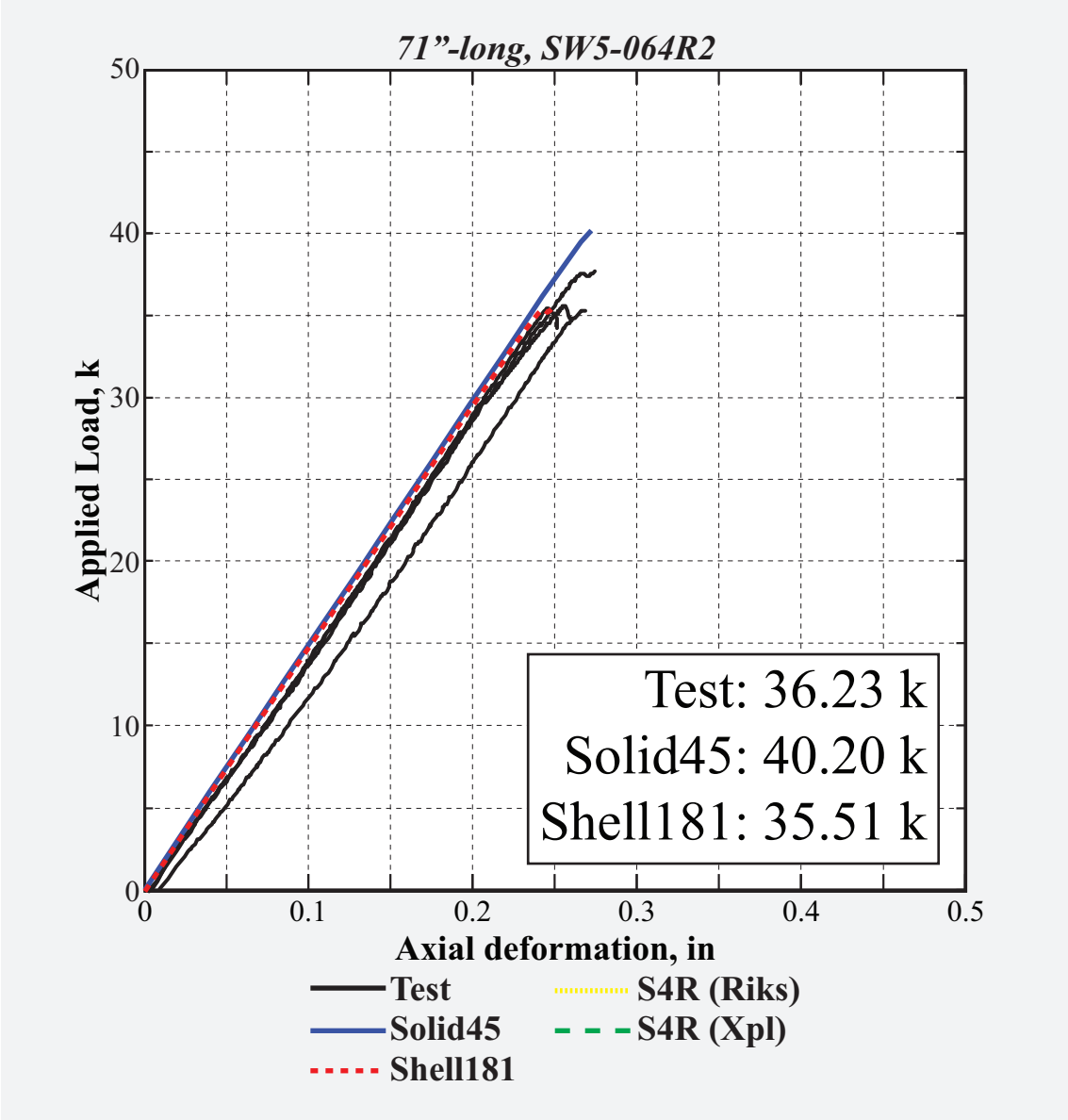


Figure 105: Load vs. deformation history of 71”-long, 0.064”-thick *SW5-R2*.

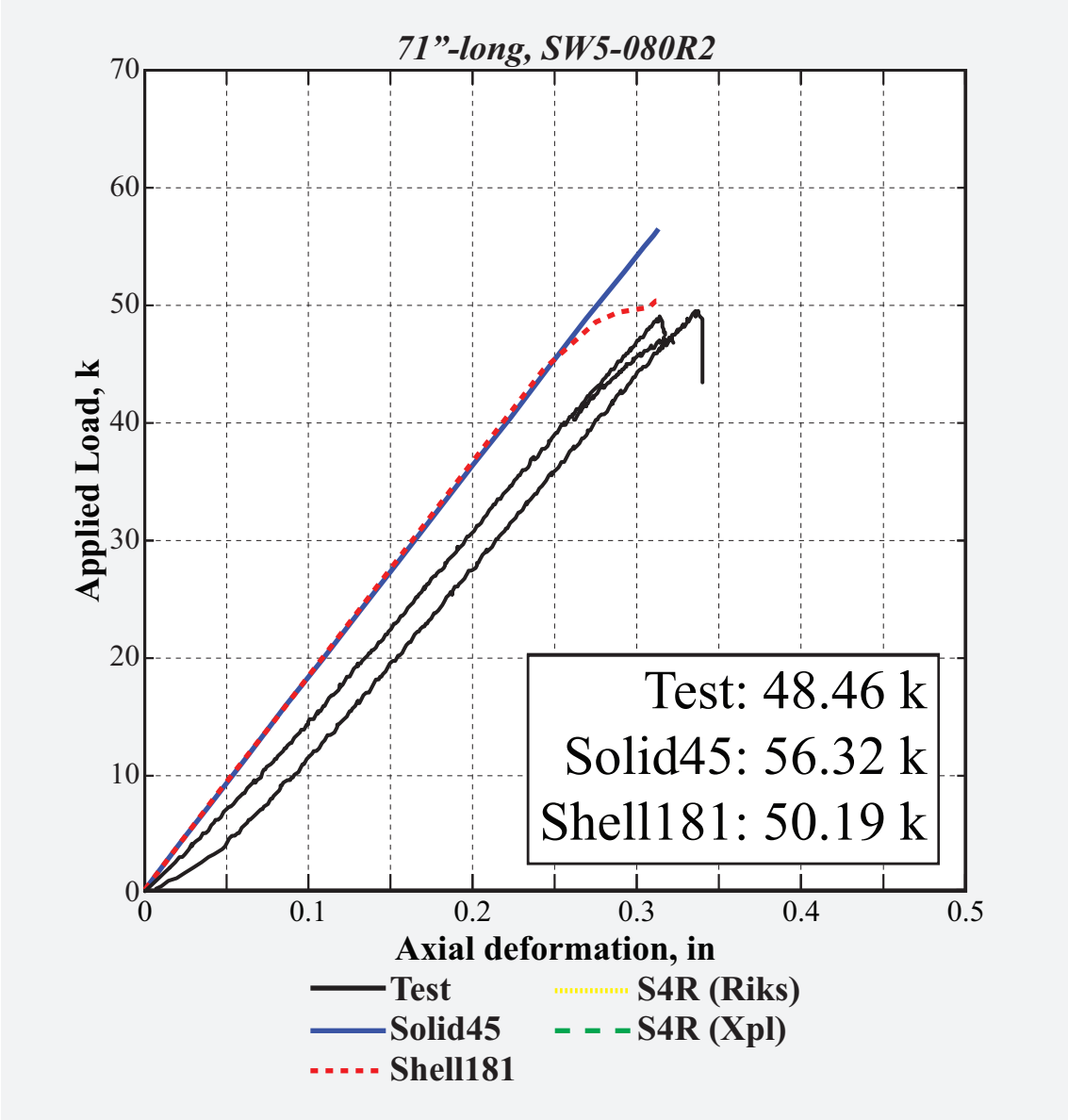


Figure 106: Load vs. deformation history of 71”-long, 0.08”-thick *SW5-R2*.

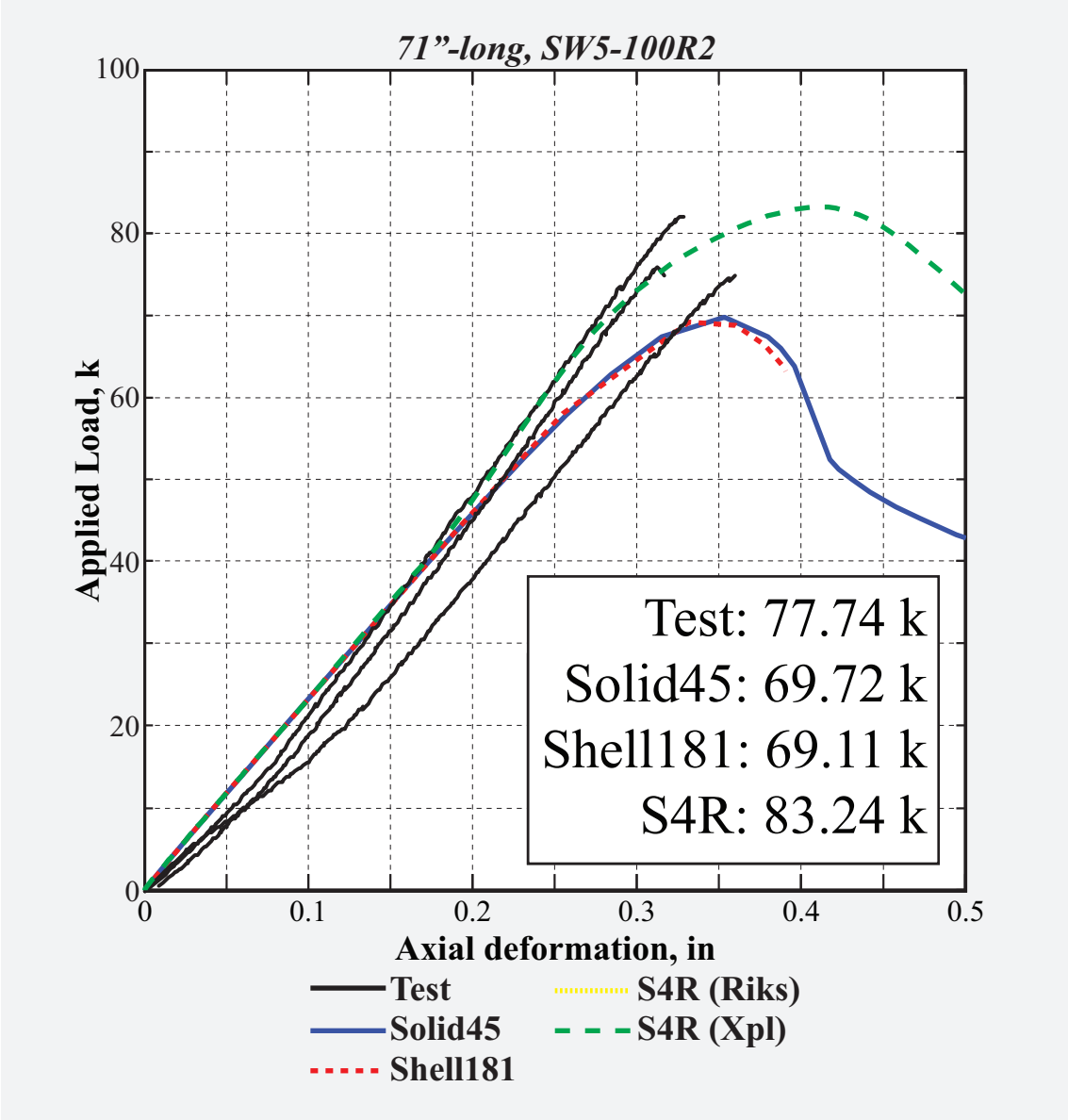


Figure 107: Load vs. deformation history of 71”-long, 0.1”-thick *SW5-R2*.

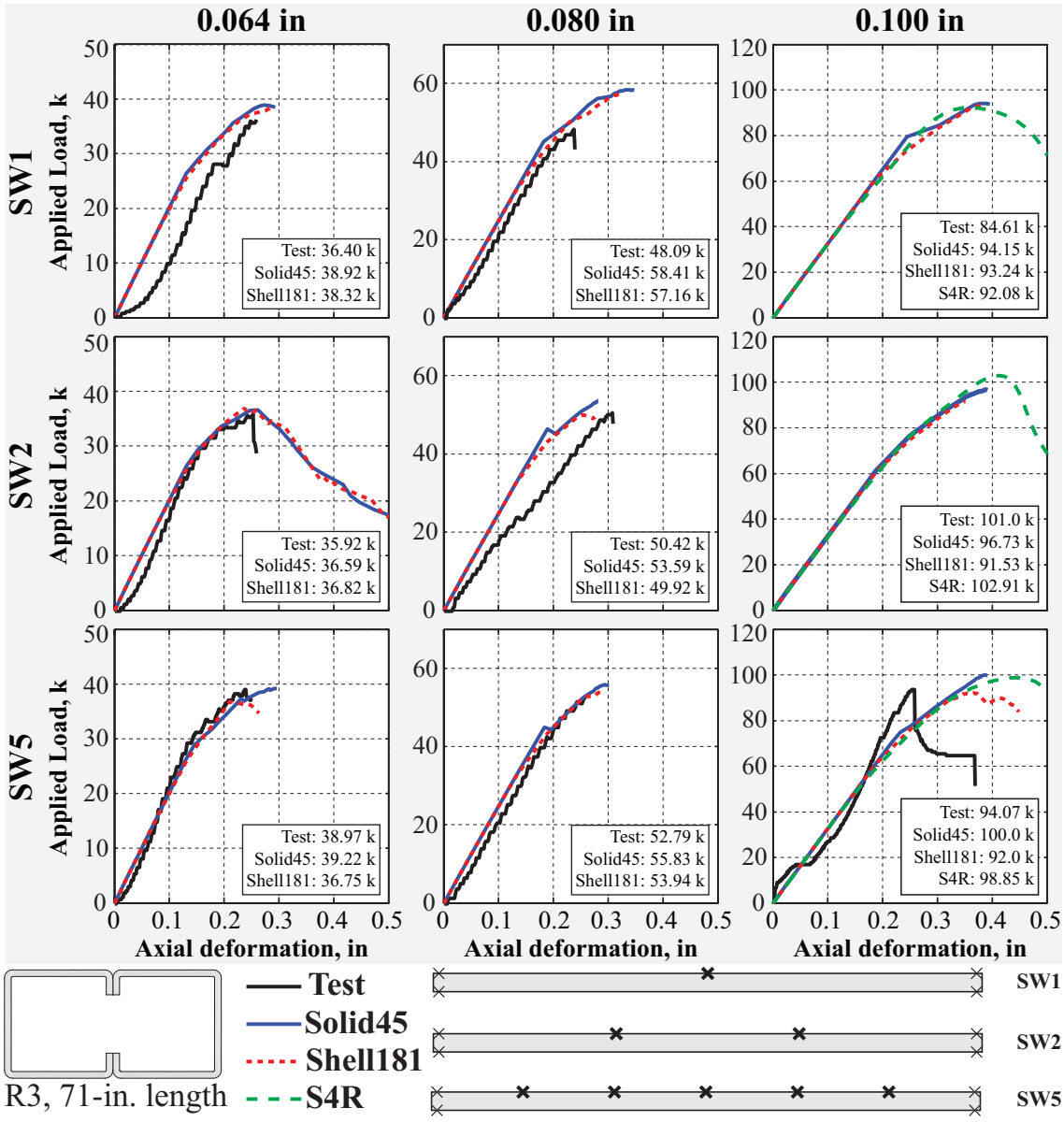


Figure 108: Overview of load vs. deformation history of 71”-long, single-sided *R3*-sections presented in Figs 109-117.

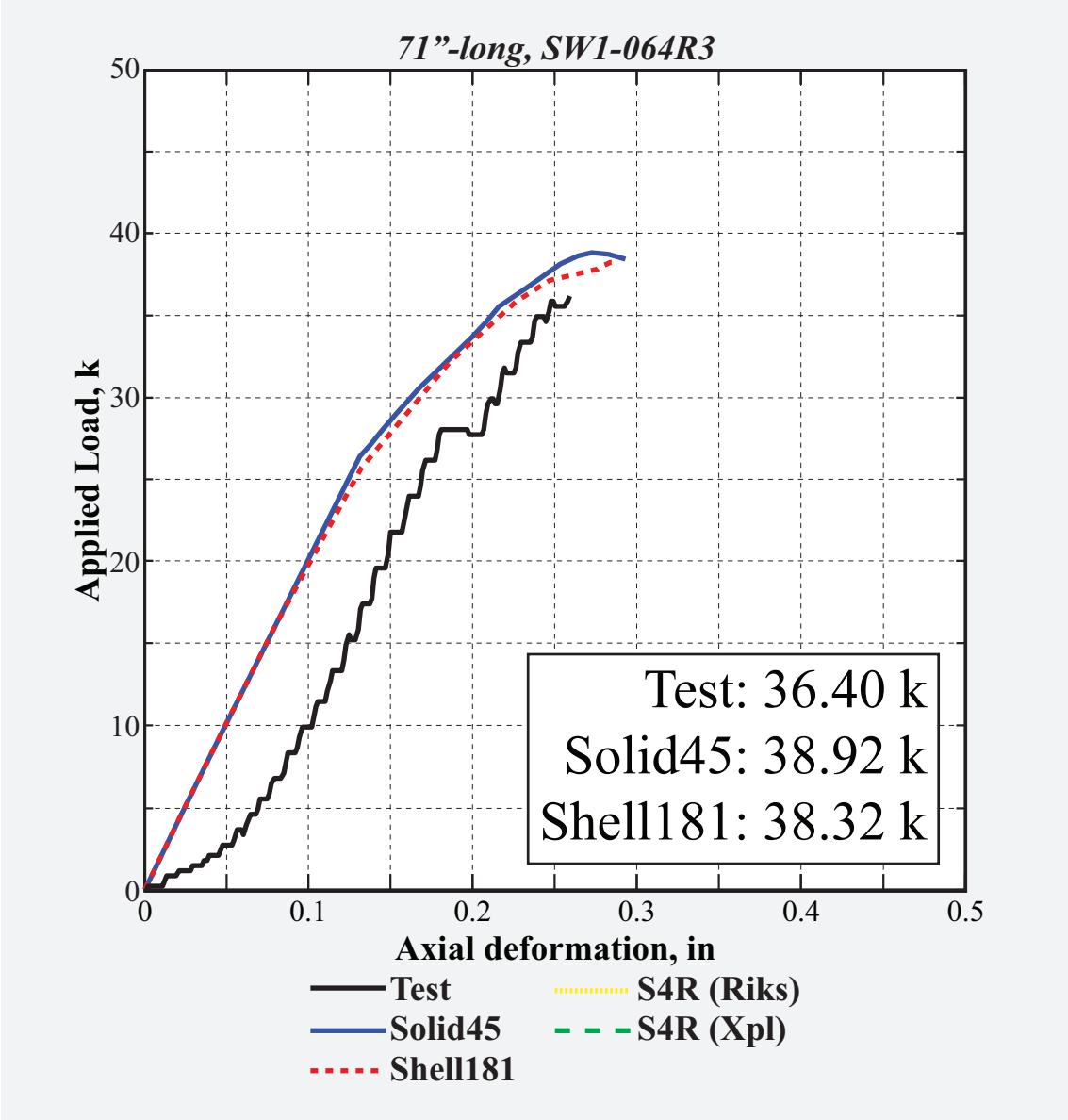


Figure 109: Load vs. deformation history of 71”-long, 0.064”-thick *SW1-R3*.

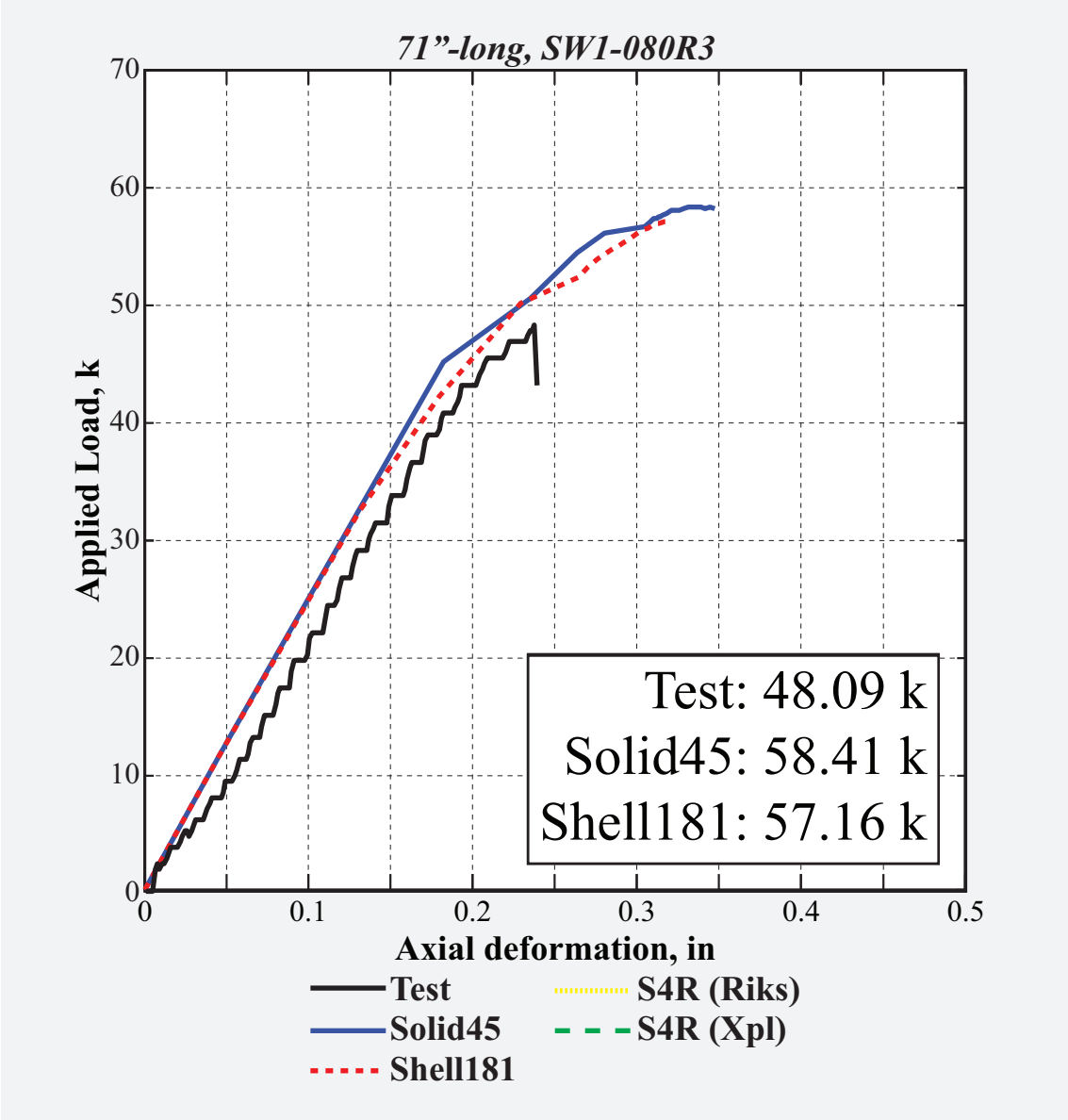


Figure 110: Load vs. deformation history of 71”-long, 0.08”-thick *SW1-R3*.

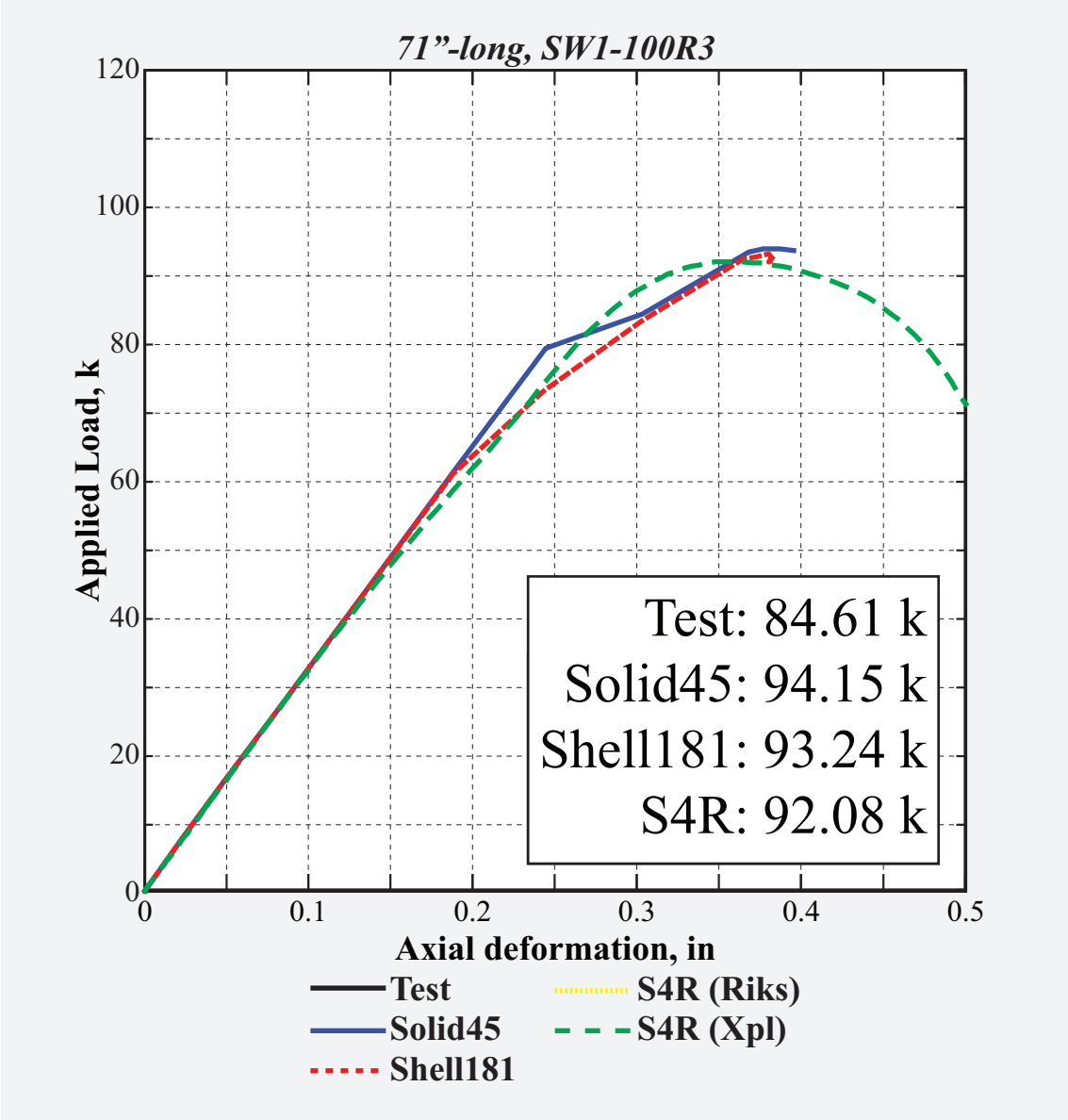


Figure 111: Load vs. deformation history of 71”-long, 0.1”-thick *SW1-R3*.

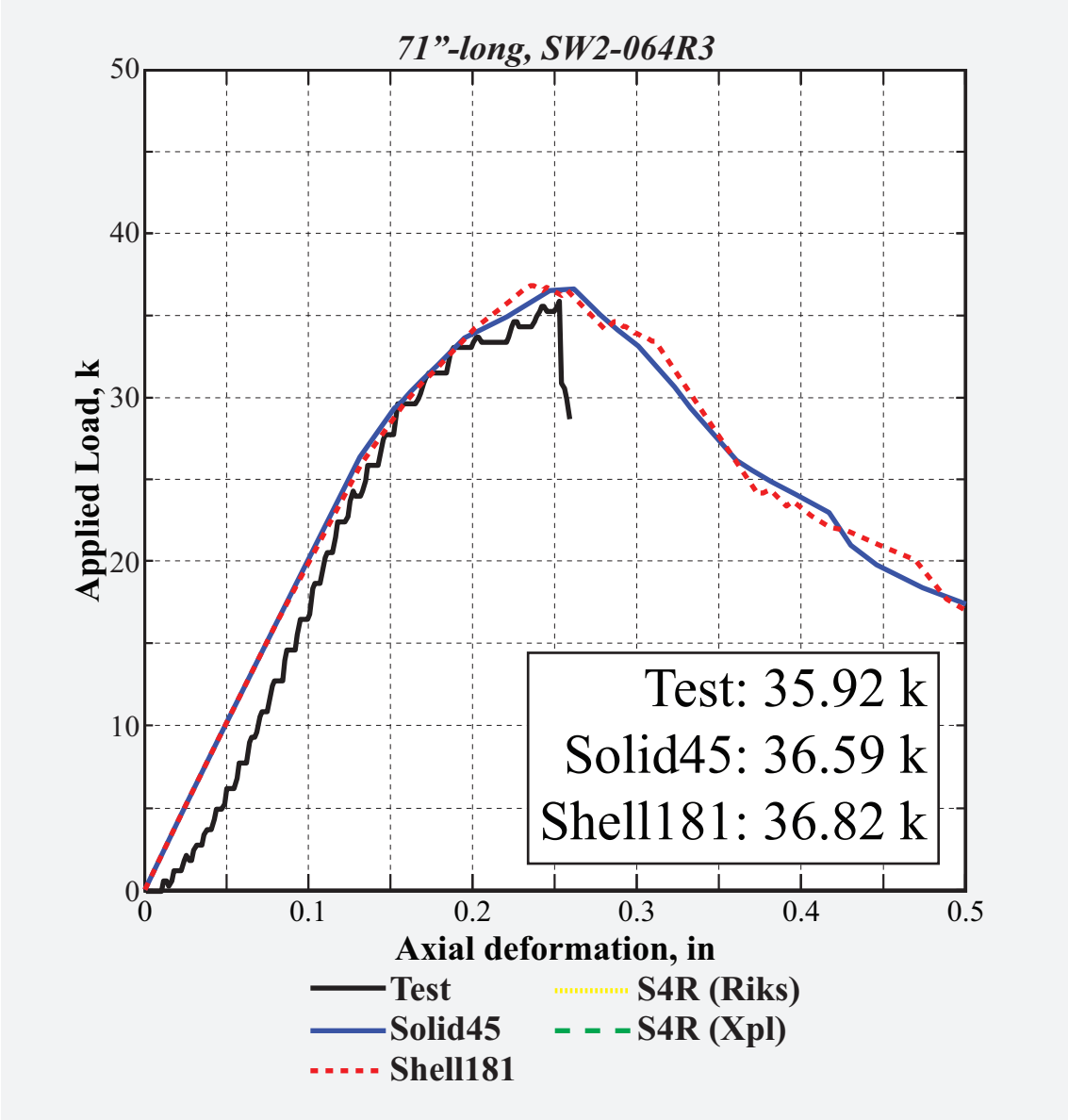


Figure 112: Load vs. deformation history of 71”-long, 0.064”-thick *SW2-R3*.

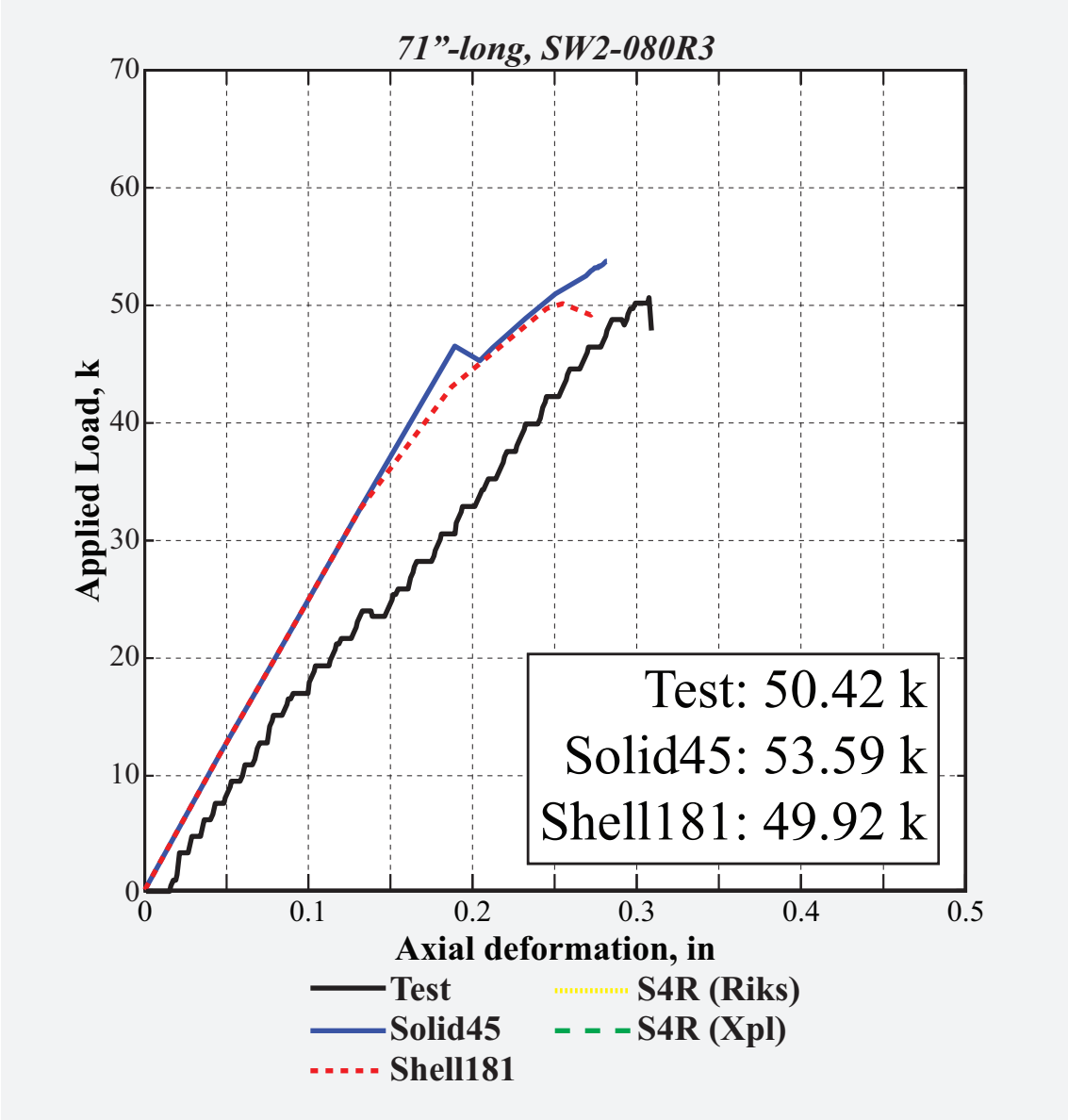


Figure 113: Load vs. deformation history of 71”-long, 0.08”-thick *SW2-R3*.

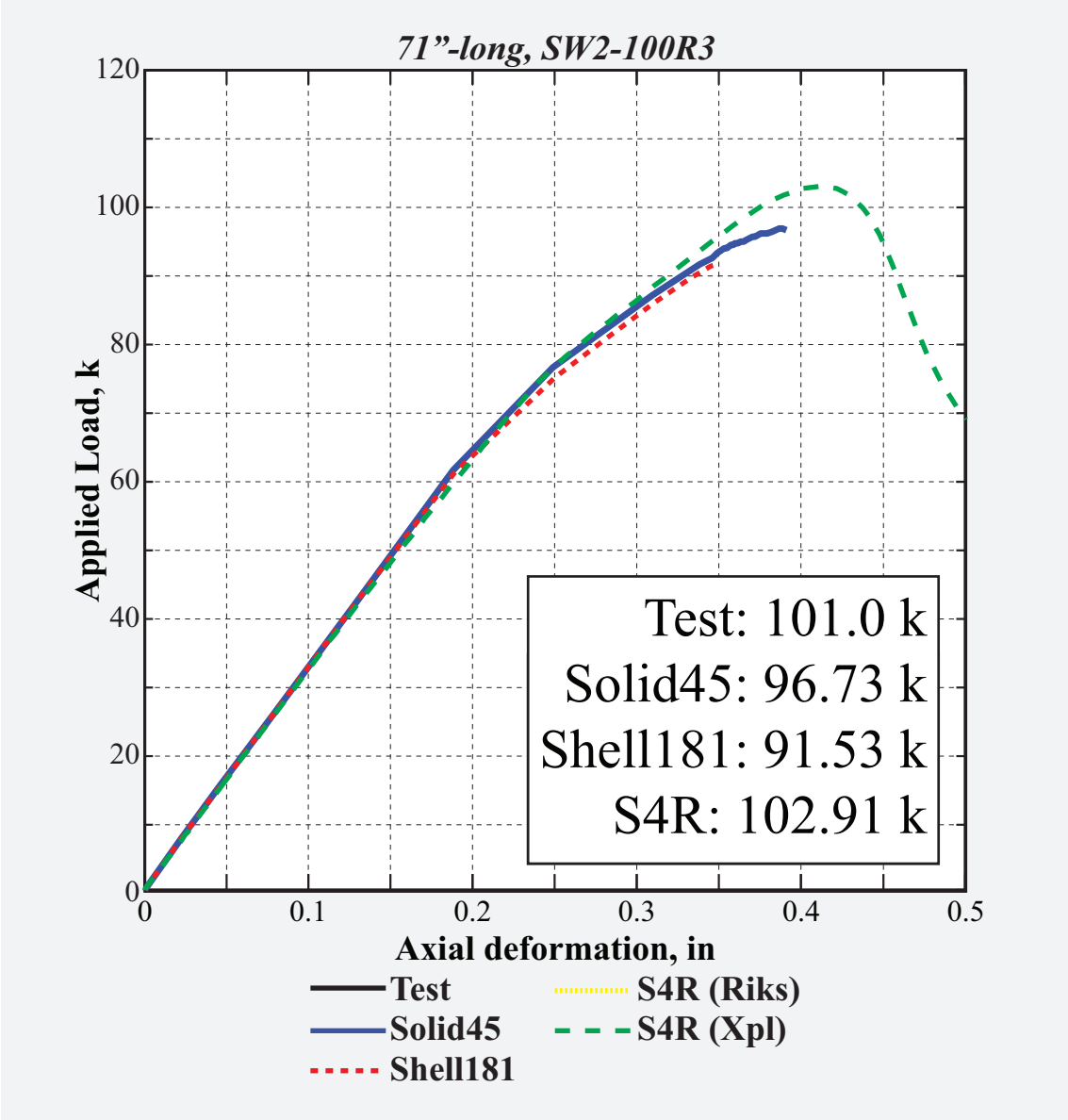


Figure 114: Load vs. deformation history of 71”-long, 0.1”-thick *SW2-R3*.

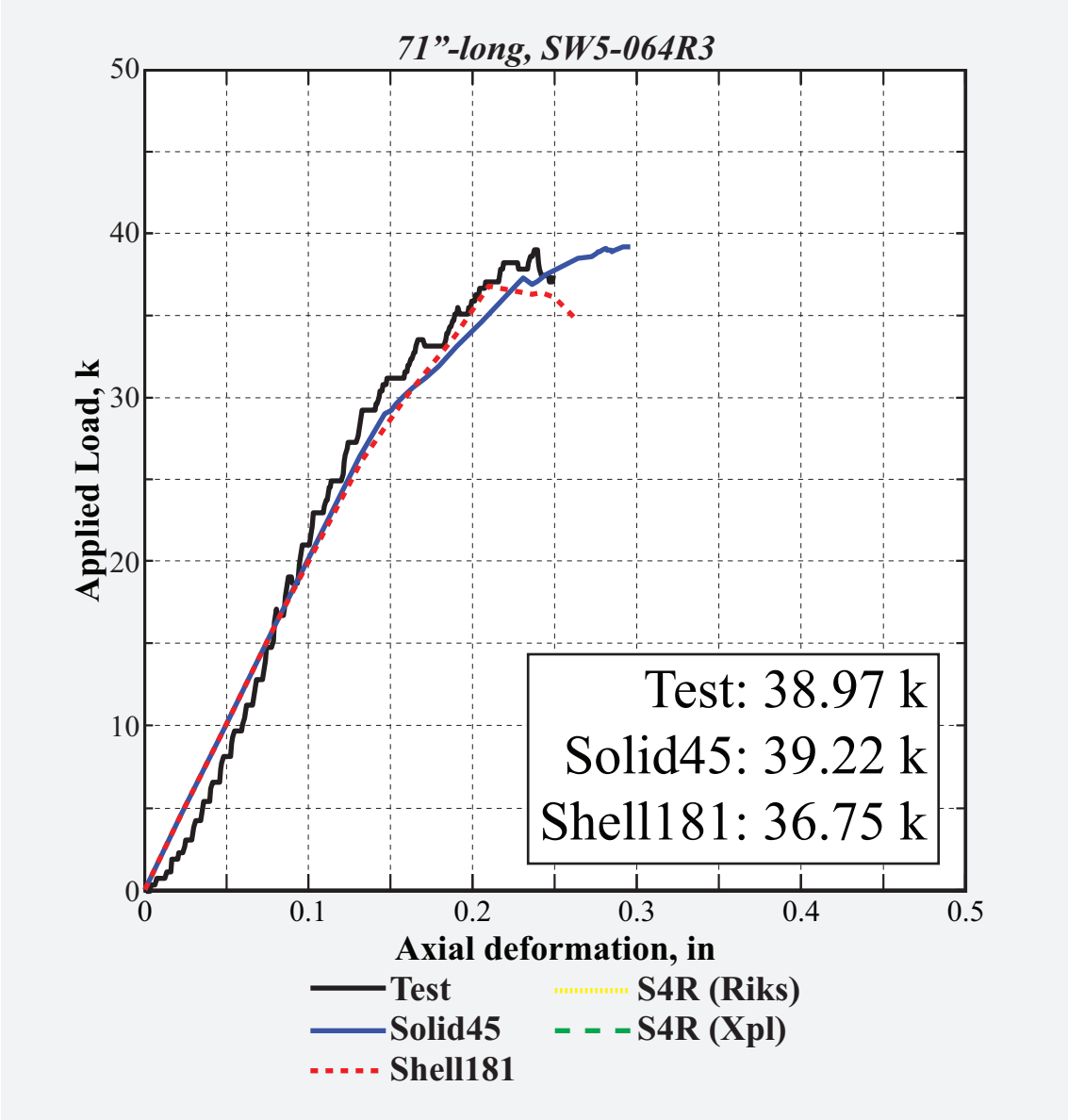


Figure 115: Load vs. deformation history of 71”-long, 0.064”-thick *SW5-R3*.

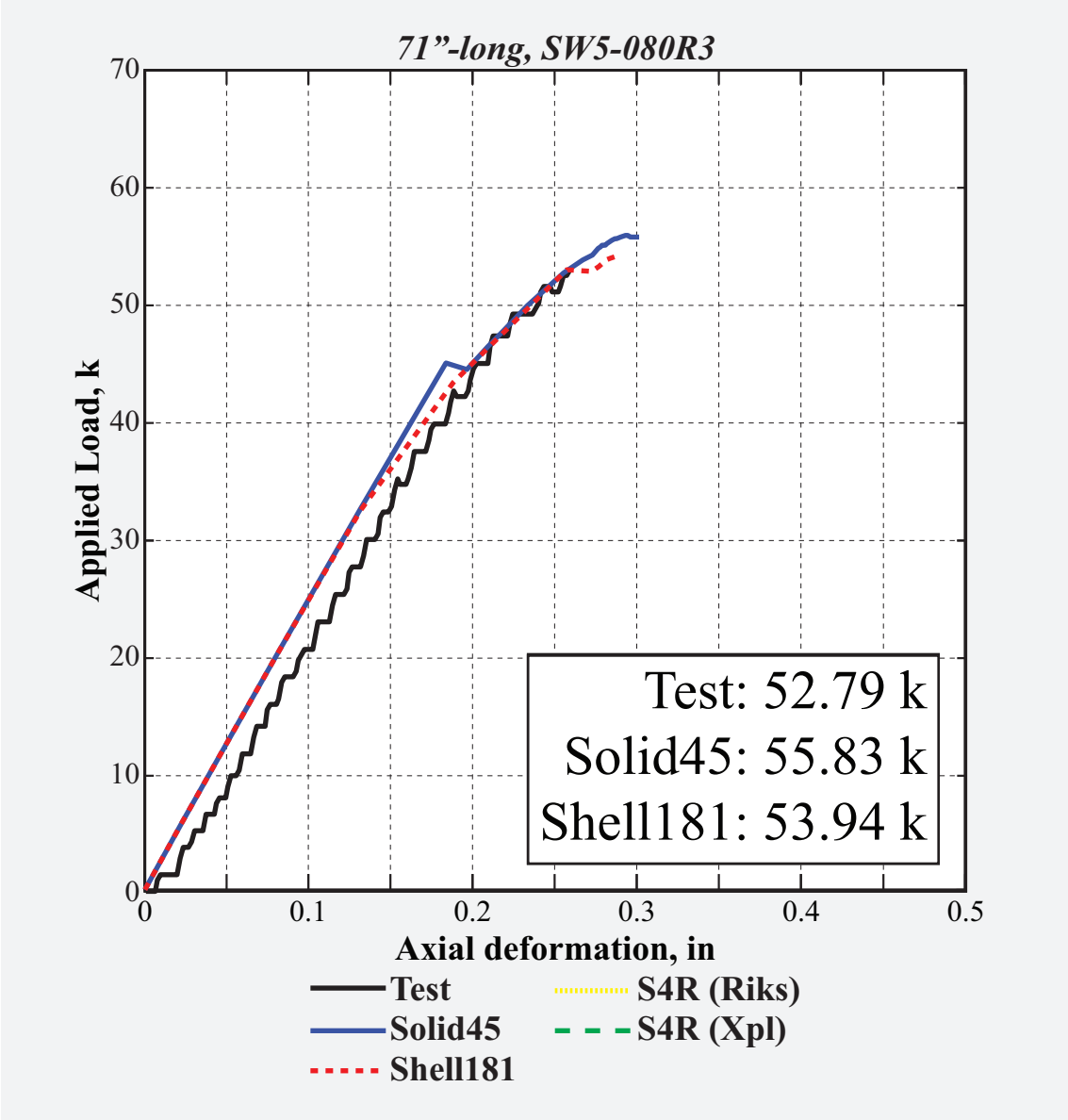


Figure 116: Load vs. deformation history of 71”-long, 0.08”-thick *SW5-R3*.

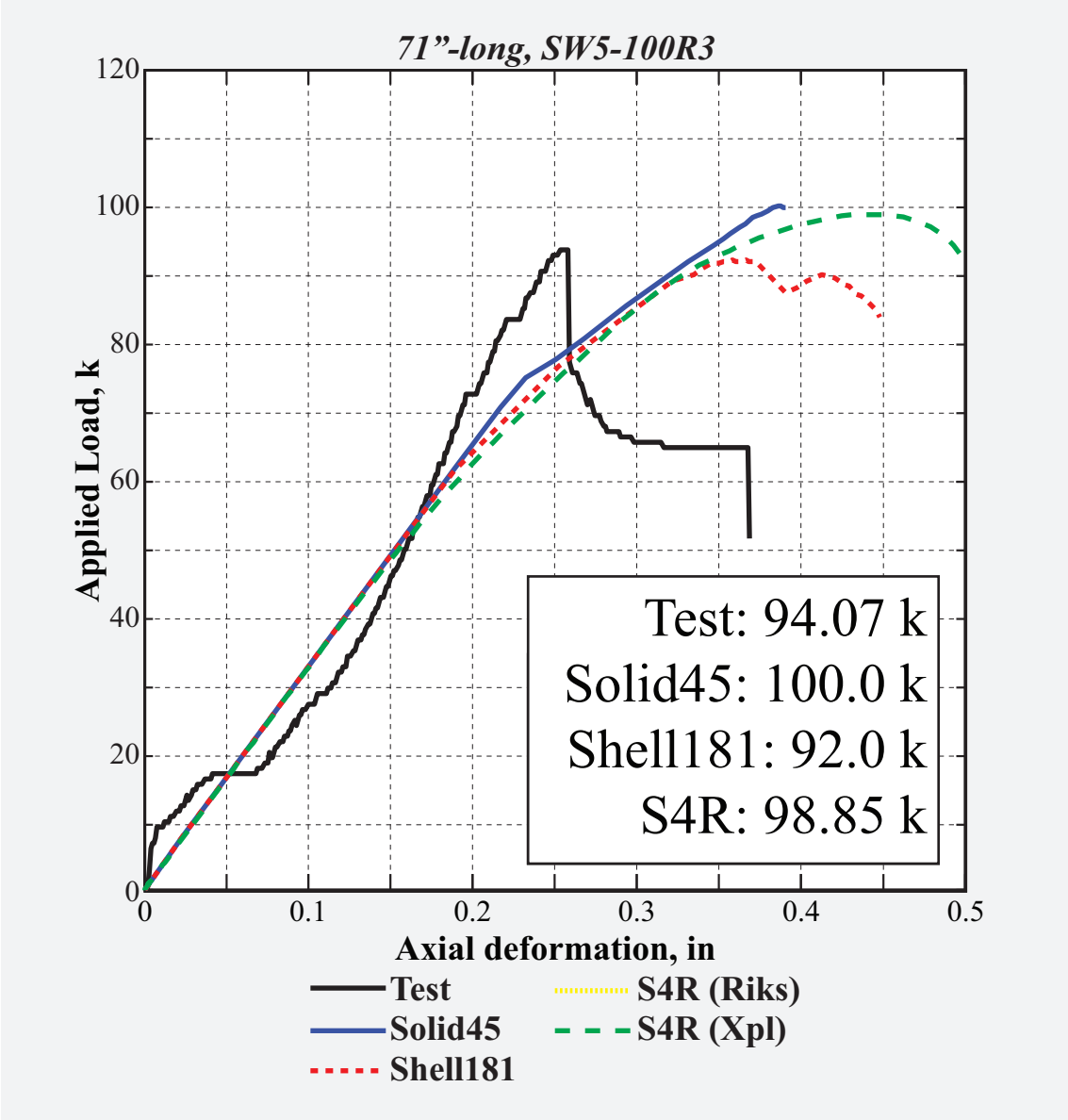


Figure 117: Load vs. deformation history of 71”-long, 0.1”-thick *SW5-R3*.

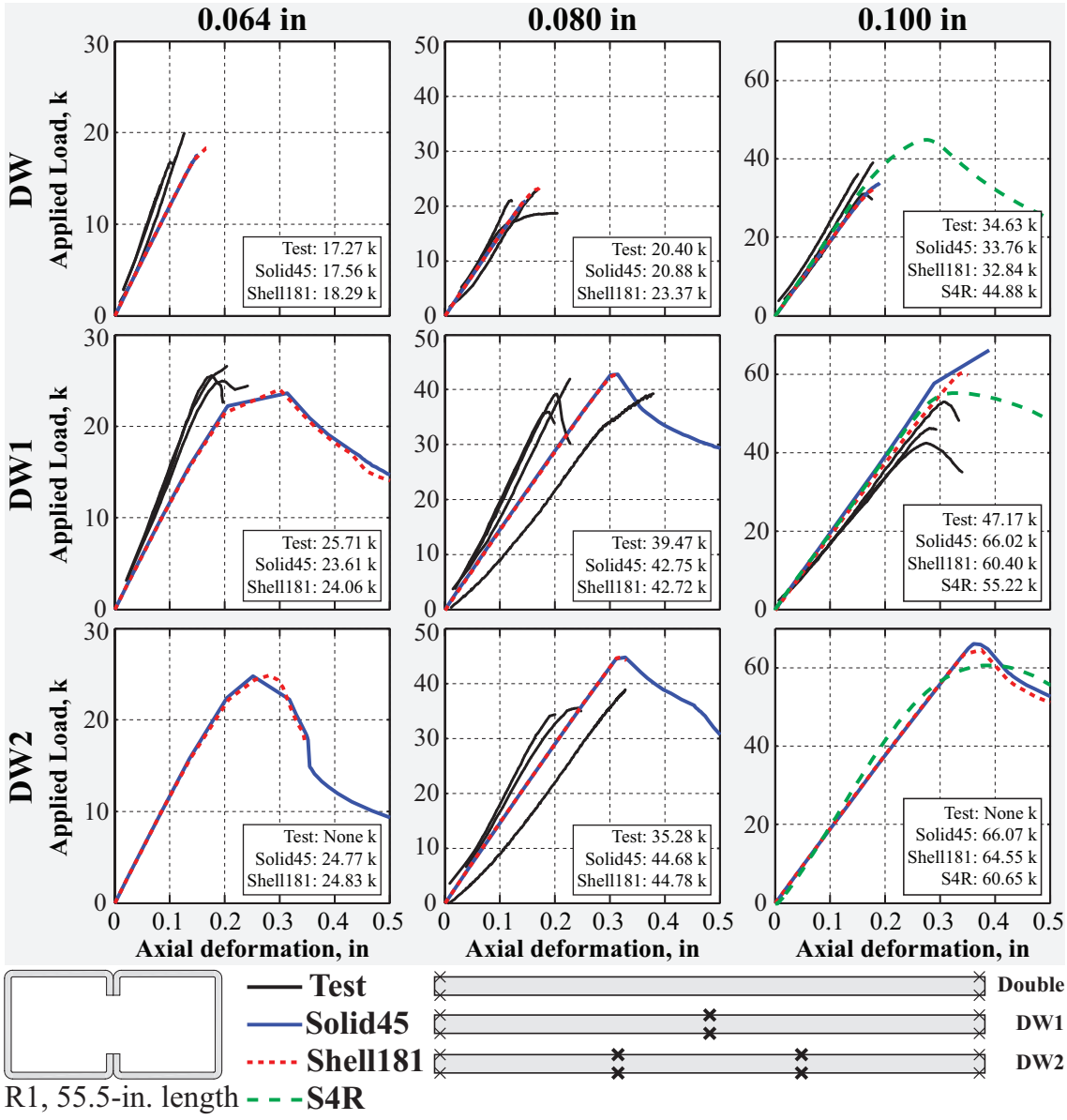


Figure 118: Overview of load vs. deformation history of 55.5”-long, double-sided *R1*-sections presented Figs. 119-127.

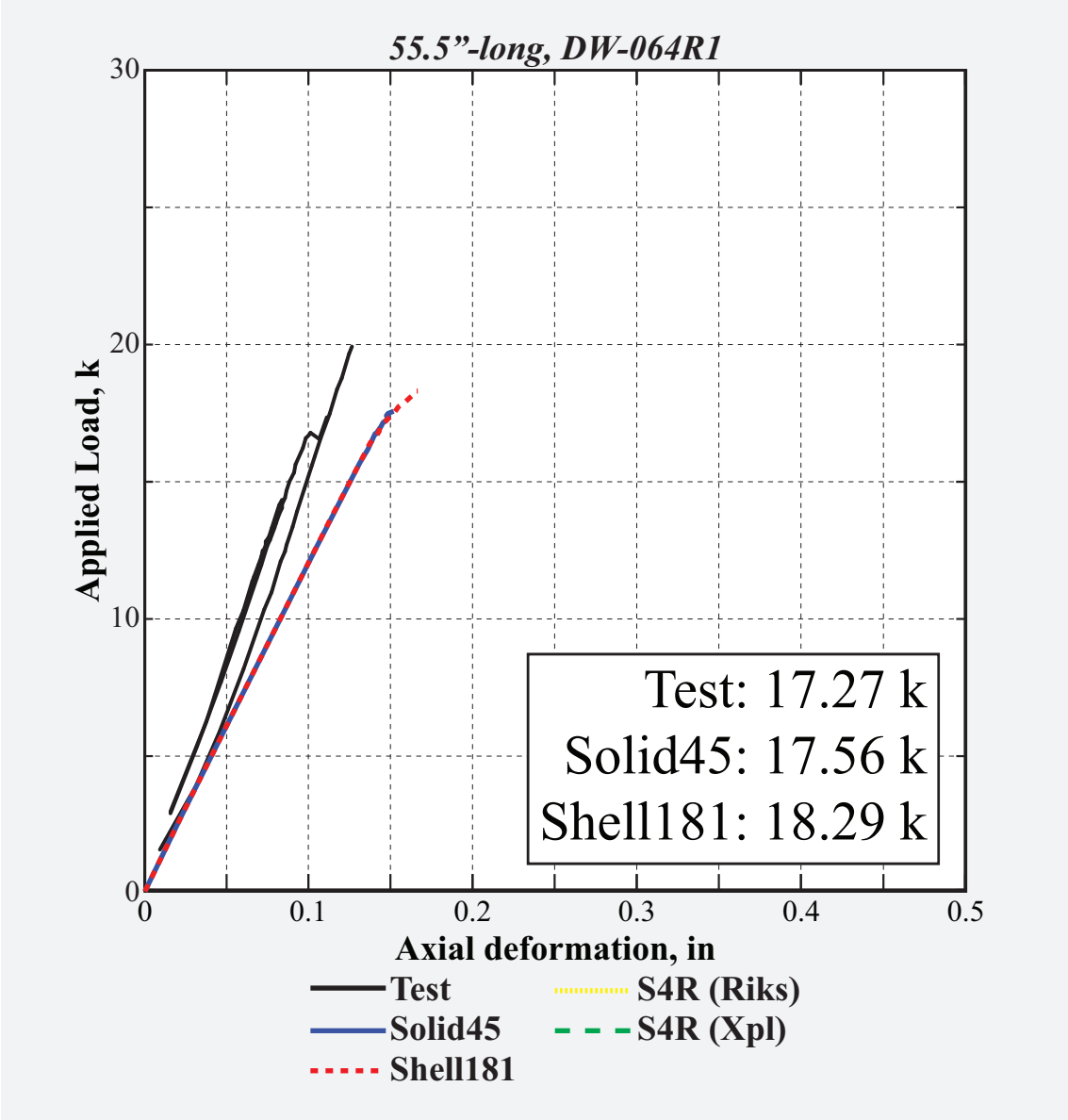


Figure 119: Load vs. deformation history of 55.5”-long, 0.064”-thick *DW-R1*.

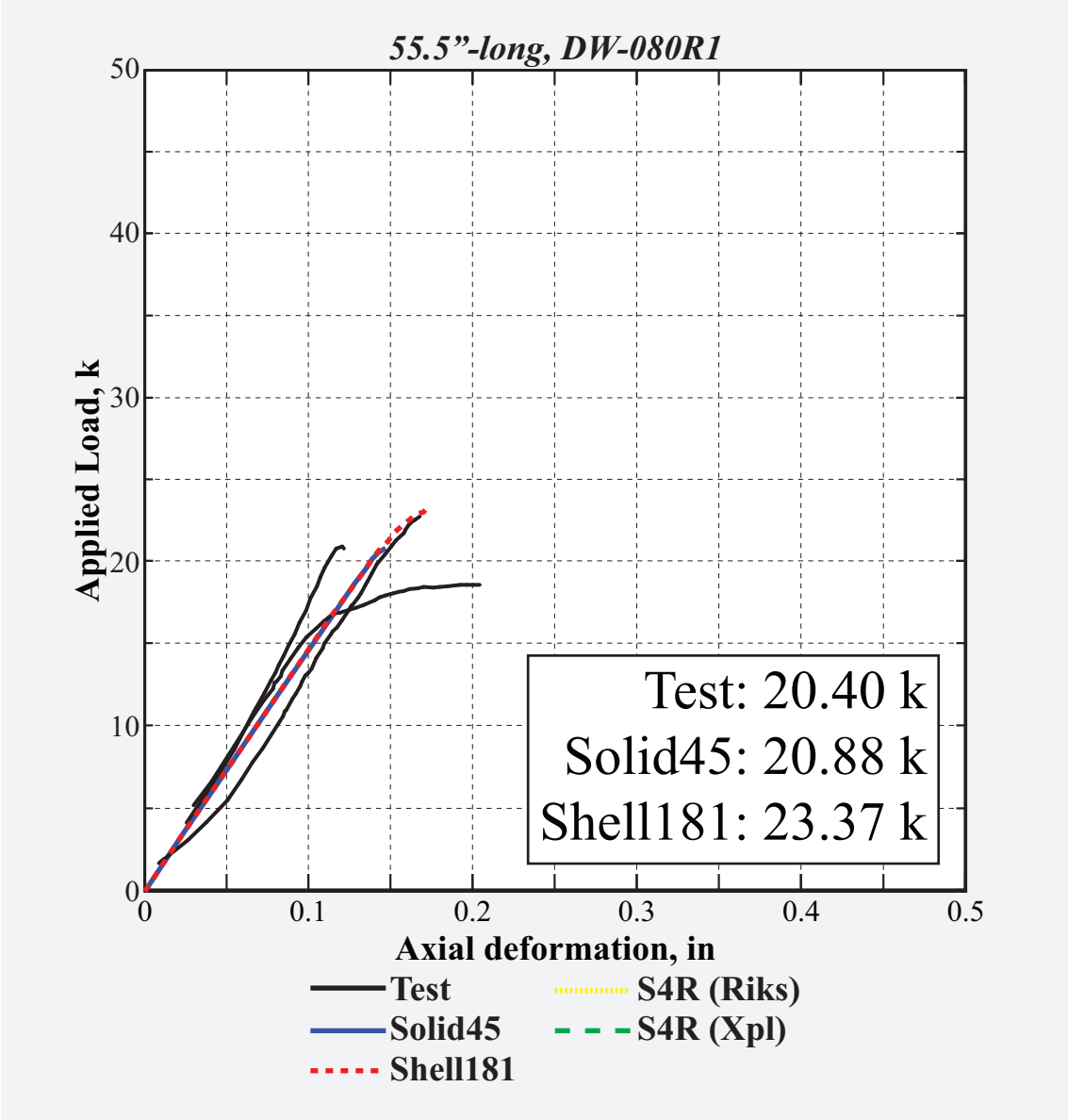


Figure 120: Load vs. deformation history of 55.5”-long, 0.08”-thick *DW-R1*.

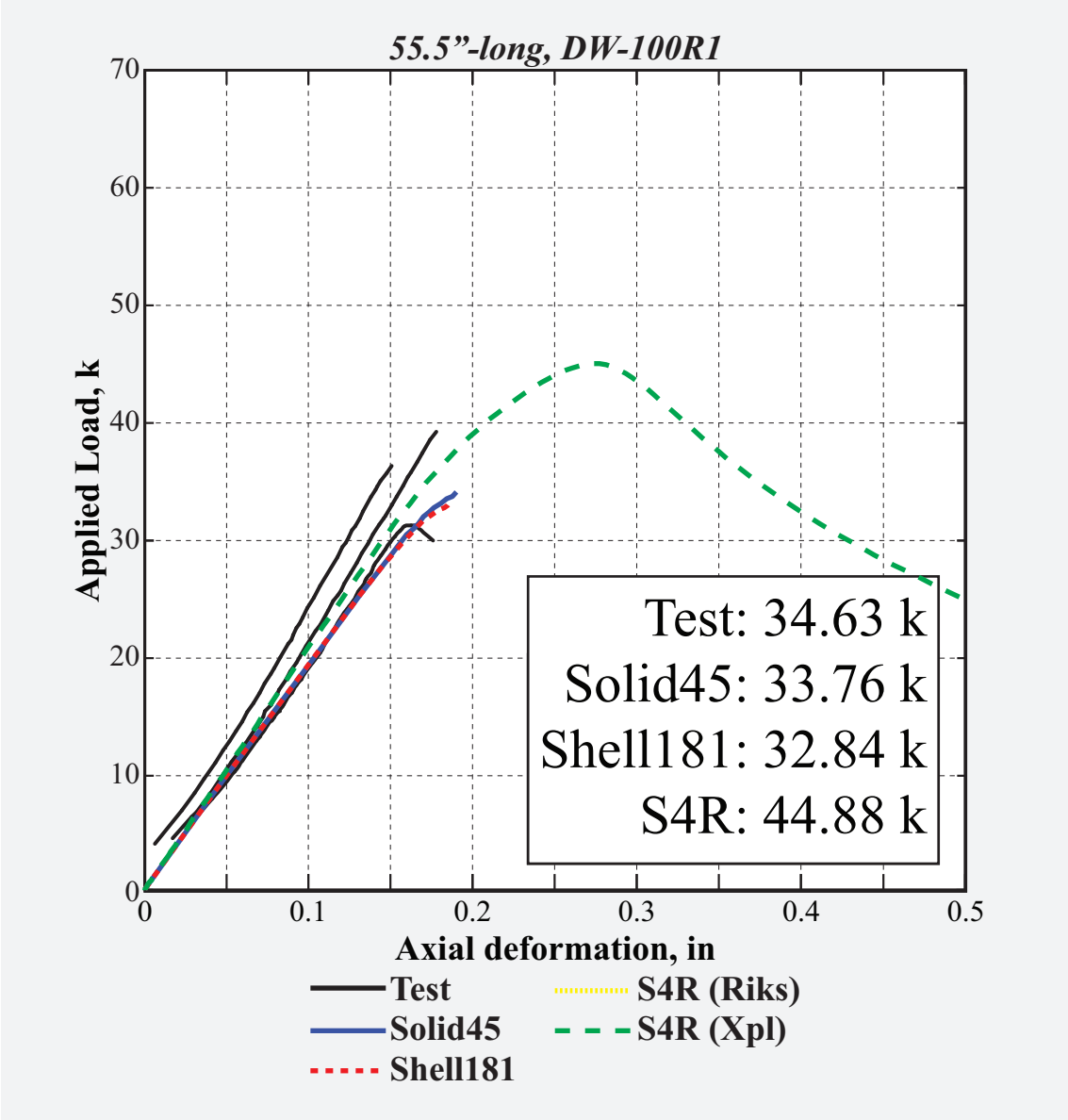


Figure 121: Load vs. deformation history of 55.5”-long, 0.1”-thick *DW-R1*.

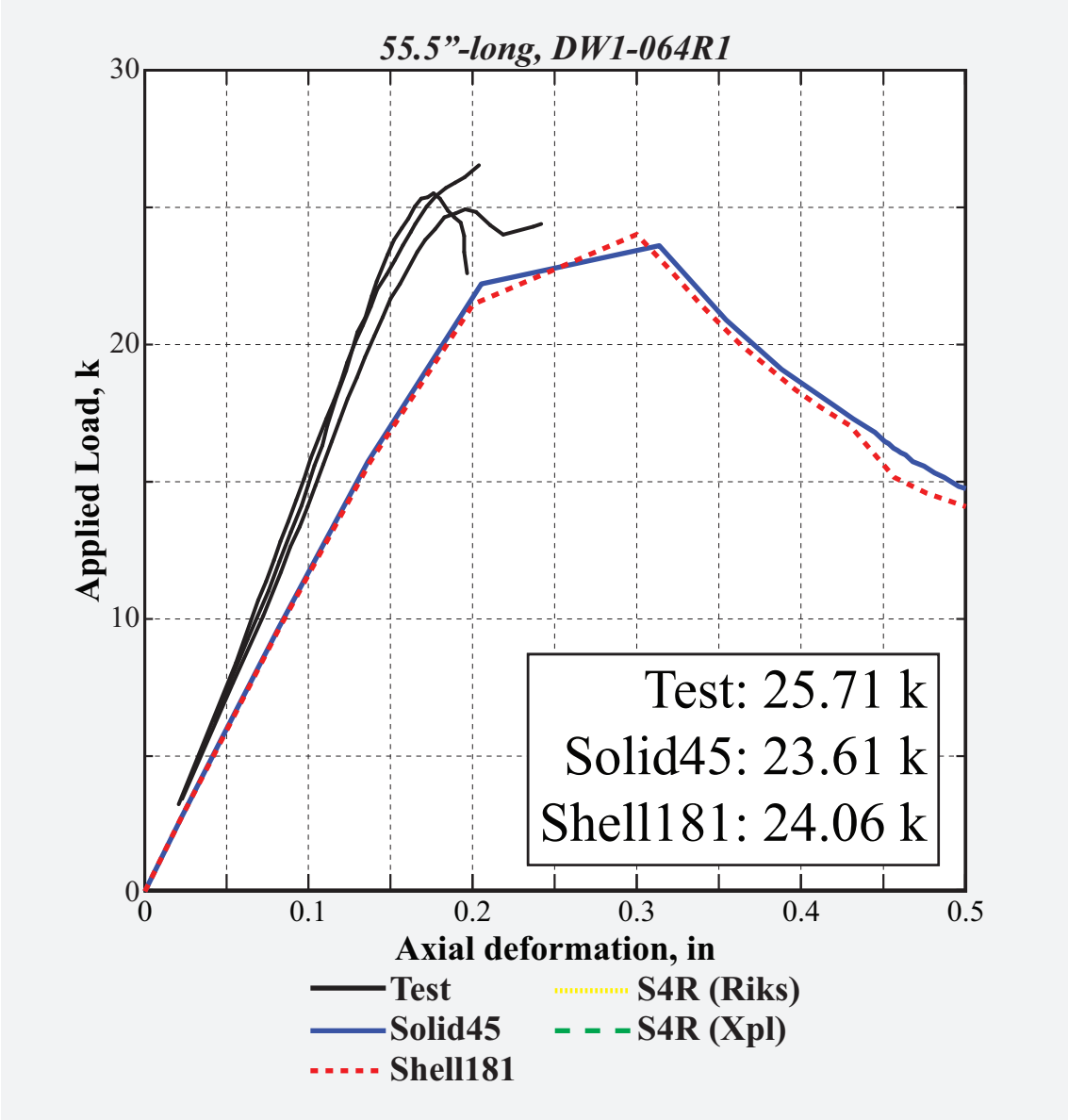


Figure 122: Load vs. deformation history of 55.5”-long, 0.064”-thick *DW1-R1*.

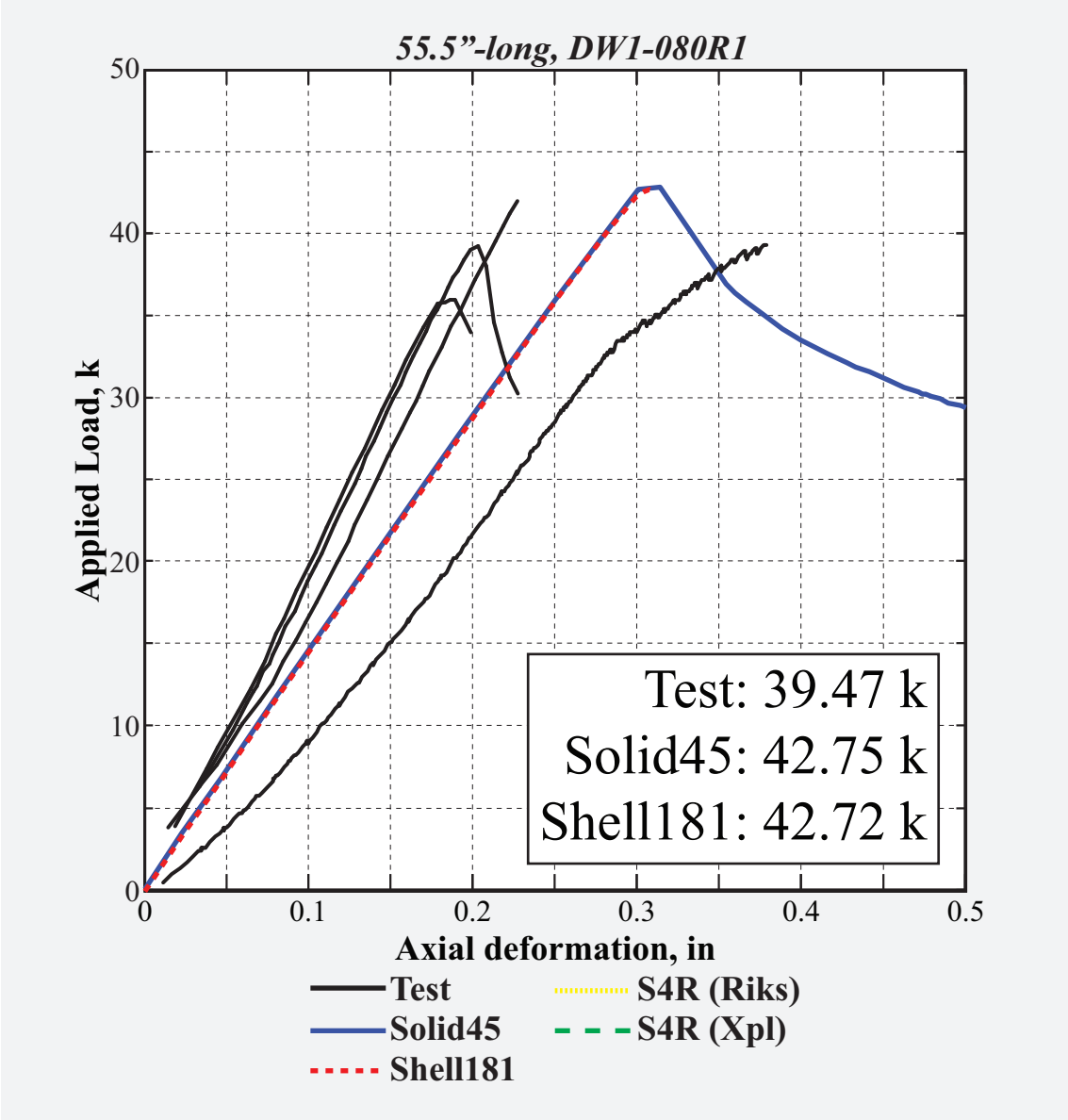


Figure 123: Load vs. deformation history of 55.5”-long, 0.08”-thick *DW1-R1*.

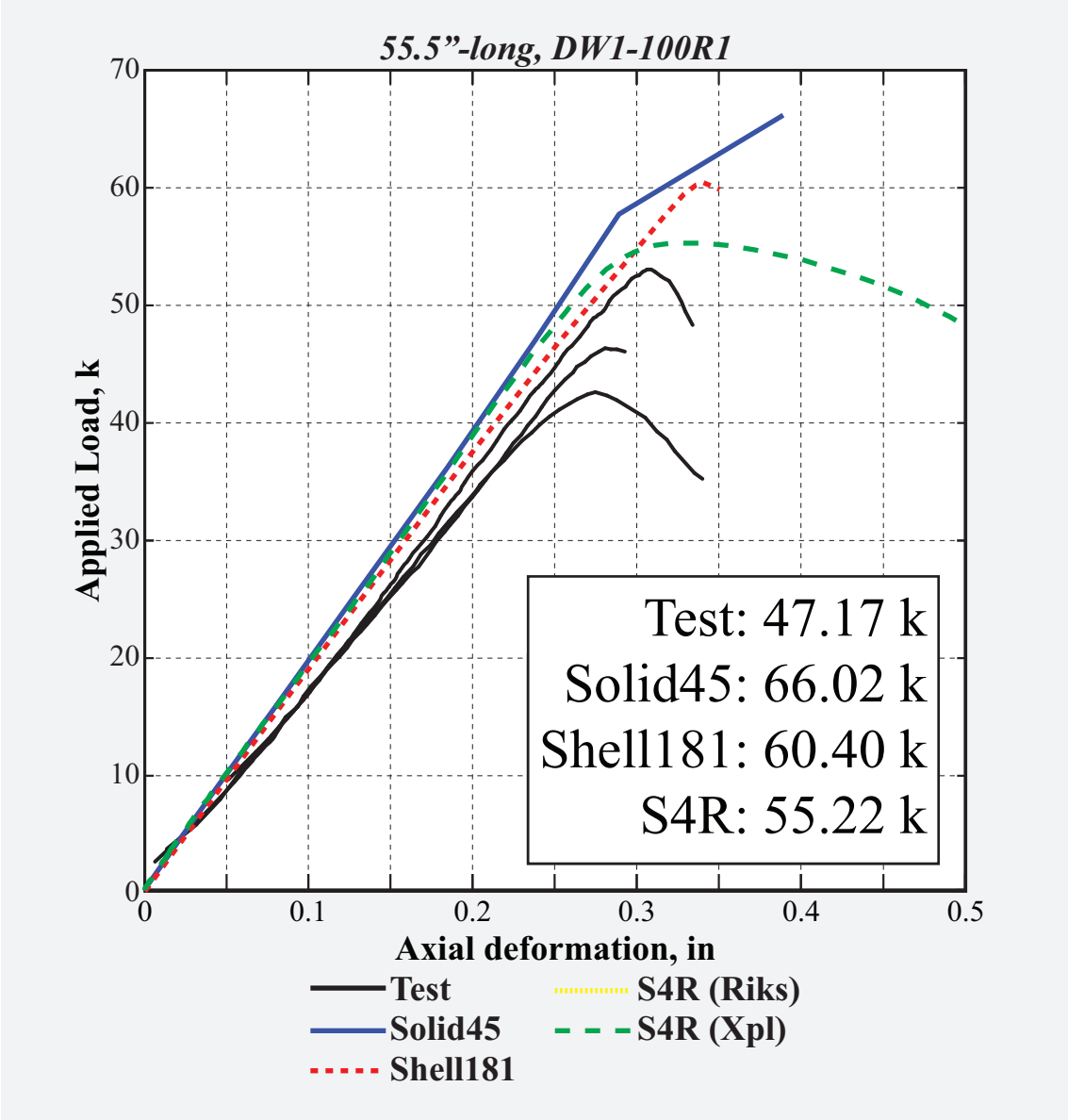


Figure 124: Load vs. deformation history of 55.5”-long, 0.1”-thick *DW1-R1*.

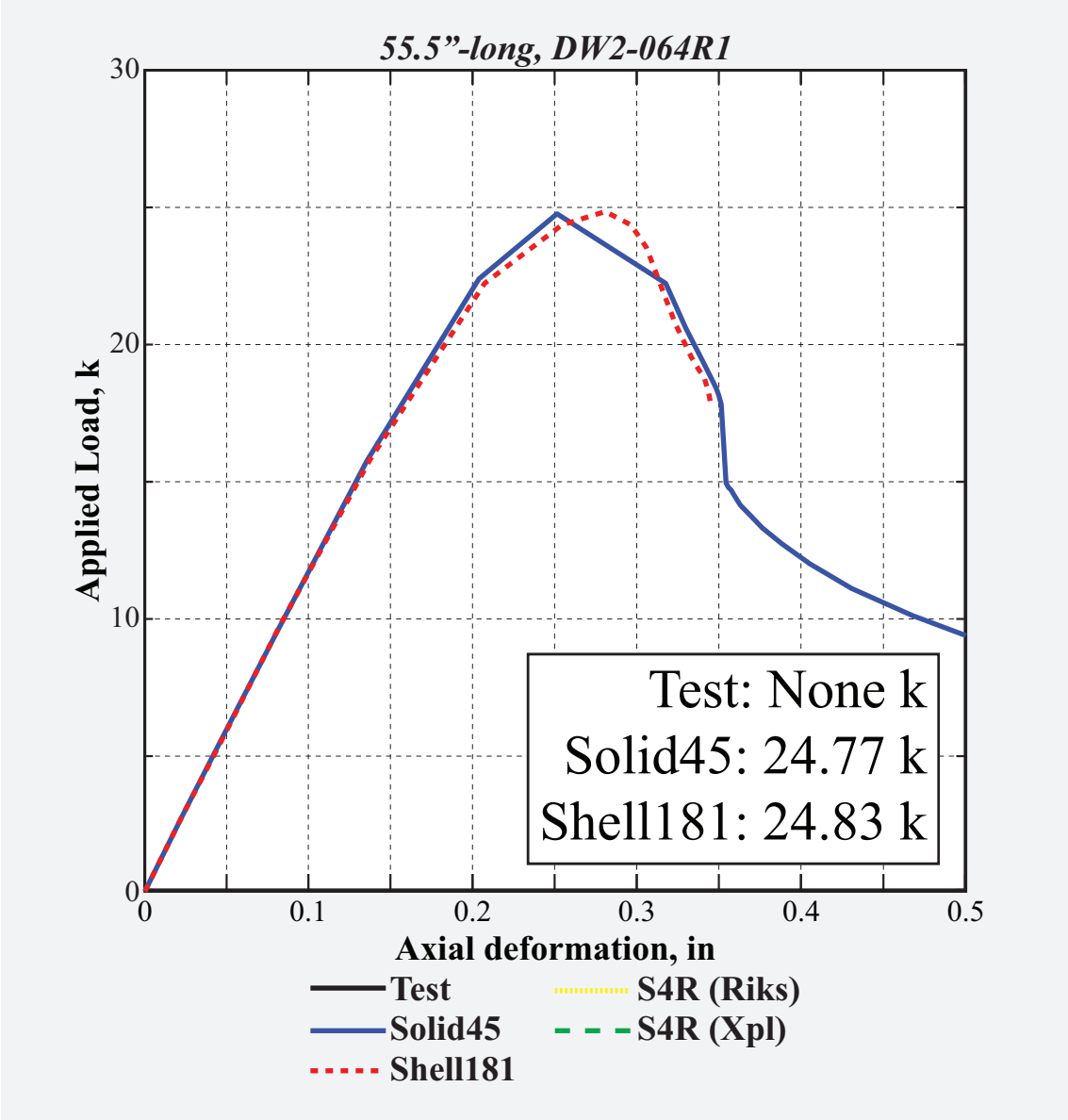


Figure 125: Load vs. deformation history of 55.5”-long, 0.064”-thick *DW2-R1*.

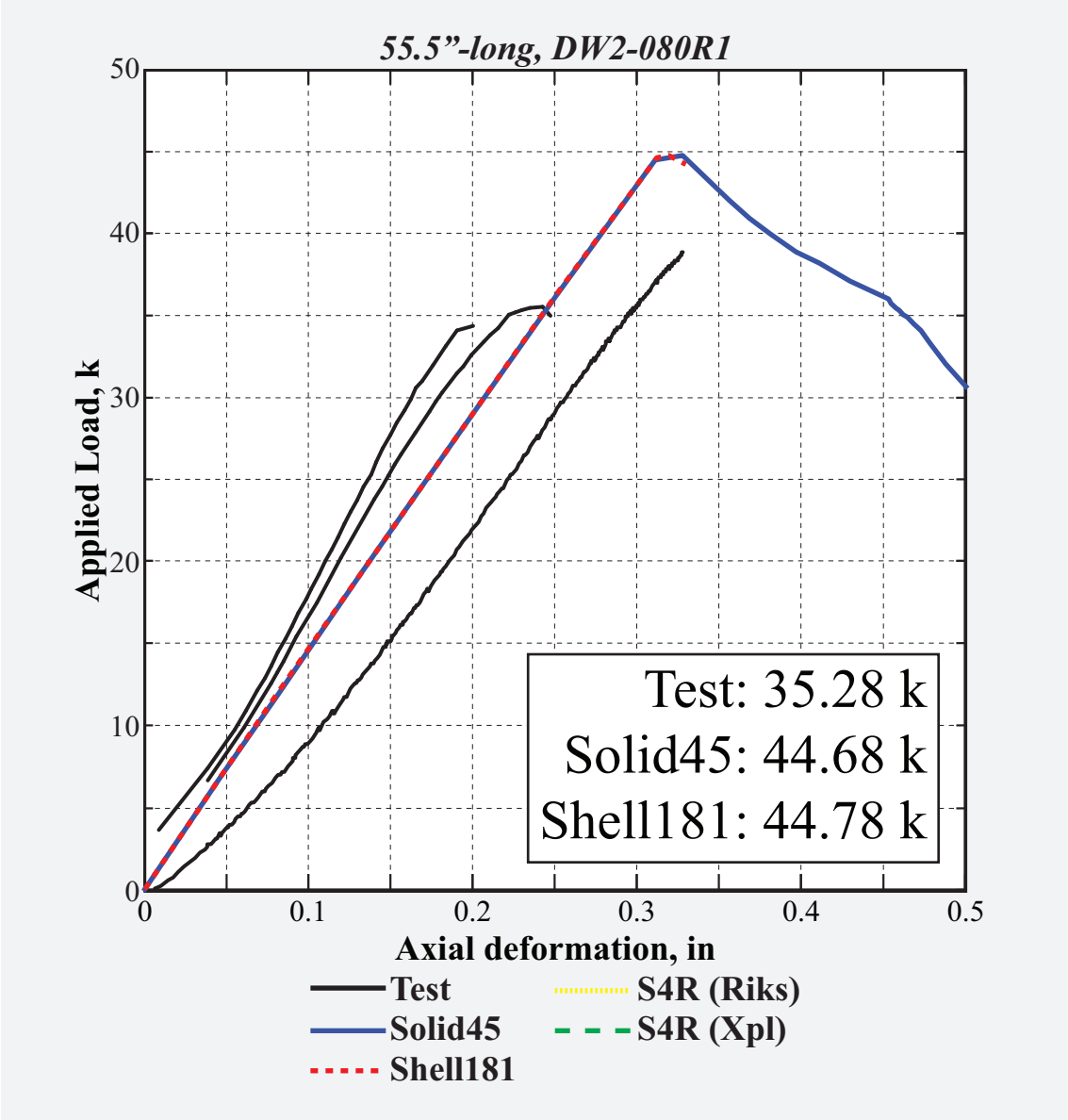


Figure 126: Load vs. deformation history of 55.5”-long, 0.08”-thick *DW2-R1*.

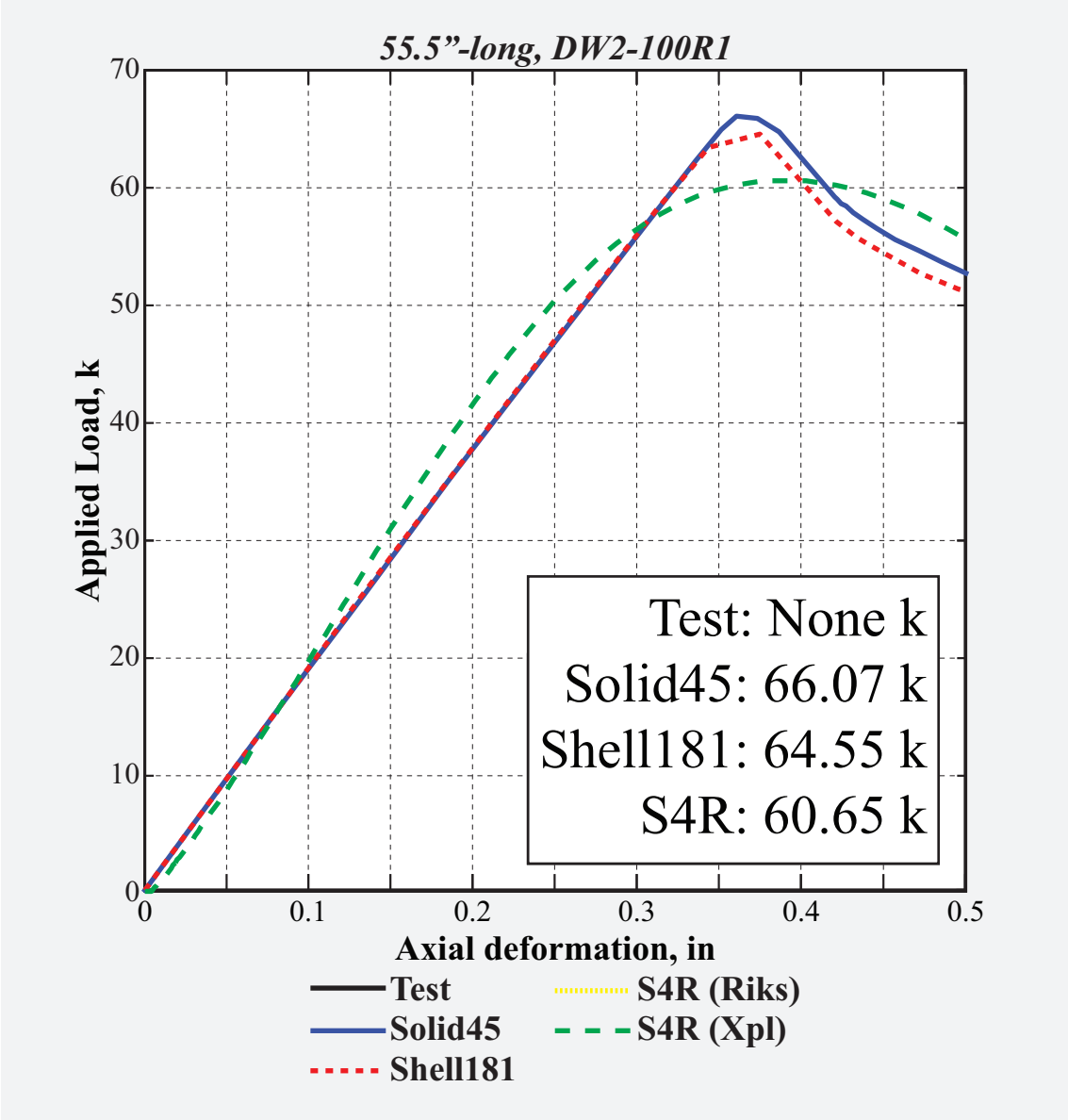


Figure 127: Load vs. deformation history of 55.5”-long, 0.1”-thick *DW2-R1*.

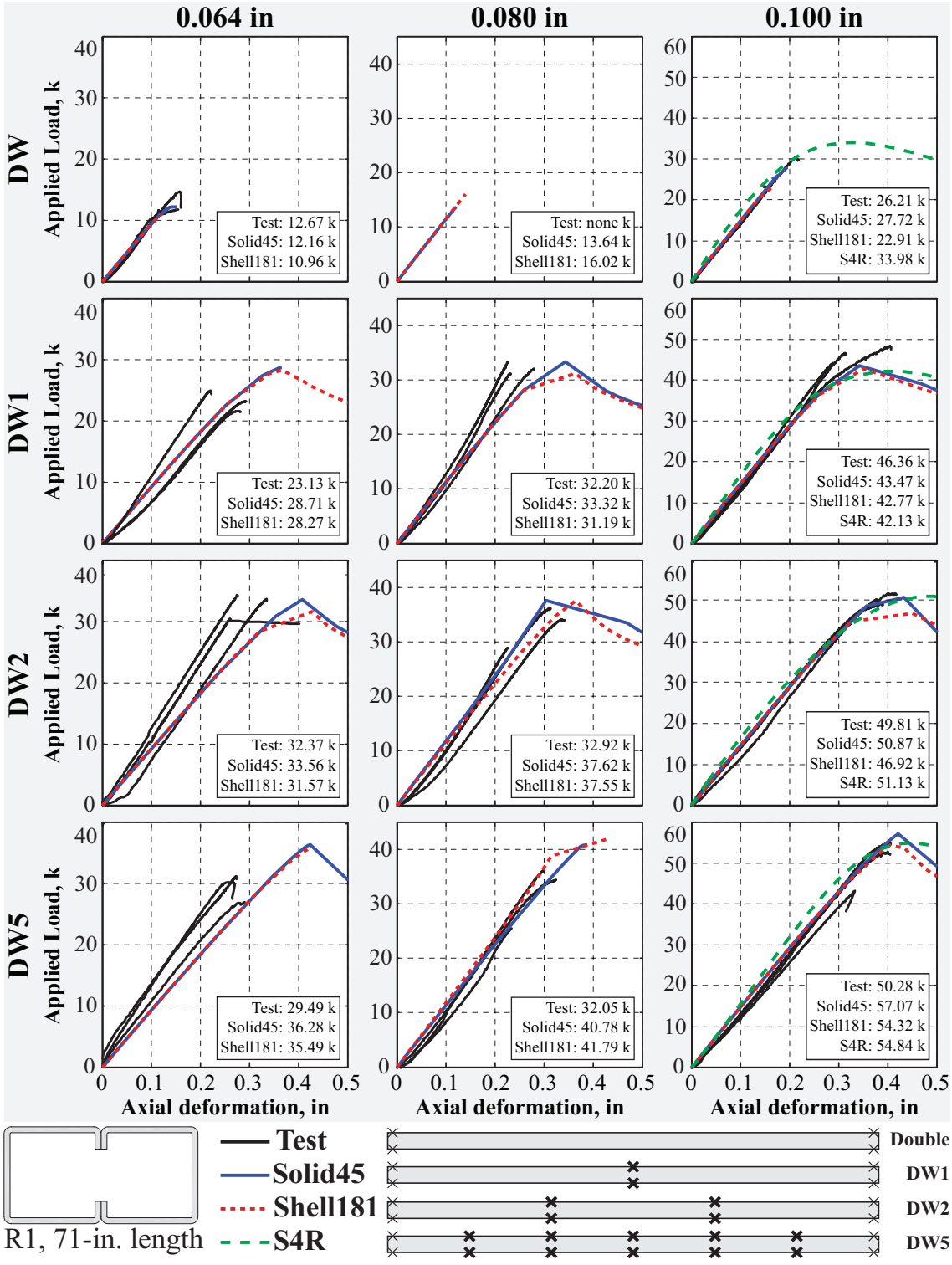


Figure 128: Overview of load vs. deformation history of 71”-long, double-sided *R1*-sections presented in Figs. 129-140.

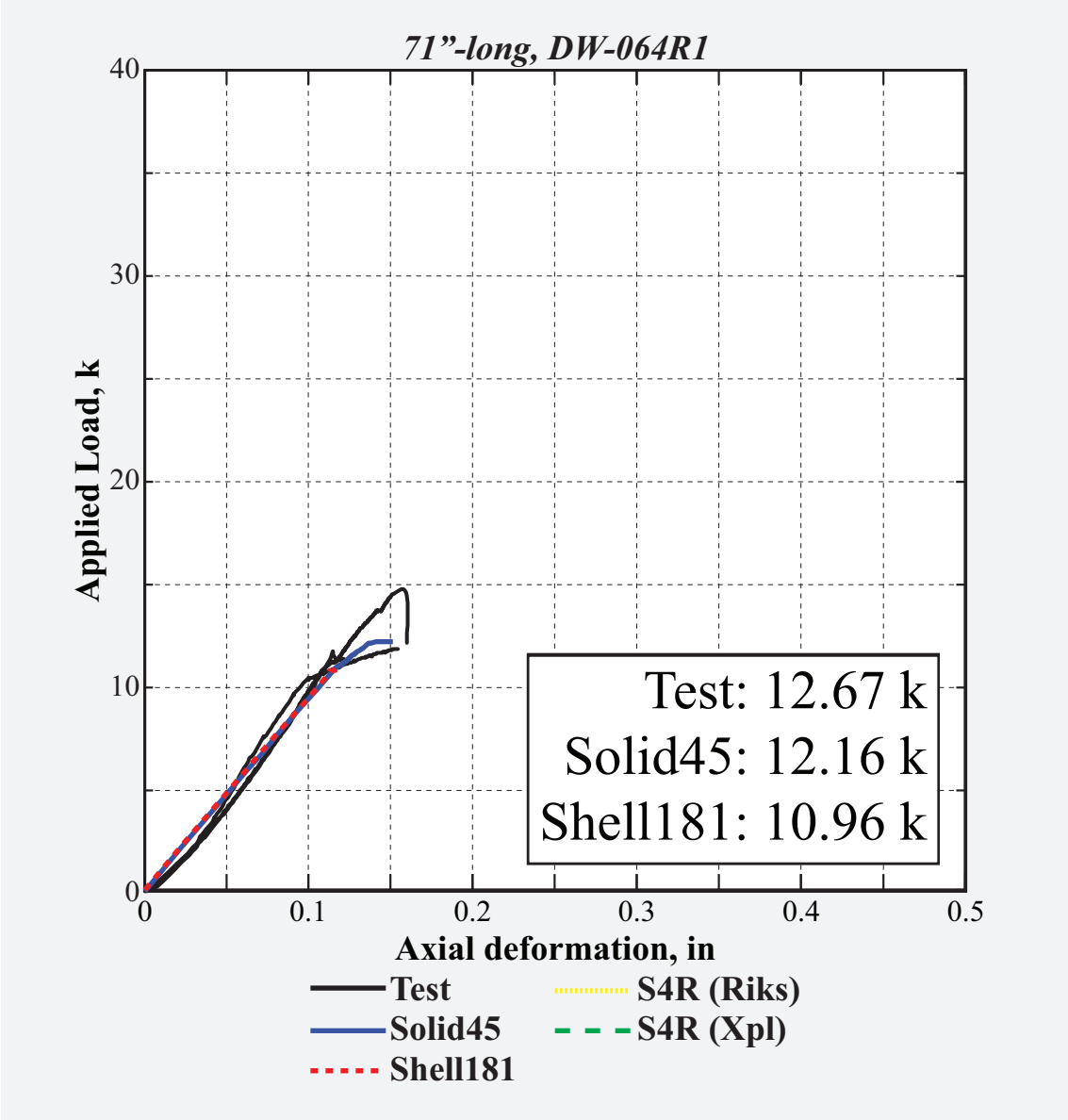


Figure 129: Load vs. deformation history of 71”-long, 0.064”-thick *DW-R1*.

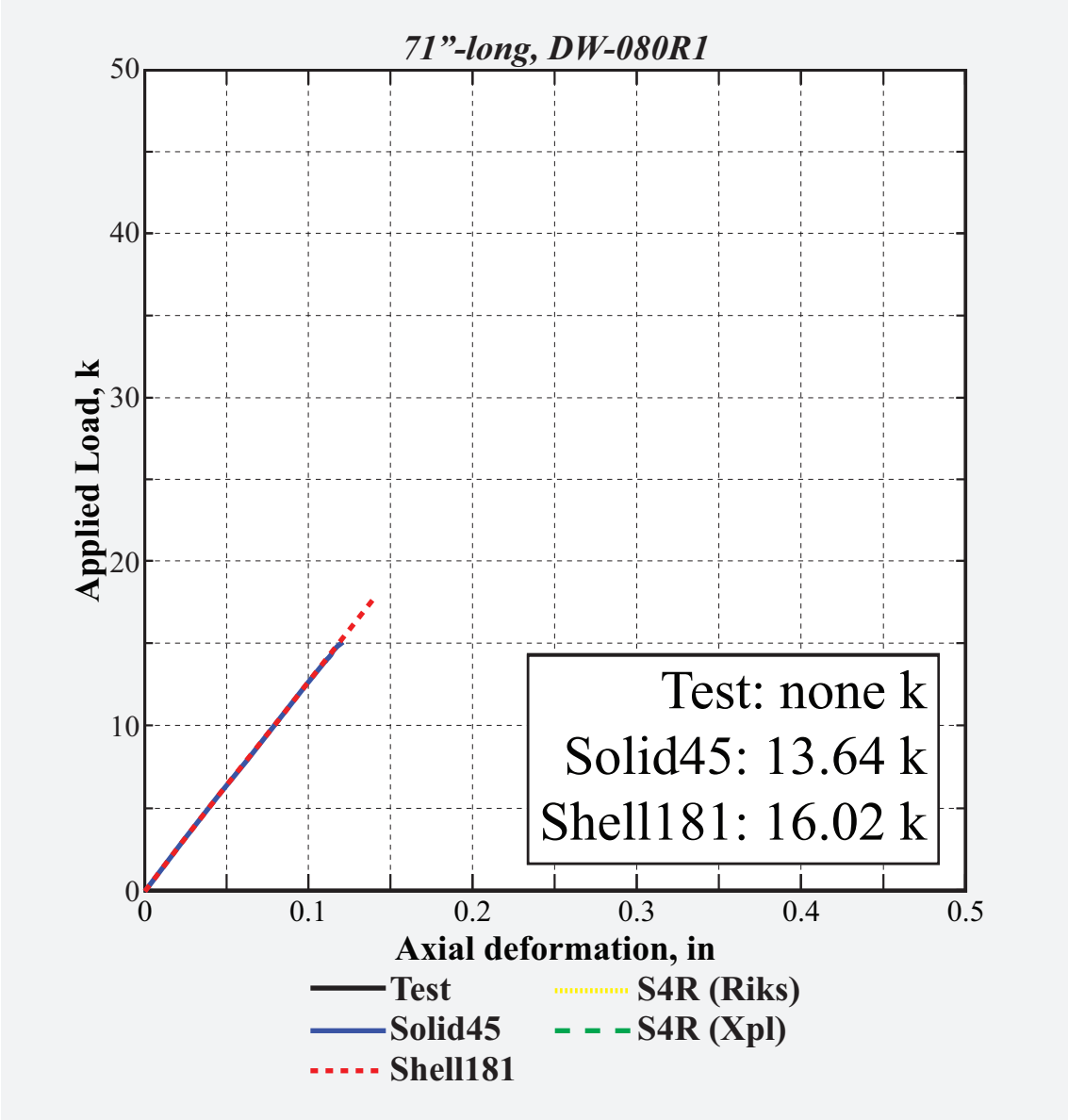


Figure 130: Load vs. deformation history of 71”-long, 0.08”-thick *DW-R1*.

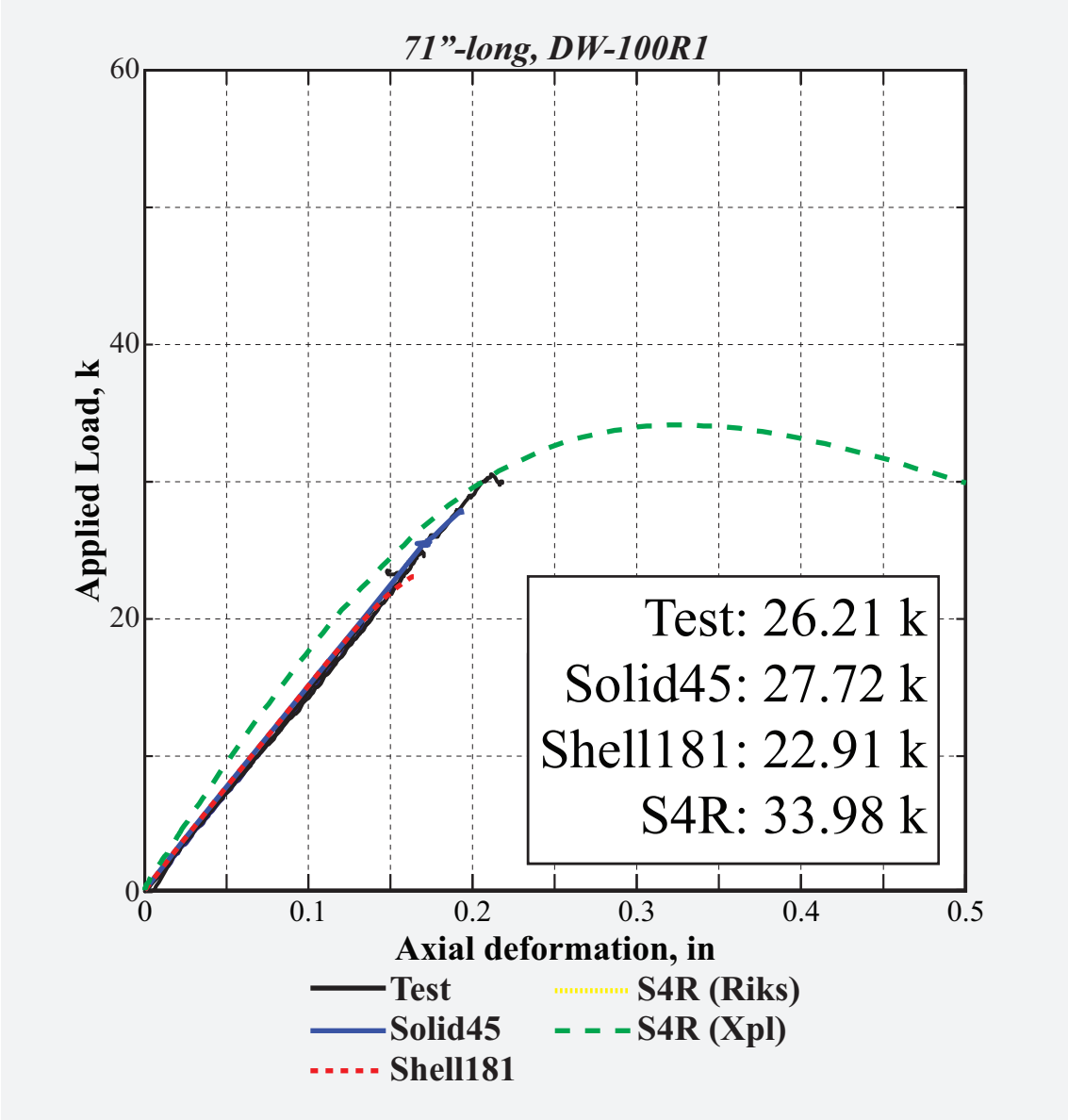


Figure 131: Load vs. deformation history of 71”-long, 0.1”-thick *DW-R1*.

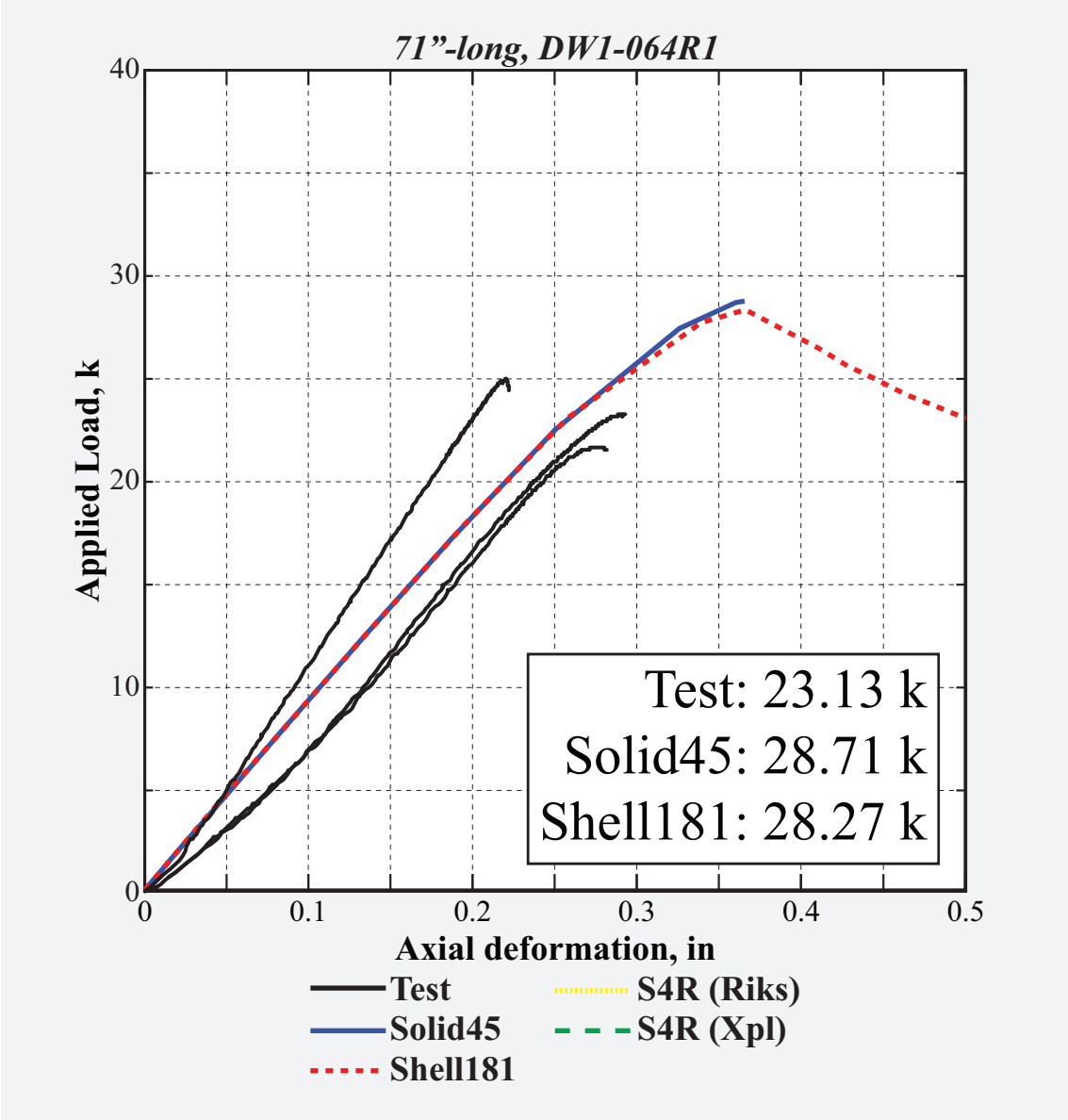


Figure 132: Load vs. deformation history of 71”-long, 0.064”-thick *DW1-R1*.

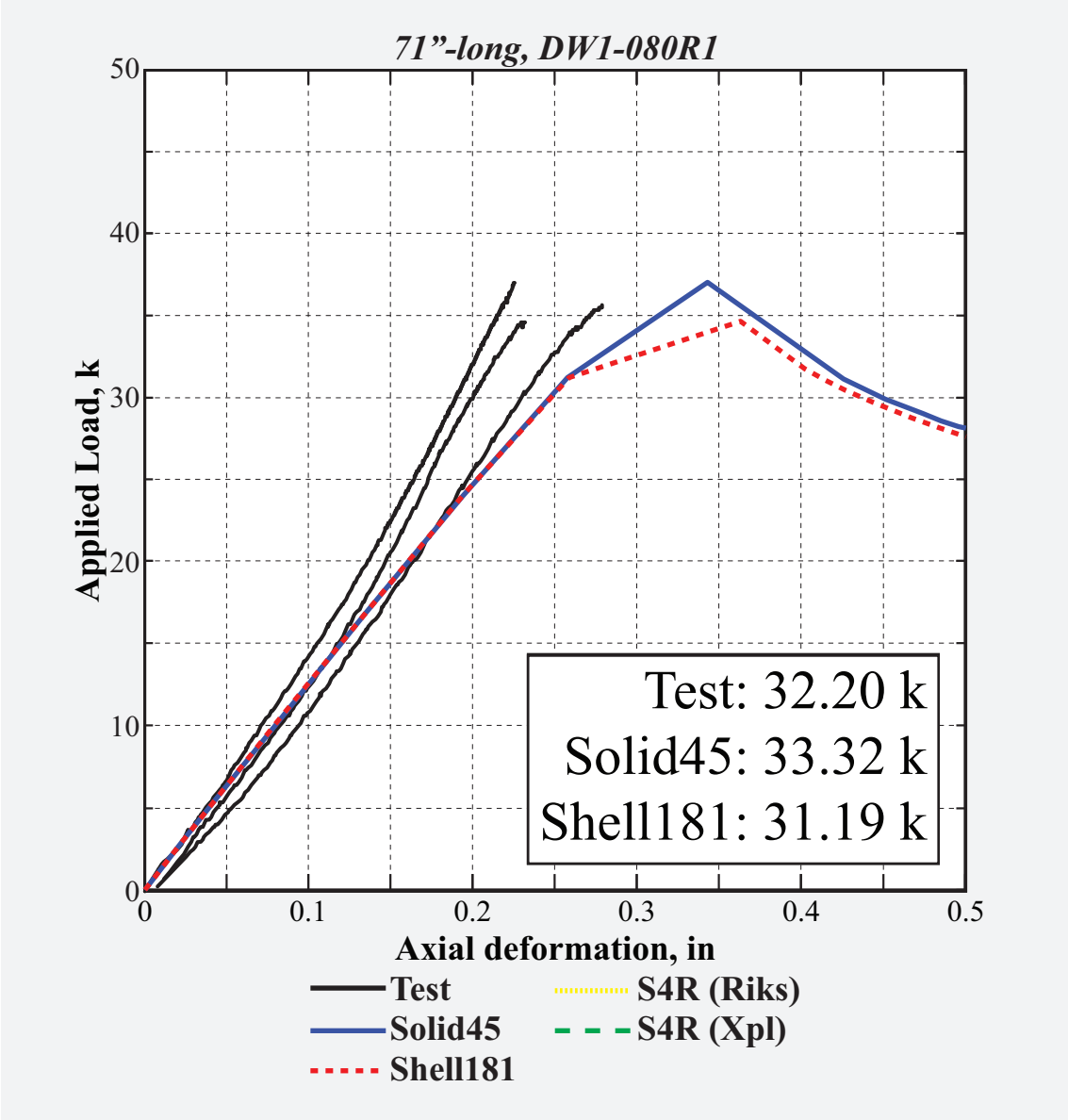


Figure 133: Load vs. deformation history of 71”-long, 0.08”-thick *DW1-R1*.

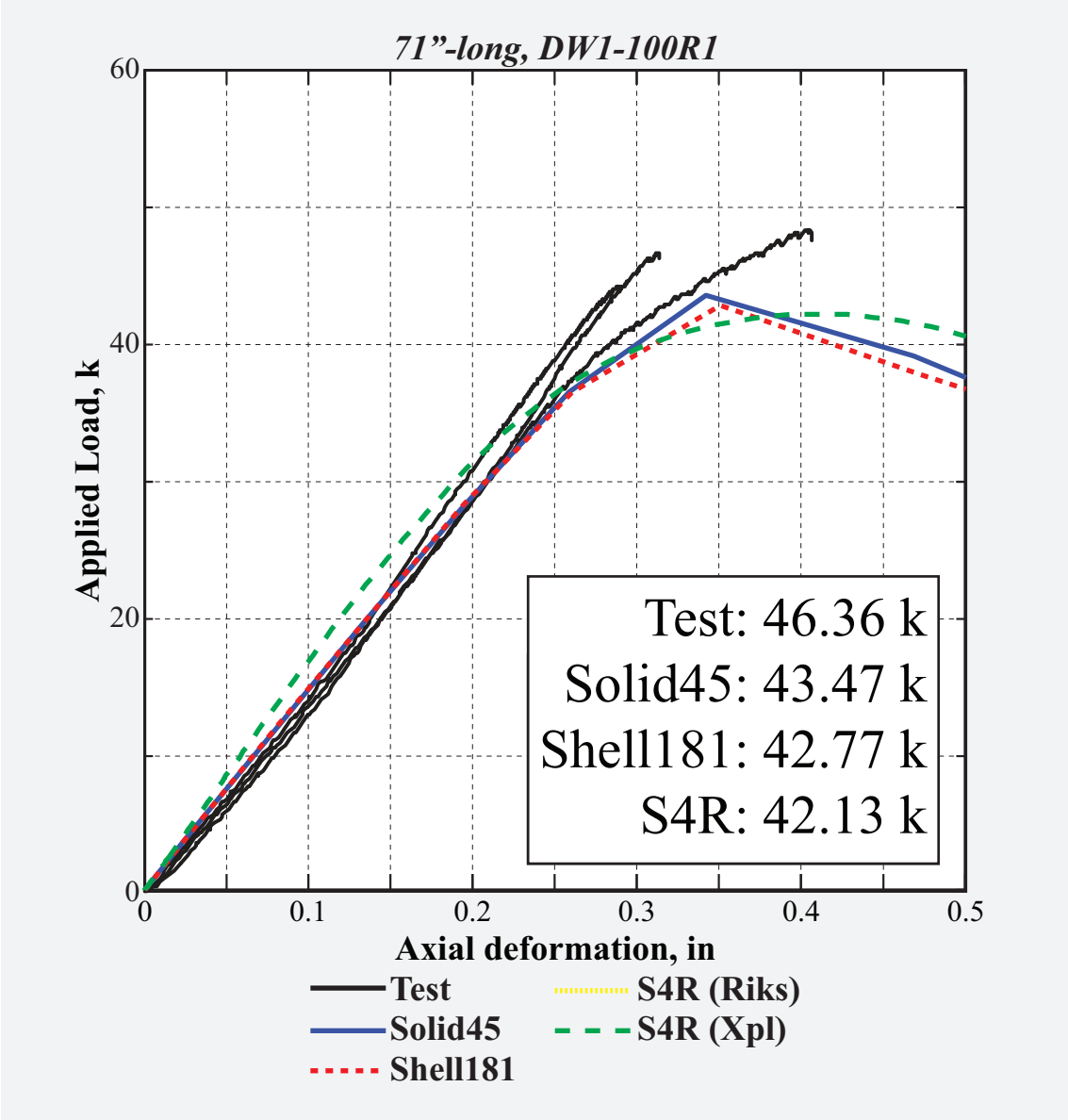


Figure 134: Load vs. deformation history of 71”-long, 0.1”-thick *DW1-R1*.

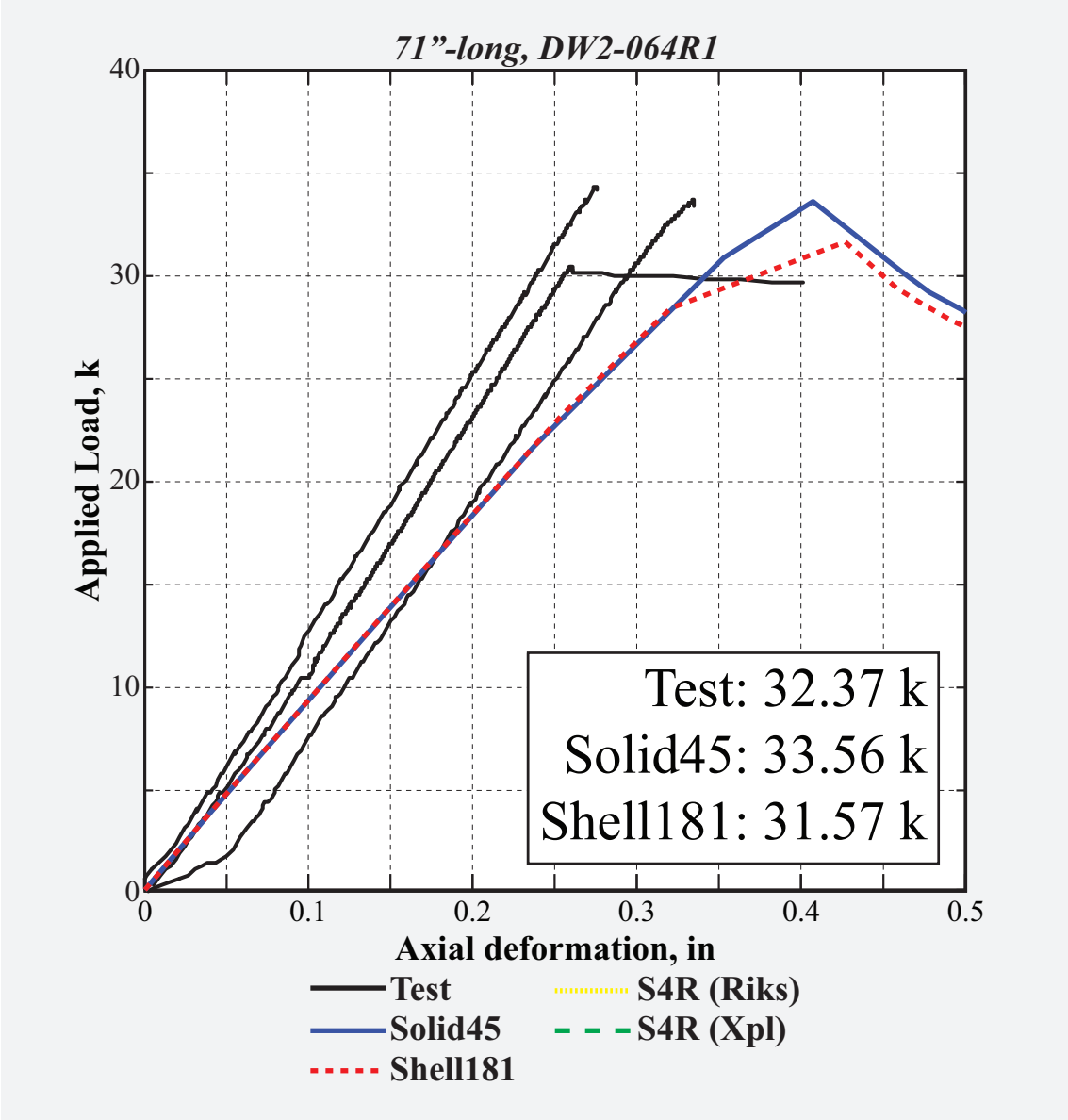


Figure 135: Load vs. deformation history of 71”-long, 0.064”-thick *DW2-R1*.

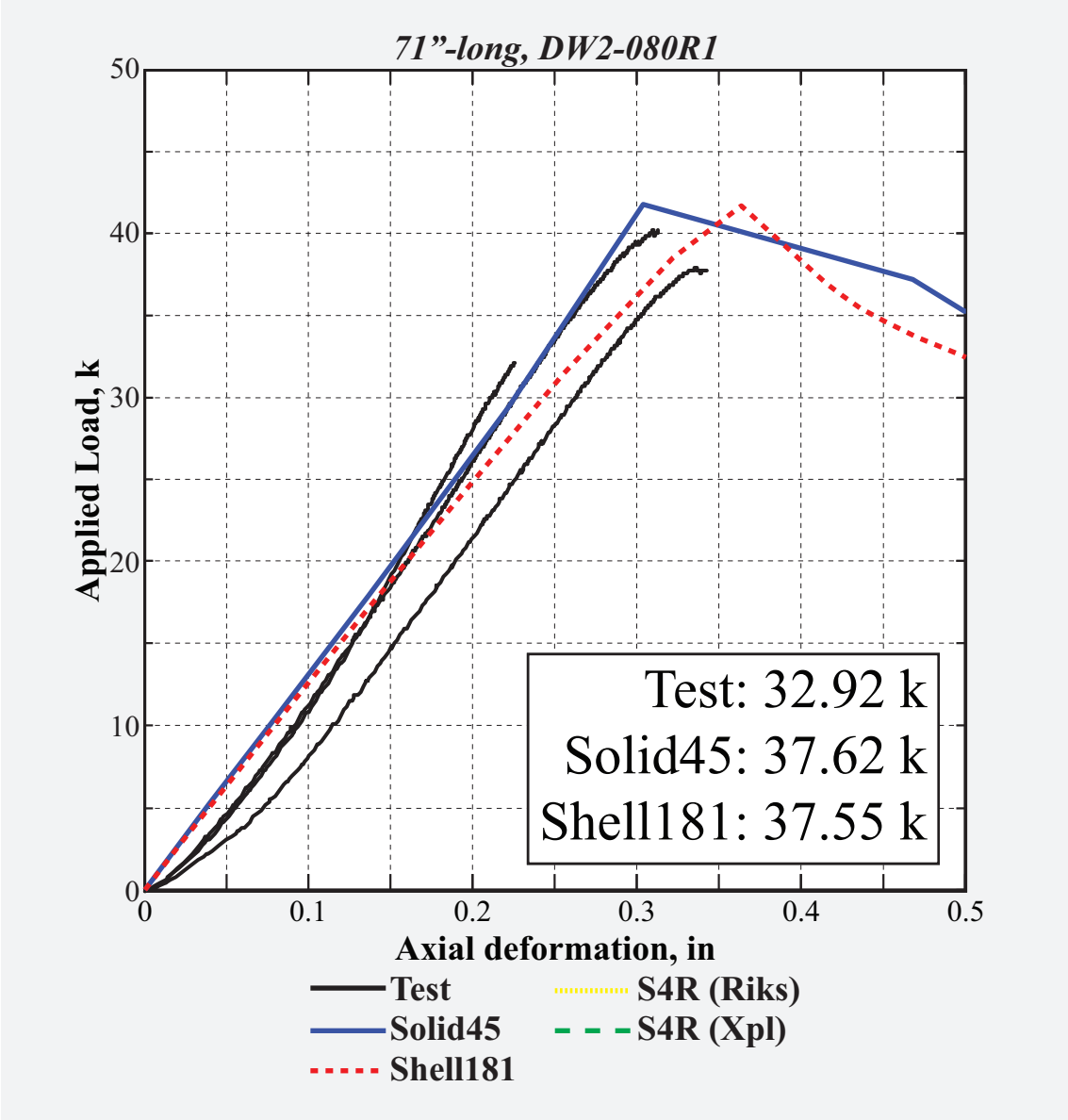


Figure 136: Load vs. deformation history of 71”-long, 0.08”-thick *DW2-R1*.

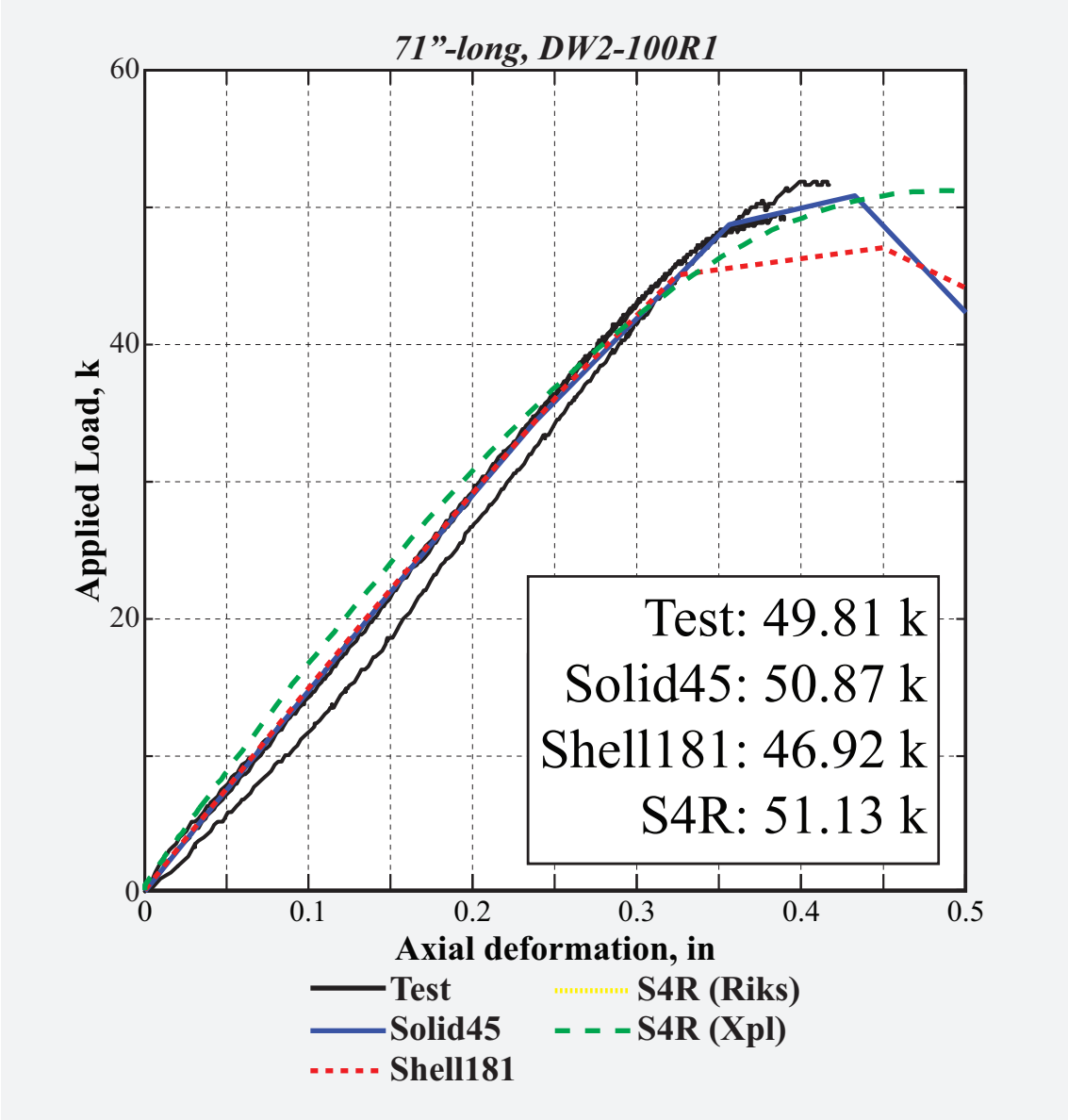


Figure 137: Load vs. deformation history of 71”-long, 0.1”-thick *DW2-R1*.

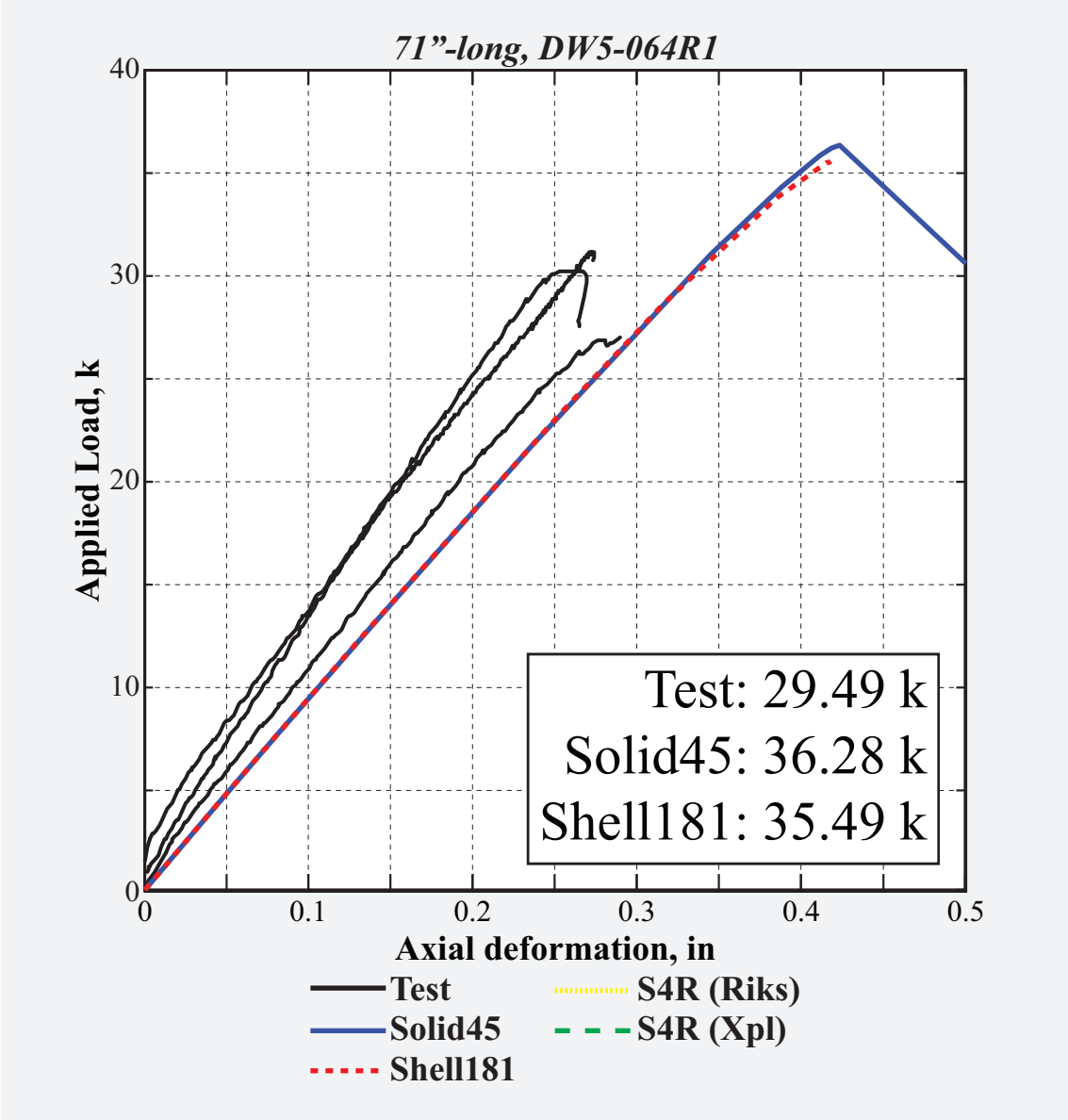


Figure 138: Load vs. deformation history of 71”-long, 0.064”-thick *DW5-R1*.

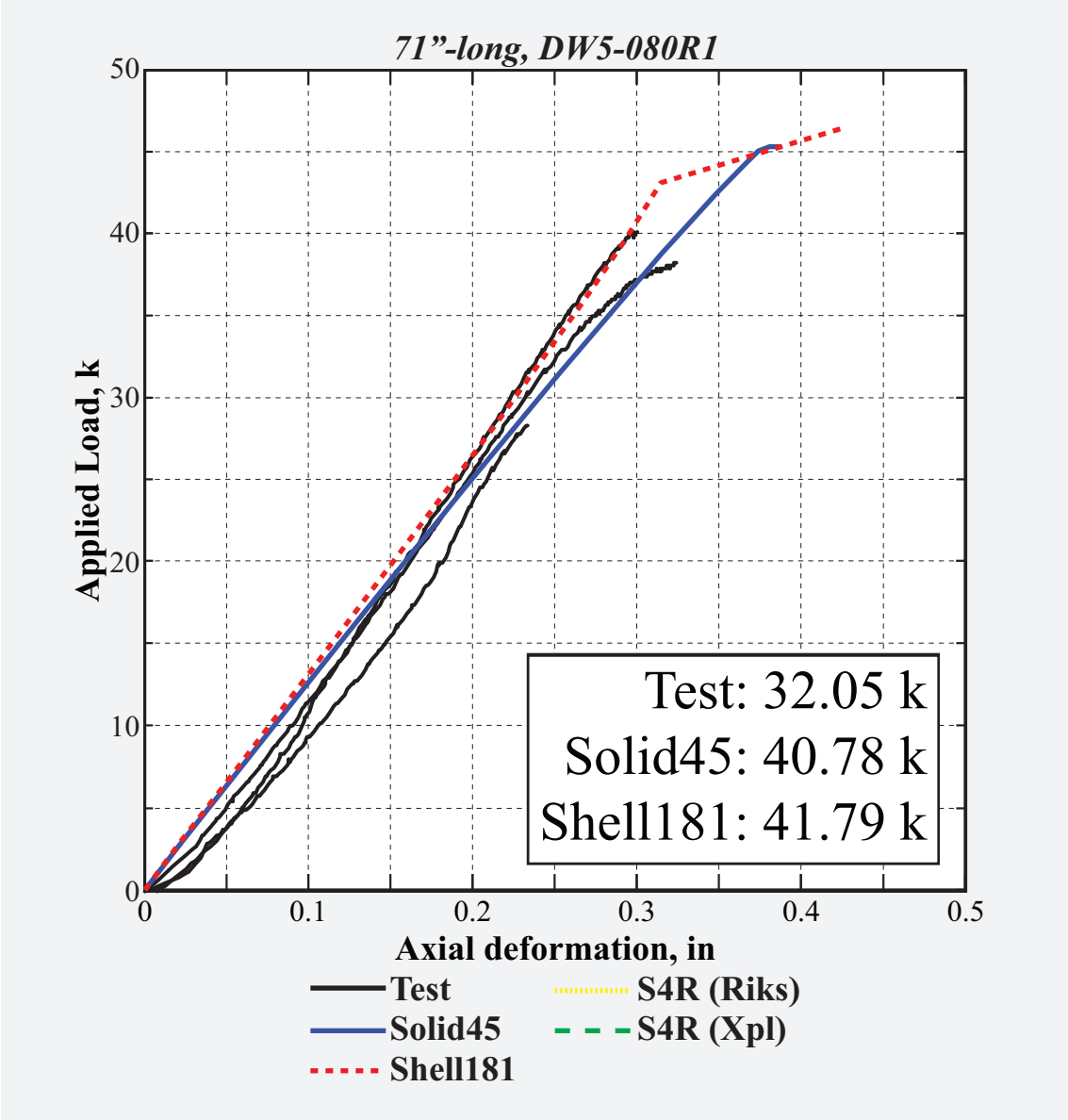


Figure 139: Load vs. deformation history of 71”-long, 0.08”-thick *DW5-R1*.

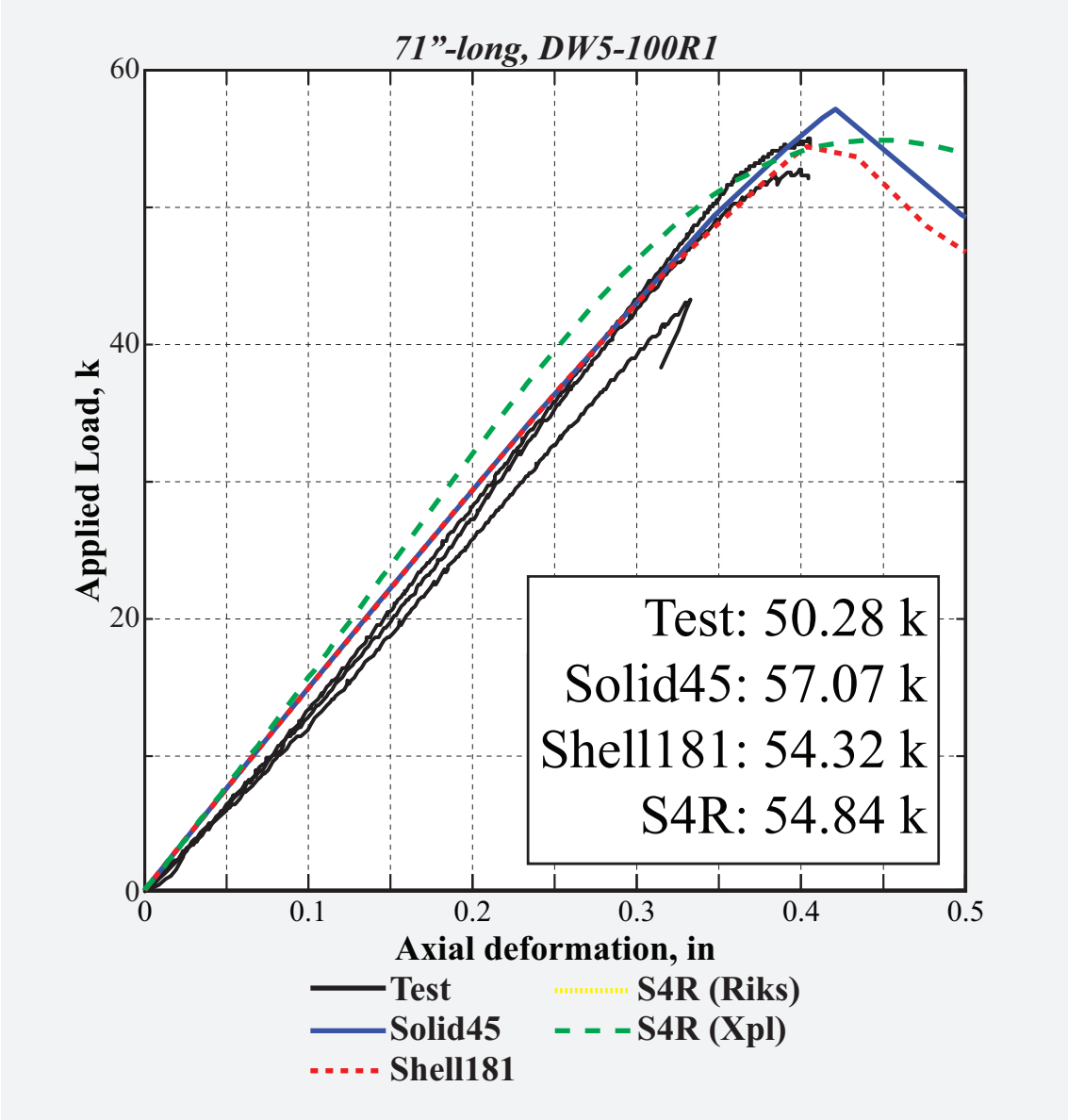


Figure 140: Load vs. deformation history of 71”-long, 0.1”-thick *DW5-R1*.

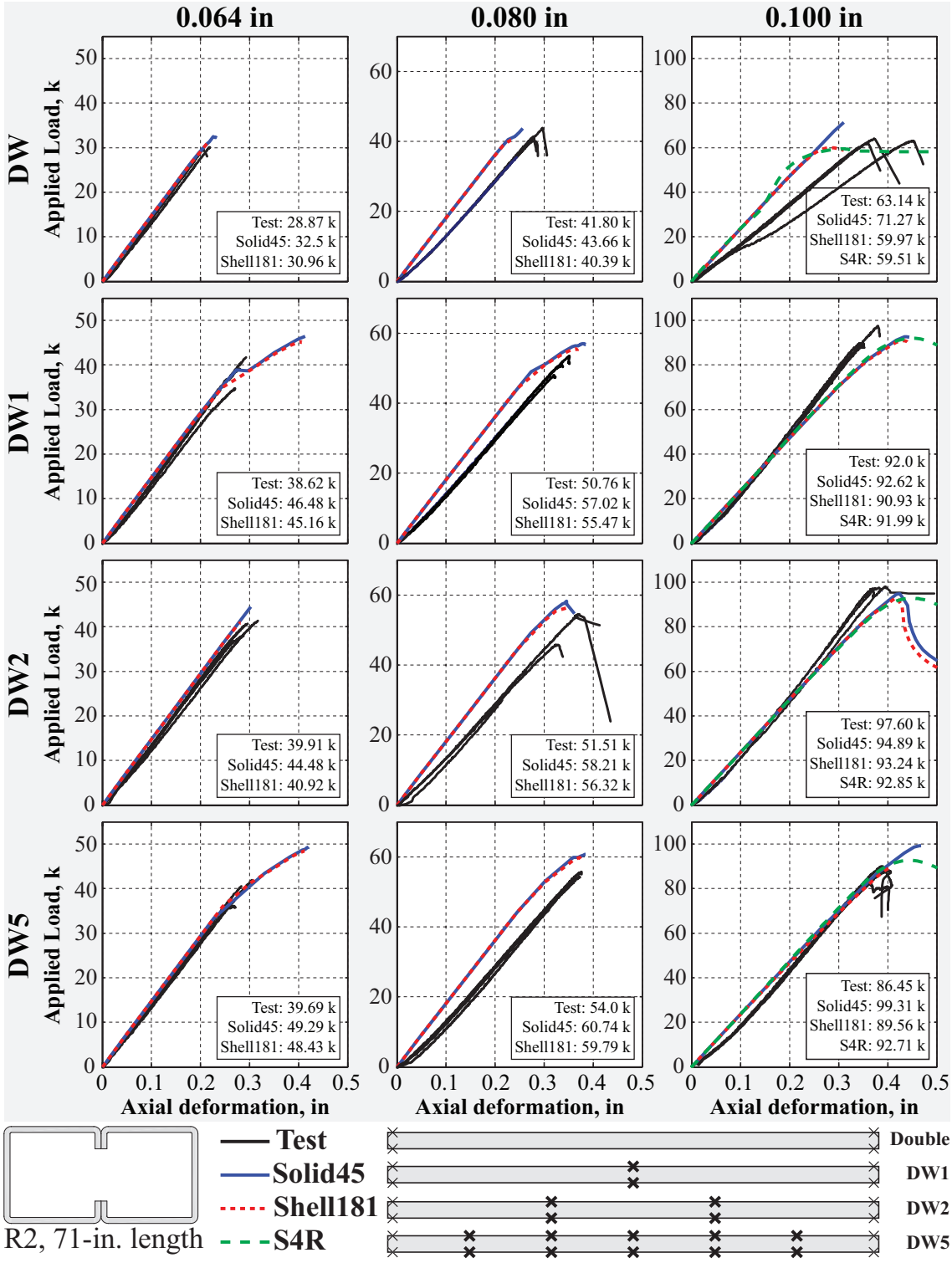


Figure 141: Overview of load vs. deformation history of 71”-long, double-sided *R2*-sections presented in Figs. 142-153.

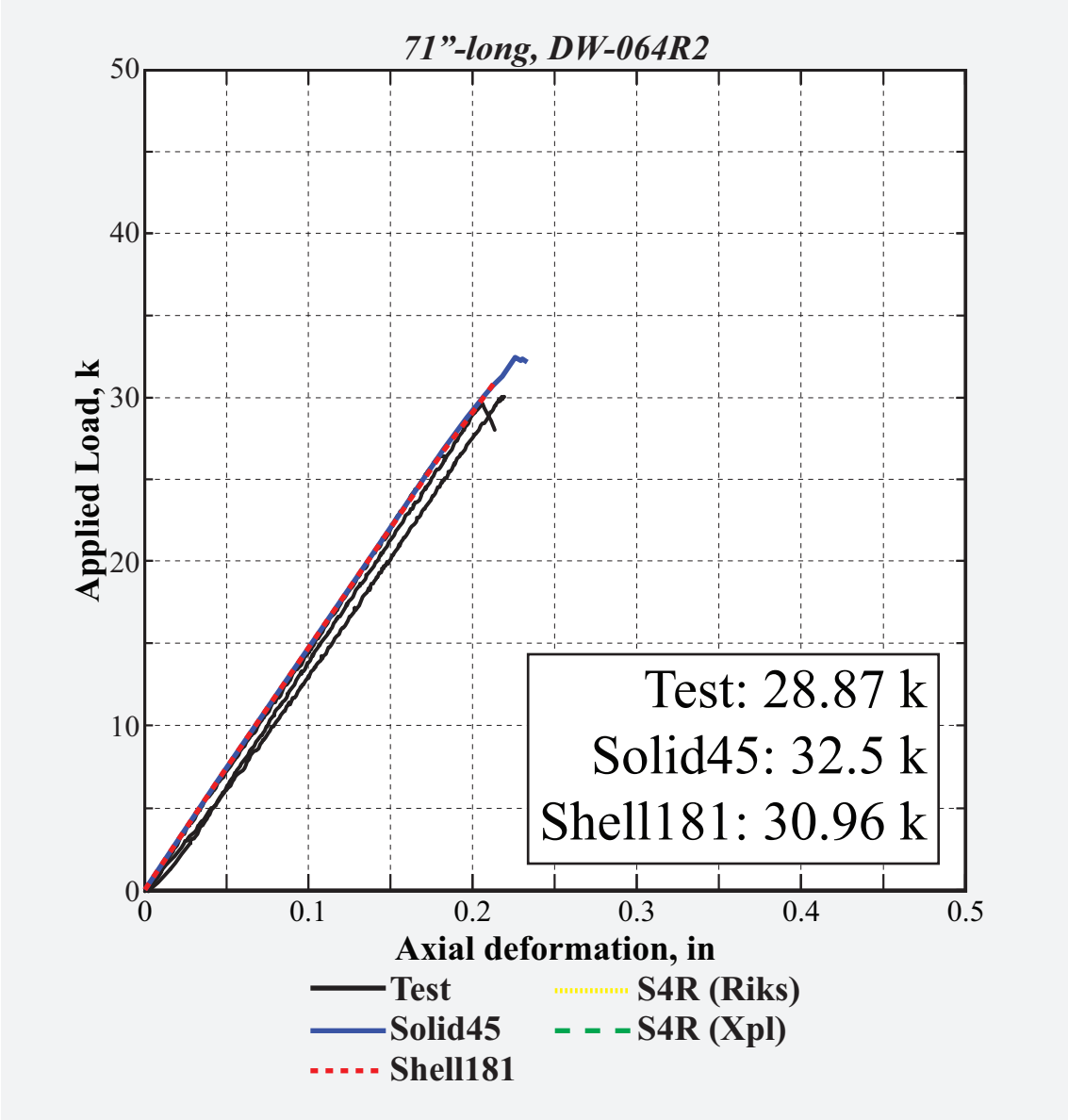


Figure 142: Load vs. deformation history of 71”-long, 0.064”-thick *DW-R2*.

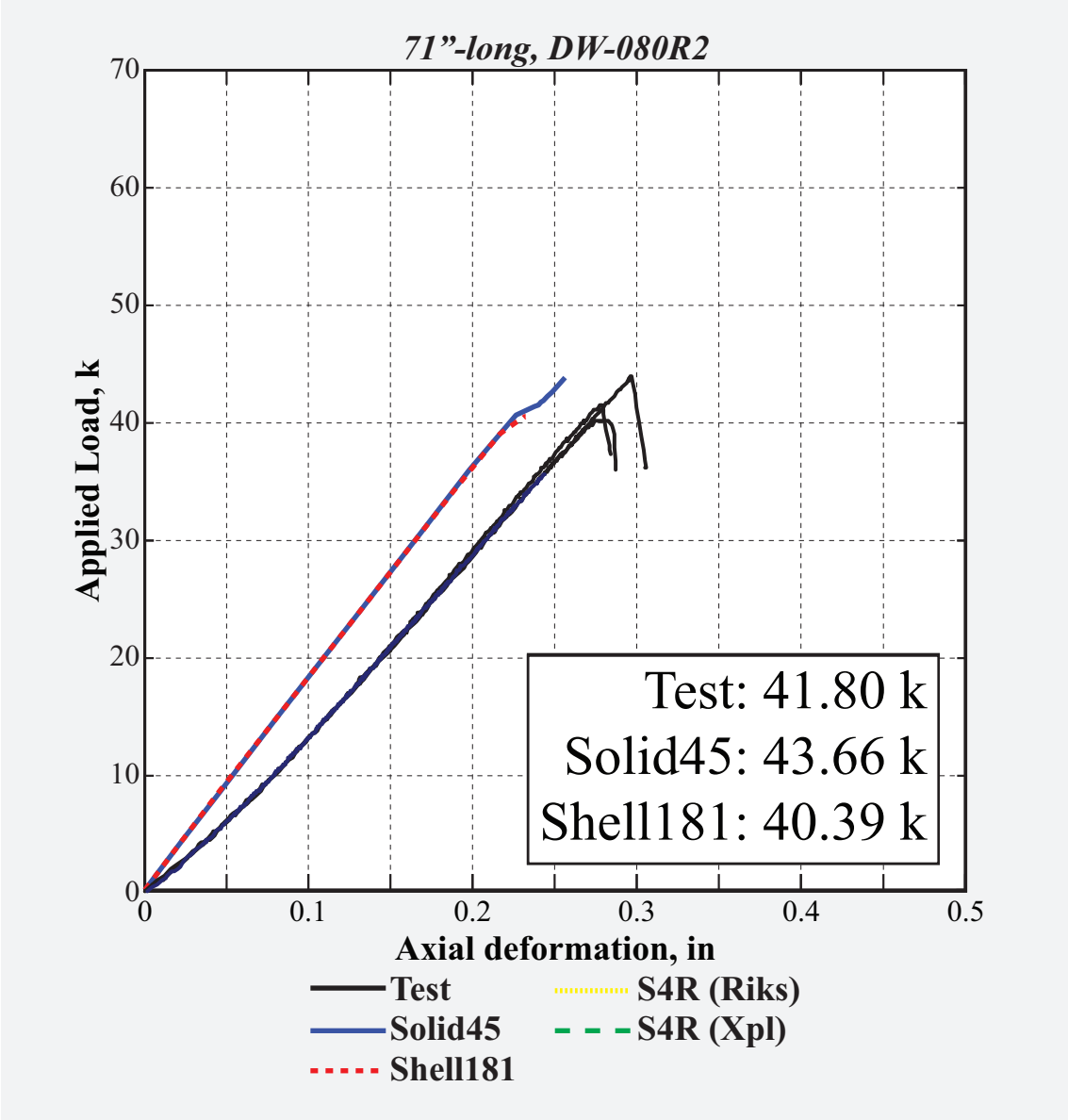


Figure 143: Load vs. deformation history of 71”-long, 0.08”-thick *DW-R2*.

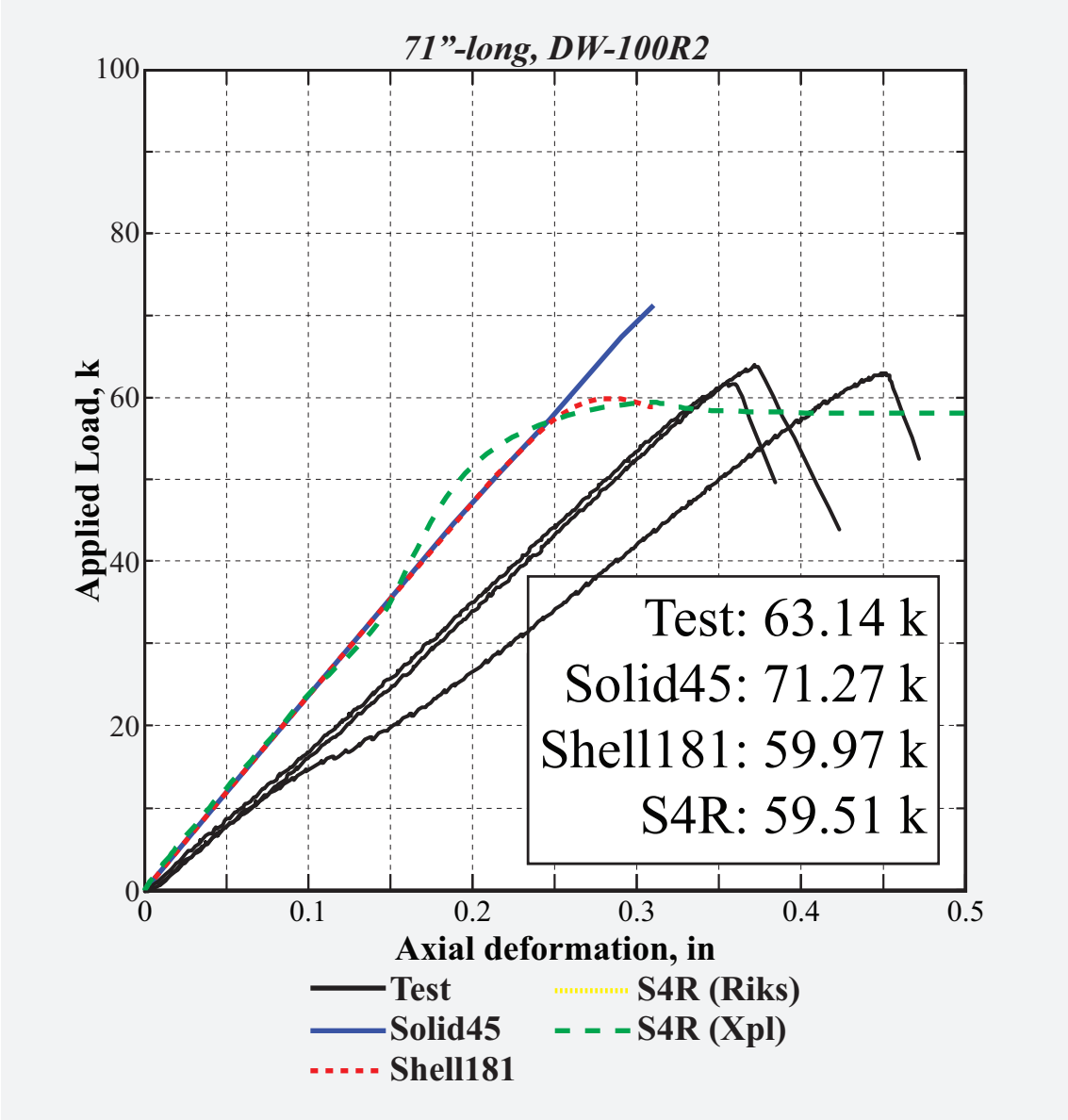


Figure 144: Load vs. deformation history of 71”-long, 0.1”-thick *DW-R2*.

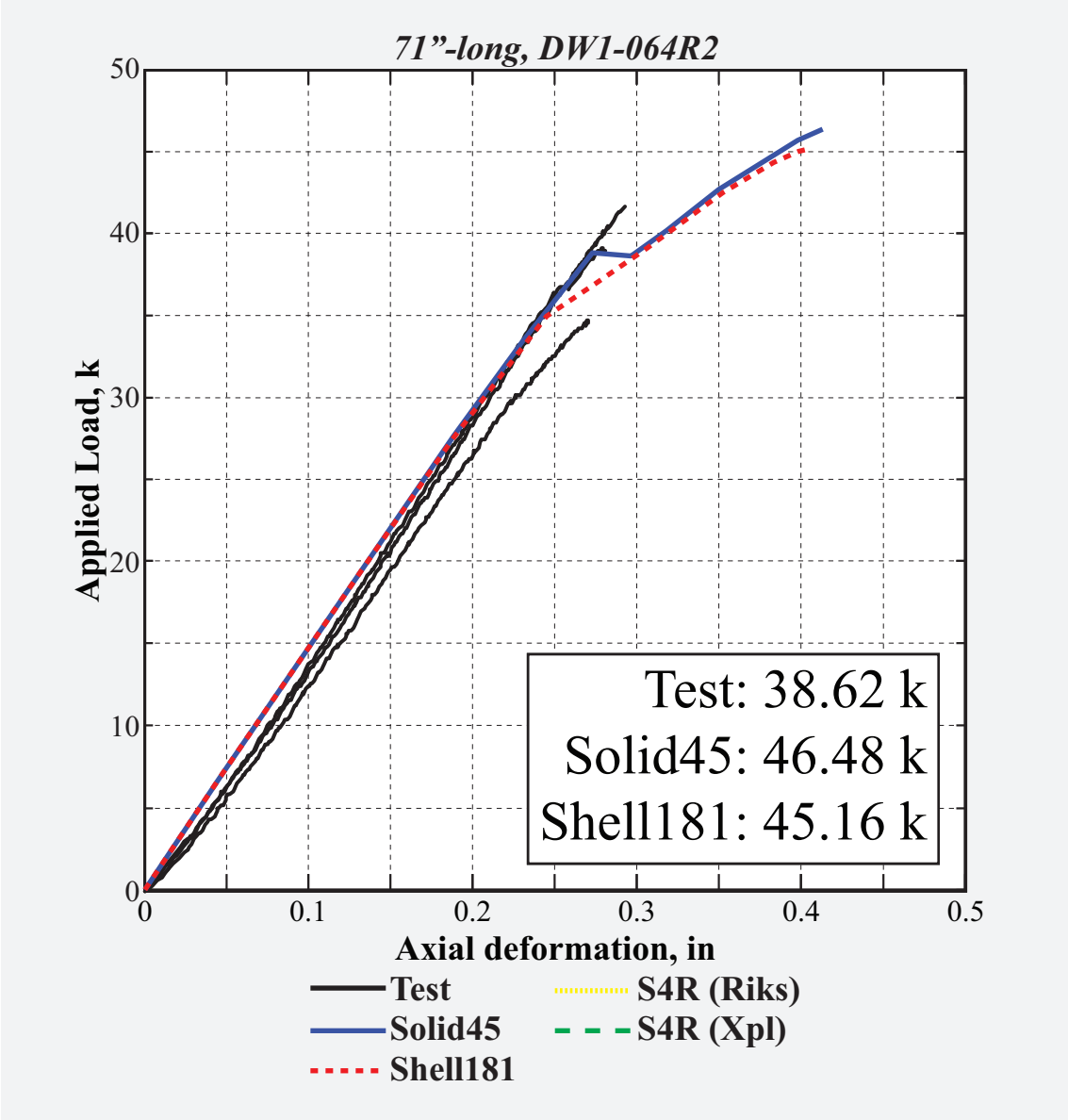


Figure 145: Load vs. deformation history of 71”-long, 0.064”-thick *DW1-R2*.

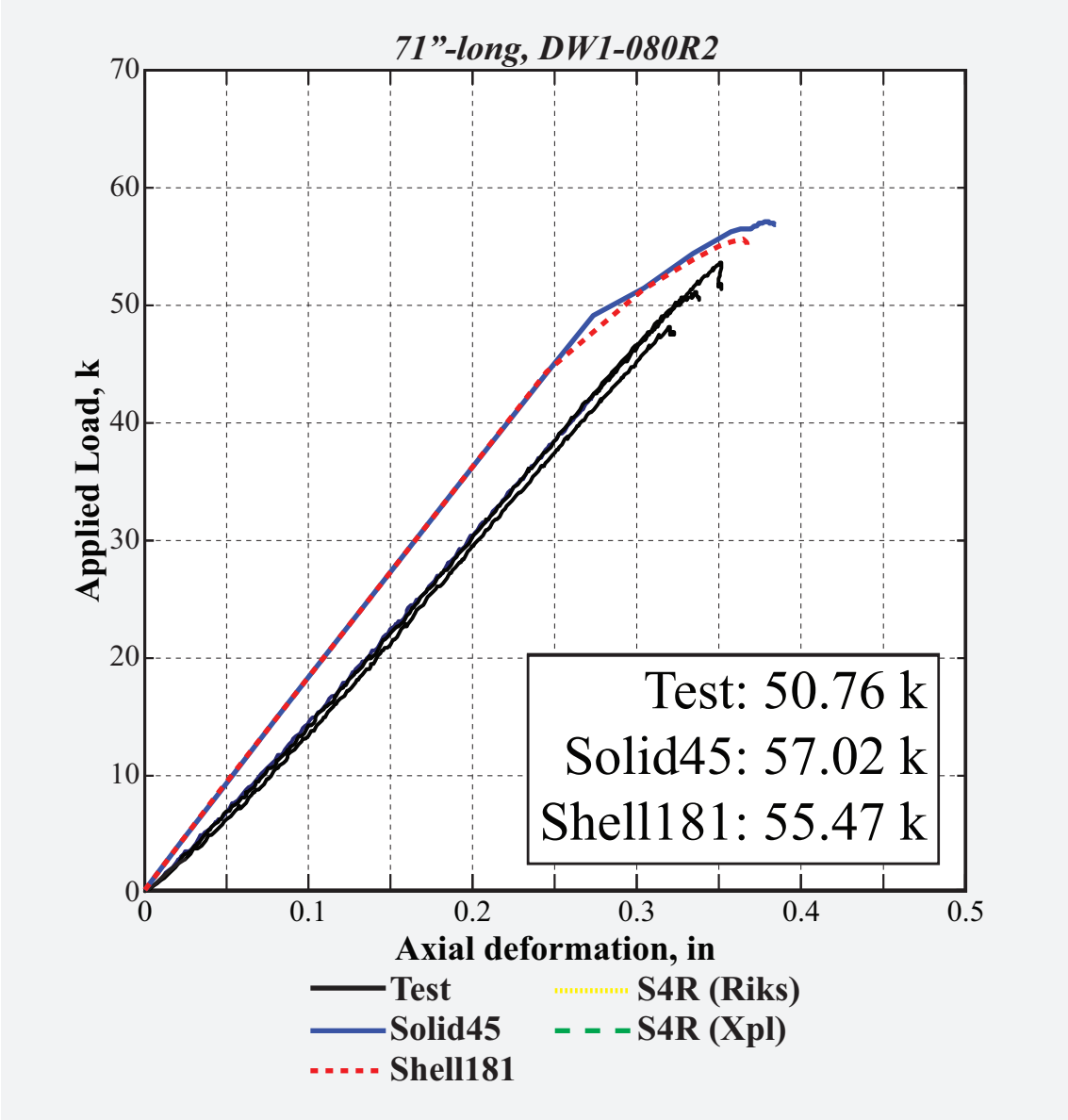


Figure 146: Load vs. deformation history of 71”-long, 0.08”-thick *DW1-R2*.

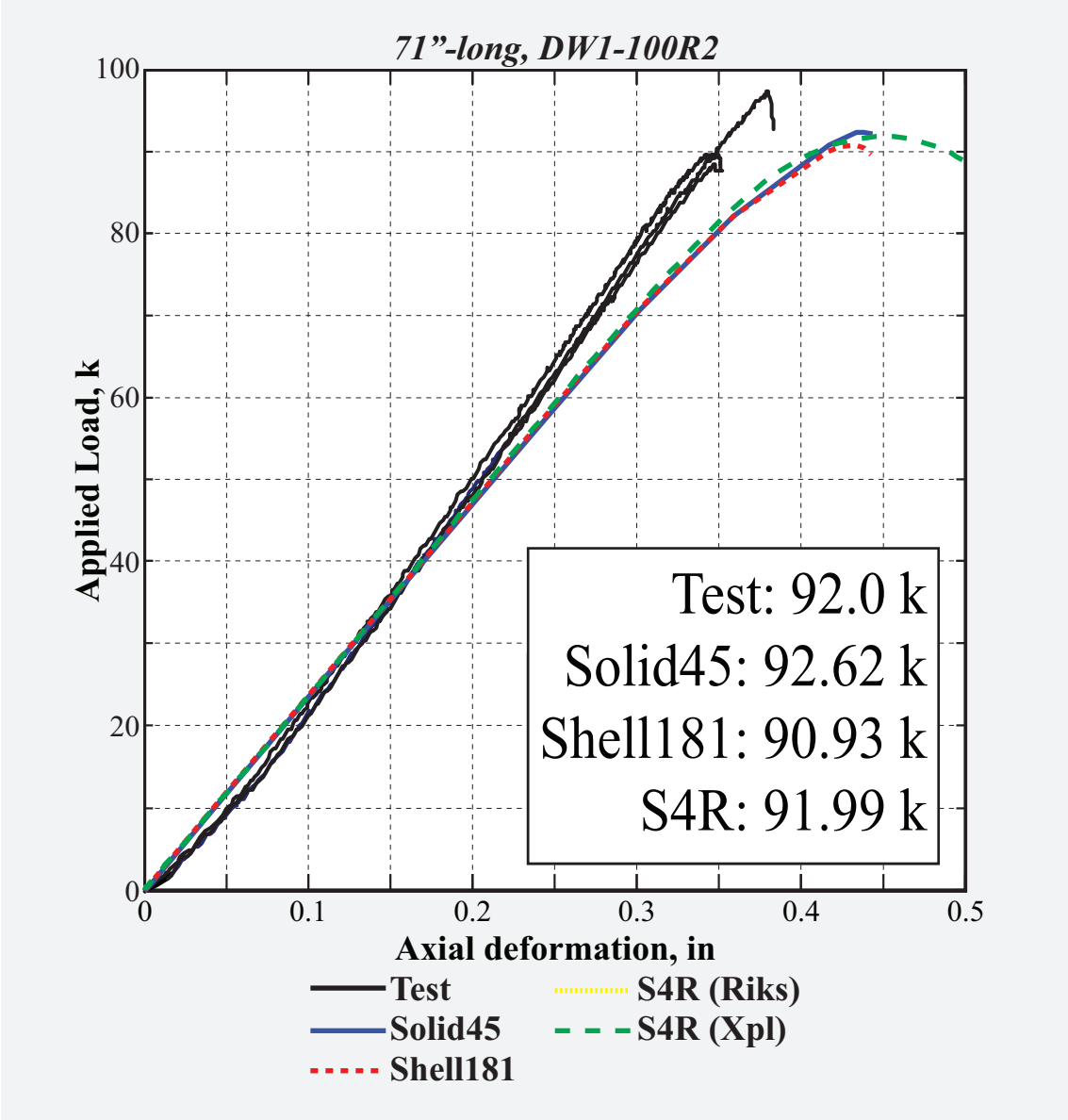


Figure 147: Load vs. deformation history of 71”-long, 0.1”-thick *DW1-R2*.

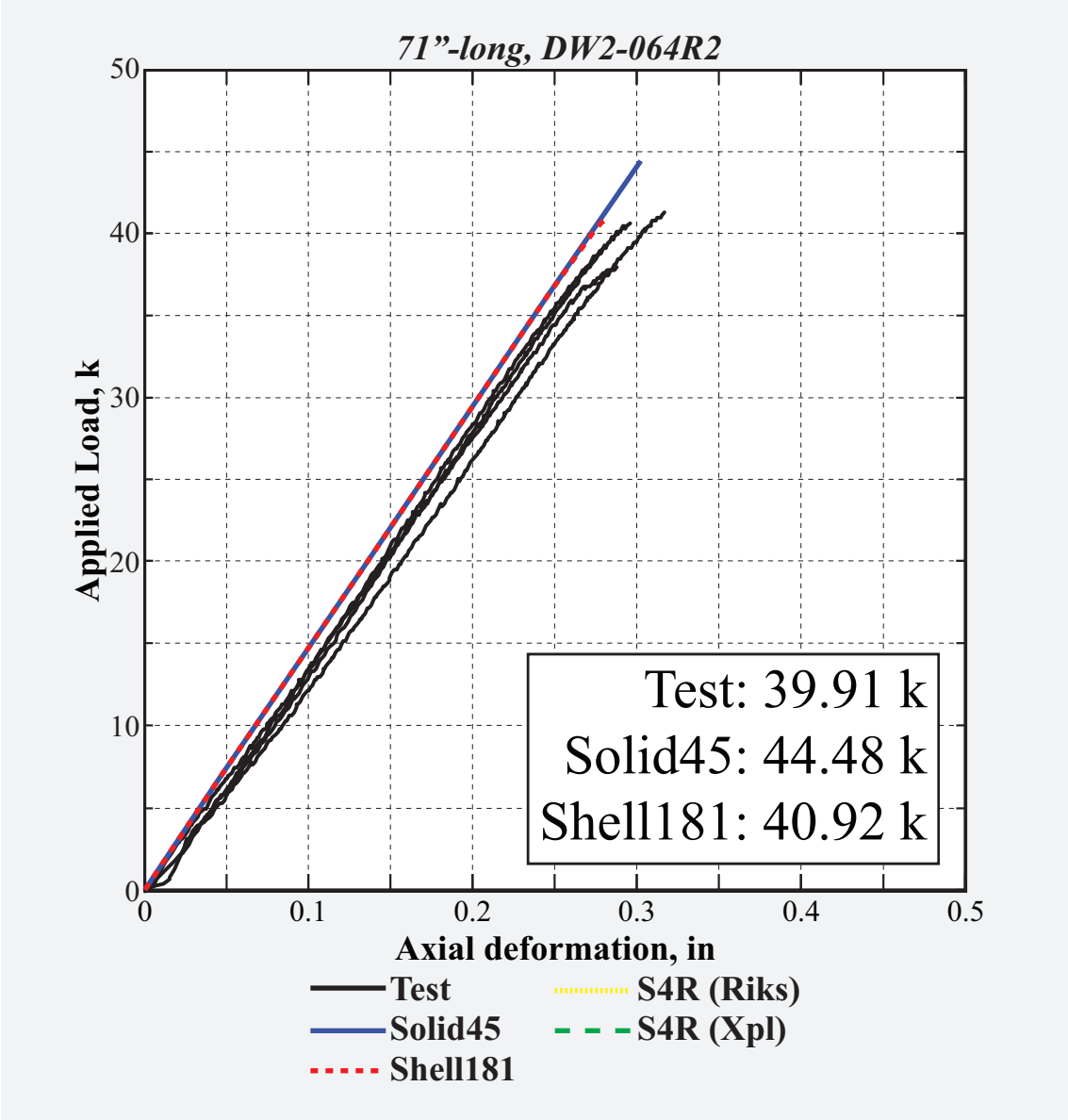


Figure 148: Load vs. deformation history of 71”-long, 0.064”-thick *DW2-R2*.

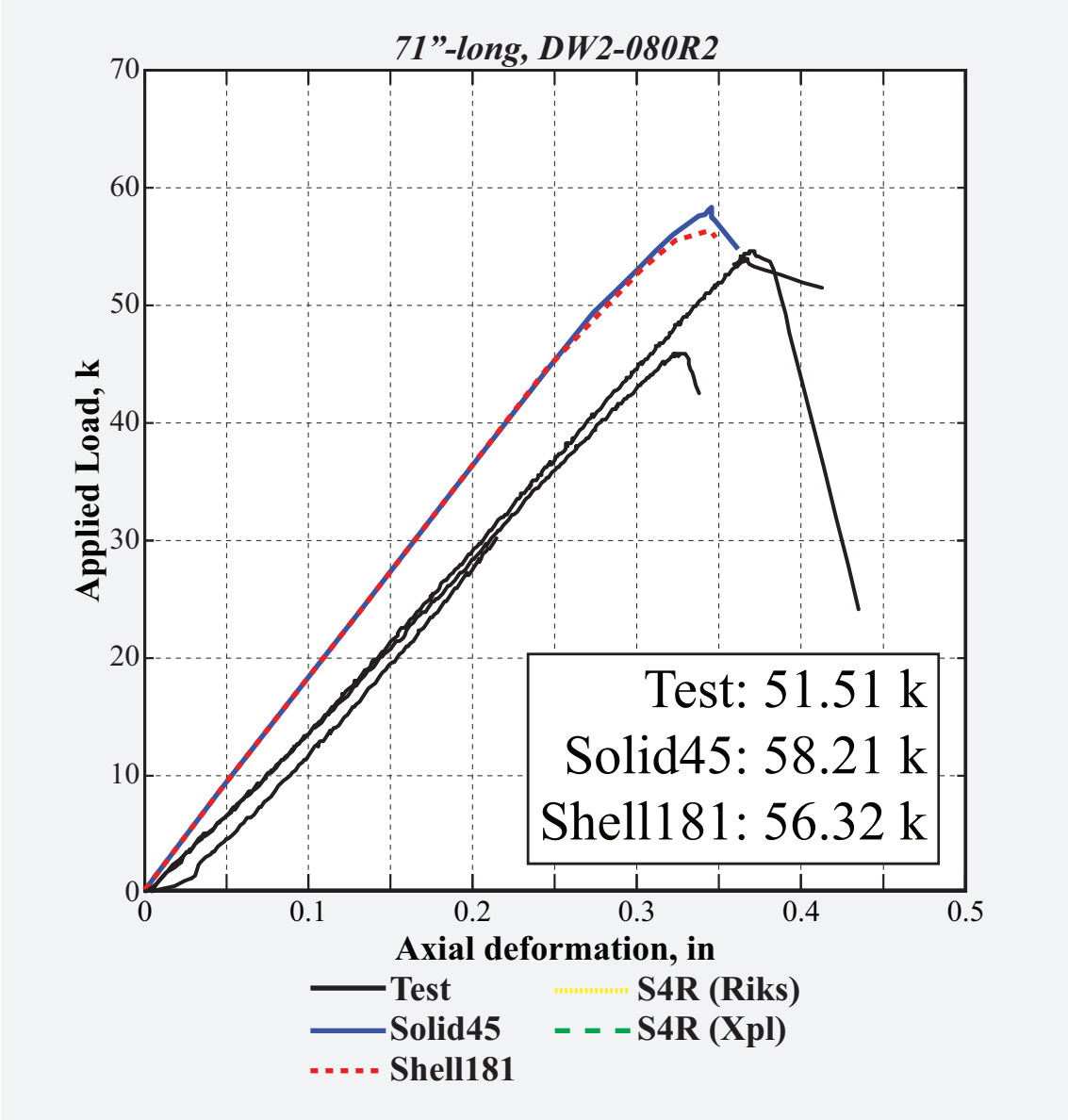


Figure 149: Load vs. deformation history of 71”-long, 0.08”-thick *DW2-R2*.

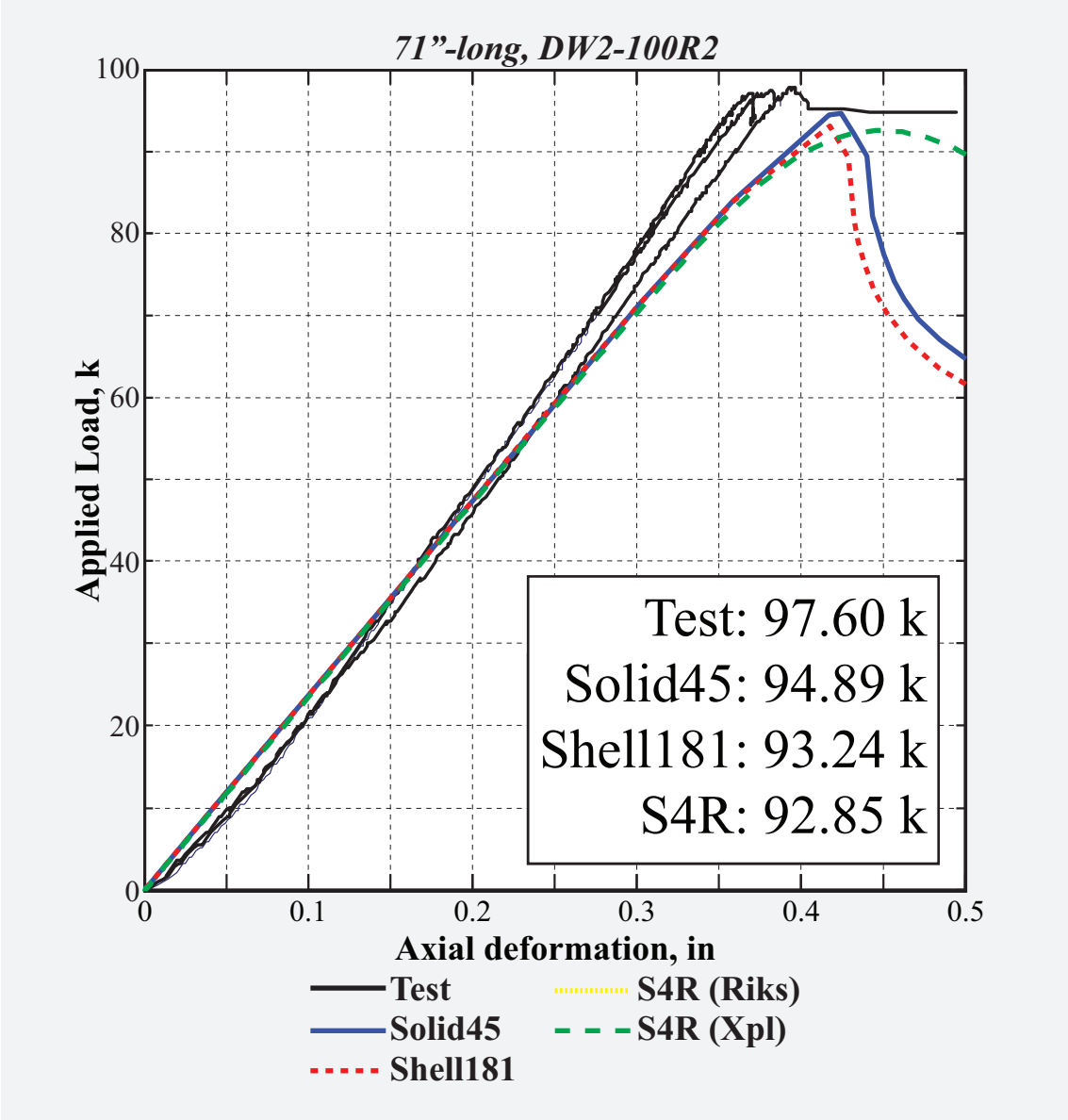


Figure 150: Load vs. deformation history of 71”-long, 0.1”-thick *DW2-R2*.

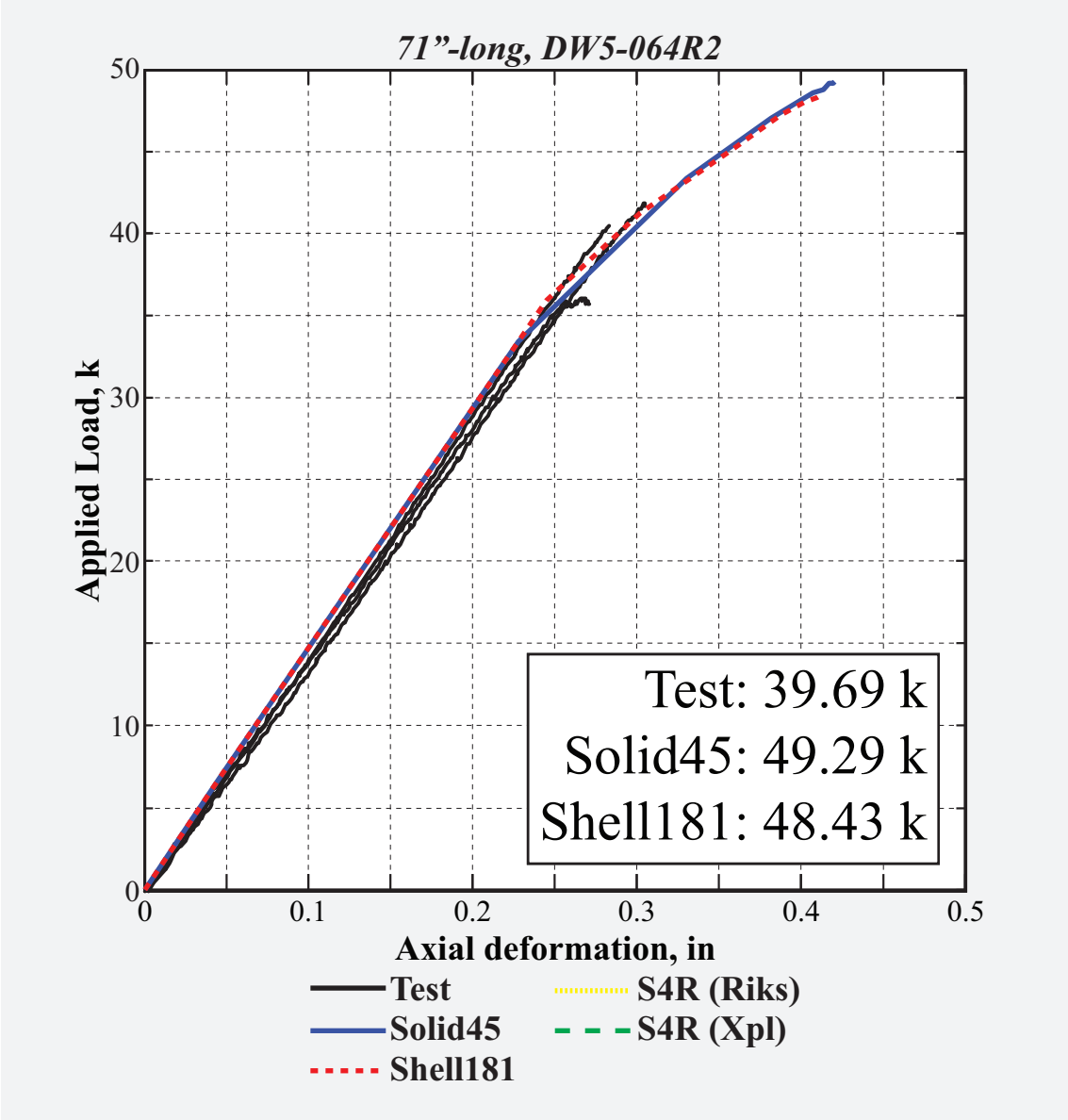


Figure 151: Load vs. deformation history of 71”-long, 0.064”-thick *DW5-R2*.

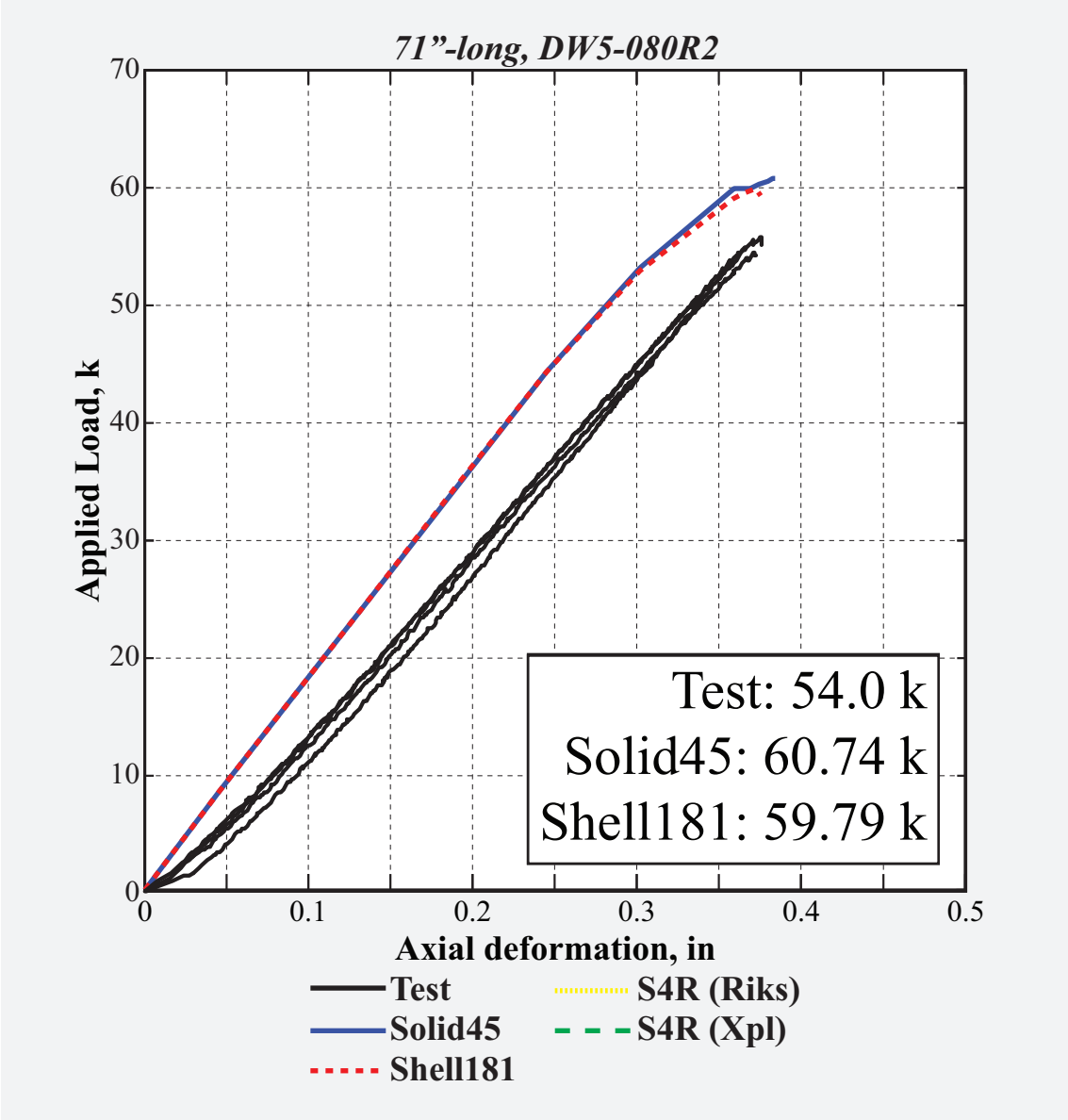


Figure 152: Load vs. deformation history of 71”-long, 0.08”-thick *DW5-R2*.

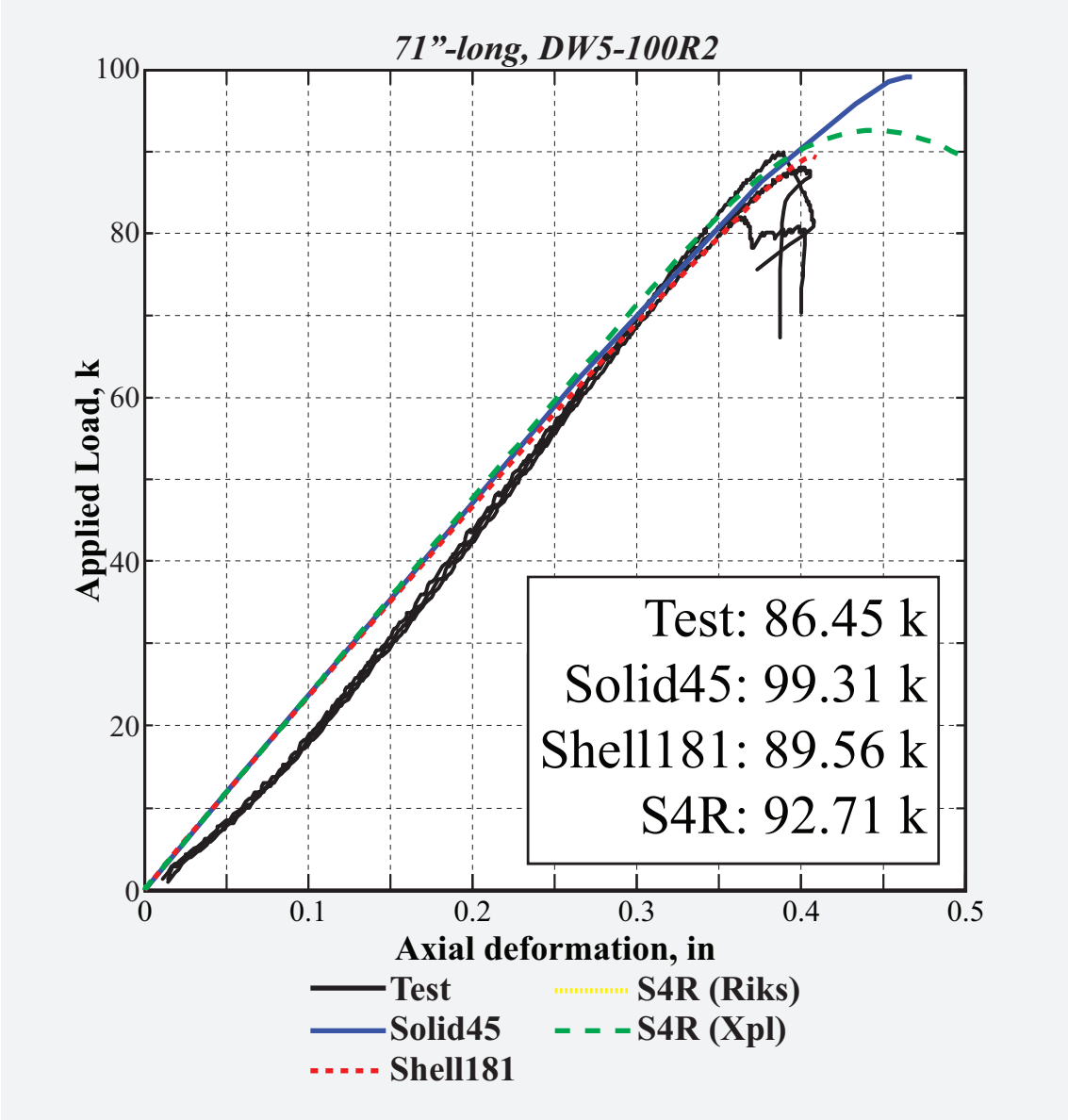


Figure 153: Load vs. deformation history of 71”-long, 0.1”-thick *DW5-R2*.

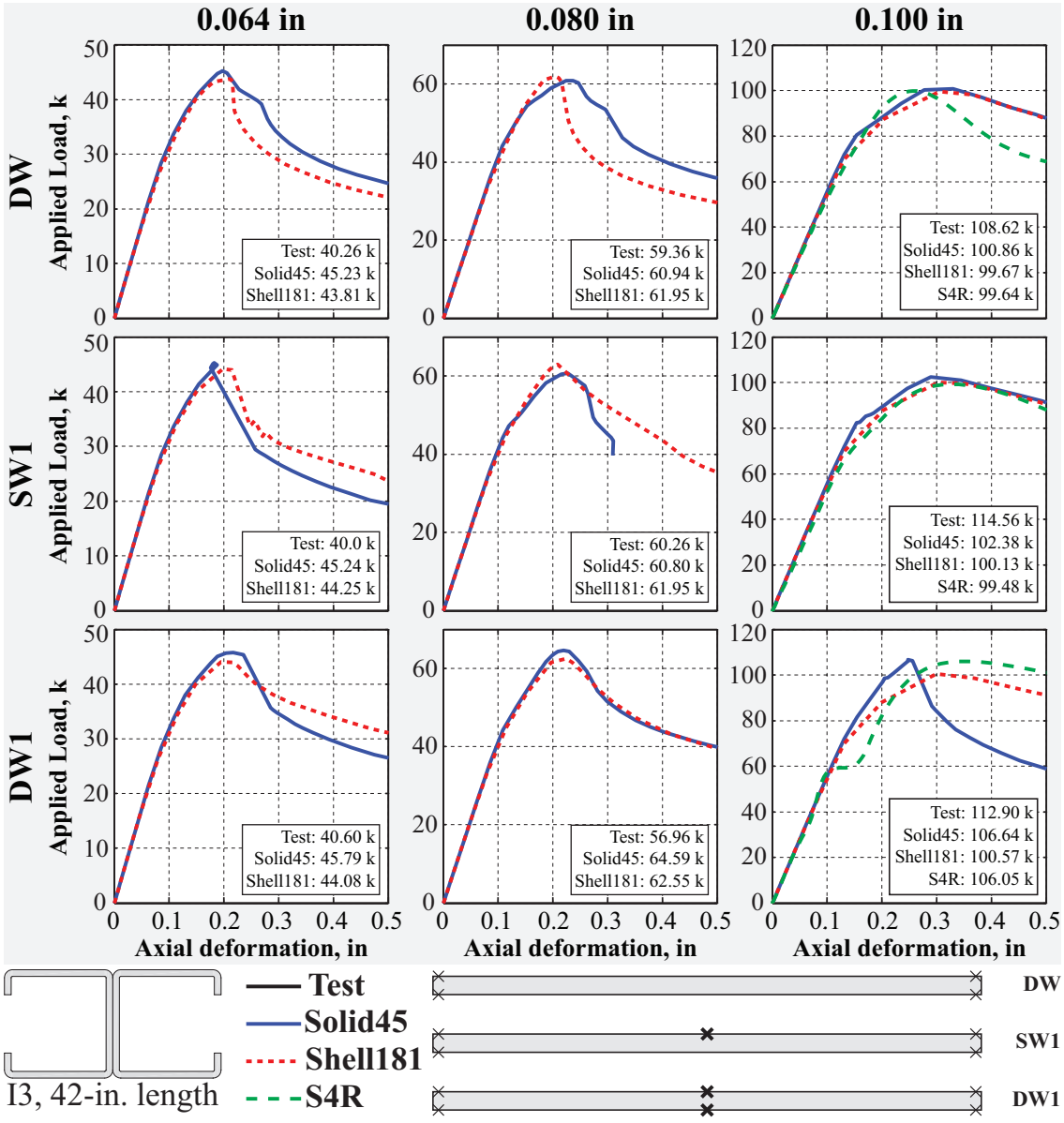


Figure 154: Overview of load vs. deformation history of 42”-long *I3*-sections presented in Figs. 155-163.

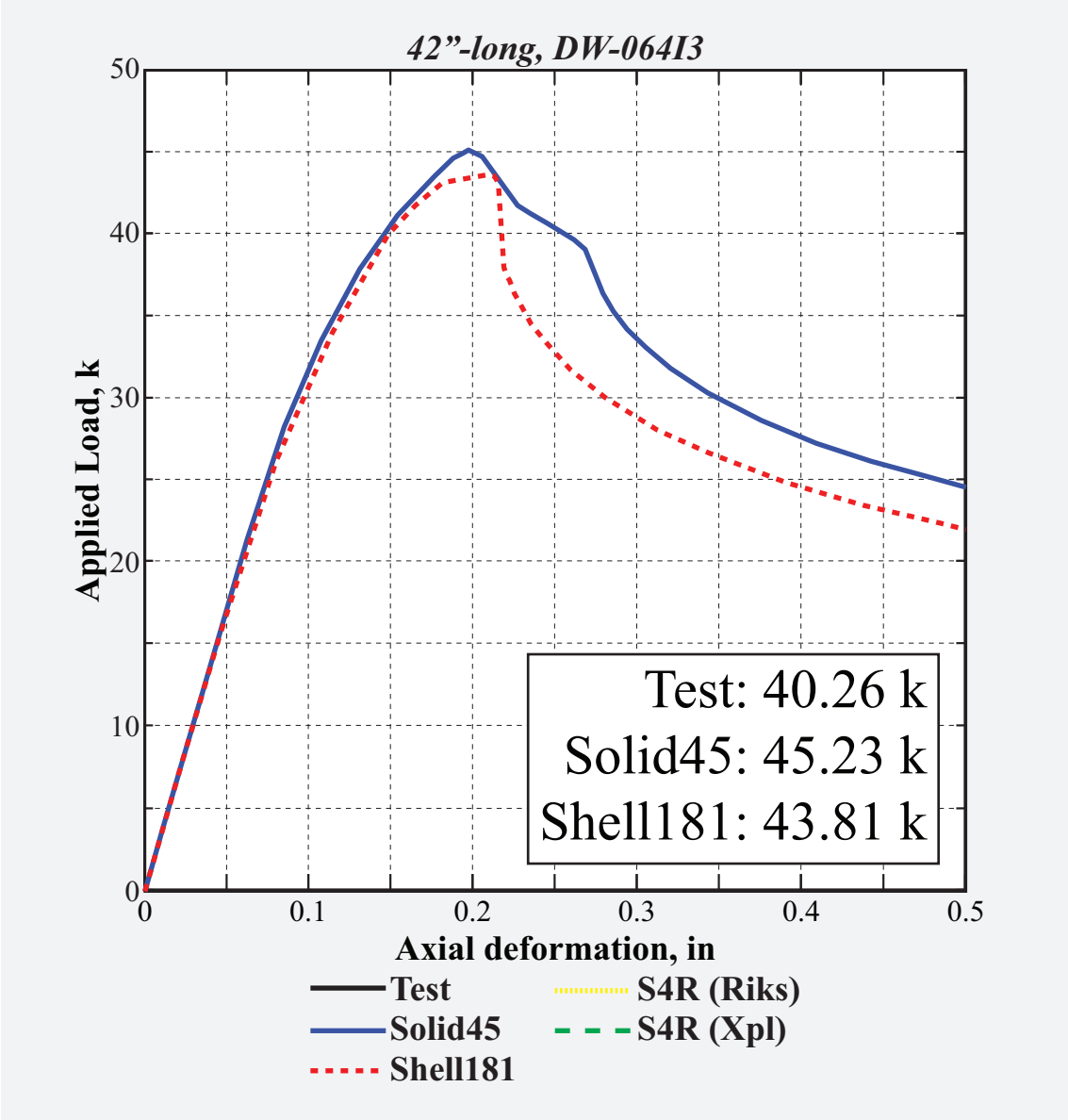


Figure 155: Load vs. deformation history of 42”-long, 0.064”-thick *DW-I3*

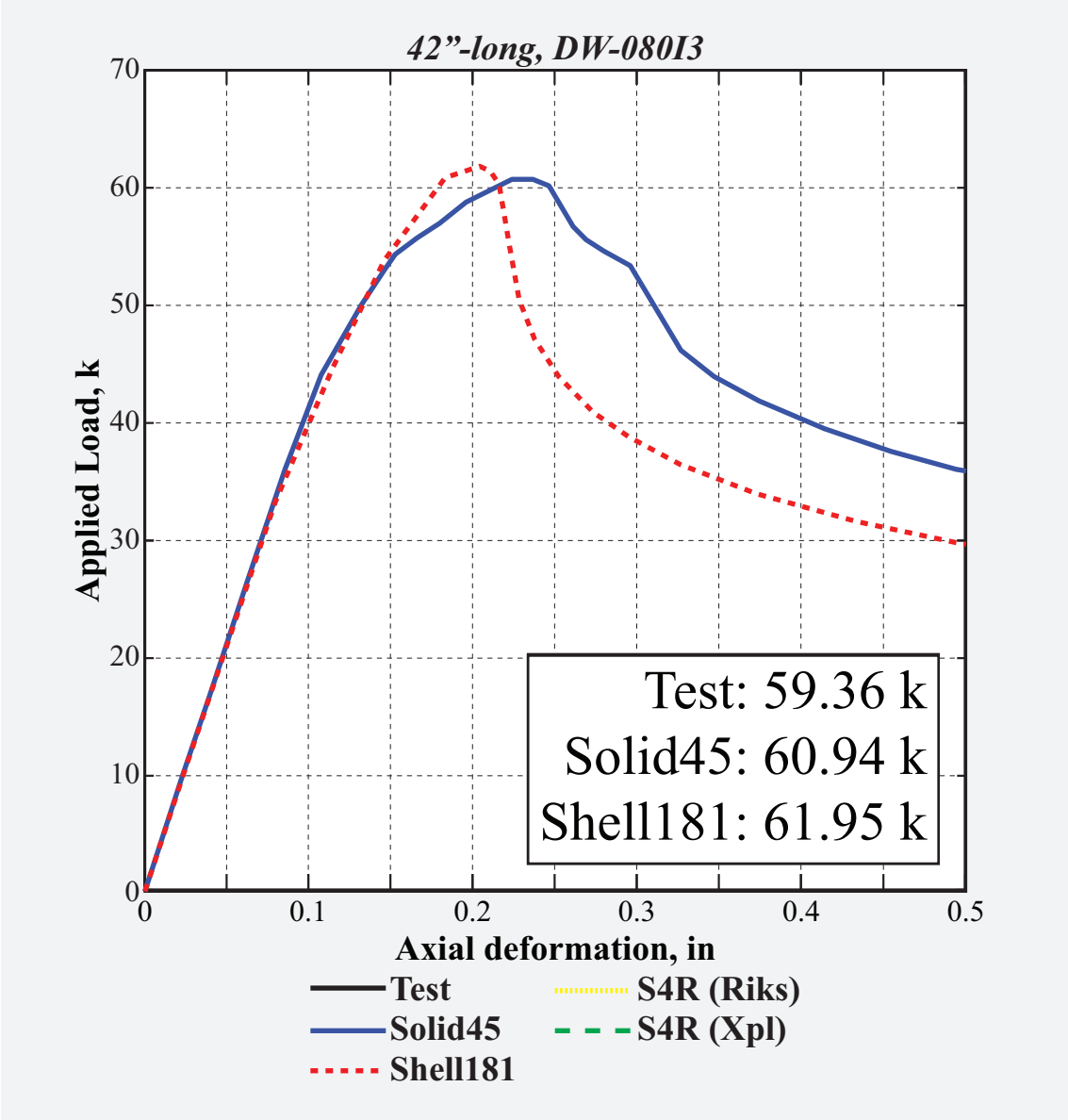


Figure 156: Load vs. deformation history of 42”-long, 0.08”-thick *DW-I3*

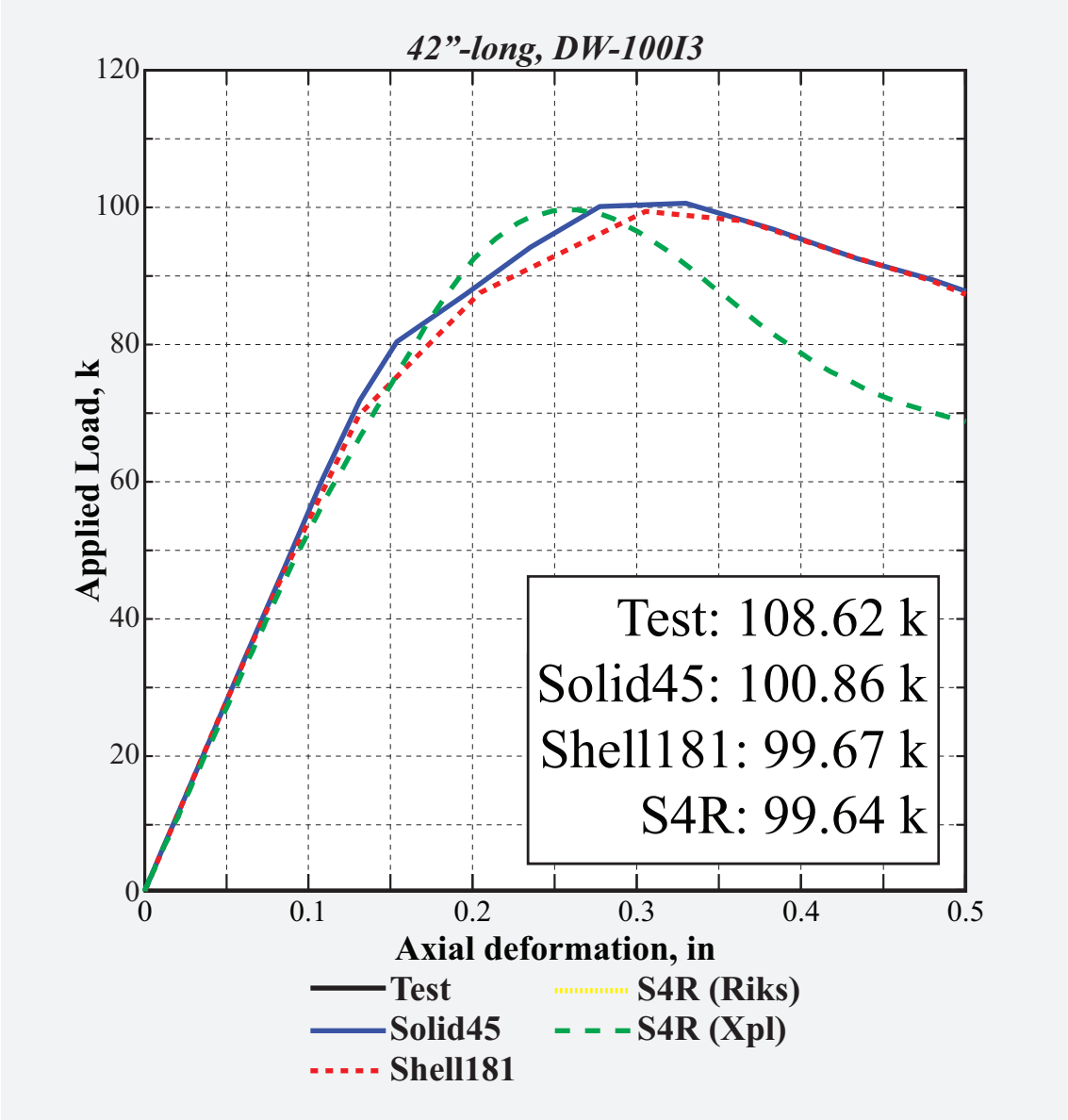


Figure 157: Load vs. deformation history of 42”-long, 0.1”-thick *DW-I3*

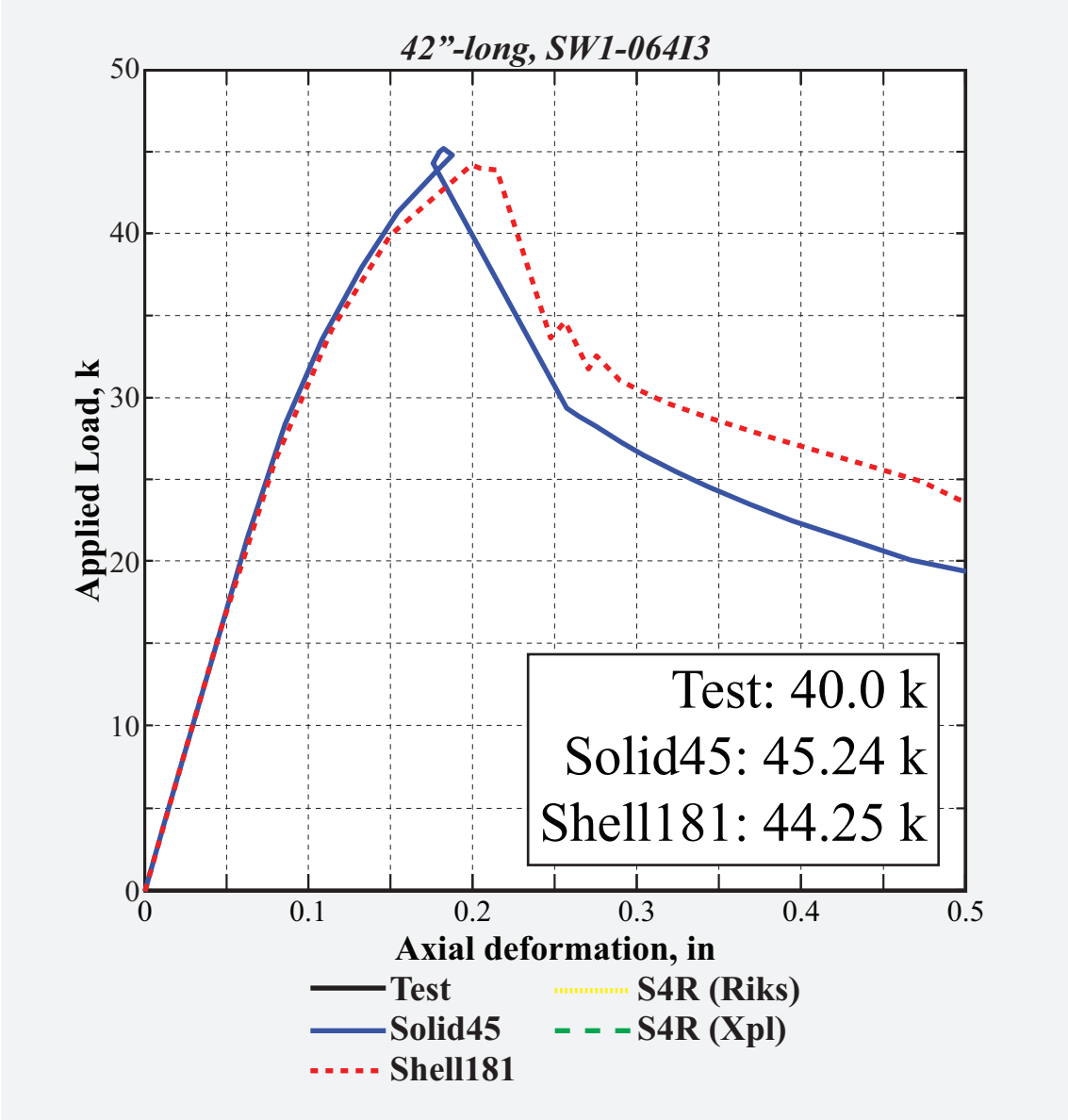


Figure 158: Load vs. deformation history of 42”-long, 0.064”-thick *SW1-I3*

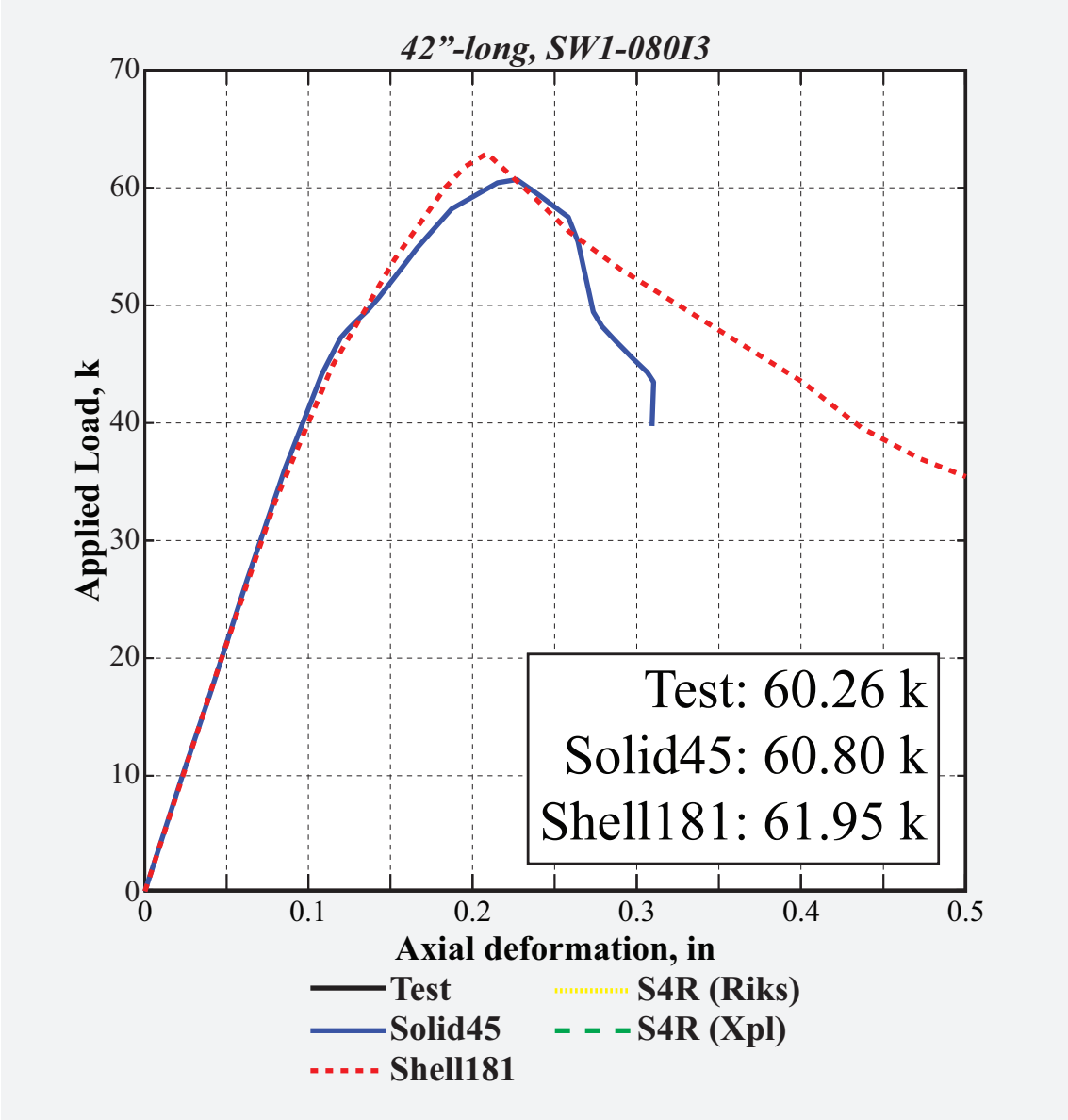


Figure 159: Load vs. deformation history of 42”-long, 0.08”-thick *SW1-I3*

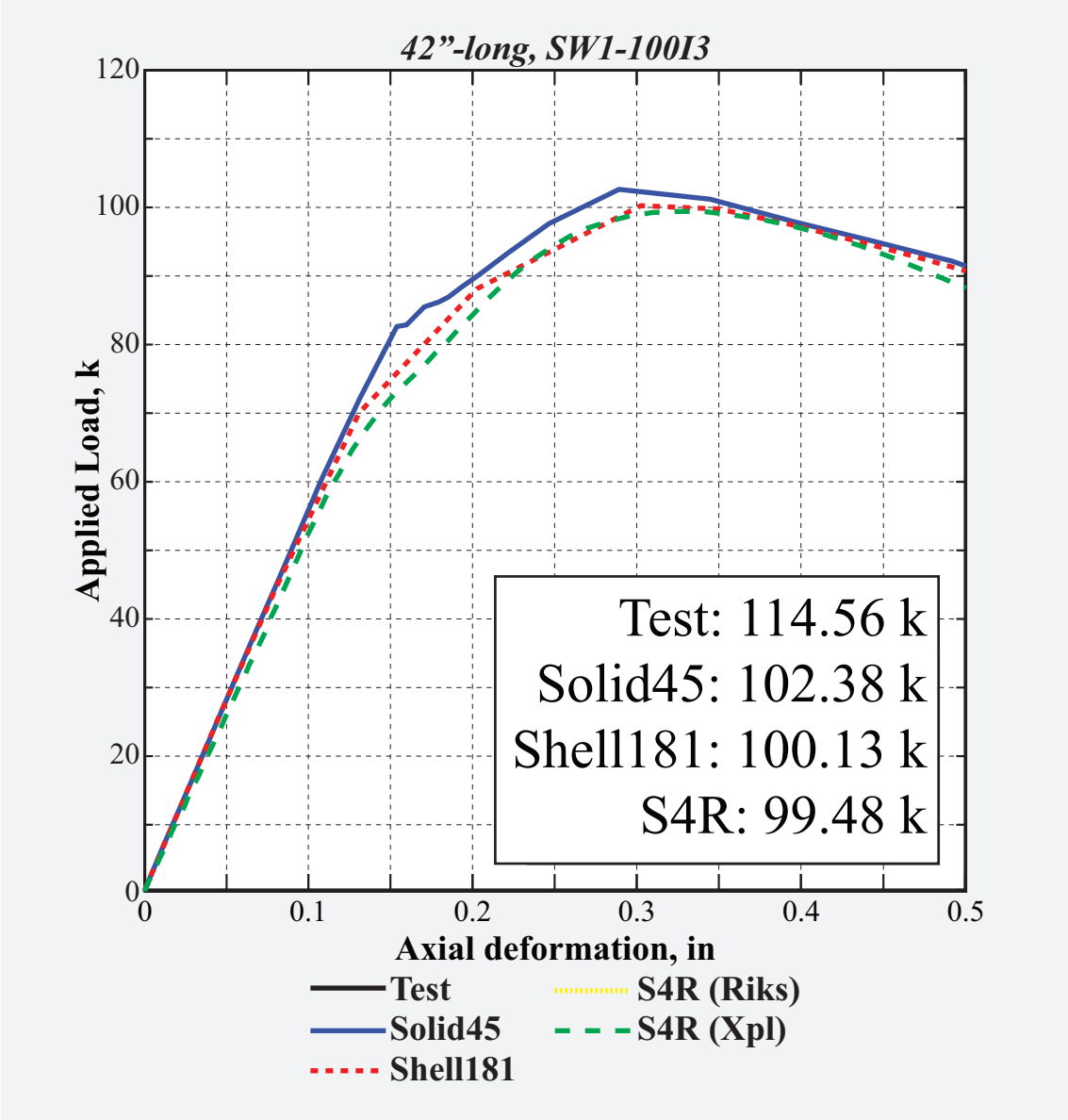


Figure 160: Load vs. deformation history of 42”-long, 0.1”-thick *SW1-I3*

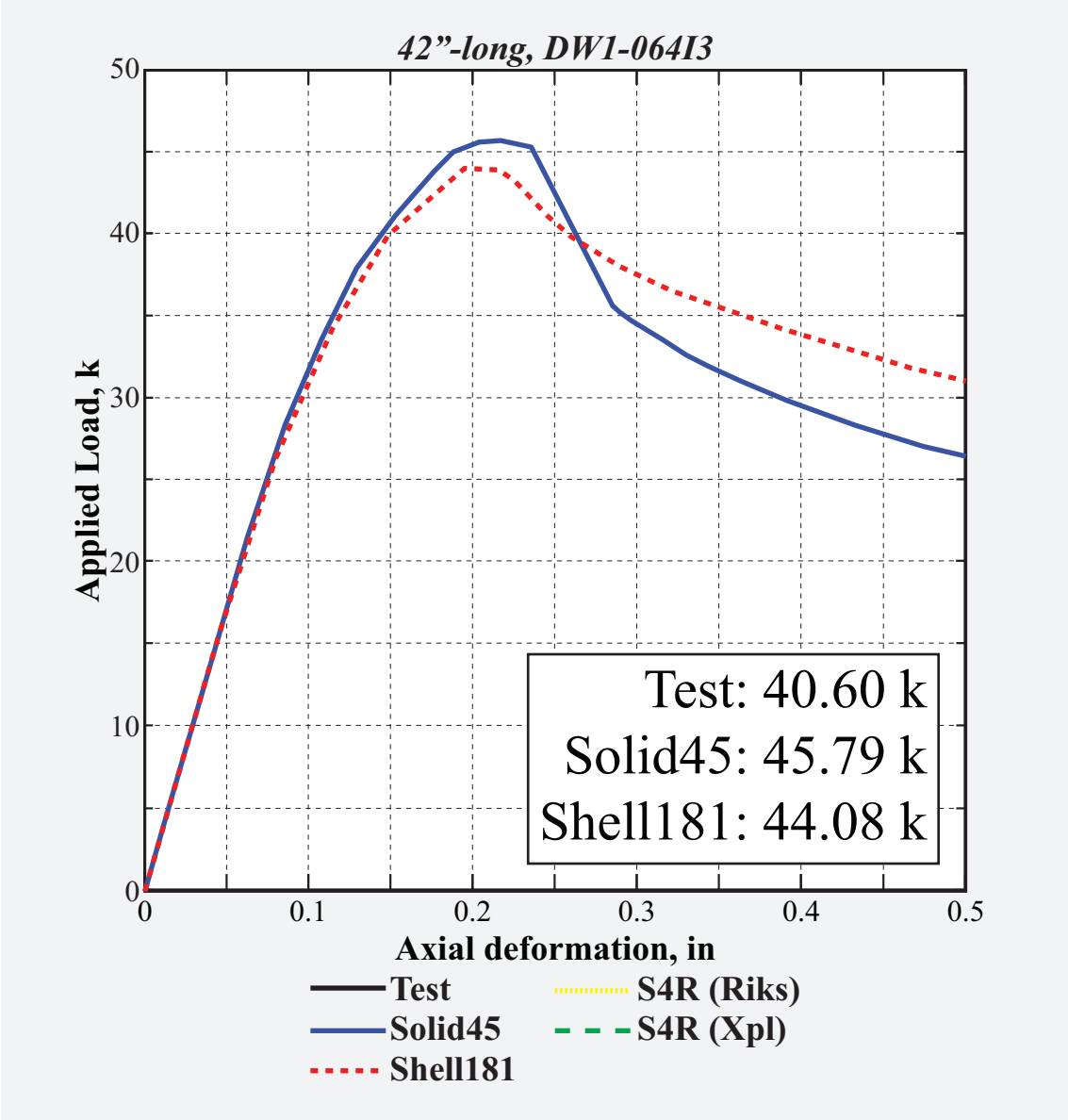


Figure 161: Load vs. deformation history of 42”-long, 0.064”-thick *DW1-I3*

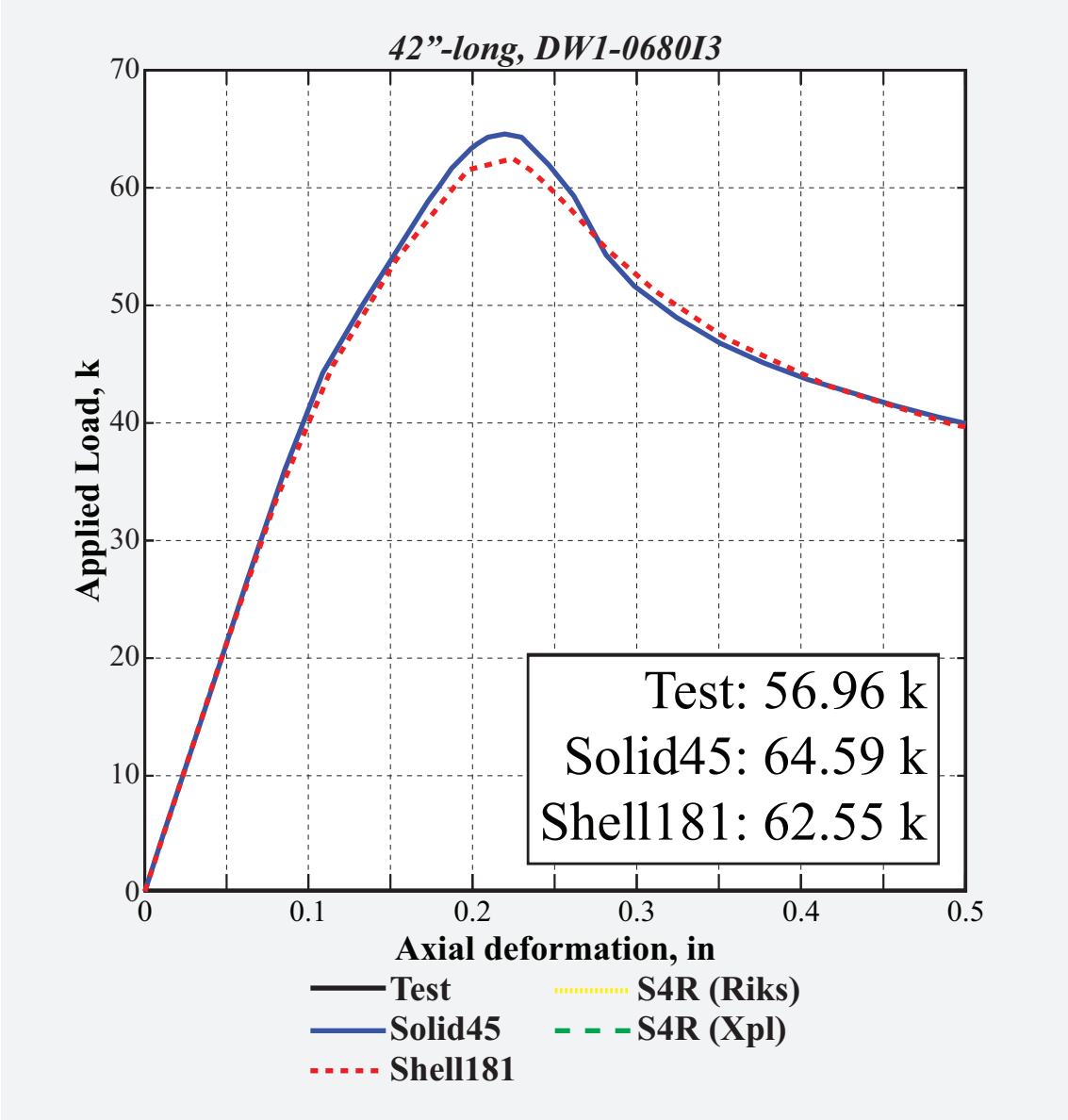


Figure 162: Load vs. deformation history of 42”-long, 0.08”-thick *DW1-I3*

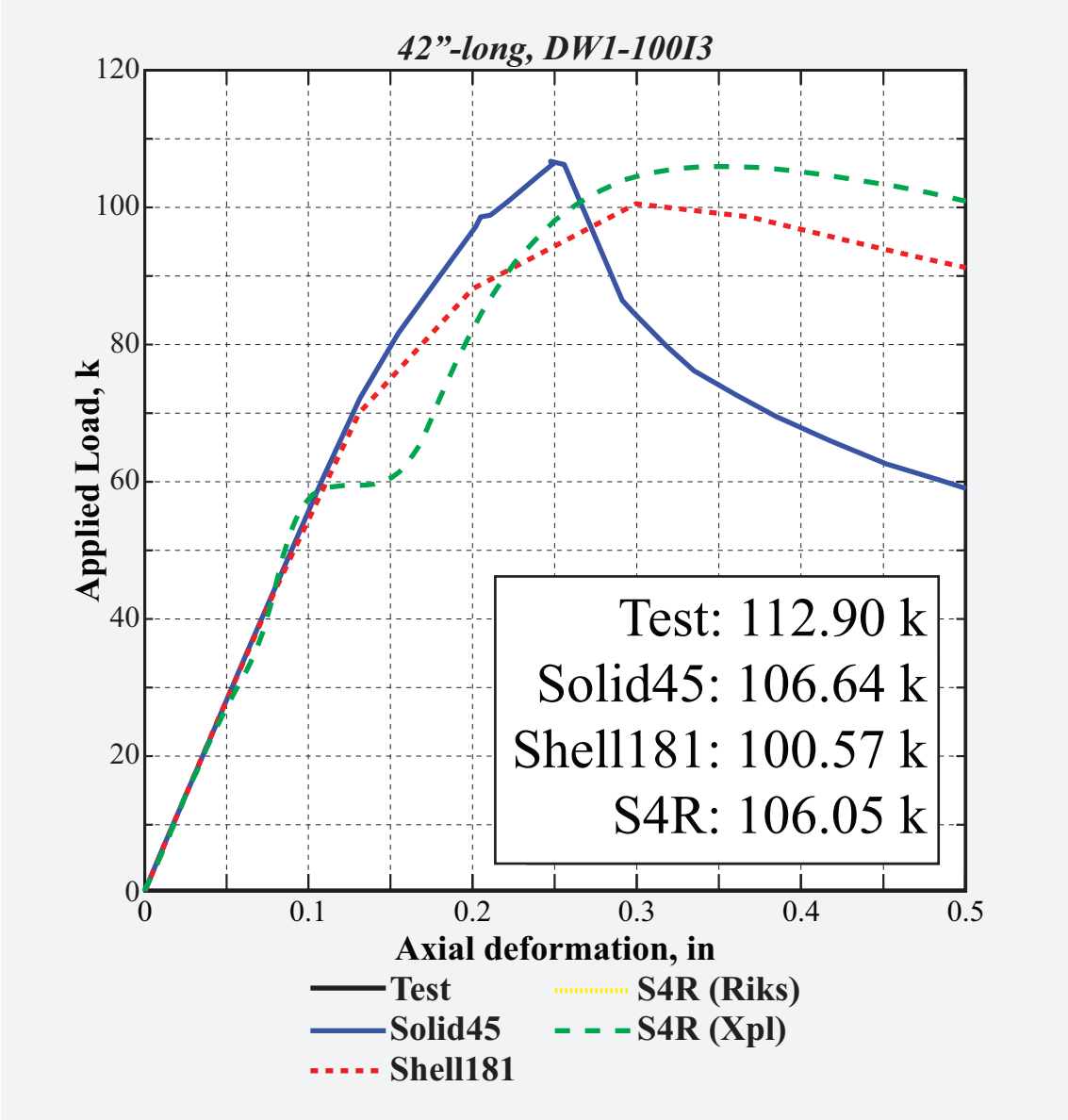


Figure 163: Load vs. deformation history of 42”-long, 0.1”-thick *DW1-I3*

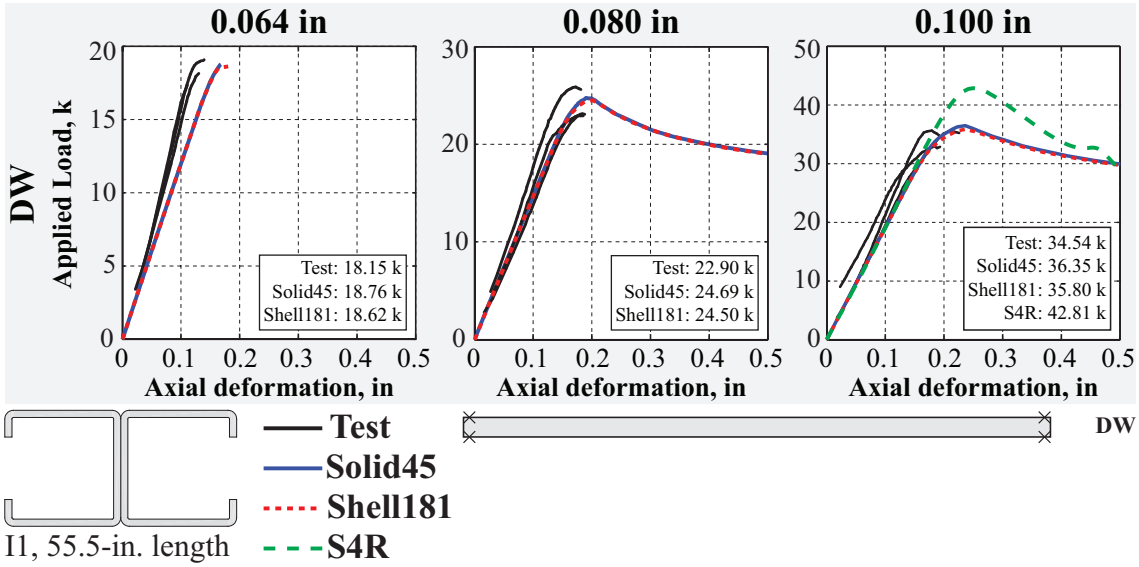


Figure 164: Overview of load vs. deformation history of 55.5”-long, *DW-I1* presented in Figs 165-167.

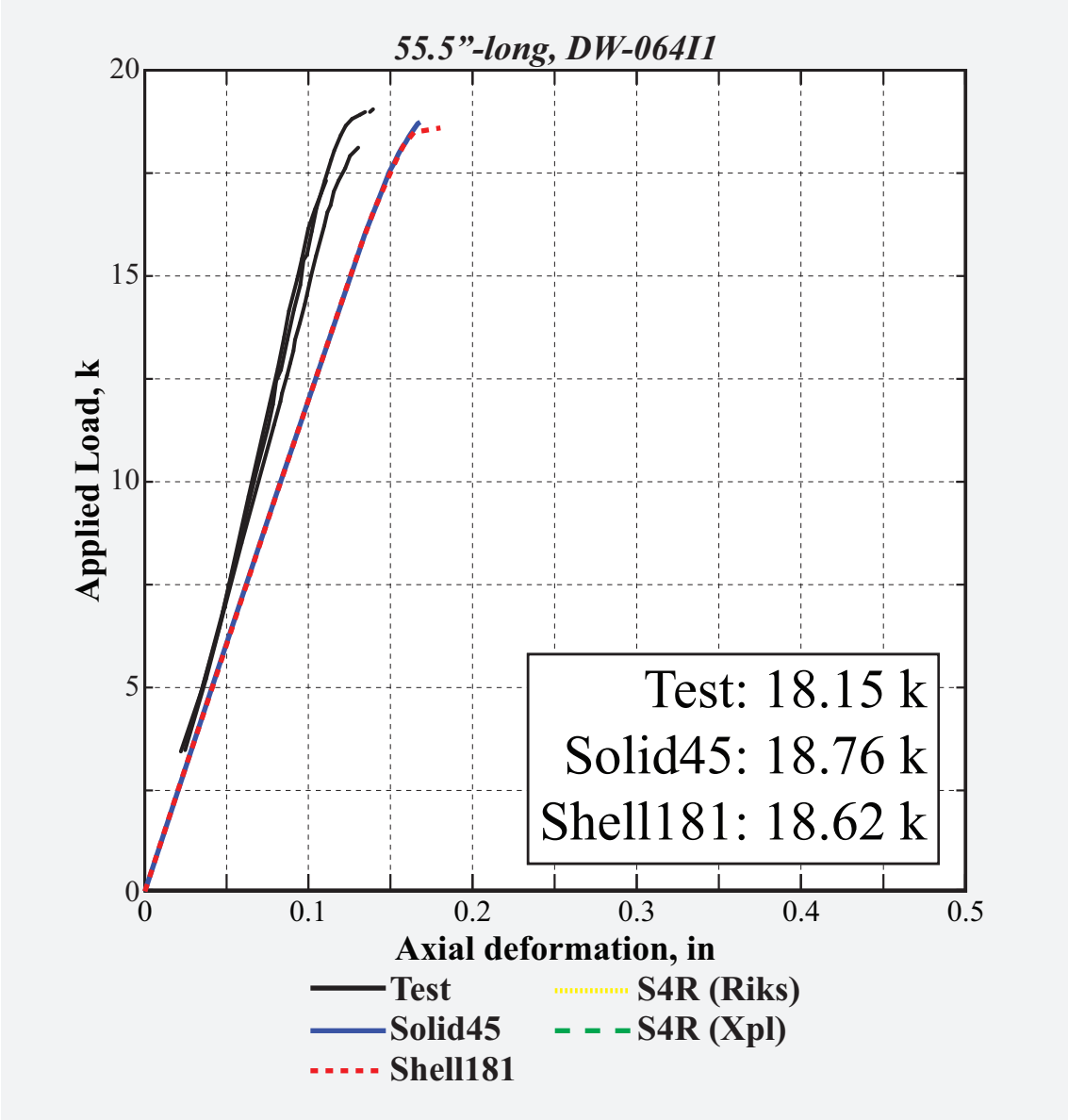


Figure 165: Load vs. deformation history of 55.5”-long, 0.064”-thick *DW-I1*.

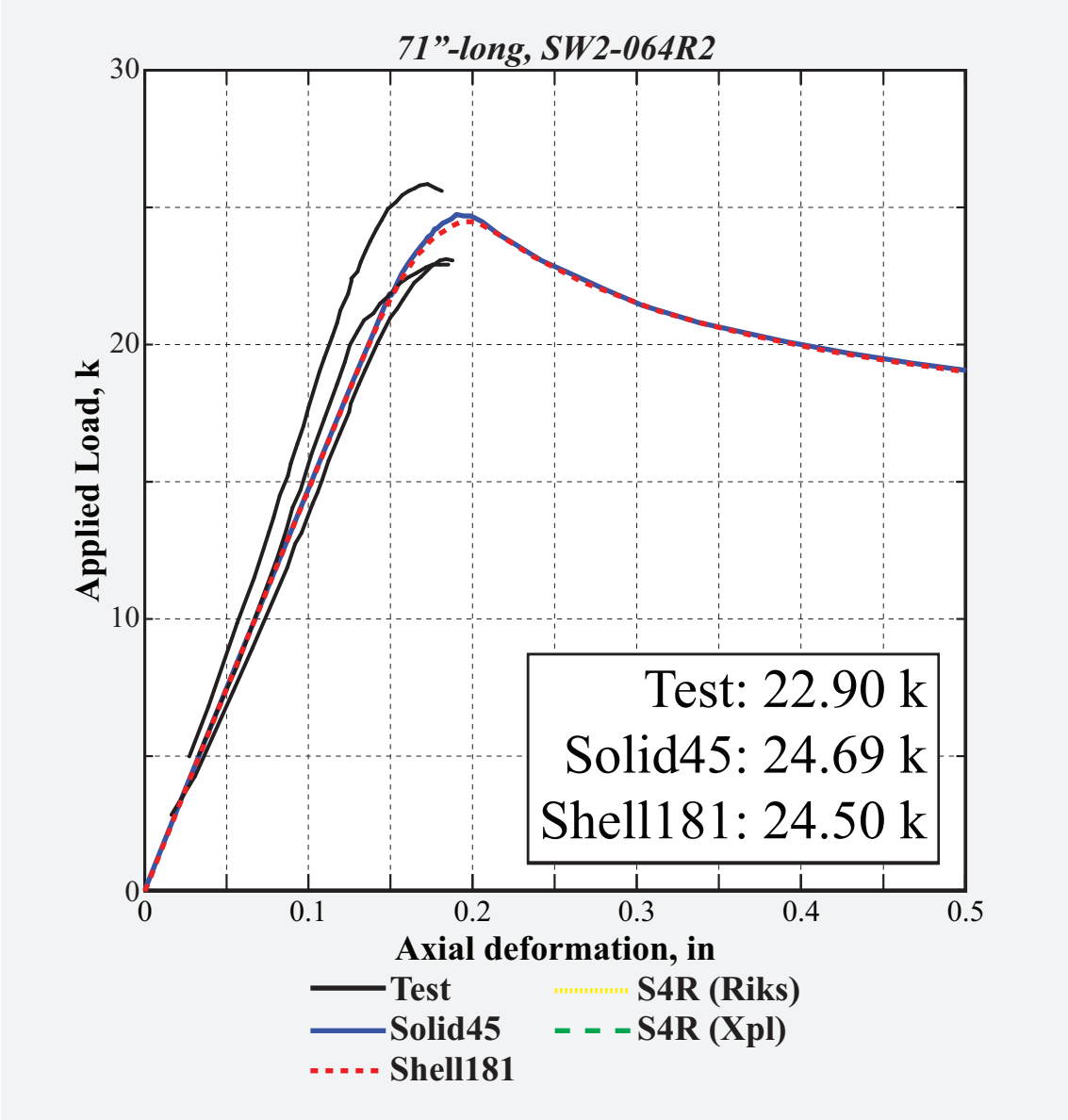


Figure 166: Load vs. deformation history of 55.5”-long, 0.08”-thick *DW-I1*.

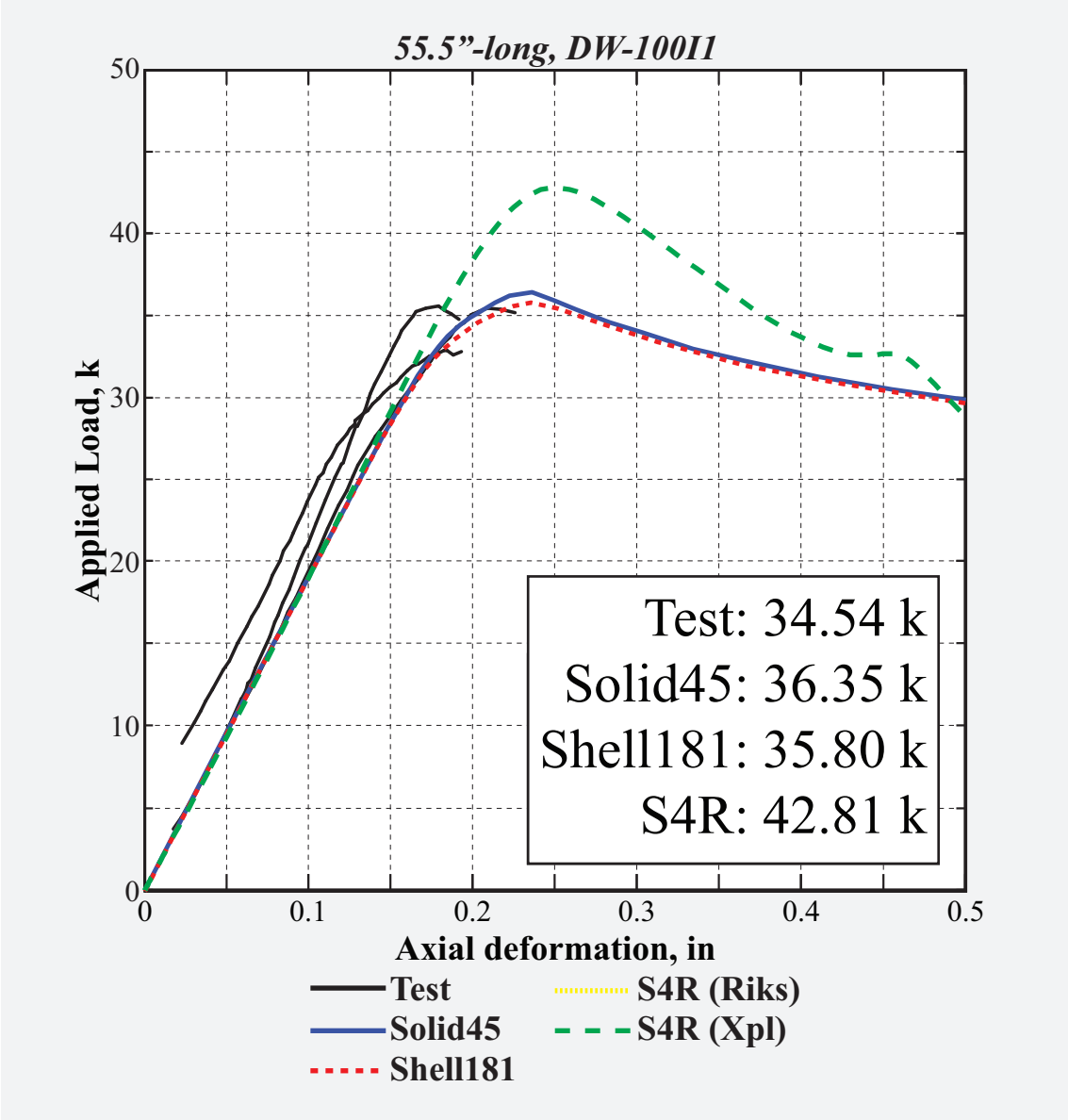


Figure 167: Load vs. deformation history of 55.5”-long, 0.1”-thick *DW-I1*.

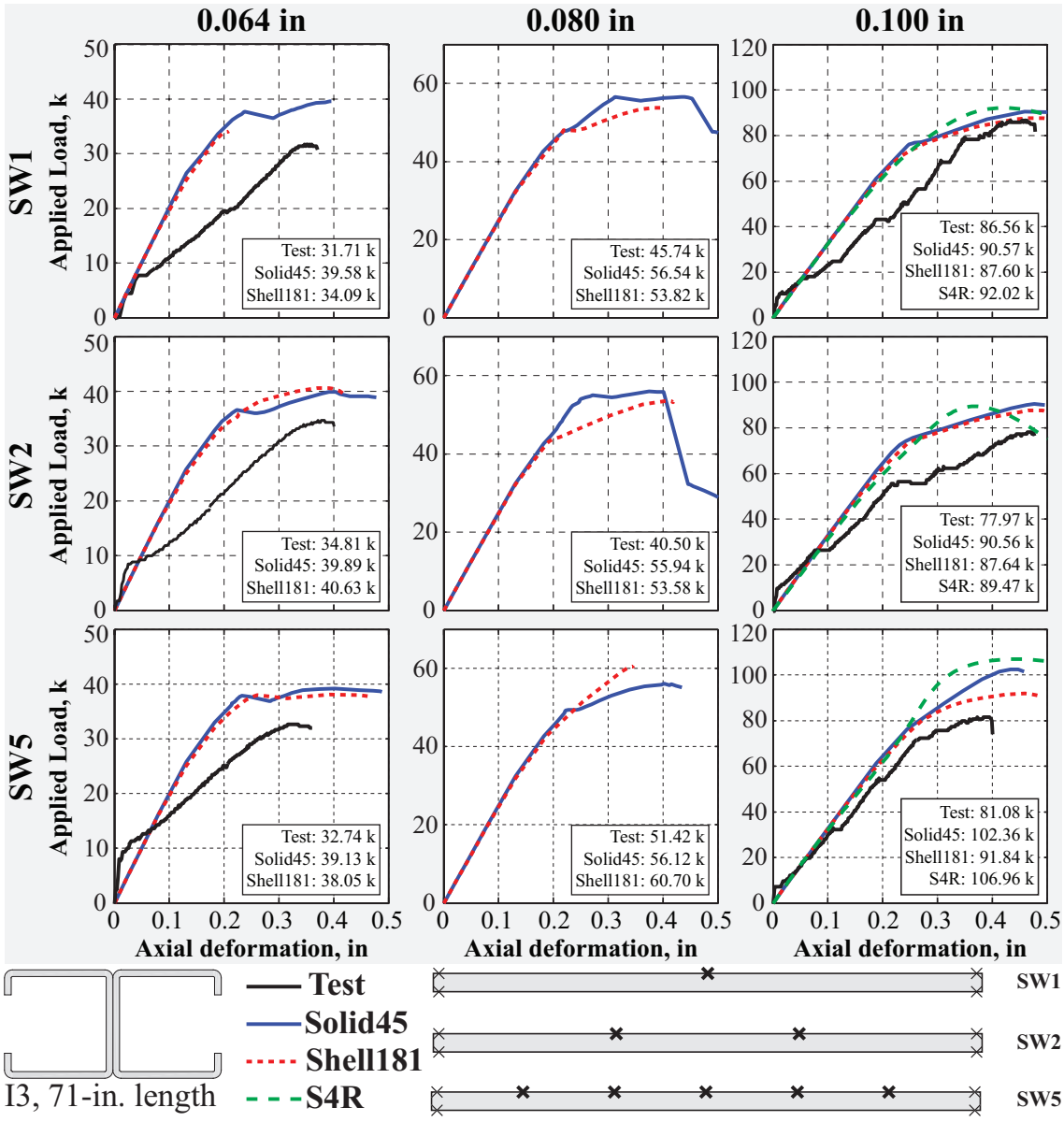


Figure 168: Overview of load vs. deformation history of 71”-long, single-sided *I3*-sections presented in Figs 169-177.

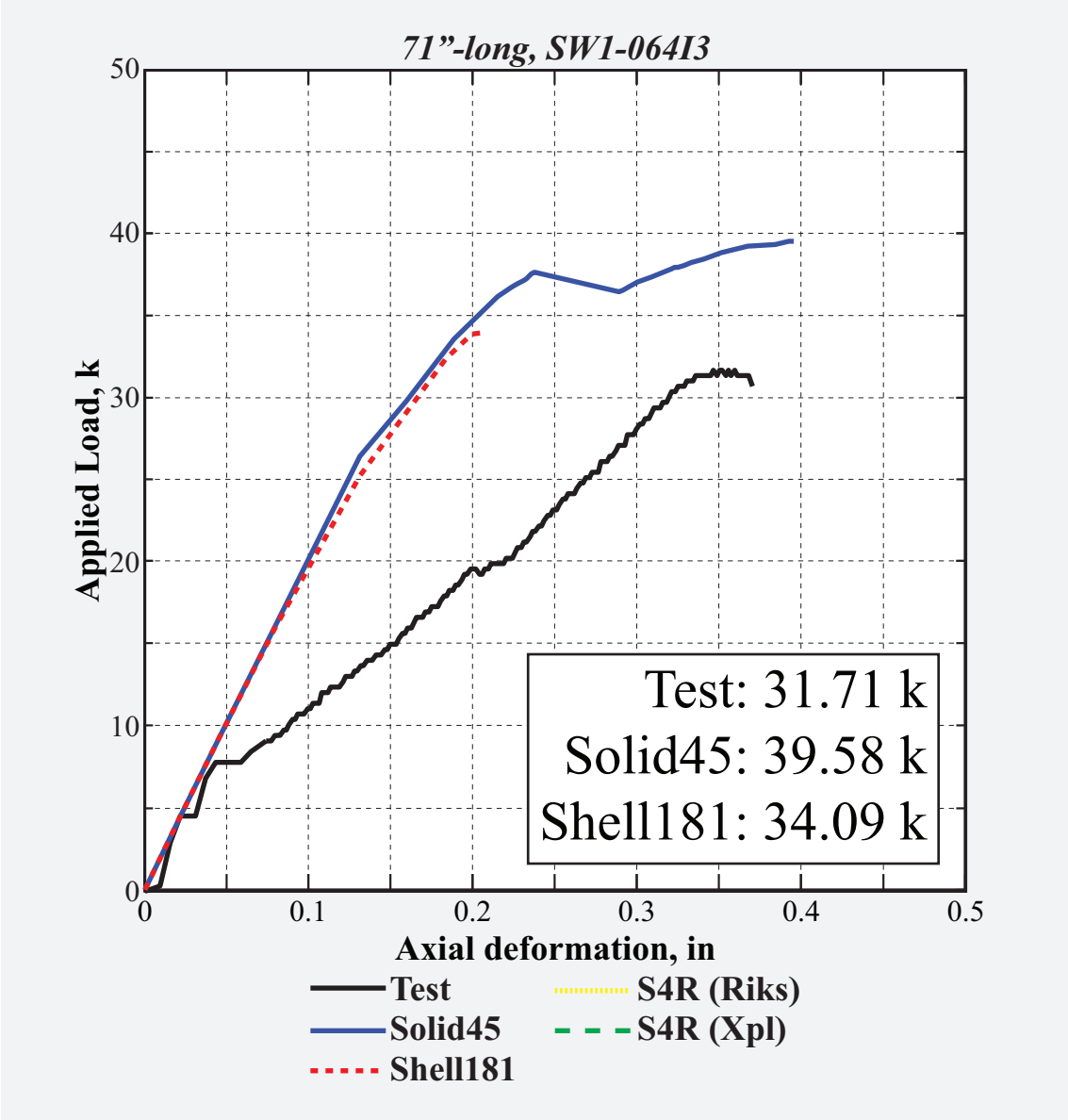


Figure 169: Load vs. deformation history of 71”-long, 0.064”-thick *SW1-I3*.

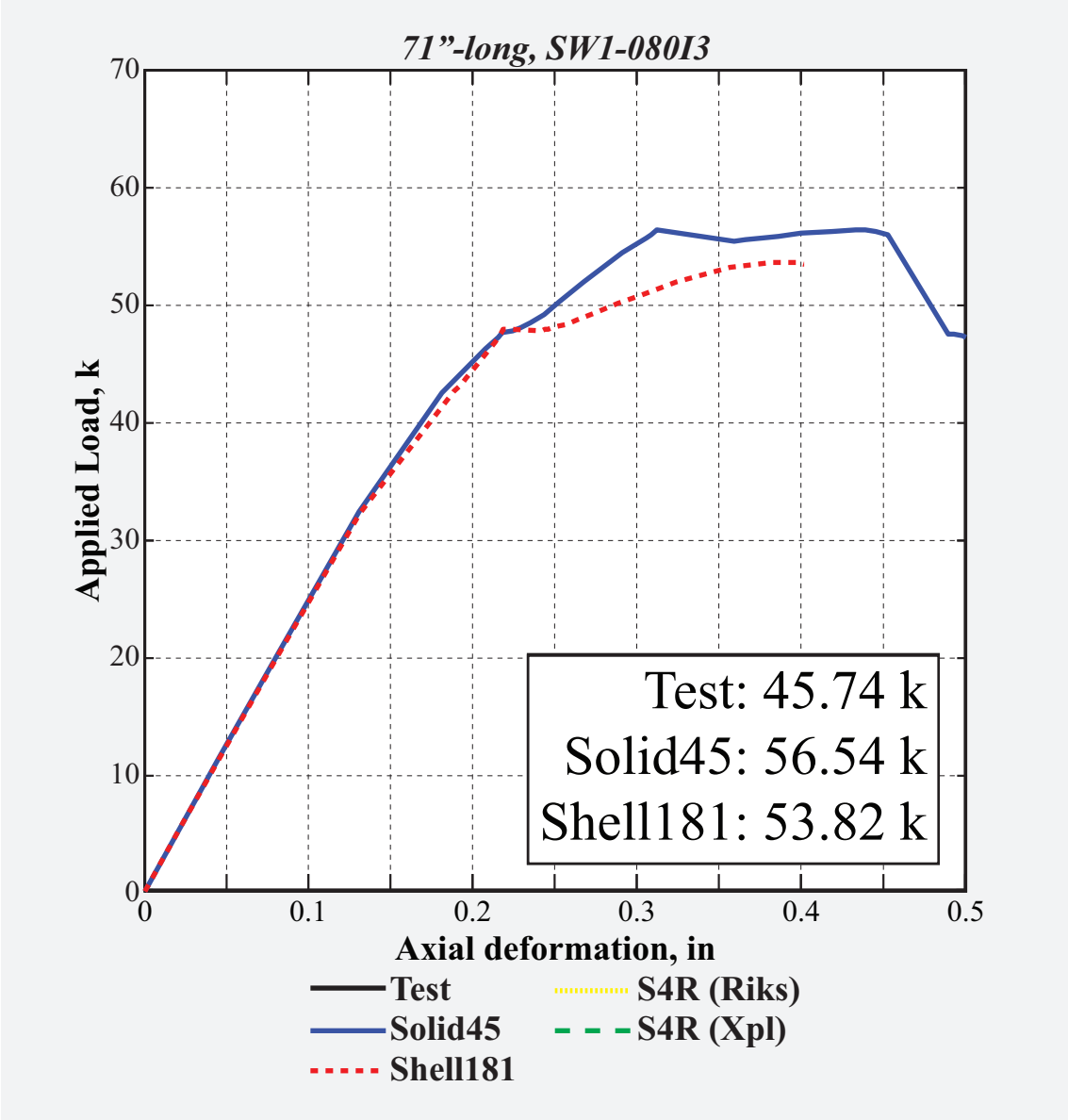


Figure 170: Load vs. deformation history of 71”-long, 0.08”-thick *SW1-I3*.

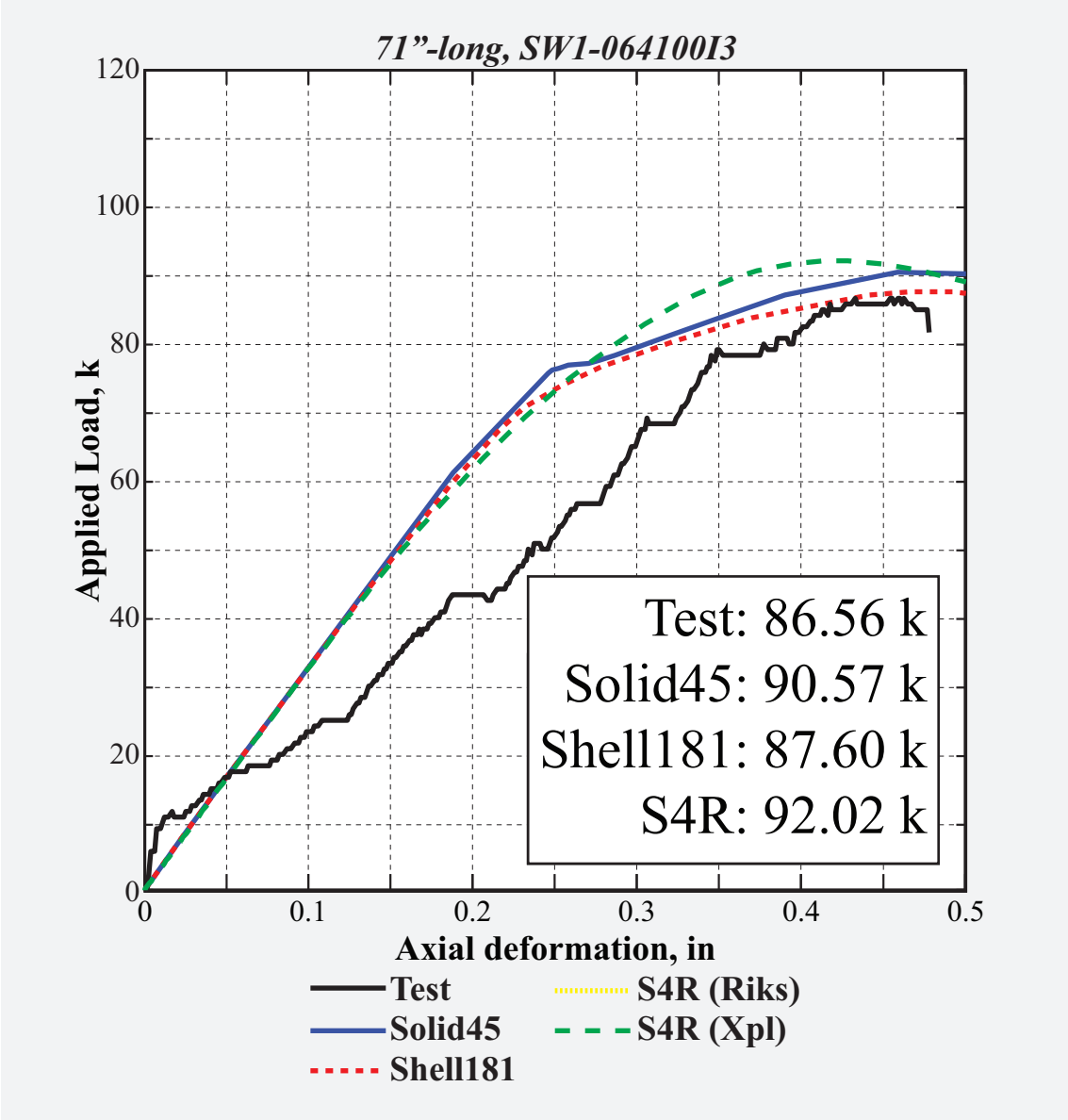


Figure 171: Load vs. deformation history of 71”-long, 0.1”-thick *SW1-I3*.

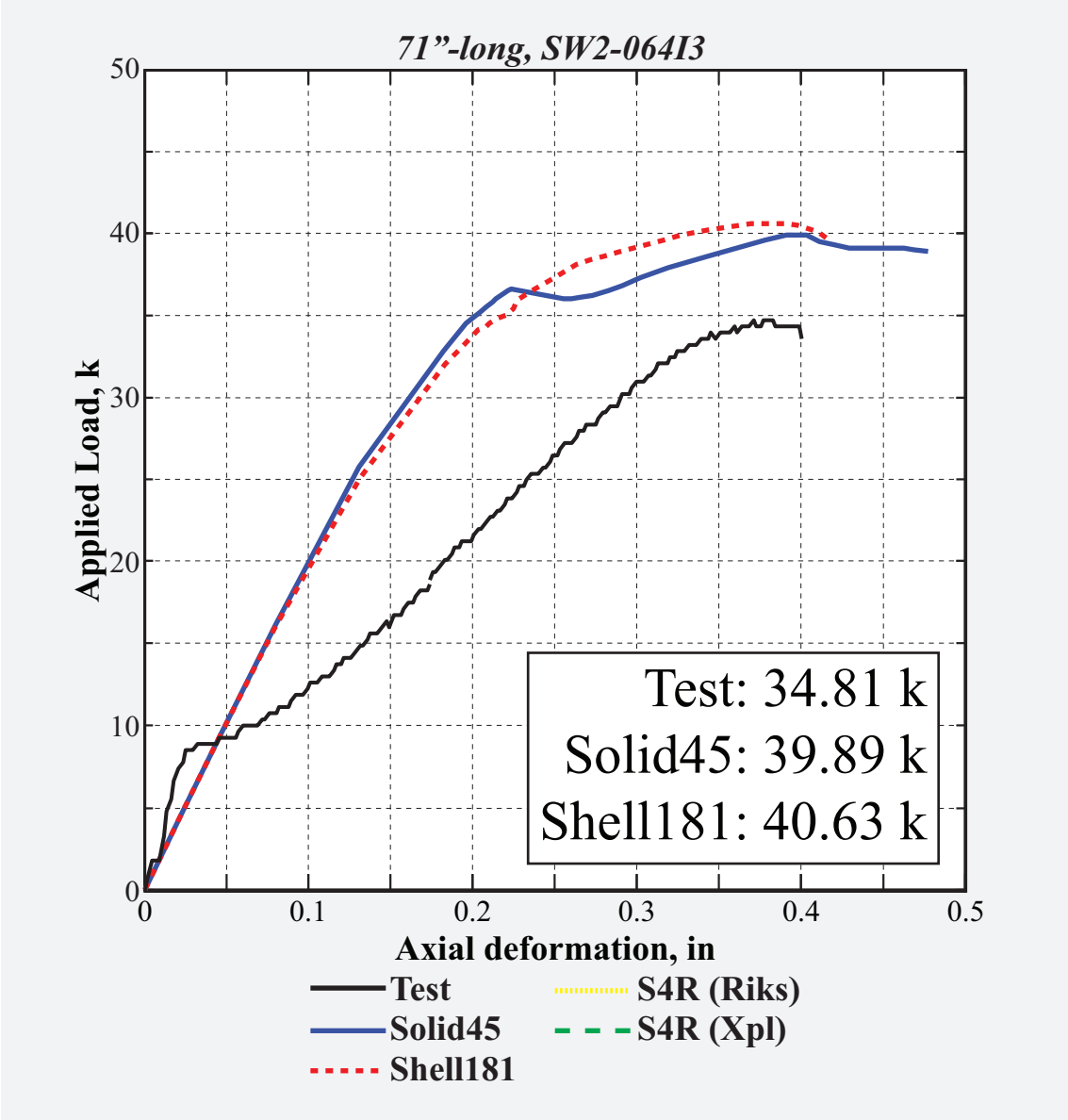


Figure 172: Load vs. deformation history of 71”-long, 0.064”-thick *SW2-I3*.

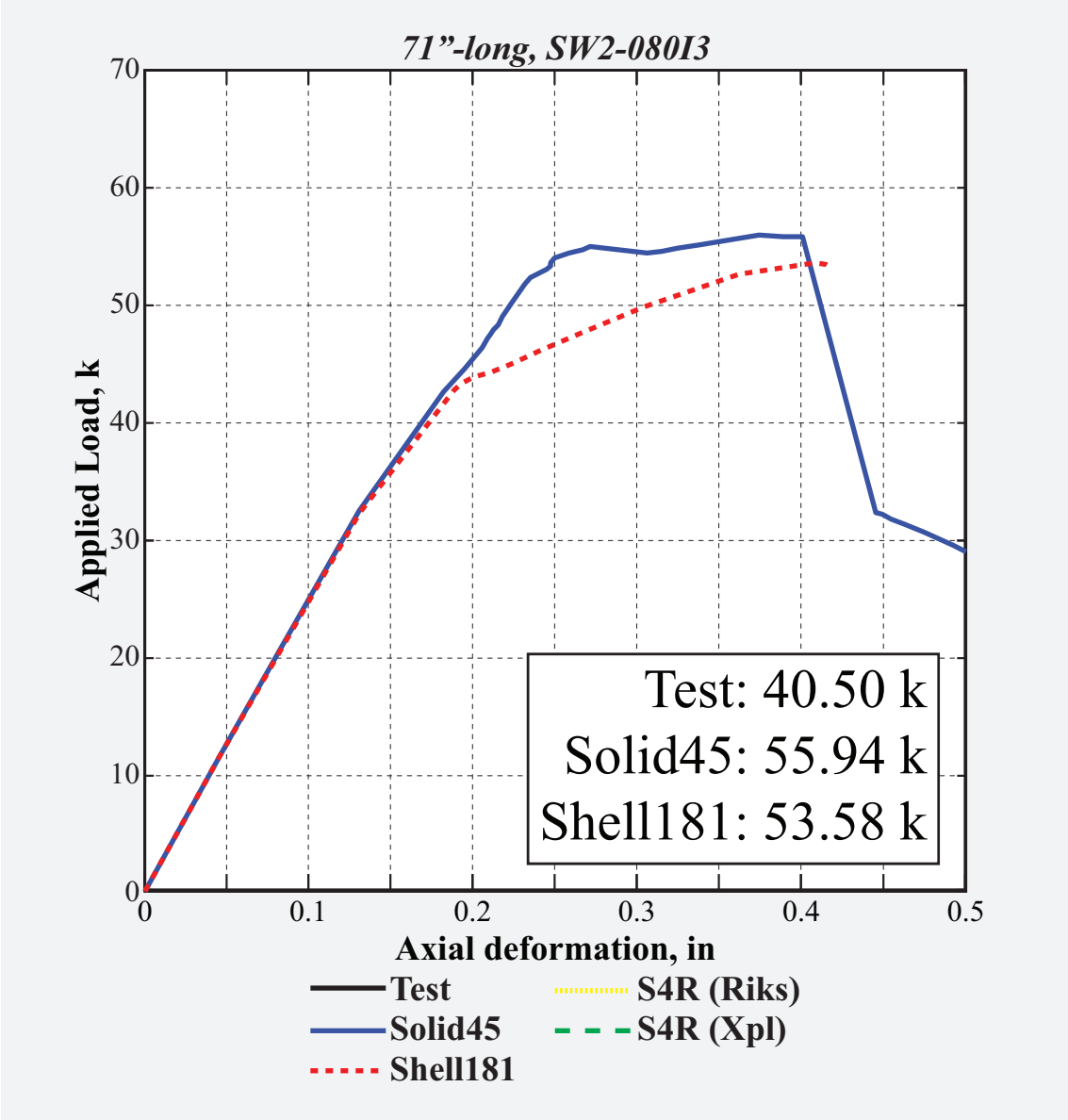


Figure 173: Load vs. deformation history of 71”-long, 0.08”-thick *SW2-I3*.

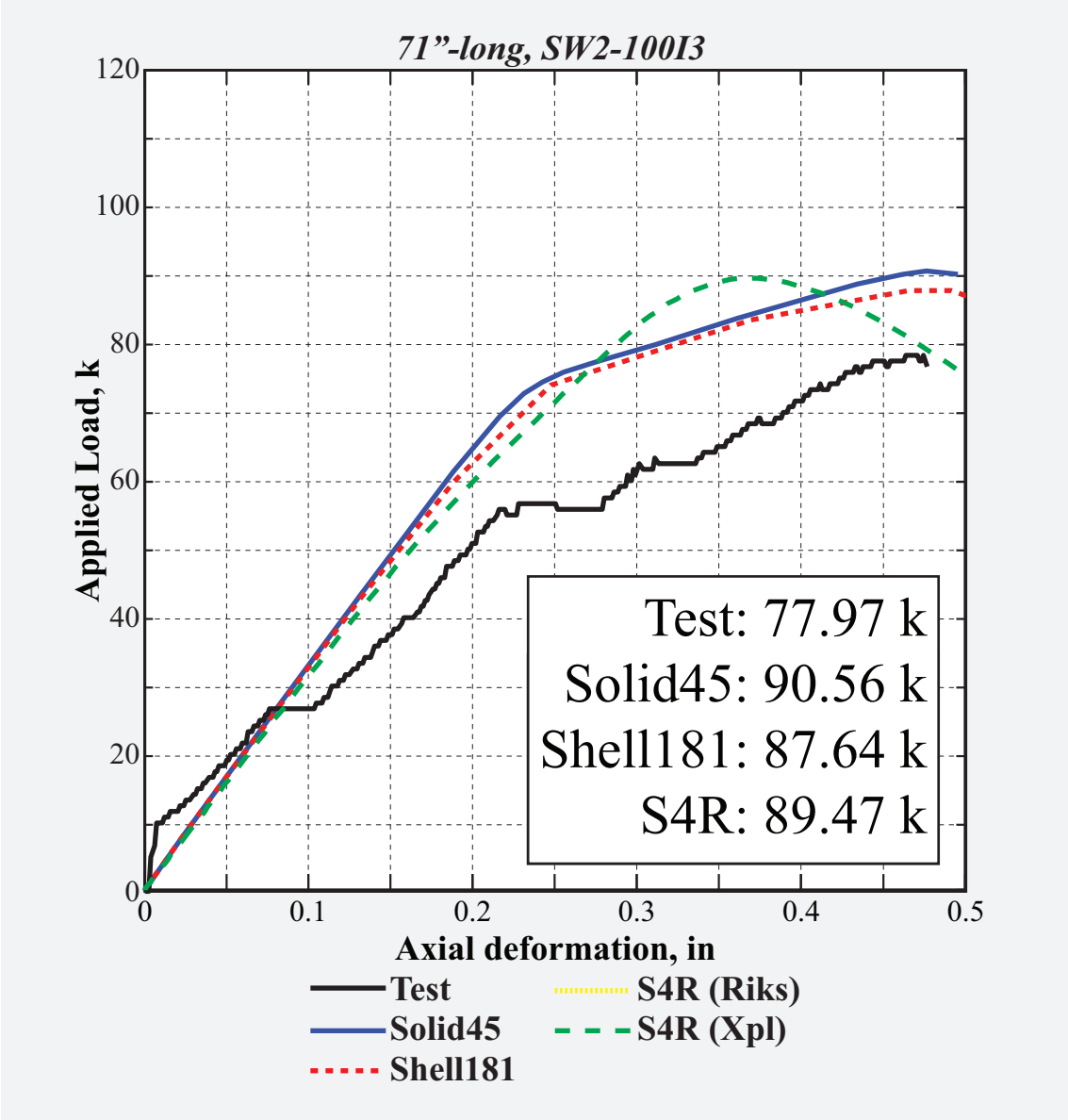


Figure 174: Load vs. deformation history of 71”-long, 0.1”-thick *SW2-I3*.

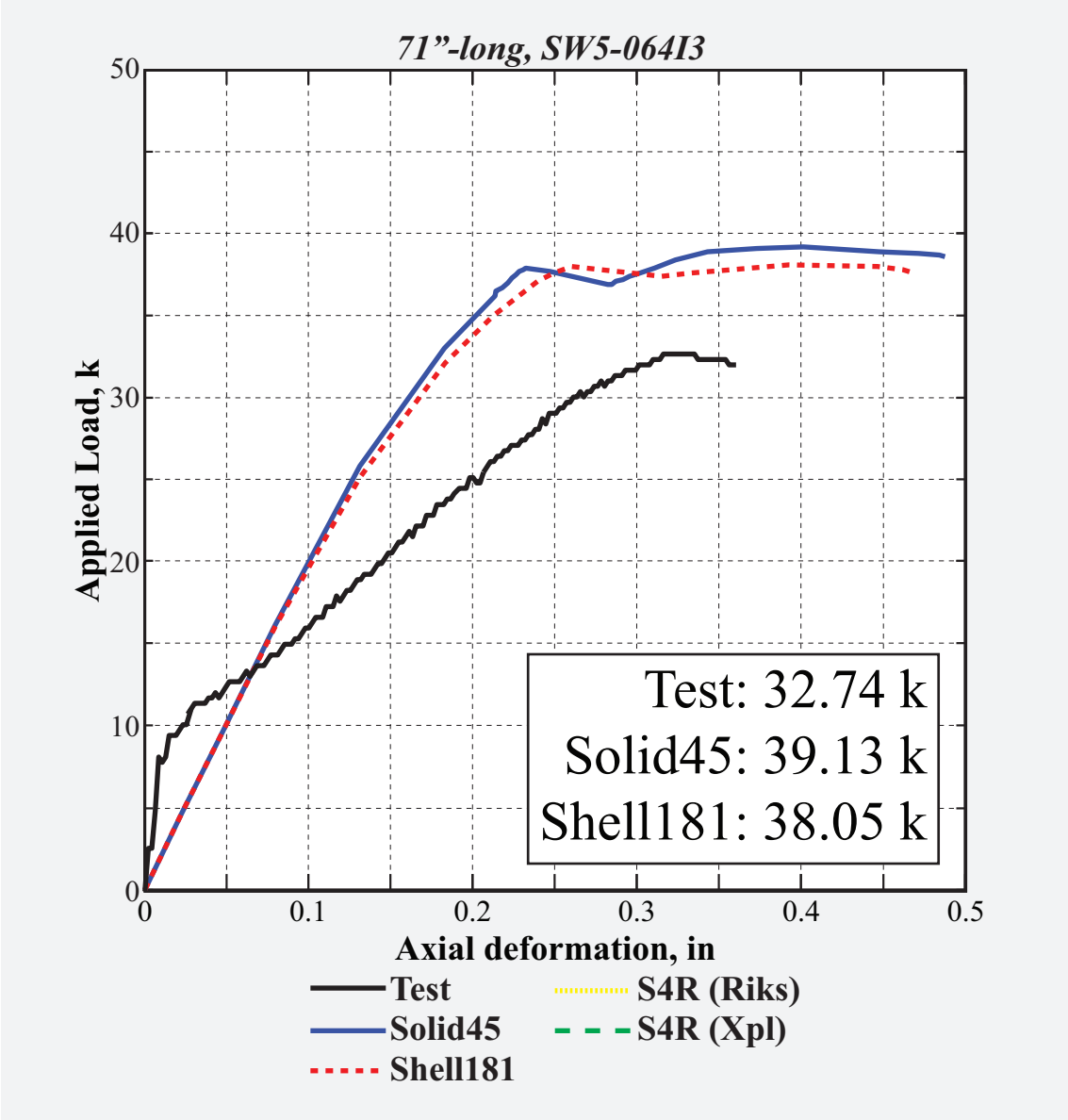


Figure 175: Load vs. deformation history of 71”-long, 0.064”-thick *SW5-I3*.

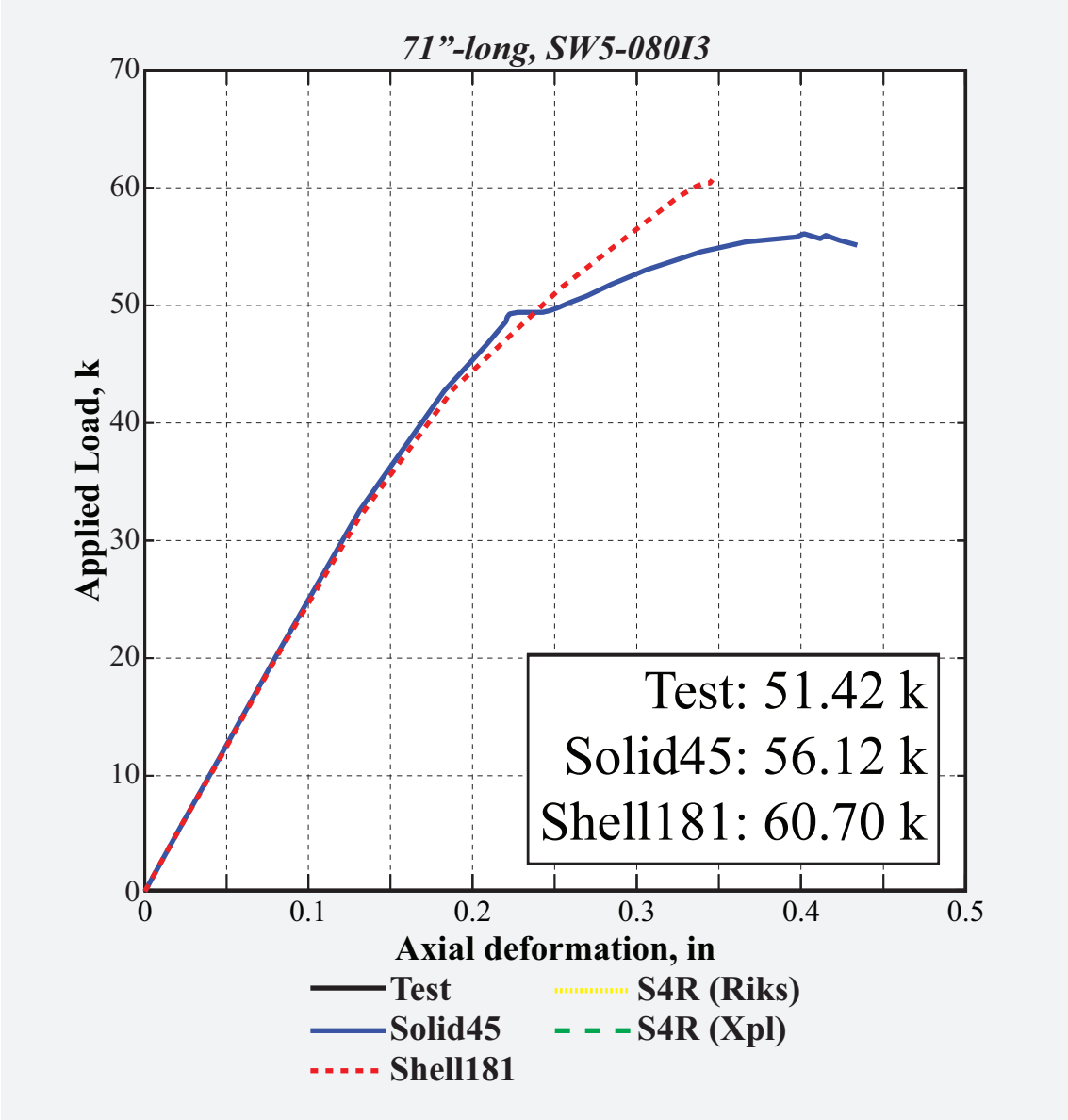


Figure 176: Load vs. deformation history of 71”-long, 0.08”-thick *SW5-I3*.

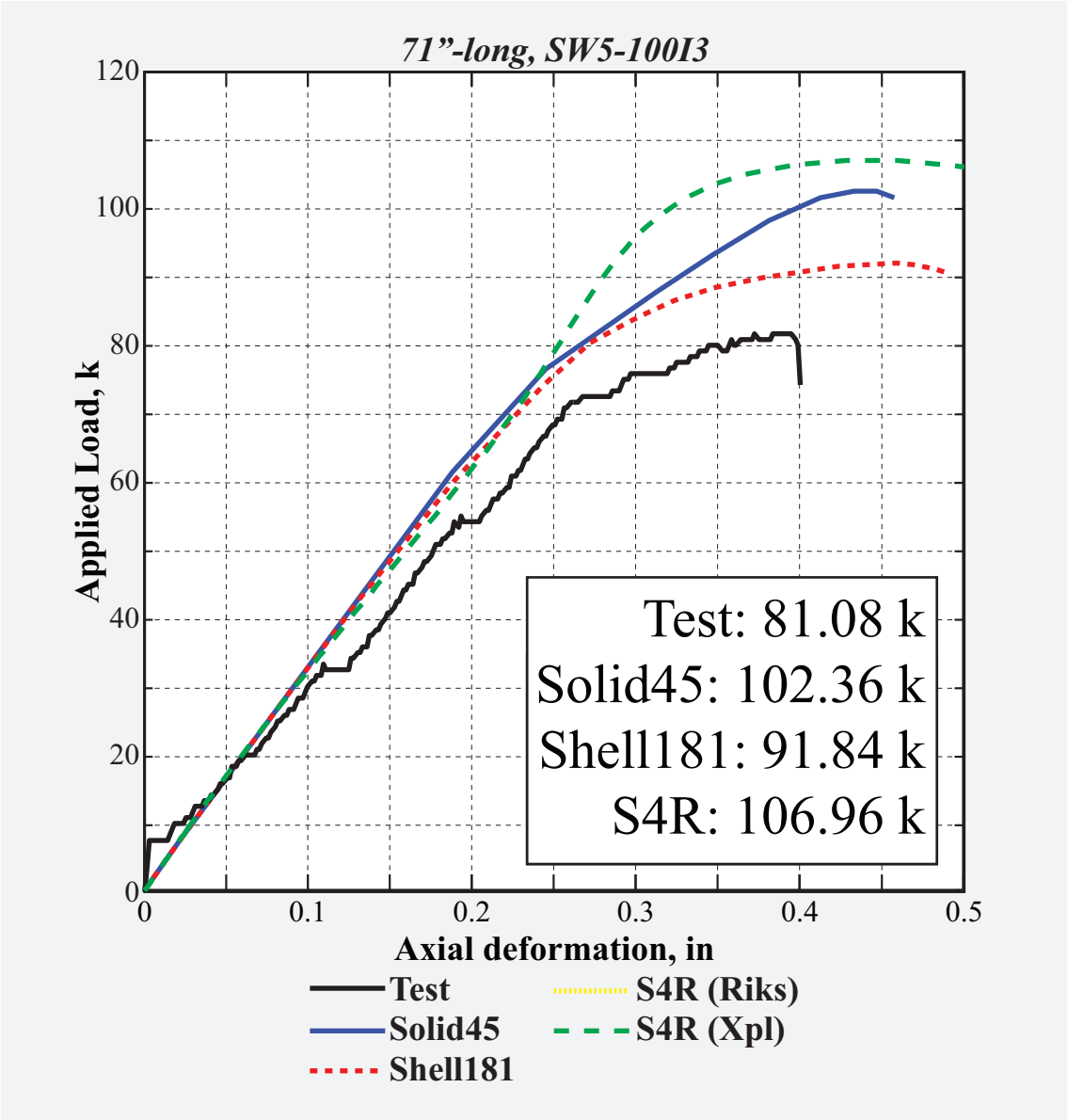


Figure 177: Load vs. deformation history of 71”-long, 0.1”-thick *SW5-I3*.

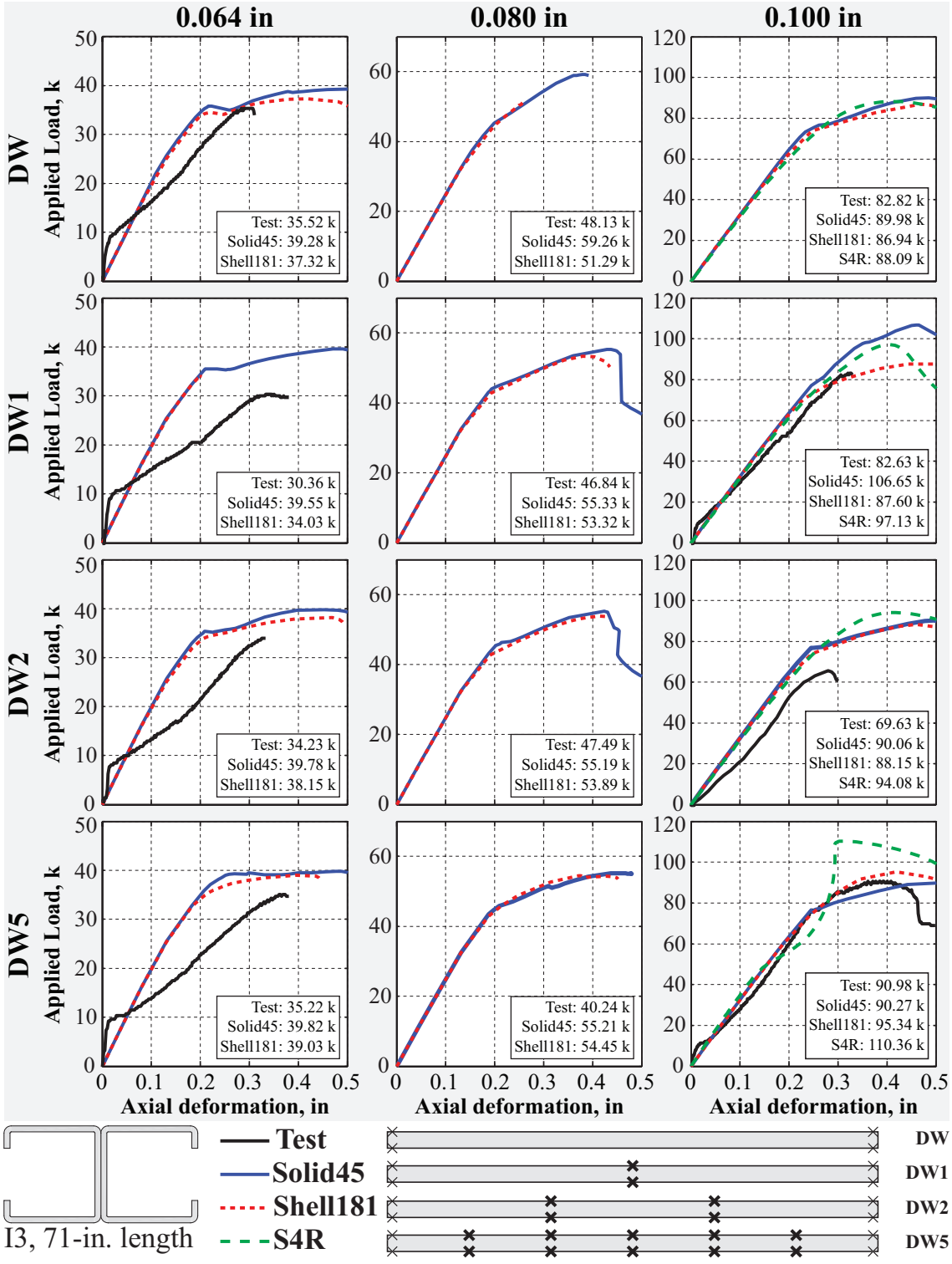


Figure 178: Overview of load vs. deformation history of 71”-long, double-sided *I3*-sections presented in Figs. 179-190.

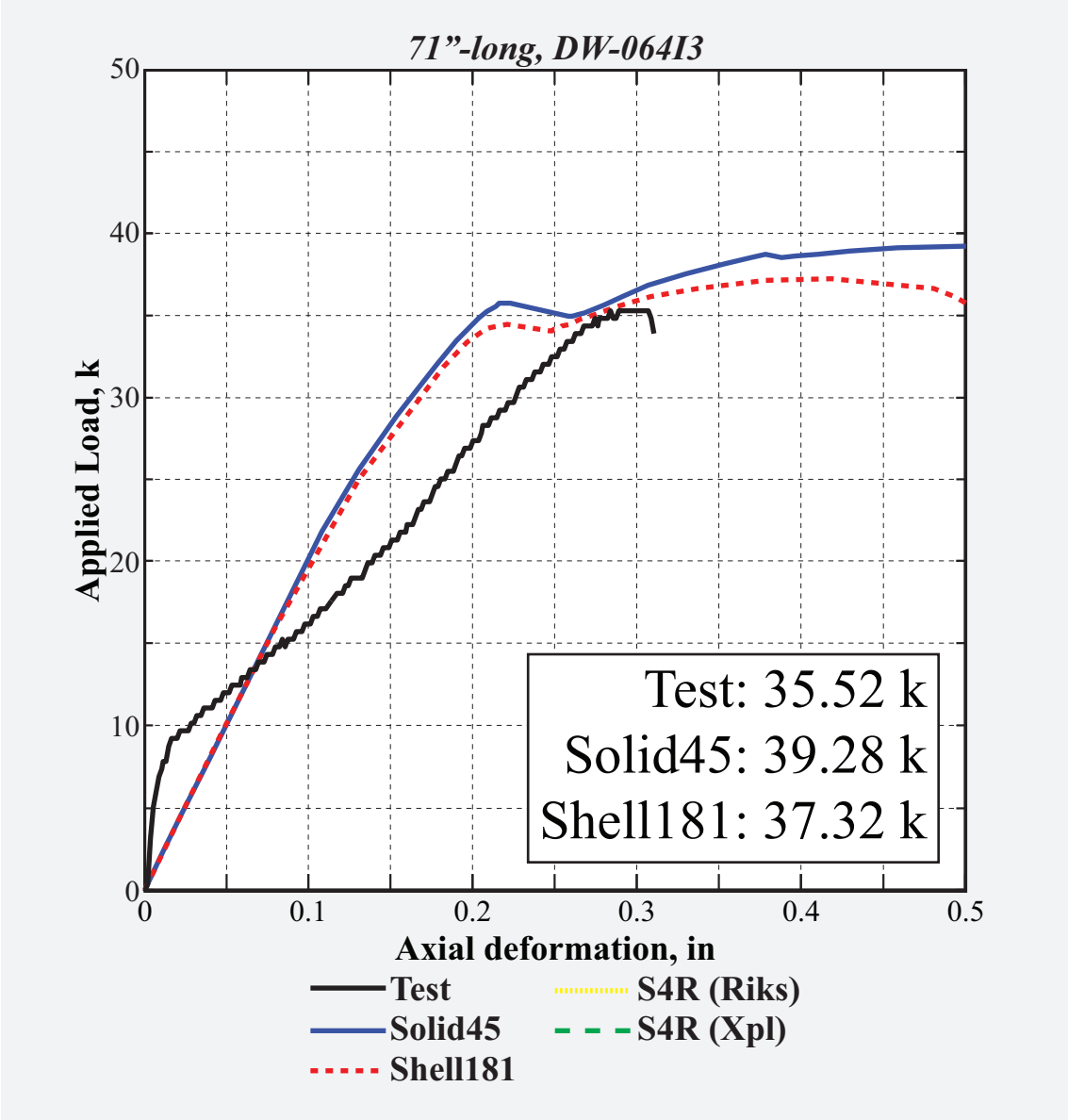


Figure 179: Load vs. deformation history of 71”-long, 0.064”-thick *DW-I3*.

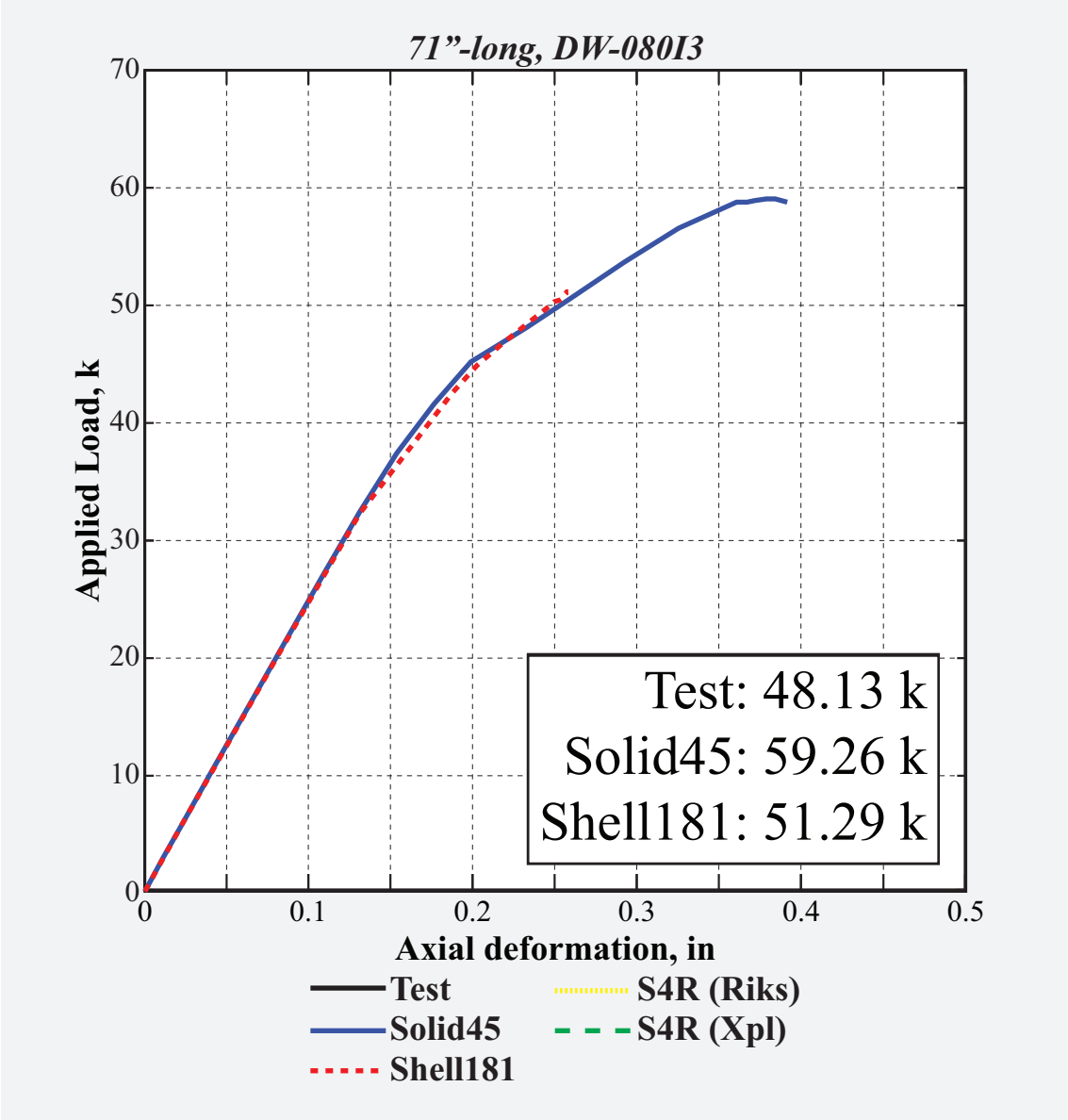


Figure 180: Load vs. deformation history of 71”-long, 0.08”-thick *DW-I3*.

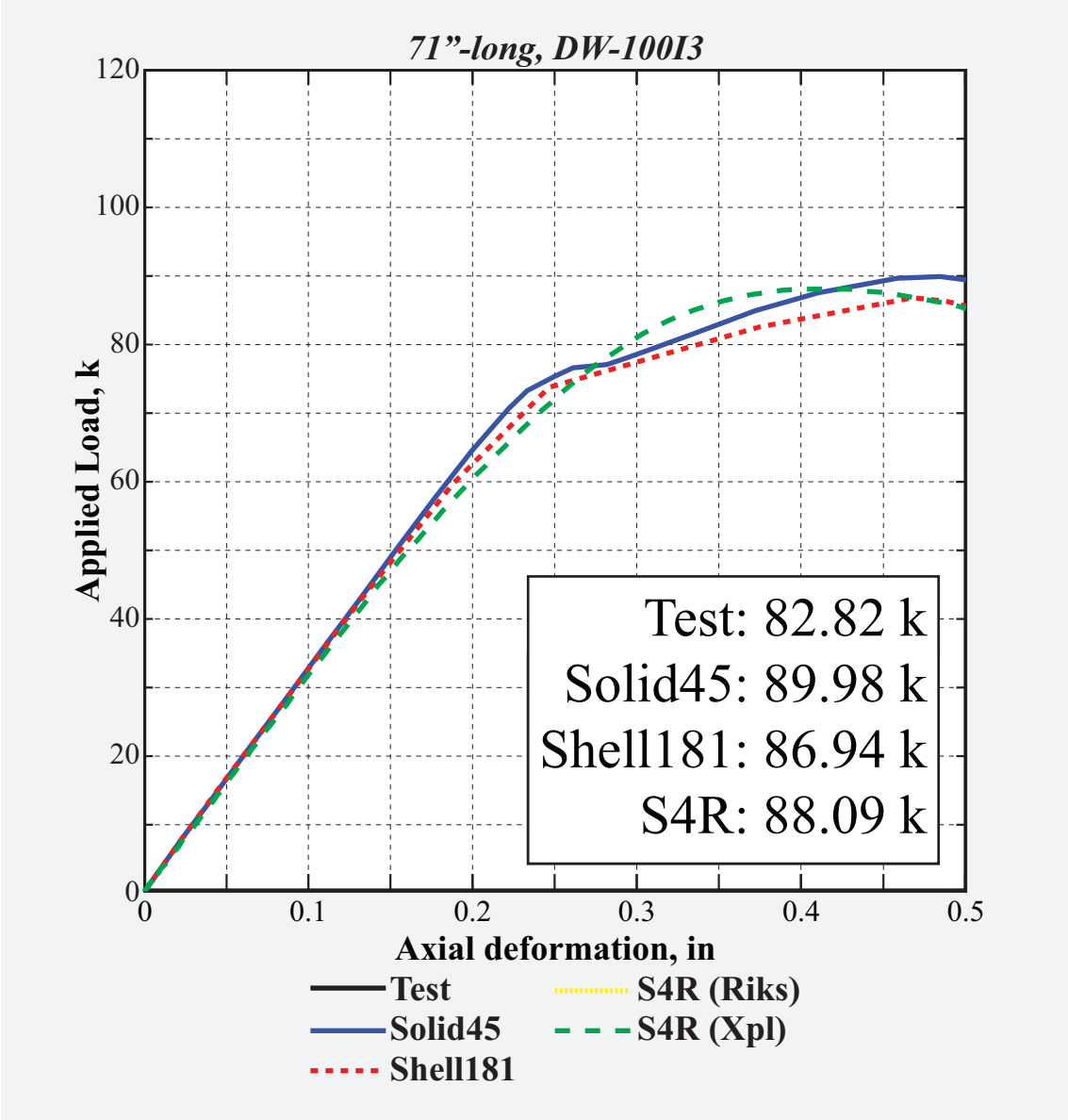


Figure 181: Load vs. deformation history of 71”-long, 0.1”-thick *DW-I3*.

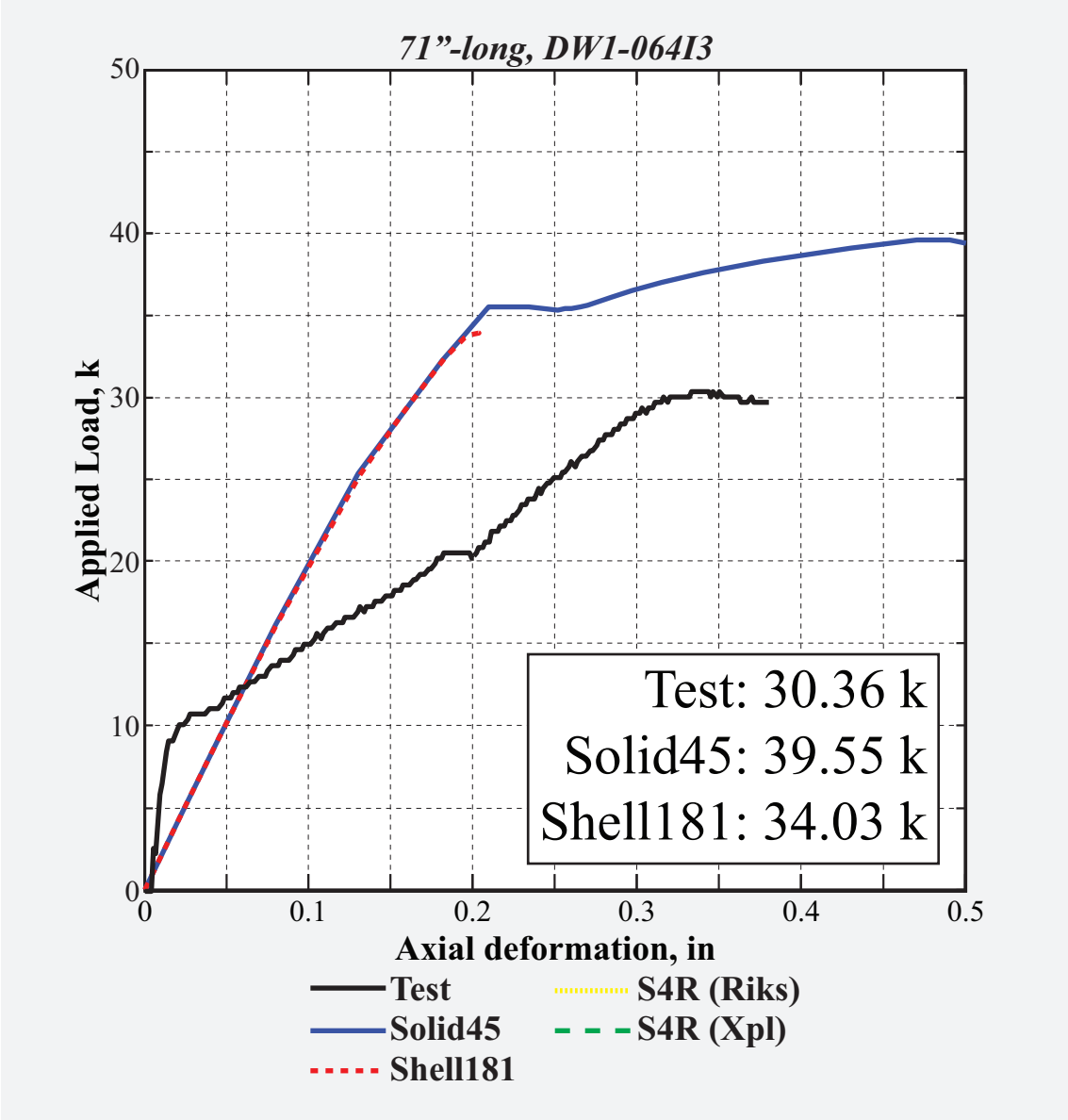


Figure 182: Load vs. deformation history of 71”-long, 0.064”-thick *DW1-I3*.

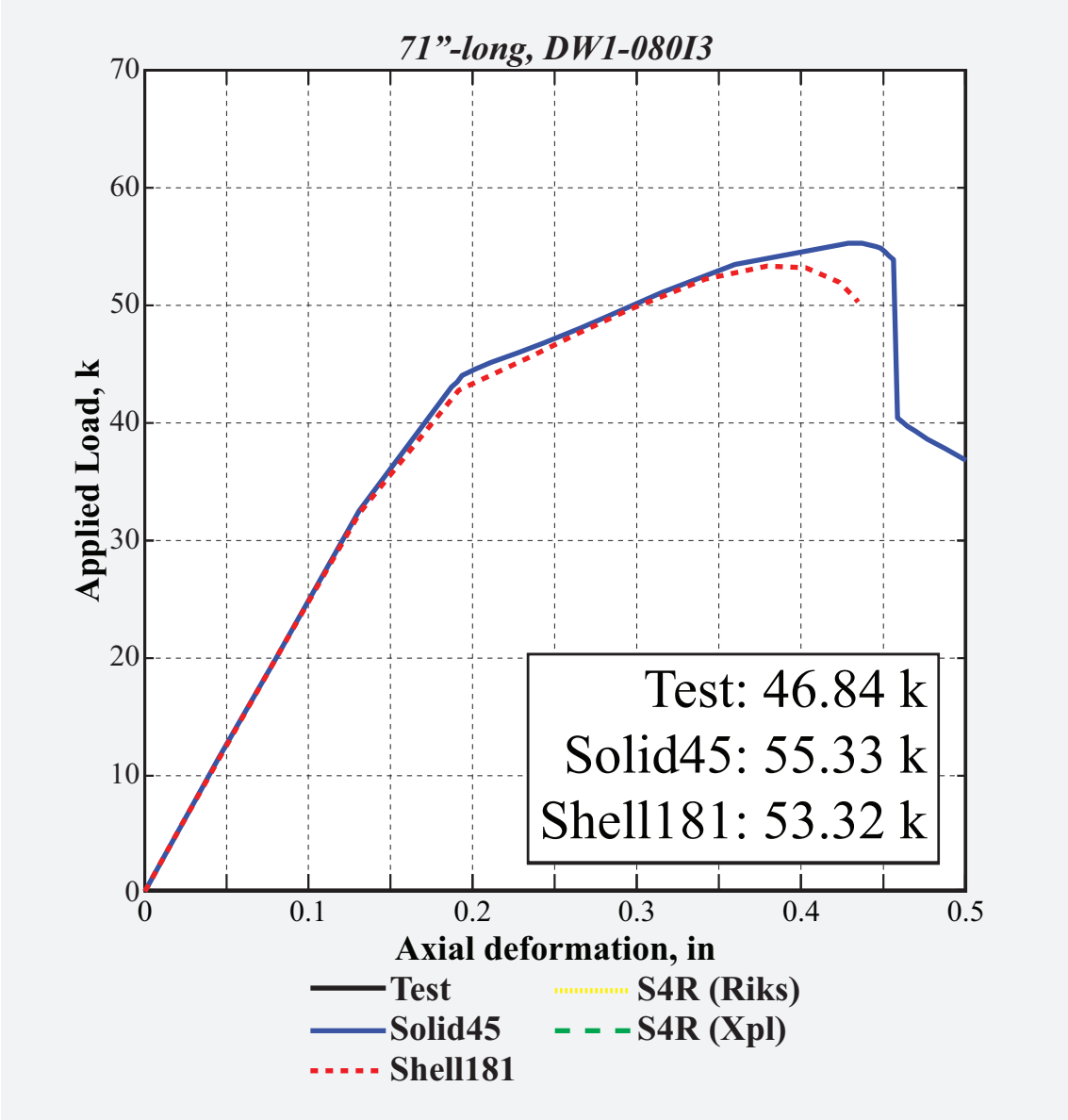


Figure 183: Load vs. deformation history of 71”-long, 0.08”-thick *DW1-I3*.

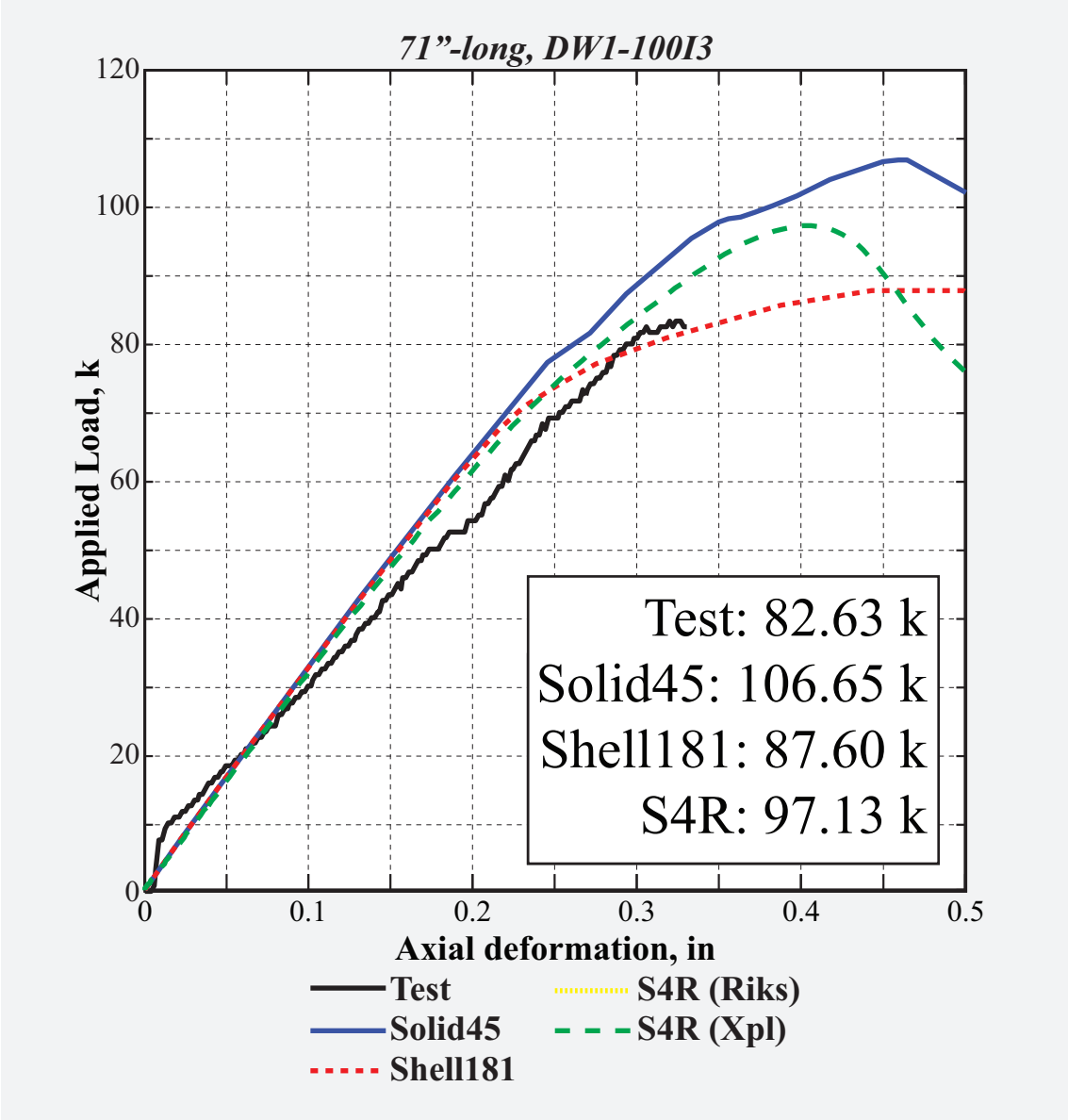


Figure 184: Load vs. deformation history of 71”-long, 0.1”-thick *DW1-I3*.

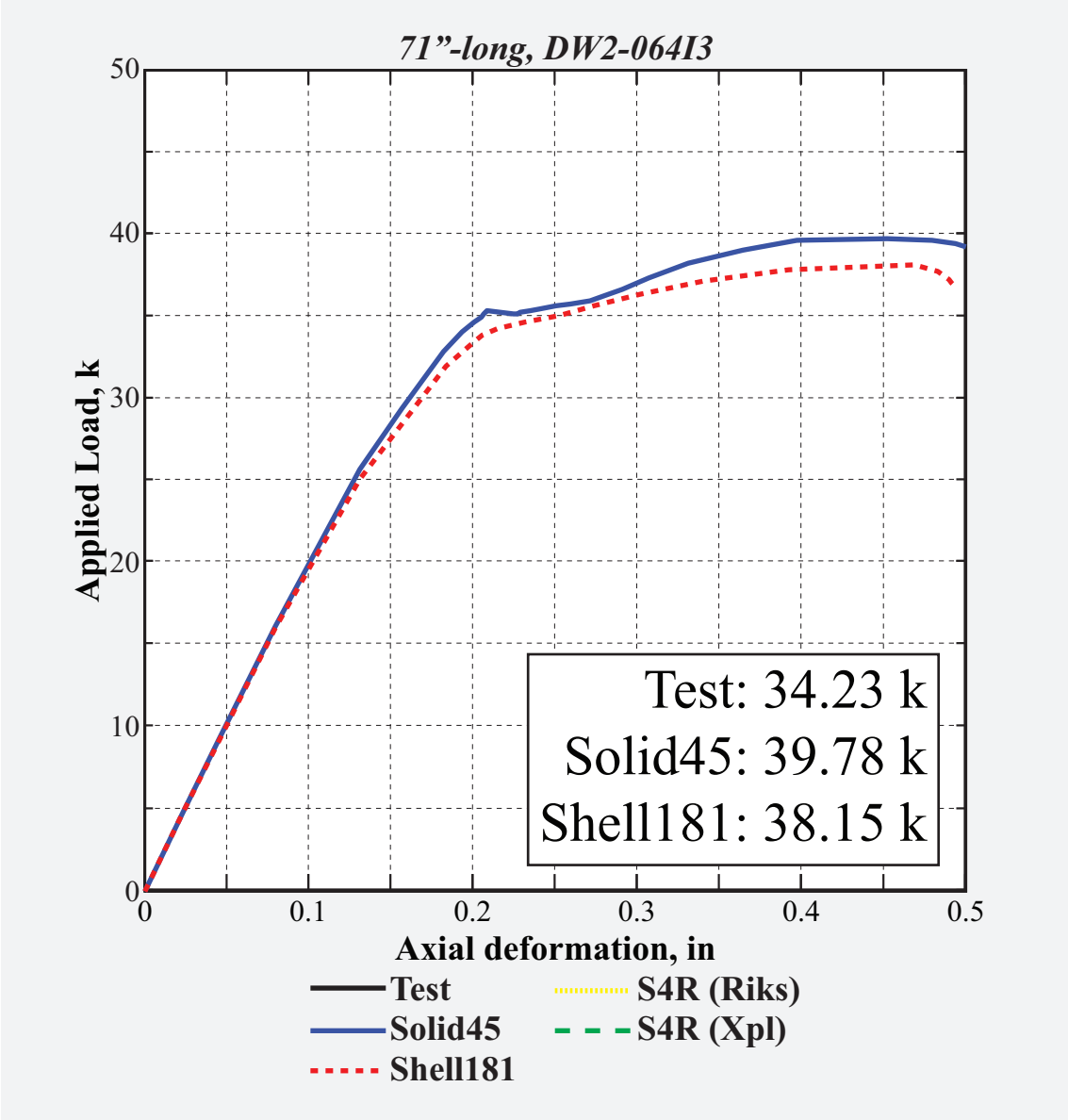


Figure 185: Load vs. deformation history of 71”-long, 0.064”-thick *DW2-I3*.

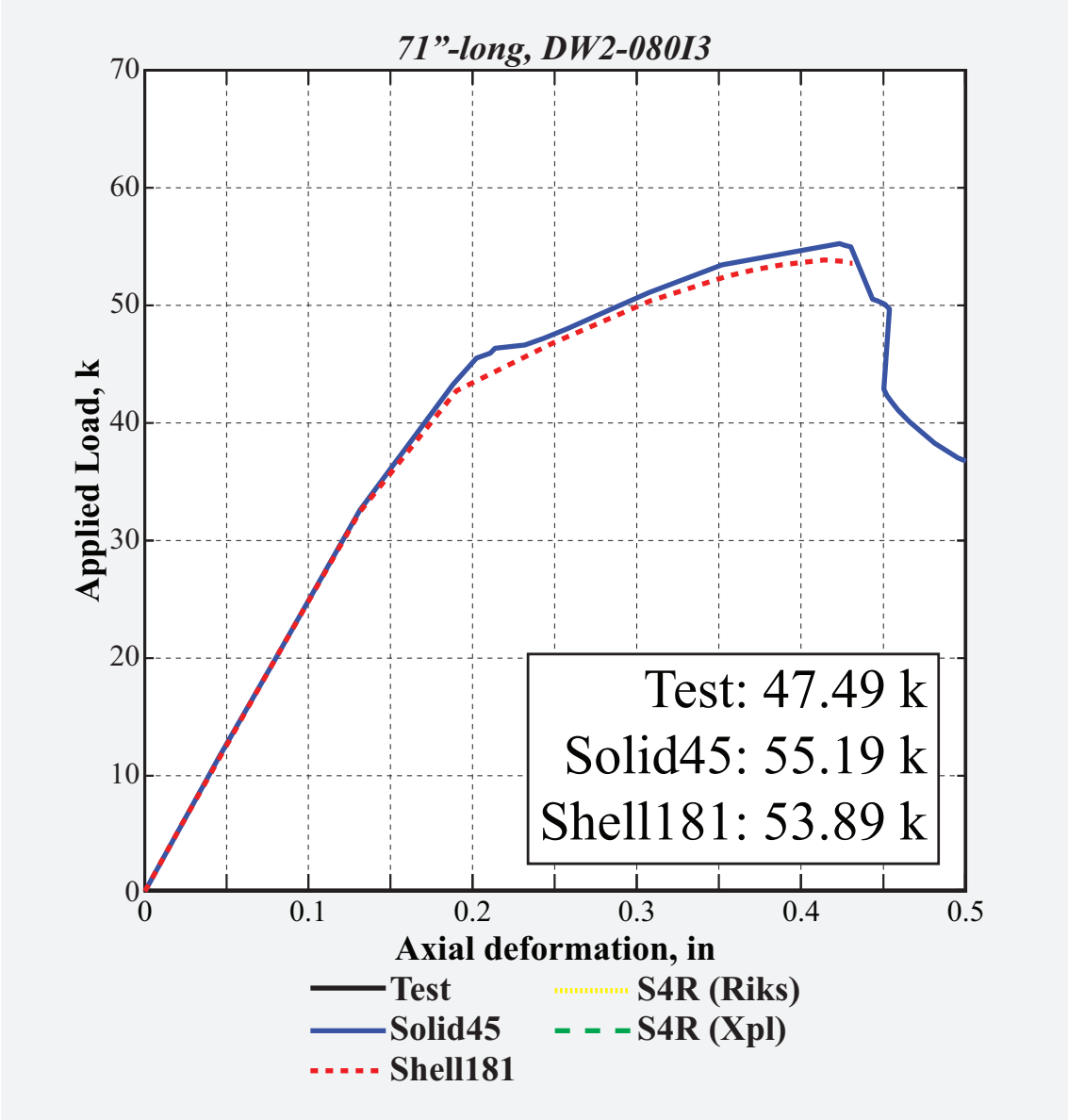


Figure 186: Load vs. deformation history of 71”-long, 0.08”-thick *DW2-I3*.

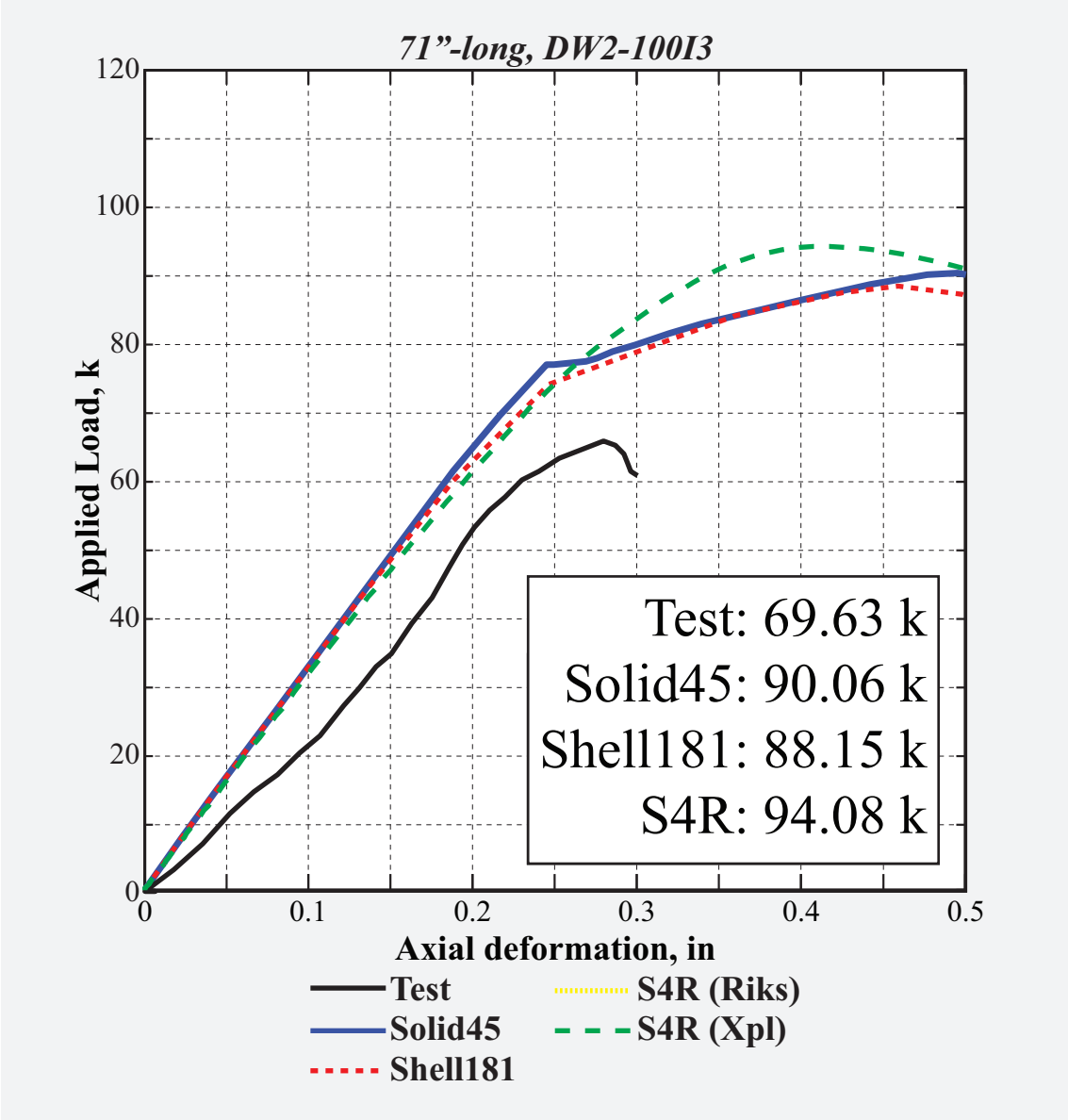


Figure 187: Load vs. deformation history of 71”-long, 0.1”-thick *DW2-I3*.

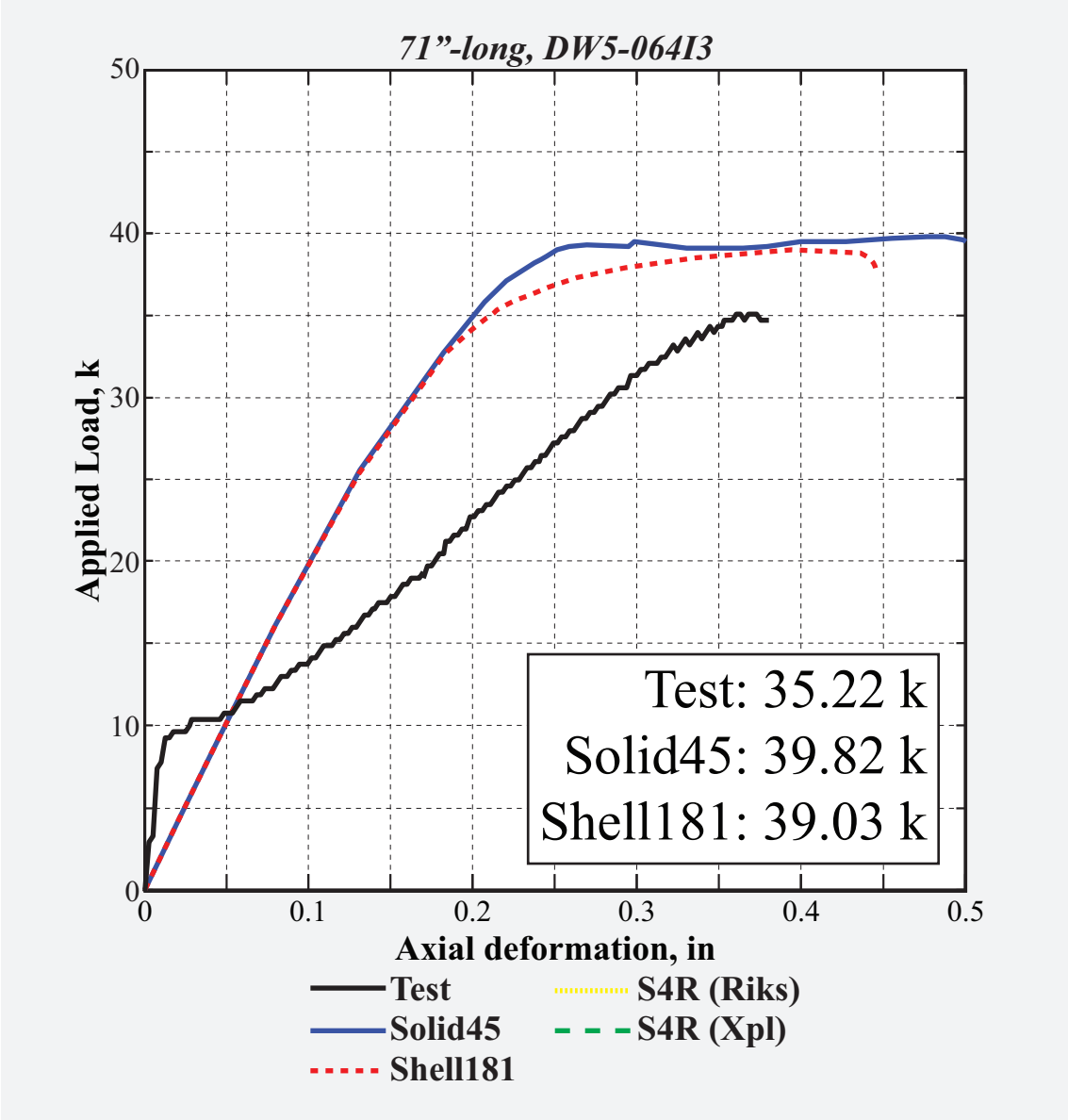


Figure 188: Load vs. deformation history of 71”-long, 0.064”-thick *DW5-I3*.

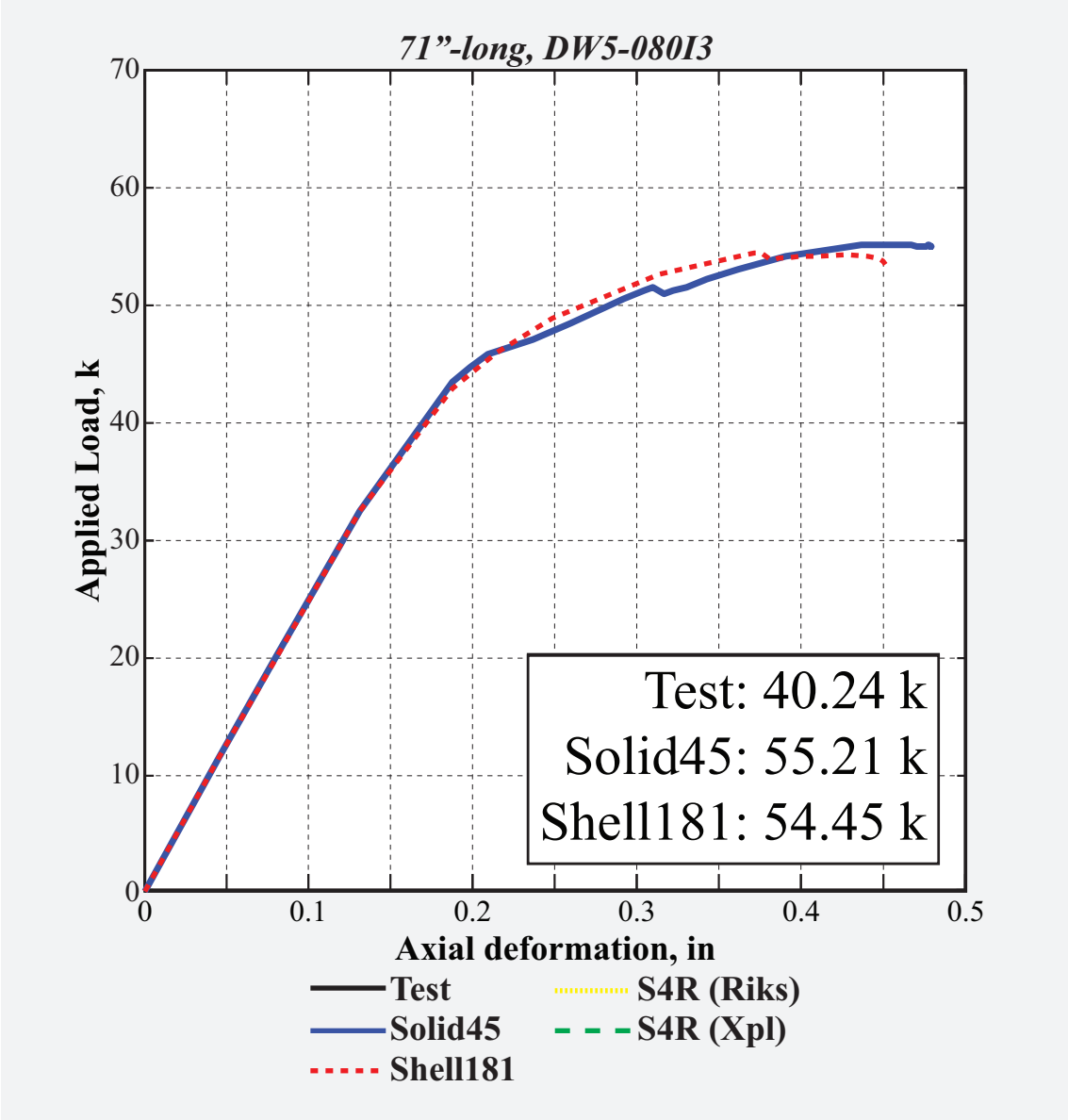


Figure 189: Load vs. deformation history of 71”-long, 0.08”-thick *DW5-I3*.

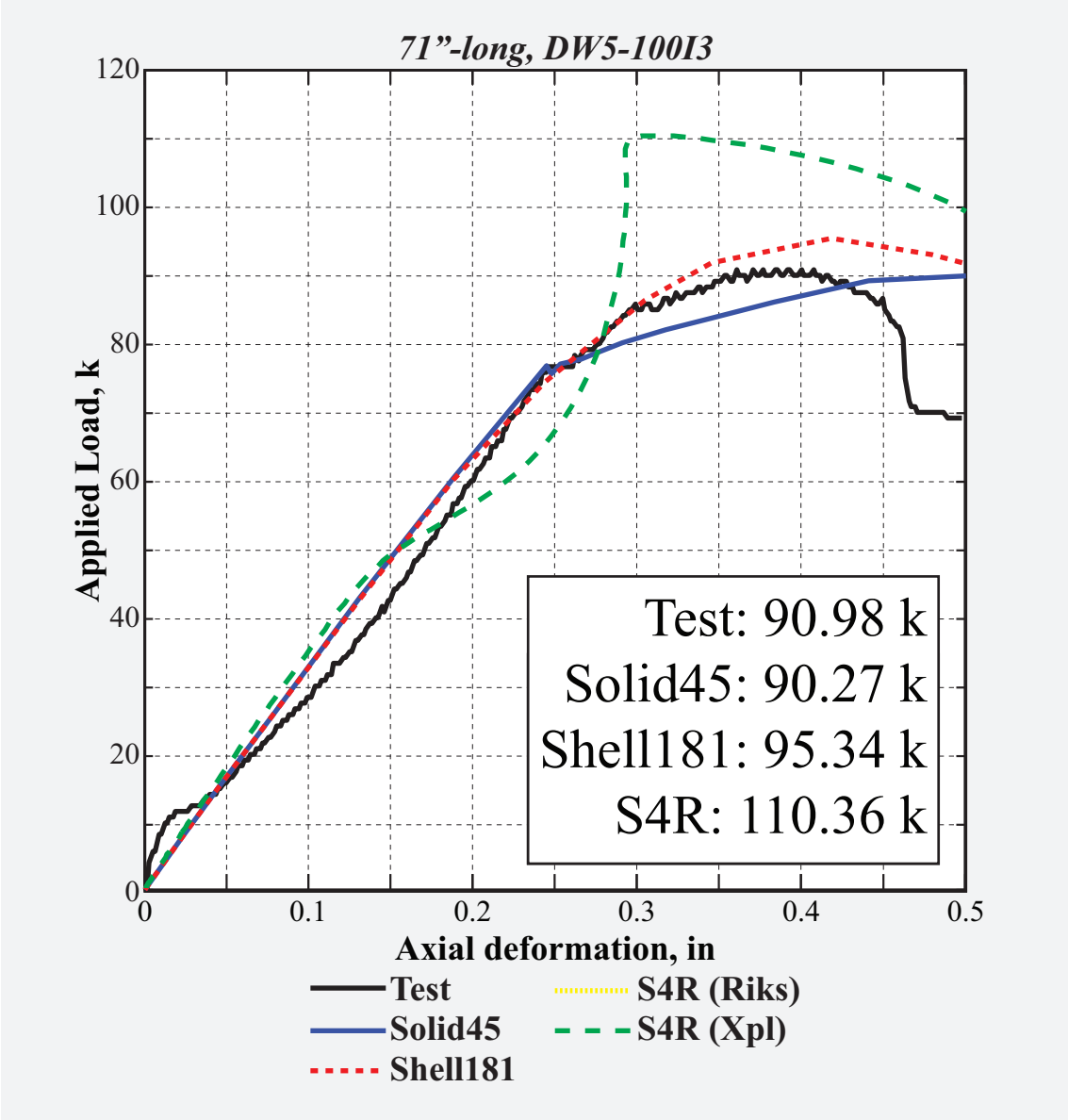


Figure 190: Load vs. deformation history of 71”-long, 0.1”-thick *DW5-I3*.

C QUALITATIVE COMPARISON OF BUCKLED SHAPES

ANSYS deformed configurations at buckle of the members presented in the last columns of Figs. 51-178 are illustrated in Figs. 191-195. Comparisons with actual deformed shapes demonstrating capability of ANSYS and ABAQUS to capture various failure modes are made in Figs. 27-31.

Figure 191: Post-buckling, deformed shapes with von Mises stress contours of the chord and the channel members.

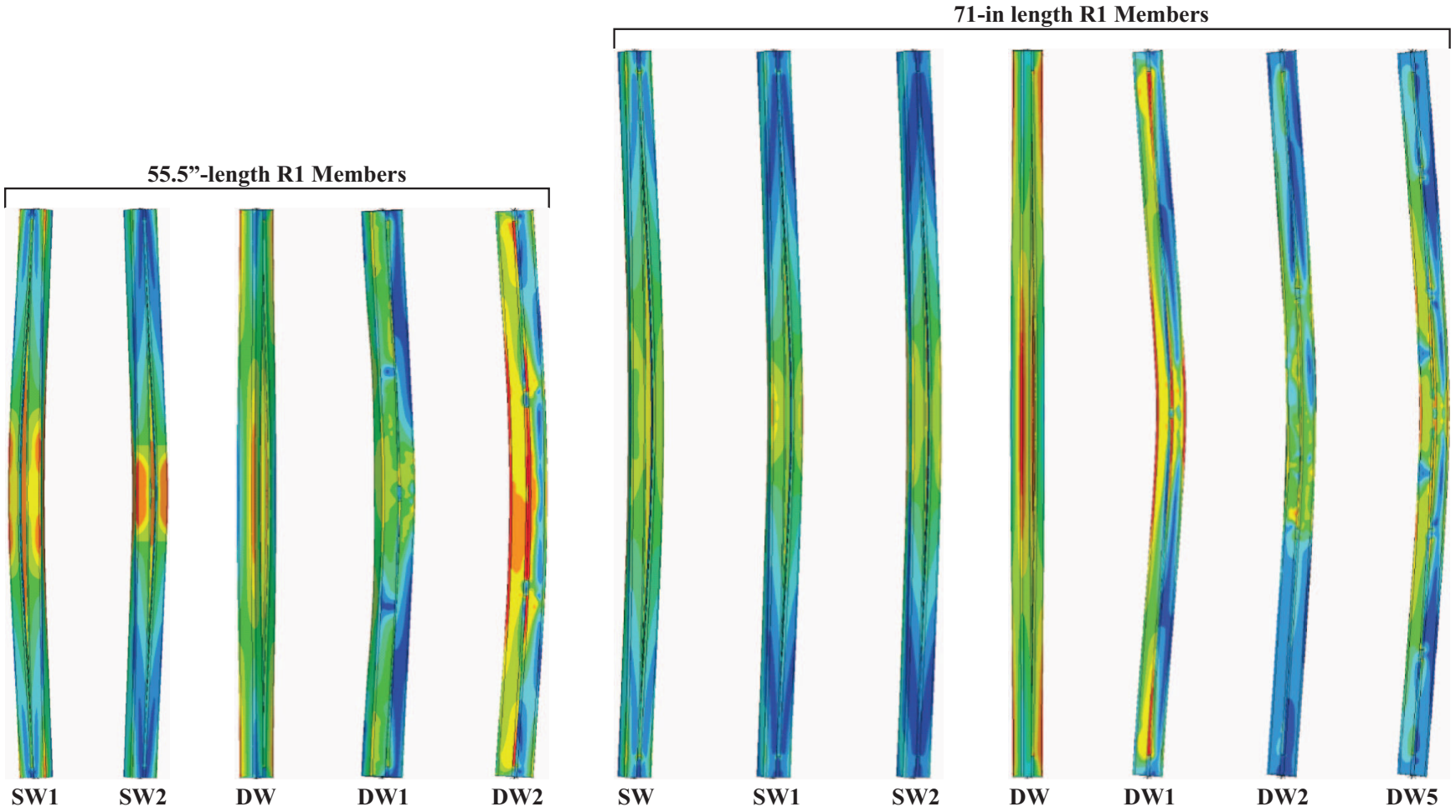


Figure 192: Post-buckling, deformed shapes with von Mises stress contours of *R1*-sections.

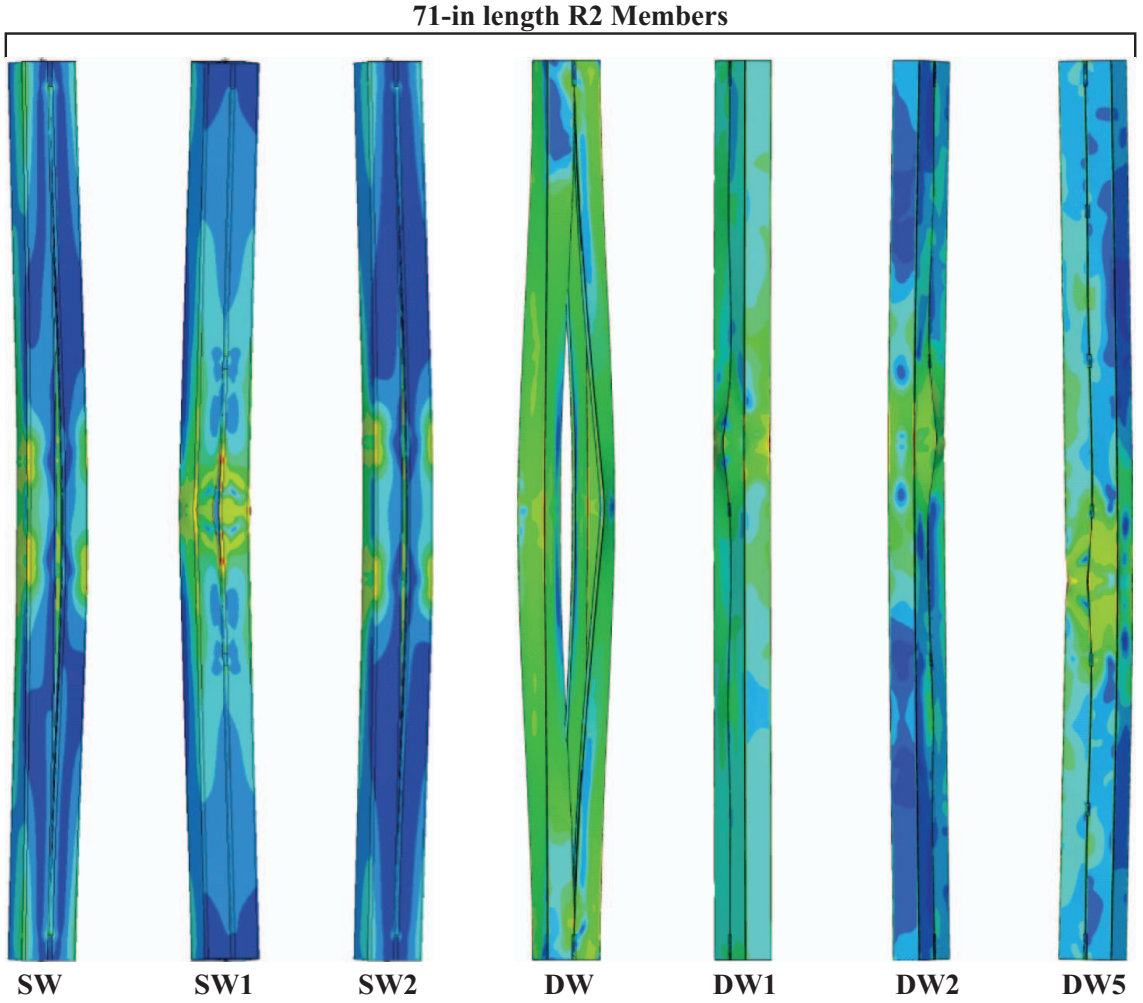


Figure 193: Post-buckling, deformed shapes with von Mises stress contours of *R2*-sections.

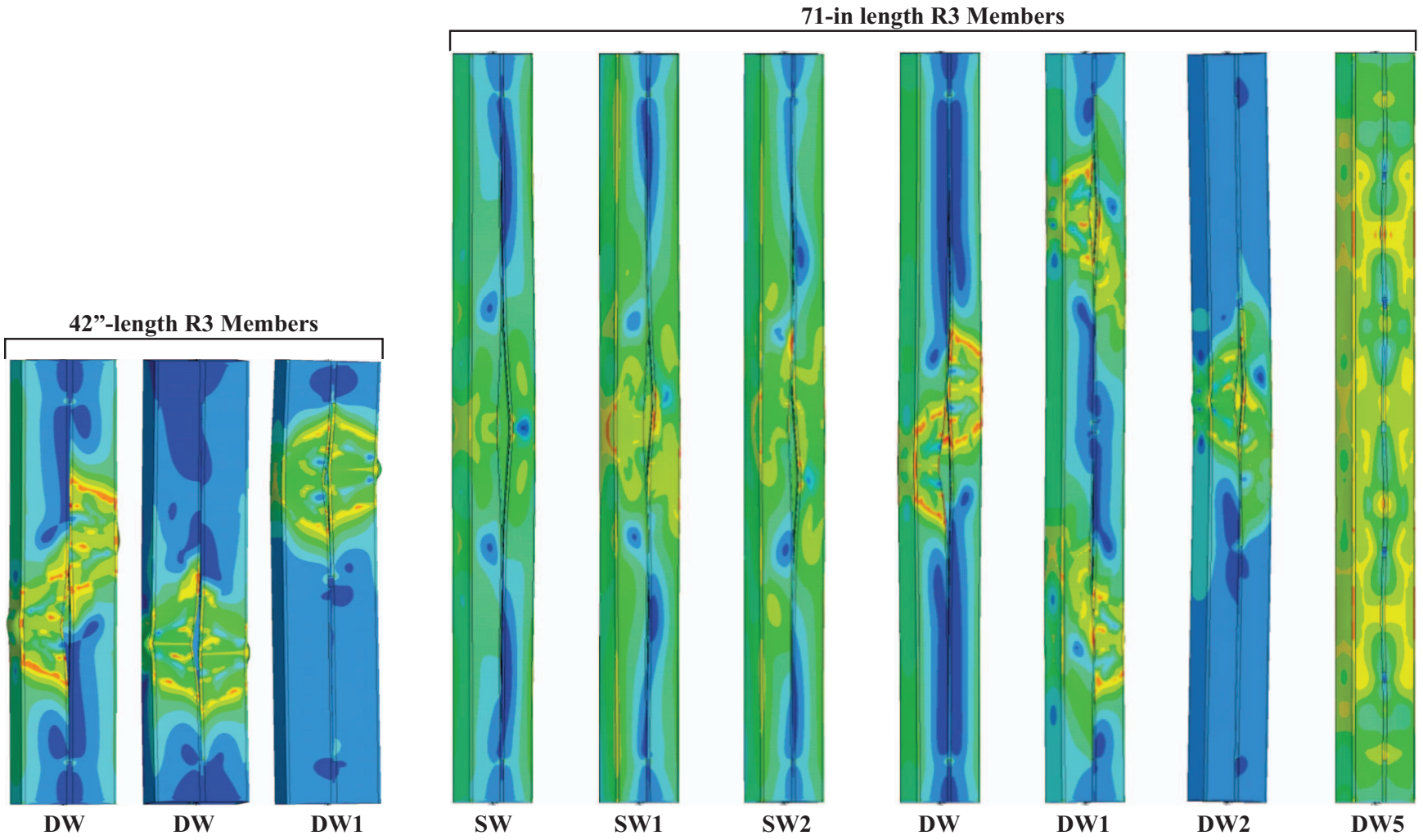


Figure 194: Post-buckling, deformed shapes with von Mises stress contours of *R3*-sections.

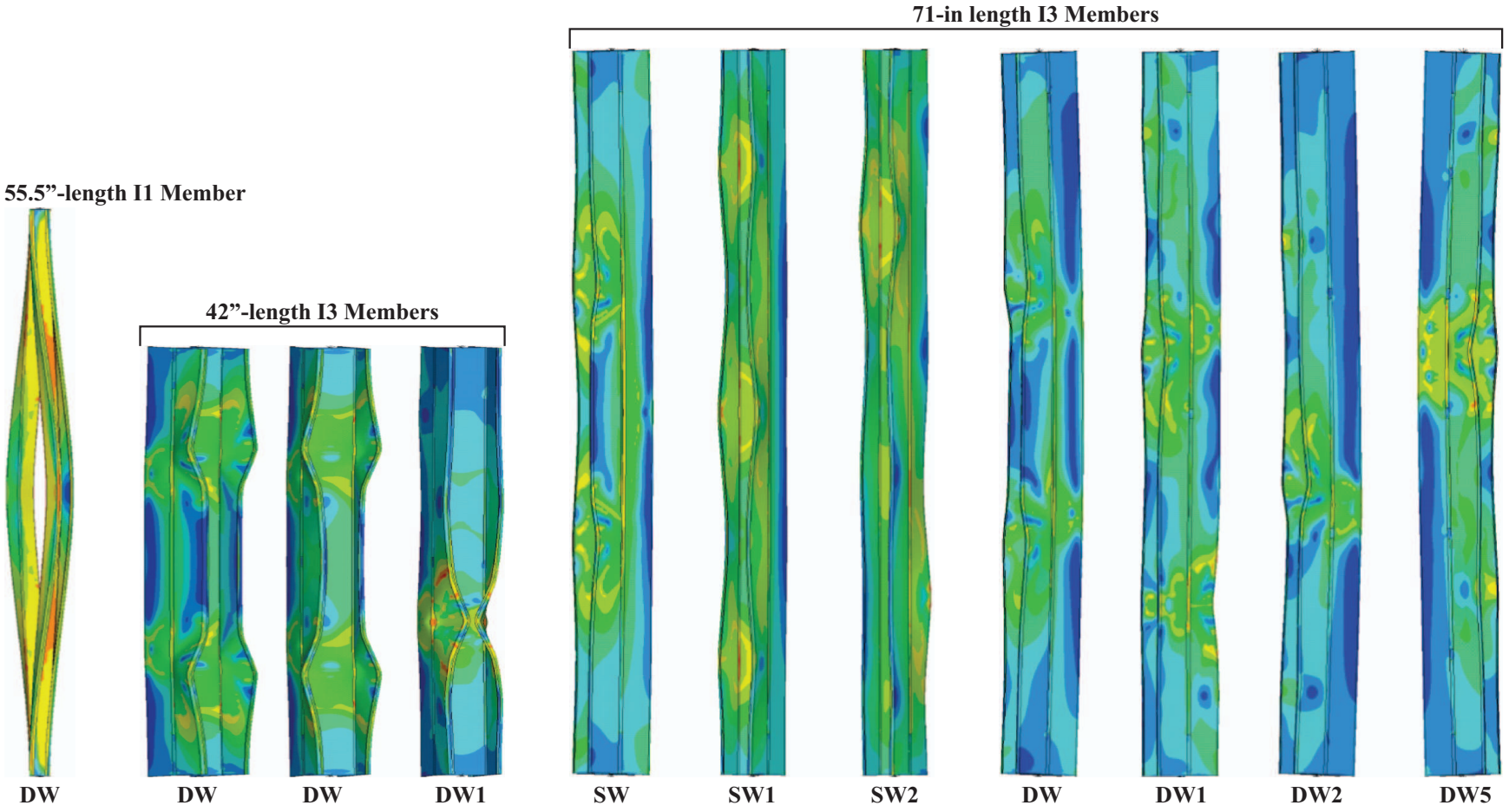


Figure 195: Post-buckling, deformed shapes with von Mises stress contours of *I1*- and *I3*-sections.